Patch antenna and arrays directivity enhanced by adjacent reflective surfaces for satellite communications

Ana-Maria Dorobat

A thesis submitted for the degree of Doctor of Philosophy

Department/School of CSEE

University of Essex

October 2024

To my loving parents ...

Acknowledgements

First of all, I would like to thank The Lord God, Almighty, for guiding me, helping me and granting me the patience and willingness to accomplish this work.

I would like to acknowledge and to thank my supervisor, Prof. Dariush Mirshekar-Syahkal, for his continuous support, encouragement and guidance throughout this research.

I am thankful to Nick Warren and Shahin Salarian for their help and patience to build the antennas. Also, many thanks to Rogers Corporation for providing the necessary material for the antennas.

I would also like to say thank you to Surrey Satellite Technology Ltd for giving me the permission to use their test equipment and facilities for the evaluation of the antennas.

I owe an immense debt of gratitude to my parents, Mandita Ciopeica and Ion Ciopeica, who nurtured my curiosity, supported my educational endeavours from the very beginning and have always believed in me.

Most especially, I would like to thank my husband, Dr. Philip Whittaker, for his love, unconditional support and encouragement.

Abstract

The microstrip antenna is a metallic patch printed on a thin grounded dielectric material. The microstrip antenna operating in its dominant mode, TM010, has been extensively studied and referred to in the literature, and used in applications where broadside and wide beamwidth features are required.

So far, the second mode (TM020) has not been effectively utilised, although there are two noteworthy applications of the second mode which are recorded. In one of them, the design of a reconfigurable pattern rectangular patch antenna based on TM01 and TM02 is presented, using PIN diodes, with the second mode providing a relatively low gain. In the other application, a dual mode patch antenna has been proposed using two different feeding points for pattern diversity applications. In both studies, the pattern reconfigurability of the patch antenna is exploited and not the gain improvement.

In this thesis, the second mode of a microstrip patch antenna (TM020) has been exploited for enhancing the gain of the patch, without resorting to an array configuration. The structure has then been used to develop a steerable array which could be implemented in an application involving Low Earth Orbit (LEO) satellite communications at 30GHz. The small profile and weight of the antenna recommends it for applications where the transmitter dimensions and weight constraints are tight.

A link budget has been calculated based on a scenario with 22 satellites and 58 satellites orbiting at 550 km above the Earth. Based on this scenario, the requirements of the antenna were generated. It resulted in a maximum required antenna beamwidth of 69.3° and 37° (depending on the number of satellites in the orbiting plane) for good adjacent satellite discrimination.

This translated into an antenna gain of 8 dBi and 13.5 dBi respectively. The antenna array designed in this work exceeds these specifications.

A set of 5 antennas have been scaled, built and tested at 10GHz. In general, the measurement results showed good agreement with the simulation results.

For one patch antenna operating in the second mode, both the measured and simulated 10 dB bandwidths were approximately 3.2%. The measured and simulated radiation patterns were very similar, with the gain difference within 0.5 dB (7.3 dB versus 7.1 dB).

The radiation pattern of the patch antenna operating in the second mode showed that the axes of the two beams were almost perpendicular to each other. This led to the anticipation that the gain of the antenna could be improved if a flat conductor or a grounded substrate was fixed perpendicularly under the patch antenna substrate in order to act as a reflector for one of the beams.

The measured 10 dB fractional bandwidth of a feeding patch antenna attached perpendicularly to a reflecting substrate was approximately 3.3%. The presence of the reflecting substrate has improved the gain by approximately 3 dB. The simulated and measured radiation patterns looked very similar, however the measured gain was higher than the simulated gain by approximately 1 dB (11.4 dB vs 10.4 dB).

The measurements of two patch antennas array attached to a reflecting substrate showed 3.4% 10 dB fractional BW. The obtained gain was 13.78 dB (versus 13.3 dB simulated gain).

The measurement of four patch antennas array showed a 10 dB fractional bandwidth of approximately 3.2%.

Although the measured and simulated patterns looked very similar, the measured gain was slightly higher by approximately 1 dB compared to the gain from the simulation (17.3 dB vs 16.2 dB), which translated into 16˚ beamwidth in Phi (+Y) direction.

The gain of the linear structure was further improved by adding reflecting patches on the reflecting substrate. The reflecting patches were illuminated by the lower beam of the feeding patches, which got reflected with a different phase, depending on whether the patches were resonant or not. This concept resembled the mode of operation of a reflect-array antenna.

Two sets of four reflecting patches have been added on the reflecting substrate and the measurement results showed a 10 dB fractional bandwidth of approximately 2.2%. The measured and simulated patterns looked very similar. The measured gain was within 0.5 dB of the simulated gain (18.8 dB vs 18.96 dB), which translated into 21˚ beamwidth in Phi (+Y) direction. The presence of the reflecting patches on the reflecting substrate improved the gain by approximately 1.5 dB compared to 2.5 dB improvement seen in simulations. This was because of the build tolerances and the angle under which the reflecting patches were illuminated by the feeding patches.

30˚ progressive phase was added at the input of each of the feeding patches. The measured and simulated patterns were very similar and the measured gain was within 0.5 dB of the simulated gain (18.4 dB vs 18.7 dB).

The measurement results showed that with 30˚ progressive phase at the input of the patches, the beam steered by approximately 10˚, which is very close to the simulation results, where the beam steered by approximately 7-8˚.

The simulation results showed that as the beam was steered, the main lobe magnitude decreased by approximately 2 dB (for 120˚ progressive phase), and gave a total steering range of 54˚ in total.

Judging by the steering capability of the structure, with 140˚ progressive phase, the beam dropped by 3 dB (to 15.9 dB) and the beam steered 62˚ in total.

Table of Contents

1. Introduction

The microstrip patch antenna typical gain is 7 – 8 dBi [1]. Many methods for gain improvement of the patch antenna gain have been referenced in the literature, including the use of frequency selective surfaces, parasitic patches, superstrates, shorting pins and substrate removal [2]. Some of these methods, can be complex and costly, however, other simpler solutions could be implemented, as: increased substrate thickness, higher dielectric constant substrate, larger size patch, slots implementation, shaped patches, etc. Some of these methods present disadvantages like bandwidth reduction, surface waves occurrence, impedance mis-matching and profile increase [3].

Another simple method for improving the gain of a patch antenna is presented in this thesis, where the second mode of operation of the patch antenna is used in combination with an adjacent reflecting substrate to improve the beam directivity. TM020 mode produces two symmetrical beams around the broadside, which can be combined constructively if an adjacent reflecting plane is conveniently (at 90˚) attached to the microstrip patch substrate.

The microstrip patch antenna operating in a higher order mode can result in lower radiation efficiency due to surface waves and non-optimal current distribution on the patch [4], [5]. However, the exact efficiency depends on the specific design and substrate material used. A higher mode operating patch antenna can provide different radiation patterns, which may be advantageous, depending on the application.

The efficiency, gain and beamwidth that can be obtained with a microstrip antenna operating in the second mode are presented in this work. As demonstrated, these characteristics prove to be sufficient for a satellite communications application, where a small profile, lightweight antenna would be necessary.

The main objective of this thesis is to research and develop a low profile, beam steerable planar antenna array, based on the microstrip antenna operating in the second mode, at 30 GHz mm wave frequency band. This antenna is planned to be used either as a gateway for satellite communications (29.5 GHz to 30 GHz, for example for SpaceX, OneWeb, Telesat,), as a user terminal antenna (as the antennas used on Kuiper Systems [6]) or as a 5G antenna scaled to operate for the 28 GHz frequency band. The 5G antenna would be suitable for different applications like mobile communications (5G antenna integrated in a cellular handset or in a satellite phone handset), Wi-Fi applications (5G antenna integrated in laptops, tablets, etc.), or Internet of Things (IoT) applications. In some cases, the dimensions of the antenna might need to be further decreased, depending on the operating frequency, to meet the low-profile requirements of the application. This could be done by replacing the antenna dielectric material with a higher dielectric constant material.

For 5G cellular applications, this antenna needs to have a high directivity in order to provide a narrow beam to serve the user residing in a very small cell. Beam scanning is also essential because it allows the user to freely move within its cell, while keeping a good, and acceptable contact with the cellular base station.

For the satellite handset application, this antenna requires to have a good communication link with the Earth Observation satellites, especially in cases when the terrestrial infrastructure cannot be employed or used, or in case of natural disasters. Millimetre Wave Laptop antennas can also be developed using the planar antenna array model of this research for providing a good wireless connectivity to the mm wave Gateway.

In the third chapter, a set of requirements are determined for a gateway/user terminal antenna. A directivity of 15 dB has been assumed to allow for a power level of about -90 dBm at the satellite antenna. The antenna must be able to acquire the orbiting satellites and to track them at a maximum speed of 0.79˚/s. This speed occurs when the satellite is at the antenna's zenith point (overhead).

When the satellite is in the furthest point from the tracking antenna, i.e. at nadir (1126 km range if 22 satellites are considered in the orbital plane), the tracking speed for that particular distance is 0.38˚/s. It should also be capable of beam scanning for at least 40˚, which is the minimum required when the orbit is fully populated with satellites (58 in total).

The tracking duration depends on the tracking speed and the distance to the satellite. If it is considered the highest tracking speed (0.79˚/s), then the 40˚ range would be covered in approximately 50 seconds. However, given that the tracking speed decreases as the satellite moves away from the ground station, the tracking duration increases to about 1.5 mins.

This analysis suggests that the required beam scanning is rather slow and hence no fast phase shifters are necessary in the case of the antenna array of concern in this research.

The antenna beamwidth should not be wider than 69.3˚ (for 22 satellites per plane) or 37˚ (if the number of satellites increases to 58) for a good satellite discrimination. This constrains the antenna gain. If the planar antenna to be developed for satellite communication applications, it must comply with the EPFD limits in order to avoid creating interference to the existing Geostationary Satellites.

The uplink Effective Power Flux Density (EPFD) limits of the transmitting earth station are presented in 47 CFR §25.146(c) and Article 22 of the ITU Radio Regulations [7]. For 27.5-28.6 GHz and 29.5-30 GHz bandwidths, the EPFD limit is -162 dBW/m^2 measured in 40 KHz bandwidth.

For 5G applications, the antenna must comply with the RF EMF exposure guidelines published by the International Commission on Non-Ionizing Radiation Protection (ICNIRP), IEEE and US Federal Communications Commission (FCC). The values required by the aforementioned regulators determine the Total Radiated Power and the Effective Isotropic Radiated Power Levels required by the 3rd Generation Partnership Project (3GPP) to support sufficient coverage and limit interference.

As presented in [8], the Incident power density limits set by ICNIRP and IEEE are 30.12W/m^2 measured on an averaging area of 4 cm^2, at 30 GHz frequency and 10W/m^2 limit set by FCC. The Maximum Permissible Transmitted Power due to Incident Power Density limits determines the Maximum Peak EIRP which must comply with the 3GPP requirements.

In general, for small antenna arrays, at 30 GHz, The Maximum Permissible Transmitted Power is measured at a distance d = 5 mm away from the surface of the antenna in a 1 cm^2 area. For a 4x4 Antenna array, at 30 GHz, the Maximum Permissible Transmitted Power to comply with FCC requirements is 10.4 dBm and 11.9 dBm for ICNIRP and IEEE. For the same antenna size, the Maximum EIRP levels that comply with the RF EMF exposure Limits specified by ICNIRP, IEEE and FCC are: 30 dBm and 24.6 dBm.

Publication [9] presents a good example of uplink budget calculation from a user equipment towards a Very Low Earth Orbiting Satellite (VLEO) at 28 GHz.

In this research work, it will be demonstrated that the microstrip patch antenna gain can be easily improved, without implementing expensive and complicated methods, and that the efficiency of the antenna operating in the second mode matches the simulated efficiency of 83%.

2. Background

Satellite broadcasting of television is a major source of revenue for the satellite communications industry compared to the satellite mobile services. Geostationary satellites have carried television programs since their inception for commercial service in the late 1960s [10]. Nowadays, as the online streaming has increasingly become of great interest for viewers, through services such as Netflix, Amazon, BBC-iPlayer, Hulu, YouTube and Roku, the traditional television networks had to re-evaluate the way they operate. However, there are still many areas on the Globe, where the Internet infrastructure (Optical Fibre) is lacking and the installation costs are very high. In those areas, the Satellites coverage is essential and as a consequence, the media convergence becomes inevitable (for example the IPTV-based satellite delivery) [11].

The satellite mobile communication providers use the Earth Orbiting Satellites to relay a signal from a terrestrial terminal or handset to another ground station. This service is essential for users that operate in areas that are not covered by the terrestrial mobile networks. The Mobile Satellite Communications are usually used by the remote industrial businesses, by the Government and defence customers, in emergency response situations or by recreational customers [12].

Satellite phone systems use geostationary equatorial orbit (GEO- for example Inmarsat, Thuraya, Sky Terra, Terrestar) or low Earth orbit (LEO- for example Globalstar, Iridium) satellites. GEO satellites orbit at about 36,000 kilometers (22,400 miles) above the Earth's equator, and can provide near-continuous global coverage with 3 satellites. These satellites are called Geostationary because they appear fixed from Earth. They move at the same angular velocity as the Earth and orbit along a path parallel to Earth's rotation, providing coverage to specific areas. From the ground, GEO satellites appear to be stationary. Because of the Earth curvature, the GEO satellites are not able to cover areas above or below ±70˚ Latitude [13], [14].

Besides the coverage inconveniences in areas closer to the Earths' Poles, the latency encountered with the GEO satellite mobile services (around 560ms signal round trip) have made the government and the private/public organisations to debate whether the LEO satellites are more effective in providing communications. As the Technology advances, topics like price, coverage, maintenance and infrastructure needed for the LEO/GEO or even MEO (Medium Earth Orbit) constellations are continually discussed [14].

2.1 Importance of Low Earth Orbiting (LEO) satellites in Mobile communications.

The Low Earth Orbits and the Medium Earth Orbits are closer to Earth (160 km-2000 km and 2000 km-35575 km) than the Geostationary Satellite Orbits (GSO-36000 km), therefore with these satellites less powerful amplifiers are required on the ground, the latency reduces substantially and the throughput can be increased. These satellites are in continuous motion and they are less susceptible to jamming or non-approved interception. [15]

With the GEO satellite system, the line of sight between the user's satellite phone and the satellite can be broken by obstacles like hills, forests, etc., especially at high latitudes. Before using the satellite phone, the user must find an area where the line of sight is clear.

With the dense LEO satellite constellations, at different altitudes and in various orbiting planes (for example, inclined, near polar orbiting planes), the high latitude limitations, encountered with the GEO systems, are eliminated.

In the worst scenario, even if the signal is blocked by an obstacle, the high dynamics of the LEO satellite constellations relative to the ground, would bring in a few minutes (or even instantaneously, if the constellation density is high) another satellite in the line of sight of the user.

Recently, small satellites like cubesats, nano and pico satellites have been manufactured and deployed to support a wide range of Internet of Things (IoT) as well as broadband applications. They form a communication network in space (for example Kepler, Telesat, Starlink constellations) to support and complement 5G New Radio and Beyond communications.

The integration of these small satellites with 5G will bring mobile broadband enhancement with increased data rates, massive Machine Type Communications to enhance the range of IoT applications, Ultra Reliable Communications to provide low latency etc.

The low manufacturing costs, size and weight (under 500Kg) of the satellites reduce the launching costs and encourage the deployment of highly dense LEO satellites constellations [14].

Figure 2-1 presents an overview of the unique characteristics of LEO small satellite constellations with respect to the GEO satellites, as they are presented in [14].

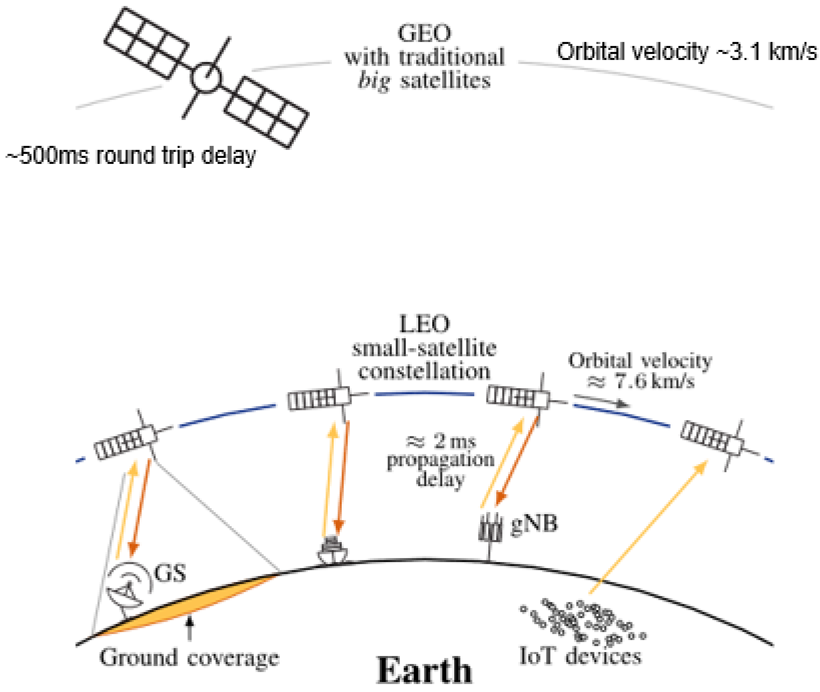

Figure 2-1: The Characteristics of LEO constellations with respect to GEO satellites [14]

The wireless communications via LEO satellites present an advantage in propagation delay compared to the terrestrial communications via fibre. This is because in free space the electromagnetic waves propagate at the speed of light, whereas in optic fibre, the speed is around 1.47 times slower. This would even lead to a lower propagation delay with a LEO constellation than with the terrestrial optical fibre networks over long distances [14].

A constellation of LEO satellites can provide continuous, global coverage as the satellite moves. Unlike GEO satellites, LEO satellites also rotate around Earth at a much faster speed because of their proximity to Earth. For example, an Iridium satellite travels at approximately 27,358 km/h (completing an orbit every 100 minutes), compared to a GEO satellite that typically has a speed around 11,265 km/h [15].

Each NGSO (Non-Geostationary Satellite Orbit) satellite is visible to an Earth station for a short period of time (5-20 mins) and during this period, the Earth station must upload and download as much data as possible [16].

LEO satellites typically have an orbital period of about 90-110 minutes, they travel at an approximate speed of 7.5 km/sec, which makes them visible to a ground station for a short period of time, about 6-8 times during a day. The position between a satellite with regards to a ground station will vary on each pass of the satellite because the Earth is moving at the same time - See Figure 2-2 [18], [19]. In consequence, on each pass, the orbiting satellite will appear at a different elevation angle to the ground station.

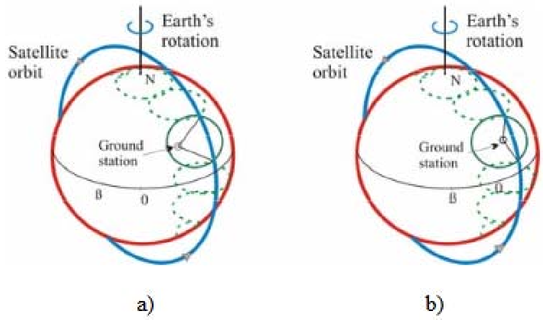

Figure 2-2: Satellite pass for an Earth rotation angle of B per orbit a) first pass and b) second pass [17]

Once the ground antenna has lost the line of sight to the satellite, it must move in the direction of the next up-coming satellite and link to it. The Earth station, must therefore be able to communicate through handoffs between satellites, it must continuously move and be high performing. The LEO constellations require smaller ground antennas, but a larger number than the GEO constellations do.

The satellite-to-satellite communication will require fewer terrestrial gateways, therefore the security is enhanced. Any gateway that communicates with a LEO satellite needs to receive the satellite’s position regularly and it must transmit this information to terminals continually. Types of satellite tracking employed include TLE (Two Line Element) tracking and Step tracking [16].

The satellite coverage area (footprint) is defined as a region on the Earth from where the satellite is seen under the lowest elevation angle. Achievement in antenna technology brought in the multibeam LEO systems where the footprint or coverage area is divided is many cells (multibeam arrays) in order to enhance frequency reuse policies. The frequency reuse inside a footprint is achieved by applying the space diversity policy. Handover from one cell to another is defined as ‘cell handover’. Particularly, the interference problems have to be treated carefully [19].

2.2 LEO Satellite Constellations Examples

The most important parameters in designing a satellite constellation are: the type of the orbit, the altitude of the orbit, the number of orbits, the number of satellites in each orbit, the satellite phase factor (which defines the angular distance between satellites) between different orbit planes.

Presently, there are two popular LEO satellite constellation topologies: The Walker Delta constellation with circular orbit geometry and the Walker Star constellation with circular near polar orbit. The two constellation types are illustrated in Figure 2-3.

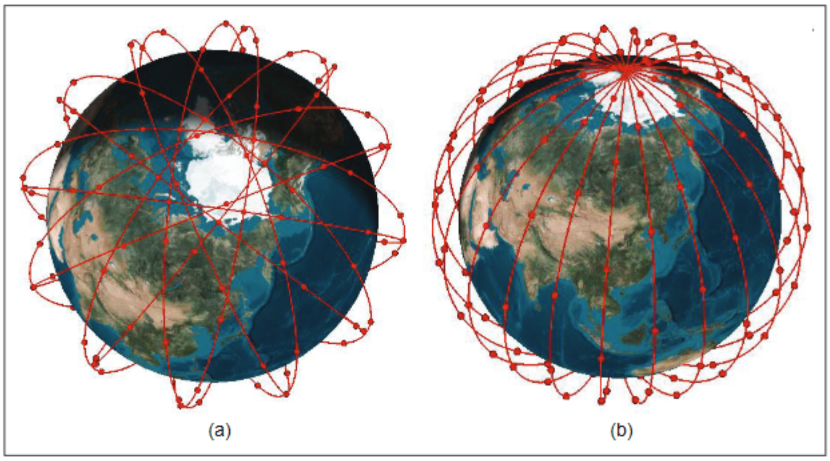

Figure 2-3: Constellation types for LEO satellite system: a) Walker Delta; b) Walker Star [20]

In Delta configuration, the orbit inclination can be adjusted to control the overlapping coverage in certain areas. For example, the overlapping coverage at the poles can be minimised, while the overlapping at the Equator can be increased. With this configuration, it is not possible to establish a stable ISL (Inter-Satellite Link) with satellites in adjacent orbital planes because the relative position between satellites constantly changes.

In the Star configuration, the satellites move constantly from North to South or from South to North. As a consequence, each satellite can connect with another satellite in the same plane or in adjacent planes. One problem that occurs in this constellation type is the 'orbital seam' phenomenon. The movement of a satellite can be in an ascending orbit (S-N) or in a descending orbit(N-S). An orbital seam is formed between two orbits in different directions (retrograde orbits). This is a region where satellites in counter rotating planes pass each other in opposite directions. The relative movement of the satellites moving in the same direction, but in different orbits, (i.e. in prograde orbits) is fixed, but in retrograde orbits, the relative speed of satellites is twice the speed of one satellite. As a consequence, the handover between satellites becomes more frequent. Another problem in the Walker Star constellation is the overlapping coverage at high latitudes, especially at the poles. This produces severe interference between satellites, especially if some of them use the same frequency. In this sense, beam turn-off and turn-on strategy is usually applied between satellites [20]. This strategy represents one coordination method between satellites operators, required by the International Telecommunication Union (ITU). By switching off during the inline geometry cases, interference can be reduced to acceptable levels.

In terms of coverage schemes, there are two popular schemes adopted for the LEO satellite constellations: the Spot Beam coverage and the Hybrid-Wide Spot Beam coverage.

In the spot beam coverage scheme, the LEO satellites provide multiple spot beams to cover one area on Earth. These beams can be arranged in different shapes, but the pattern of the individual beams cannot be changed and this can lead to an inefficient coverage system. Also, as the coverage area of an individual spot beam is small (for example 450 km diameter beam on the Iridium System), frequent handovers between beams occur and this could degrade the user experience.

In the Hybrid-Wide Spot Beam coverage scheme, each LEO satellite provides a wide beam to cover the service area, but also some steering beams (within the wide beam coverage area) for users employing digital beam forming techniques. The spot beams are fixed to the users, even when the satellite is moving, and this assures high data-rates, according to the user's demands. The wide beam is fixed and used for telemetry and control and the handover between the satellites happen only when the user with its spot beam comes at the edge of the wide beam. This coverage scheme is very complex and requires a sophisticated access procedure for the user terminal [20].

2.2.1 SpaceX – Under development

According to the first application to the Federal Communication Commission (FCC), in 2018, the SpaceX NGSO satellite system would consist of 4,425 satellites arranged in a Delta constellation (plus in-orbit spares) operating in 83 inclined orbital planes (53˚, 53.8˚, 74˚, 81˚, 70˚, at altitudes ranging from 1,110 km to 1,325 km), as well as associated ground control facilities, gateway earth stations and end user earth stations [21].

However, in December 2019 SpaceX received the approval from FCC to reduce the number of satellites to 4409 and to operate 1584 satellites at the lower altitude of 550 km, instead of 1150 km, as it was initially planned, in 72 inclined planes at 53˚, with 22 satellites per orbit.

In April 2021, FCC approved another request from SpaceX, to reduce the total number of satellites to 4408 and to operate the rest of the remaining satellites, i.e. 2824, at altitudes between 540-570 km range as follows: 1,584 satellites operating at 540 km, with an inclination of 53.2˚, in 72 orbital planes with 22 satellites per plane, 720 satellites operating at 570 km, with an inclination of 70˚, in 36 orbital planes with 20 satellites per plane; 348 satellites operating at 560 km, with an inclination of 97.6˚, in 6 orbital planes with 58 satellites per plane; and 172 satellites also operating at 560 km, with an inclination of 97.6˚, in 4 orbital planes with 43 satellites per plane [22]. Because of the atmospheric friction at this lower altitude, this relocation will significantly enhance space safety by ensuring that any orbital debris will quickly re-enter and demise in the atmosphere. Due to its closer proximity to consumers on Earth, this modification will allow SpaceX's system to provide low-latency broadband to unserved and underserved Americans that is on par with service previously only available in urban areas. Given the atmospheric drag at these lower altitudes, this relocation will ensure that all of SpaceX's satellites will quickly re-enter and demise in the atmosphere when no longer needed for operations [23].

The system is designed to provide a wide range of broadband and communications services for residential, commercial, institutional, governmental and professional users worldwide. The total throughput per satellite in envisioned to be 17-23 Gbps, depending on the characteristics of the user terminals [21], [24]. Advanced phased array beamforming and digital processing technologies within the satellite payload give the system the ability to make highly efficient use of Ku-Ka-band spectrum resources and the flexibility to share that spectrum with other licensed users. The system will employ optical inter-satellite links for seamless network management and continuity of service. The optical intersatellite links operate at a much higher frequency than RF links, generally at near infrared bands (for example at 1064 nm or 1550 nm wavelength).

User terminals operating with the SpaceX system will use phased array technologies to allow for highly directive, steered antenna beams that track the system's LEO satellites. Gateway Earth stations also apply advanced phased array technologies to generate high gain steered beams to communicate with multiple NGSO satellites from a single gateway site [21], [24].

Table 2-1 and Figure 2-4 present the Frequency bands used by SpaceX. It uses RHCP (Right Hand Circular Polarisation) for user uplink and downlink and LHCP (Left Hand Circular Polarisation) for telemetry data. It also uses 250 MHz downlink channels and 500 MHz uplink channels (in both RHCP and LHCP) for the gateway links. SpaceX's system architecture allows for on-board demodulation, routing and re-modulation, in this way, decoupling the user and gateway links. This allows them to use different spectral efficiencies in the uplink/downlink channels, maximizing the capacity of the satellites, to dynamically allocate resources for the user beams and mitigate the interference by selecting the convenient frequency bands [24].

The contours for all transmit and receive beams are essentially the same for satellites operating in all planes and altitudes. With the new satellites' altitudes, SpaceX is authorized to operate with earth station elevation angles as low as 25˚ for user terminals and gateways, and for gateways in the polar regions (above 62˚ latitude) it is authorized to operate with earth station elevation angles as low as 5˚ [22].

Table 2-1: Frequency Bands Used by the SpaceX System [25]

Type of Link and Transmission Direction	Initial Frequency Ranges	Final Frequency Ranges
User Downlink Satellite-to-User Terminal	10.7 - 12.7 GHz	10.7 - 12.7 GHz
Gateway Downlink Satellite to Gateway	10.7 - 12.7 GHz	10.7 - 12.7 GHz 17.8 - 18.6 GHz 18.8 - 19.3 GHz 19.7 - 20.2 GHz
User Uplink User Terminal to Satellite	14.0 - 14.5 GHz	12.75 - 13.25 GHz 14.0 - 14.5 GHz
Gateway Uplink Gateway to Satellite	14.0 - 14.5 GHz	14.0 - 14.5 GHz 27.5 - 29.1 GHz 29.5 - 30.0 GHz
TT&C Downlink	12.15 - 12.25 GHz	12.15 - 12.25 GHz 18.55 - 18.6 GHz
TT&C Uplink	13.85 - 14.00 GHz	13.85 - 14.00 GHz

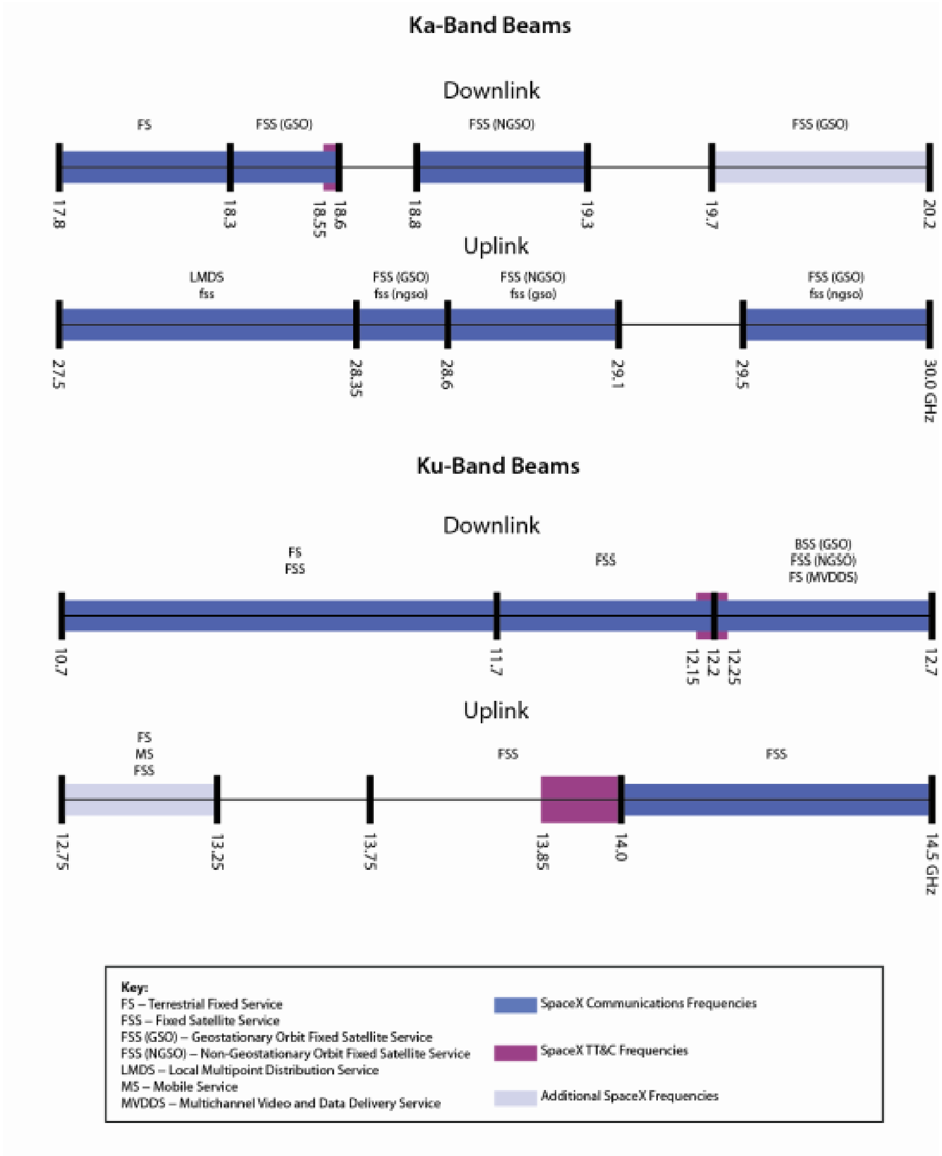

Figure 2-4: Frequency Plans and FCC Spectrum Allocations [21]

As shown in Figure 2-5, each satellite operating at an altitude of 550 km will provide service up to 25˚ away from nadir, covering an area of about 2.7 million square km (940.7 km radius). By definition, nadir is the point on the Earth’s surface that is directly below a satellite in orbit. As the transmitting beam is steered, the power is adjusted to maintain a constant PFD (Power Flux Density) at the surface of the Earth, compensating for variations in antenna gain and path loss associated with the steering angle. The highest EIRP (Effective Isotropic Radiated Power) density (-15.75 dBW/4 kHz for Ku and 15.7 dBW/4 kHz for Ka) occurs at about 53˚ steering angle for Ku and 57˚s for Ka. For the receiving beams, the antenna gain drops slightly as the beam slants away from the boresight. As a result, the maximum gain over noise temperature figure, i.e. G/T (8.4 dB/K for Ku and 13.7 dB/K for Ka) occurs at boresight, while the minimum G/T (4.9 dB/K for Ku and 11.1 dB/K for Ka) occurs at maximum slant.

SpaceX launches its satellites using its own launch vehicles (Falcon 9 or Falcon Heavy) and there will be two launching stages: in the initial stage, 1600 satellites will be launched into the orbits and the system will become operational after the launch of the first 800 satellites. In this stage, SpaceX will be offering services in the ± 60˚latitude band. In the second stage, the remaining 2825 satellites will be launched and this will ensure global coverage [24].

The deployment to a lower altitude guarantees removal of satellites from orbit within a relatively short period of time, and consequently has beneficial effects with respect to orbital debris mitigation. At the same time, the power flux density (PFD) emissions are reduced and the interference environments improved. Lowering the minimum elevation angle improves the customer experience and the low altitudes also improve the speeds and latency.

In order to avoid interference with other systems (GSO or NGSO), SpaceX has the following attributes:

- Highly directional earth station beams
- Ability to select from multiple visible satellites for service
- EPFD (Effective Power Flux Density) limits

- Avoiding in-line events (22˚ or less) or apply the band segmentation in absence of any coordination agreement with the other operators [21].

SpaceX seeks to operate in the V-band frequencies (40 GHz-75 GHz) as well and it intends to launch another 7,518 VLEO (Very Low Earth Orbiting) satellites in order to provide robust broadband services, as a result of combining the LEO and VLEO systems into one coordinated system [26].

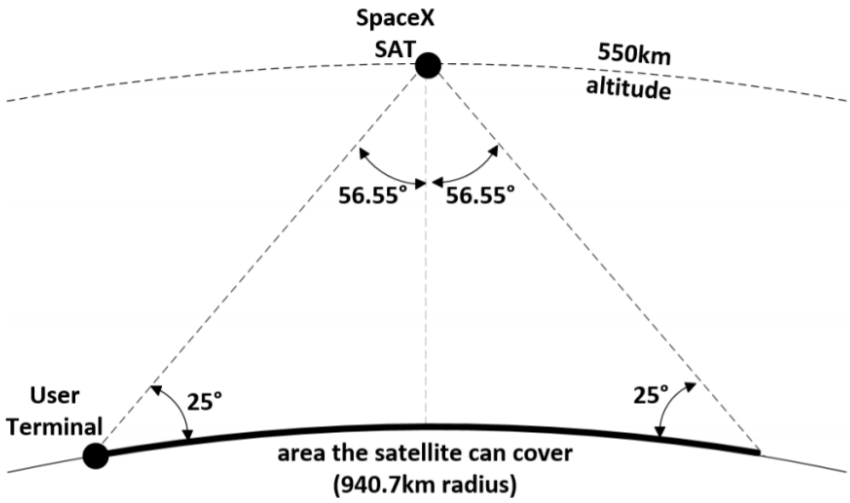

Figure 2-5: Steerable Service Range of Ku-band Beams [25]

As of March 2024, the total number of satellites operating at LEO altitudes is over 6000.

The satellites provide broadband services in rural and remote areas in the world where the population density is relatively low. The first generation of Starlink Satellites, is capable of providing internet speeds of 80Mbps to 150Mbps for downlink and 30 Mbps for uplink. However, SpaceX promised improved services with the second-generation satellites launched into the constellation The system is already serving users in Washington, Oregon, Idaho, and other states in the northern US. The company has also brought the service overseas to the UK, Germany, and New Zealand.

To benefit from the Starlink's service, the user must use the 59 cm diameter Starlink phased array antenna and a Wi-Fi Router, which has been assigned to a single cell. Given the User Uplink and Downlink frequencies shown in Table 2-1, it results a Tx and Rx antenna gain of about 36-38 dBi. If the user attempts to remove the Starlink dish from its assigned cell, the service will be disrupted [27].

2.2.2 Eutelsat OneWeb

The initially planned Eutelsat OneWeb NGSO satellite system consisted of a Star type constellation of 720 LEO satellites, plus in-orbit spares, in 18 near polar circular orbits (87.9° inclination), at altitudes of 1200 km, as well as associated ground control facilities, gateway earth stations and end user earth stations. Each orbiting plane contained 40 satellite and the overall system implemented the bent-pipe architecture (there is no on-board processing capability) [24].

This NGSO system uses Ku-band for the RF links between the satellites and user terminals. The user terminals consist of small and inexpensive antennas (30 cm-75 cm which means a gain between 32.86 dBi-40.8 dBi at 14 GHz and a 3 dB beam width between 2°-5°) that can be: mechanically steered parabolic reflectors and/ or low-cost phased array designs or other beam steering technology already under development. In April 2023, Intellian signed a contract with OneWeb for flat panel user terminals production.

For the mechanically steered antennas, the satellite tracking is achieved by the use of two independently steerable apertures, or for certain applications of a single antenna aperture that can quickly switch pointing direction between the active satellites using data buffering to ensure no loss of transmitted information.

The Ka band gateway Earth Stations (envisioned to constitute 50 or more, with up to 10 gateway antennas each [24]), typically use 2.4m (which means a gain of 57.24 dBi at 29 GHz and a beam width of 0.3°) or larger antennas depending on their location, service requirements and propagation characteristics.

Table 2-2 presents the frequency bands used by the One-Web NGSO satellite system. OneWeb uses RHCP polarisation for the user downlinks and LHCP for the user uplinks [24].

Table 2-1: OneWeb NGSO system Frequency bands [28]

Type of Link and Transmission Direction	Frequency Ranges
Gateway - to - Satellite	27.5 - 29.1 GHz 29.5 - 30.0 GHz
Satellite - to - Gateway	17.8 - 18.6 GHz 18.8 - 19.3 GHz 19.7 - 20.2 GHz
User Terminal - to - Satellite	12.75 - 13.25 GHz 14.0 - 14.5 GHz
Satellite - to - User Terminal	10.7 - 12.7 GHz

According to [28], Each OneWeb satellite has 16 identical Ku-band user beams (250 MHz bandwidth), each consisting of a non-steerable highly elliptical spot beams. There are also two identical steerable gateway beam antennas (125 MHz bandwidth), operating in the Ka band and each of these antennas creates an independently steerable circular spot beam.

A user will be progressively handed over from beam to beam within a OneWeb satellite and then handed off to the beams of the next satellite in the same orbital plane, or as required, to a satellite in the adjacent orbital plane. For gateway links, the second gateway antenna on each satellite is used to enable the handover so the gateway link alternates between the first gateway beam and the second gateway beam [28].

The service will be available only in regions where the users and a ground station are simultaneously within the Line Of Sight of the satellite. That is because the satellites do not use inter-satellite links [24].

The frequency reuse in the Ku-band will be achieved by reusing the same frequencies between geographically separated beams of the same satellite. In the Ka band, the orthogonal circular polarisation for the transmissions to the active gateway earth station will permit the frequency reuse.

Each of the Ku-band spot beams is highly elliptical with its major axis in the E-W direction and minor axis in the N-S direction. The 16 beams are arranged in a single row in the N-S direction to create an almost square footprint on the Earth. Figure 2-6 illustrates the highly elliptically beams in the N-S direction.

The pointing of the satellite can be adjusted so the beam pattern can be moved in the N-S direction relative to the nominal nadir pointing direction. This feature is used to control the power levels generated in certain directions by the OneWeb system [28].

For the links between the satellites and the gateway stations, there is a minimal arrival angle of 15˚. Every point on the Earth’s surface will see at all times a OneWeb satellite at an elevation no less than 55° with increasing the minimum elevation angles with latitude.

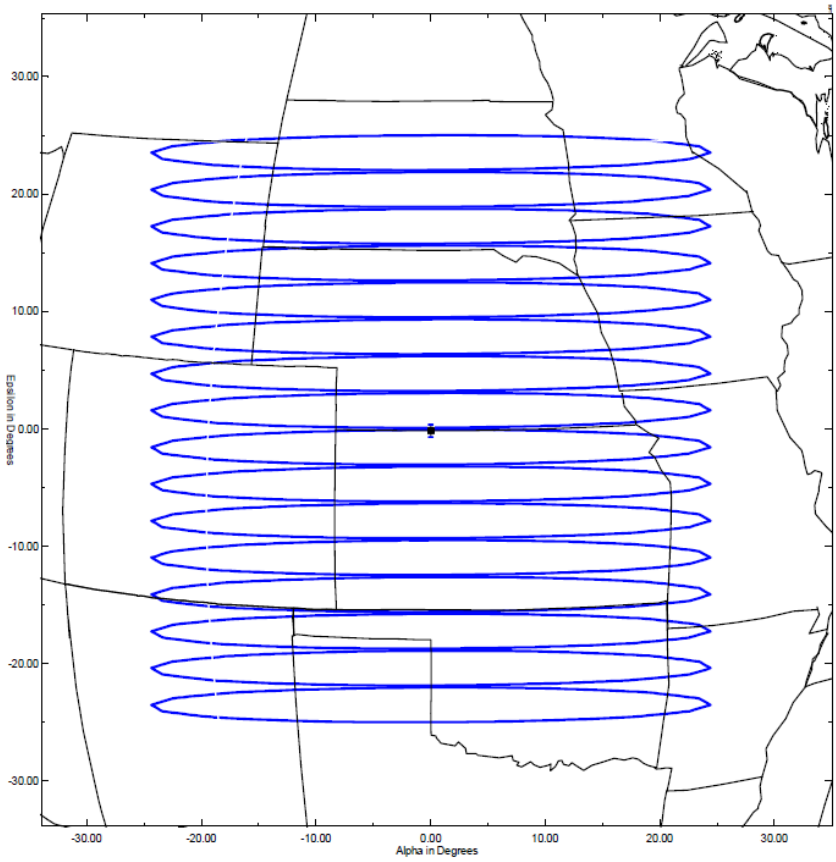

Figure 2-6: Ku band beam array for a single OneWeb satellite [28]

To protect the GSO satellite networks from interference, the pointing directions of the Ku-band beams are adjusted as the OneWeb satellites move towards the Equator. When the pointing direction adjustment is not sufficient to comply with the EPFD limits, certain Ku-band beams are turned off. [28]

The satellite broadband service should be capable of offering the following capabilities: Speed- (to/from UT) 25-50Mbps/5Mbps, Volume-100GB/month, latency-30ms for backhaul services and Internet access. As a basic service, without Internet access this should include: Speed-5Mbps/1Mbps, Volume-10GB/month, latency-30ms. [29]

With the 36 satellites launched in April 2020, OneWeb takes in its orbit constellation a total of 146 spacecrafts. That was the third in a five-launch programme to enable OneWeb's first connectivity solution to be service ready by the end of 2021 across the United Kingdom, Alaska, Northern Europe, Greenland, Iceland, the Arctic Seas and Canada [30]. As of May 2023, OneWeb launched 634 satellites which are all operational.

2.2.3 Telesat – Under development

In November, 2017, Telesat has been granted the request for building a 117 Ka band satellite constellation at low earth orbiting altitudes. The system consists of 11 orbital planes in total, from which 6 inclined circular orbital planes (99.7˚), with 12 satellites per orbit, at an altitude of 1000 km, and another 5 inclined circular orbital planes (37.4˚), with 9 satellites per orbit, at 1248 km [31].

The Polar Orbits will provide general global coverage, whereas the other 5 inclined orbits will focus on regions on the Globe where the population concentration is high. The adjacent satellites from this constellation (within the same plane or within adjacent planes) will communicate via optical inter-satellite links, therefore a user would be able to connect to the system from anywhere in the world.

It is not necessary for the user and the gateway to be simultaneously visible to the satellite, as it is on OneWeb. The minimum elevation angle for a user is 20˚ [24], [77].

The satellites are authorized to operate in the 17.8-18.6 GHz (space-to-Earth or downlinks), 18.8-19.3 GHz (space-to-Earth), 19.7-20.2 GHz (space-to-Earth), 27.5-29.1 GHz (Earth-to-space or uplinks), and 29.5-30.0 GHz (Earth-to-space) frequency bands.

Each satellite will carry on board processing module capable of demodulating, routing, re-modulation and a direct radiating array. The array will be able to form 16 beams for the uplink and another 16 for the downlink and the beams will be shapeable, with power, bandwidth, size and boresight dynamically assigned for a minimum interference to GSO and NGSO satellites.

Each satellite will present 2 steerable gateway antennas and a wide receiver beam for signalling. Several gateways are distributed geographically around the world, each presenting multiple 3.5m antennas [24], [31].

In May 2020, Telesat applied for a ‘Modification of market access authorisation’ to FCC, in which more satellites were to be added in each orbit and the constellation altitude was changed.

In the first phase of its plan, Telesat will add 181 satellites to its Constellation, bringing the total in Phase 1 to 298 satellites (the “Modified Constellation”). In the second phase of its plan, Telesat will add 1373 satellites, bringing the total at the end of Phase 2 to 1671 satellites (the “Final Constellation”). The modifications are shown in Table 2-3.

Table 2-2: The Modified Constellation of Telesat [32]

Parameter		Telesat Grant	Modified Constellation	Final Constellation
Polar Sub-constellation	Orbital planes	6	6	27
	Satellites per plane	12	13	13
	Inclination (deg)	99.5	98.98	98.98
	Altitude (km)	1000	1015	1015
	Total satellites	72	78	351
Inclined Sub-constellation	Orbital planes	5	20	40
	Satellites per plane	9	11	33
	Inclination (deg)	37.4	50.88	50.88
	Altitude (km)	1248	1325	1325
	Total satellites	45	220	1320
Total satellites in constellation		117	298	1671

Telesat's Modified and Final Constellations (named Telesat Lightspeed) will deliver Gbps downlink speeds anywhere on earth and will allow a much more affordable and ubiquitous provision of broadband services across the United States. The sub-constellation architecture will enable global coverage and low latency but will require sophisticated inter-satellite laser links (ISLLs) for military LEO constellation applications [32], [33].

Telesat launched the first satellite in its constellation in January 2018, and now it is supporting live demonstrations across a variety of markets and applications. The low-latency, high throughput performance, satellite tracking and Doppler compensation are tested and experienced as well. Recent LEO-1 demonstrations include applicability for a public safety broadband network, 5G mobile network backhaul, connectivity to transportable antenna systems, including antennas in aircraft, and advanced antenna technology for the U.S. Navy [32].

The technical specifications of the Telesat satellites are presented in [33], where the maximum data rate values show up to 7.5 Gbps offered to a single terminal and up to

20 Gbps offered to a single “hotspot” site, such as remote communities, airport hubs and sea ports. The commercial services are envisioned to commence in the second half of 2023 [34].

As of November 2023, the Lightspeed constellation has only 3 satellites launched, with up to 198 satellites being planned for launching in 2026.

2.3 LEO Shortcomings

The growing demand of satellite communications has led to new satellites, new constellations and new applications development. Most of the new satellites will be small satellites, flying in constellations in Low Earth Orbit (LEO). Most of the new Low Earth Orbits are Polar or Near Polar and a very large number of satellites are planned to be launched on these orbits. Even if the paths of the orbits vary, there are still some concerns about the eventual collisions that may occur because of the density of the satellites in the Non-Geostationary Satellite Orbits (NGSO).

Compared to GSO systems, a large number of LEO satellites must work together in order to cover the entire Earth. Many constellations need to rely on Optical Inter-Satellites Links for satellite-to-satellite communications. [17]

As the size of the LEO satellites are much smaller than the GEO satellites, their launch costs are considerably lower compared to the costs involved for the big geostationary satellites launch. The Software Defined Radio (SDR) trend, which means the replacement of the analog radio components (like modulator and filters) with software, diminishes the physical space needed on the spacecraft, and also, the development and configuration costs. For example, the 5Kg Kepler satellites (CubeSats-multiple of

10 by 10 by 10 cm units) employ the SDR technology [35]. Moreover, private companies like SpaceX developed the technology for the launch system reuse, applied on their Falcon 9, Falcon Heavy and Starship rockets [36]. All these advantages and facilities increase the number of LEO satellites in space, but raise concerns related to space debris mitigation and to the complicated manoeuvres against collisions between the spacecrafts.

However, given the low altitudes of the satellites, at their end of life, the spacecrafts will easily enter into atmosphere, but in a controllable manner, to avoid the collision with other satellites orbiting at lower altitudes [25], [37], [38].

Another disadvantage of the LEO satellites is their operating life-time which is almost half (about 5 years) of the GSOs' life-time and this is because of the effects of atmosphere on them. Because of the friction, the satellites suffer from fast orbital decay and for that, they need to be frequently re-boosted back into the orbit. Moreover, the Van Allen radiation may have effects on the sensors, integrated circuits and solar cells of the satellites and in general, on the life of the satellites [18].

At the ground, given the dynamics of the LEO satellites, the receiving antennas must be agile enough to continuously track the visible satellite. The antennas can be mechanically steerable, electronically steerable or both mechanically and electronically steerable. For the mechanically steerable antennas, the appropriate mount type must be selected in order to avoid the gimbal-lock positions of the rotational axes that may occur when the satellite passes at zenith or at low elevation angles.

The communication at low elevation angles can be hindered by the natural barriers. As a consequence, the detection of the satellite above the natural barriers enables the practical horizon to be determined. The practical horizon differs from the ideal one for around 2-3˚ in elevation. [18]

2.4 Types of Antennas Used on LEO Satellites

Tracking and communicating with LEO satellites require rugged and high performing antennas. This necessity comes from the continual movement of the satellites and their high-speed relative to the ground station. These antennas must be agile and keep the contact with the visible satellite from horizon to horizon and then retrace to a position for the next upcoming satellite. There are several types of antennas that can be used to track LEO satellites: mechanically steered antennas (the X/Y mount antennas and El/Az antennas), electronically steered antennas (phased arrays) and hybrid antennas (fixed beam antennas that use mechanical positioner) [16]. This Chapter describes different types of antennas used for LEO Satellites tracking, giving some examples of existing commercial terminals. Different types of antennas implemented in Mobile devices and 5G communications are presented in the second part of the Chapter. The last section of this Chapter outlines the main thesis objectives.

2.4.1 Mechanically steered antennas

The Elevation over Azimuth antennas with parabolic reflectors are the most common type of antenna mount, used for broadcasting services, with GEO satellites. Although the GEO satellites appear to be fixed relative to the Earth, in reality they are continuously perturbed by the Moon, Earth, Sun forces and solar radiation pressure.

These perturbations make the satellite to drift in the E-W direction, and therefore, the satellite operator must perform some manoeuvres in order to maintain the satellite within its assigned station-keeping box [39].

As a consequence, the earth station antenna must be able to track the satellite within its station keeping box, especially if the ground station antenna is large, and/or operates at high frequencies (large antennas and high operation frequencies determine a narrow beamwidth). The station keeping box represents the satellite's assigned longitude and inclination box which is typically within +/- 0.1°. For tracking, antenna controllers are usually employed to impose the pointing angles necessary for tracking to the motorised system. The tracking process involves only small Az-El axis rotations, and for this purpose, the motorised Elevation over Azimuth antennas are generally used.

For the Low Earth orbiting satellites, the Elevation over Azimuth antennas could work well, especially if the satellite is not passing right at the zenith (overhead) of the antenna. But because the maximum data rate occurs when the satellite is at the maximum visibility angle to the earth station, these passes must not be skipped. The geometry of these types of antenna mounts determines the presence of a keyhole area when the antenna is positioned at the zenith. In short, a data acquisition antenna must have its maximum slew rate capability (the rate at which the antenna's position changes) at zenith. But at zenith, the satellite's angular velocity is maximum and the slew rate could reach tens of degrees per second, which is not achievable in practice.

For LEO tracking, a third axis is required to dynamically change the base tilt of the antenna. In general, El/Az antennas need to move at a typical speed of 5˚-10˚ /s to track a LEO satellite [16].

The X-Y antennas are the most used and the most efficient mechanically steered antennas for tracking LEO satellites. The aperture can range from 1.2m to 12m. This design pushes the keyholes (areas of data loss) to the horizons. The secondary axis (Y) is placed orthogonally to the primary axis (X) such that the secondary axis is horizontal when the antenna is pointed at the zenith. These antennas must move at a typical speed of 3˚ / s to track LEO satellites.

Figure 2-7 presents the EL-Az and X-Y mount configuration.

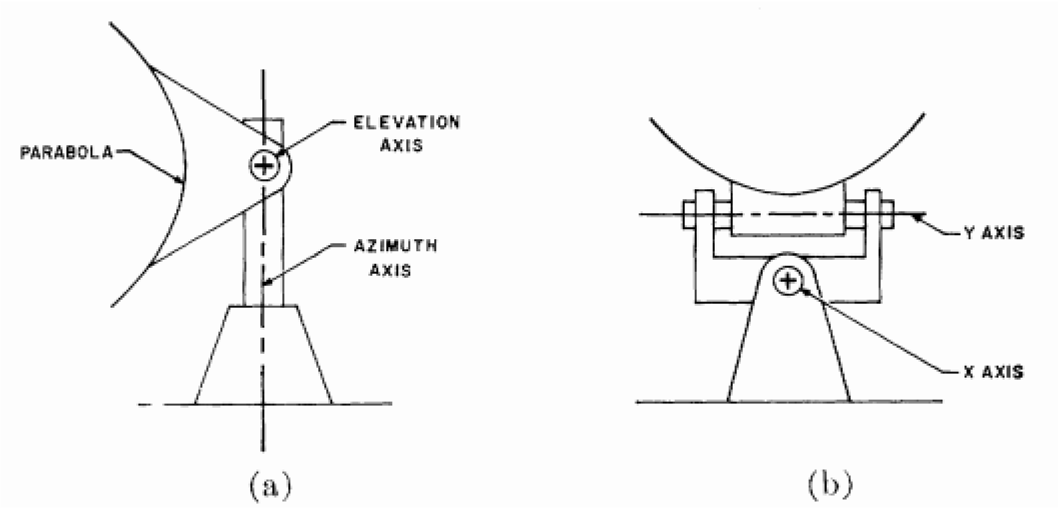

Figure 2-7: Antenna mount types: (a) Elevation over Azimuth mount, (b) X-Y mount [40]

2.4.2 Electronically steered antennas

The Flat Panel Antenna is the most convenient type of antenna for tracking LEO satellites. The Electronically steered array antennas can steer the beam very quickly, eliminating the keyhole issues encountered on mechanically steered antennas.

In a Planar Array the radiators are positioned along a rectangular grid and they are used to scan the beam toward any point in space. According to the Linear Array Theory, the total radiation field of an array, assuming no coupling between the elements, is equal to the sum of the individual element radiations. After a series of mathematical calculations and approximations, it results that the total field of the array is equal to the field of a single element positioned at the origin multiplied by a factor, referred to as Array Factor.

For the Planar Array illustrated in Figure 2-8, the overall Array Factor, in the X-Y plane, is the multiplication result between the Array Factor of the Elements along the X axis and the Array Factor of the Elements along the Y axis.

$$AF_X = \sum_{m=1}^{M} I_x e^{j(m-1)(kd_x sin\theta cos\phi + \beta_x)} \tag{2.1}$$

$$AF_Y = \sum_{n=1}^{N} I_y e^{j(n-1)(kd_y sin\theta sin\phi + \beta_y)} \tag{2.2}$$

$$AF_{TOT} = \sum_{m=1}^{M} I_x e^{j(m-1)(kd_x sin\theta cos\phi + \beta_x)} \sum_{n=1}^{N} I_y e^{j(n-1)(kd_y sin\theta sin\phi + \beta_y)} \tag{2.3}$$

Where: I_x , I_y are the magnitudes of the excitation;

d_x , d_y are the spacing between the elements along the axes.

β_x , β_y are the progressive phase shift between the elements along the axes.

k is the wavenumber: $\frac{2\pi}{\lambda}$.

The normalized form of Equation (2.3) can also be written as:

$$AF_{TOT}(\theta,\phi) = \left\{\frac{1}{M}\frac{\sin\left(\frac{M}{2}\psi_x\right)}{\sin\left(\frac{\psi_x}{2}\right)}\right\}\left\{\frac{1}{N}\frac{\sin\left(\frac{N}{2}\psi_y\right)}{\sin\left(\frac{\psi_y}{2}\right)}\right\} \tag{2.4}$$

Where:

$$\psi_x = kd_x sin\theta cos\phi + \beta_x$$

$$\psi_y = kd_y sin\theta sin\phi + \beta_y \tag{2.5}$$

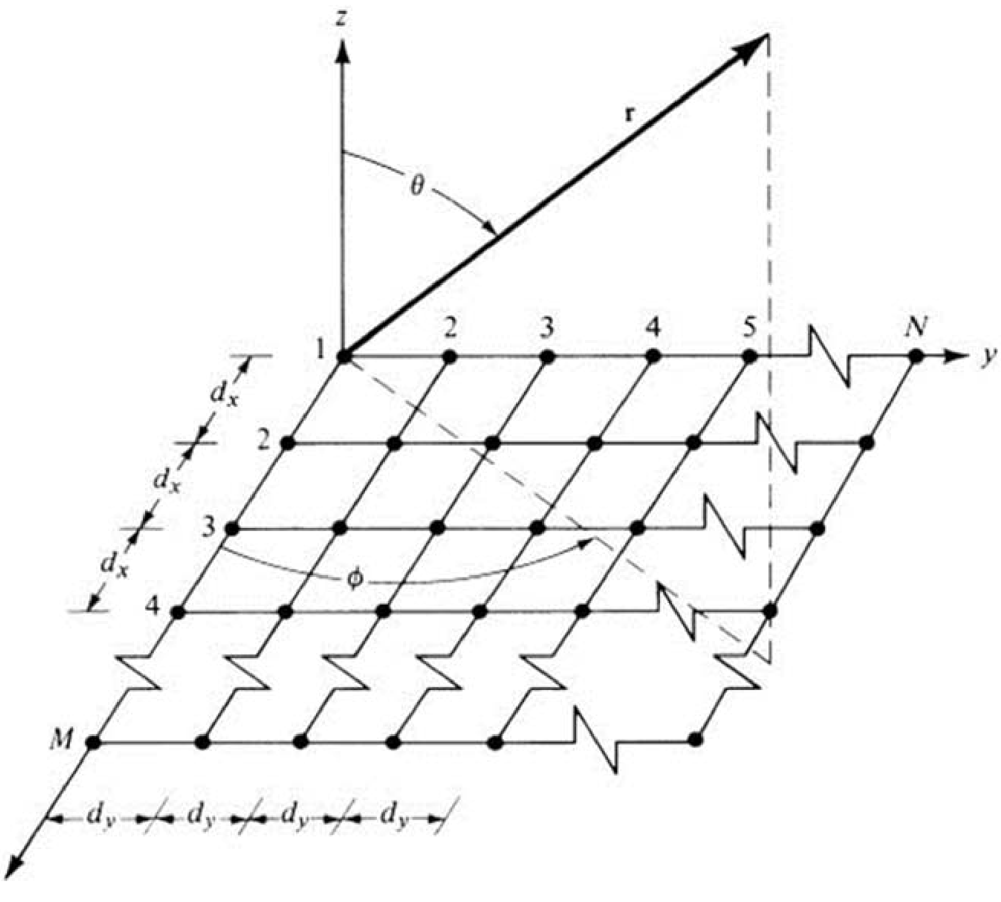

Figure 2-8: Planar Array Geometry [41]

The spacing between the elements in the x and y directions must be less than half of a wavelength (d_x , d_y < $\frac{\lambda}{2}$), otherwise the radiated fields will combine in phase in more than one direction and it will give rise to grating lobes.

Thus, by controlling the progressive phase difference between the elements, the maximum radiation can be squinted in any desired direction to form a scanning array. This is the basic principle of the electronic scanning phased array operation.

The maximum radiation of an array can be squinted in any direction if the progressive phase difference between the array elements is continuously varied. This is usually accomplished with diode phase shifters, ferrite, MEMS, Liquid Crystals [41].

The PIN diode presents an intrinsic layer between the p and n layers which makes it suitable for high frequencies applications. When reversed biased, the diode presents high impedance, while when forward biased the diode is left in a low impedance state [42][43].

With these properties, the PIN diodes can be used as RF switches. The forward bias current is typically 10-30 mA and the reverse bias voltage is typically 10-60V. The small size and the high speed make the PIN diodes more advantageous than the ferrite phase shifters. However, the diodes phase shifters require in general more power than the ferrites as they involve continuous bias current, while a latching ferrite device requires only a pulsed current to change its magnetic state [42].

There are 3 types of PIN diode phase shifters: switched line, loaded line and reflection.

Figure 2-9 presents the Switched Line phase shifter. The differential phase shift between the 2 paths is: $\Delta\phi = \beta(l_2 - l_1)$, where β is the propagation constant of the line [42]. The PIN diodes are employed as switches, switching the bias current from the forward to the reverse bias mode. The PIN diodes present a separate DC bias circuit, separate from the RF path. Under forward bias, the diodes impedance is reduced and under reverse bias the impedance is high, opening and closing the paths to provide the $\Delta\phi$ phase shift.

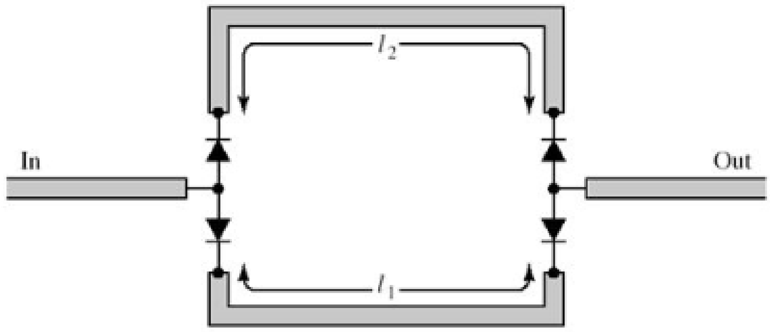

Figure 2-9: Switched Line Phase Shifter [42]

The Switched Line Phase Shifters provide phase shifts of 180˚, 90˚, 45˚, etc. One of the problems introduced by this phase shifter is the resonance of the OFF line if its length approaches λ/2 or multiple of λ/2.

For small amounts of phase shift (45˚ or less), the loaded line phase shifter is used. The phase shift introduced by the loads is:

$\Delta\phi = tan^{-1} b/2$ Where b=BZ0. B represents the shunt load susceptance and Z0 is the characteristic impedance of the line - see Figure 2-10.

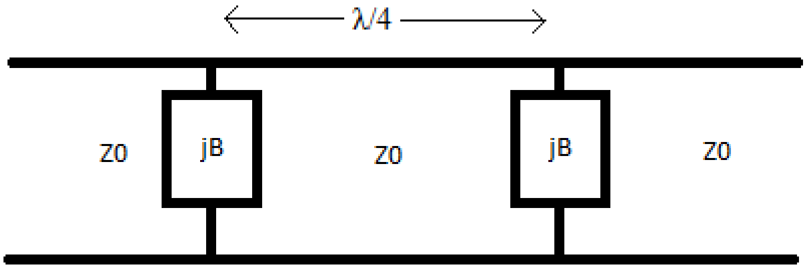

Figure 2-10: Loaded Line Phase Shifter [42]

The λ/4 length line will reduce the reflections from the shunt susceptance. The Susceptance is determined by the diodes and will change from capacitive to inductive as the diodes are switched between states [43].

The reflection type phase shifter is presented in Figure 2-11:

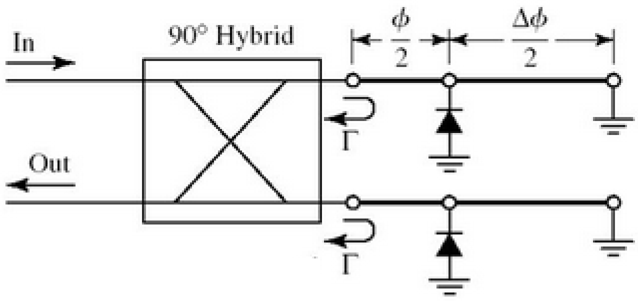

Figure 2-11: Reflection Phase Shifter using a quadrature hybrid [42]

The path length of the reflected signal is controlled by the state of the PIN diodes. The input signal is equally divided by the hybrid coupler. The diodes are biased in the same state such that the reflected signal at the output port will add in phase. The total phase shift at the output port is equal to Δφ.

The Varactor diode is also used as a phase shifter element but unlike the PIN diode, the junction capacitance varies with the applied reversed bias voltage, thus providing an electrically adjustable reactive circuit element [42].

For ferrite phase shifters, the magnetic field within the ferrite controls the phase, and the intensity of the magnetic field is controlled by the amount of current flowing through the wires that wrap the ferrite. In General, ferrite phase shifters are heavy and bulky, compared to the diode phase shifters and require significant switching power [41], [44].

MEMS are mechanical switch-based phase shifters and present insertion loss comparable to the diode devices. They are light structures, require low power for switching, the switch time is very fast, but these phase shifters are not very reliable.

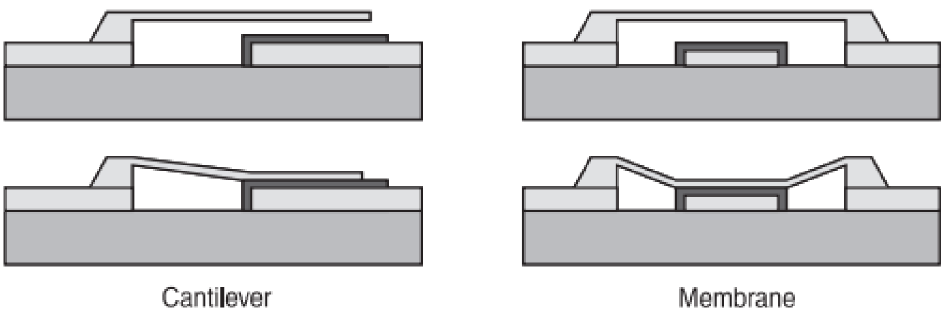

Figure 2-12: Micro Electro Mechanical Switch (MEMS) [44]

Figure 2-12 presents two types of MEMS: on the left side, the cantilever arm is pulled down by an electrostatic field to rest on a dielectric spacer, while on the right side, the membrane deflects like an oilcan. The change in capacitance is used to produce the desired isolation.

Another way to achieve beam steering is by using Liquid Crystals as substrate. The material properties (dielectric constant) are varied by an external voltage. Therefore, the resonant frequency of the radiating elements changes and this, in turn, shifts the beam [45].

The main concerns regarding these phase shifters are: the insertion loss, the number of elements needed in an antenna array and their power consumption. As these elements are directly involved in element radiation, they cause high insertion loss. High phase errors can result because of the quantization loss that provides a limited number of phase states. Liquid Crystals also introduce losses that reduce the gain and efficiency of the structure [46].

One issue that occurs with the scanning arrays is the low elevation scanning loss. This refers to a significant power transmission loss when the beam scans at low elevation angles. Beam spreading, interference from ground reflections and the reduction of the collecting area represent the reasons for the loss. If the target is at low angles, and the beam is pointed in that direction, the effective collecting area of the array decreases considerably, therefore very little signal is intercepted. The cosine roll-off represents a common term in phased array theory and it can be visualized if considering a flat surface. At broadside, there is a maximum area of interception. As the angle moves away from broadside, the area visible reduces following a cosine function [47].

When the antenna scans to wide angles, the electromagnetic wave propagates along the array structure. This can either have no effect on the total field, as the adjacent elements do not intercept the energy, or the energy can be coupled into the elements. In this case the field can be re-scattered from the structure, and combine with the original radiated field (eventually with the sidelobes). Another possibility is to have the intercepted energy directed into the input port of the element, from where it gets transmitted into the system. This energy gets absorbed by the system, resulting in gain reduction. There is also possible to get the energy reflected back to the antenna from the input port. This will re-radiate with a phase that may degrade or not the overall pattern. All these possibilities are discussed in [48].

In [49] and [50], the authors discuss about the catastrophic pattern degradation called ‘scan blindness’, which results in almost complete cancellation of all radiation for certain scan directions. Scan blindness does not occur in finite arrays, but a severe mismatch in input impedance takes place at a scan angle where the infinite array containing active elements is blind. This phenomenon occurs when the surface waves couple into transmission and no power is received or transmitted at that angle. The phase of the surface wave matches the phase propagation of a mode supported by the substrate. At this particular blind scanning angle, the mode of the periodic structure excited by the phased array, becomes complex because the array is “designed” to radiate and thus one Floquet mode of the guided mode appears into the visible range. When this occurs, the field is both propagating and attenuating along the array plane, resulting in power loss through the substrate and in a large input mismatch [49], [50].

Another issue that occurs with the scanning arrays is the beam squint phenomenon. That is, for a given beam direction, the phase shift required between elements changes with the frequency, or, for a given phase shift, the beam direction changes as a function of frequency [51].

All these challenges must be carefully treated in the antenna design stage in order to achieve the highest gain and scanning range.

Presently, there are a few companies that have developed flat panel antennas for NGSO satellite communications. The main concern about these antennas is the price, weight and dimensions. In the next sub-section, the characteristics of some of these antennas will be presented.

2.4.2.1 Kymeta Phased Array

In 2017, Kymeta introduced its first commercial metamaterial based flat panel antenna for satellite communications. Metamaterials are materials that are specially engineered to provide artificial electromagnetic properties, such as a negative index of refraction. The metamaterial properties are determined by the periodic arrangement of scattering structures that are smaller than the wavelength of the electromagnetic waves they are interacting with. These small structures are fabricated from conventional materials such as metals and plastics, but their size, shape, orientation, and configuration can be designed to interact with electromagnetic waves to create finely tuned resonances and other unconventional properties in certain frequency bands.

The resonance frequency of each antenna element is tuned to implement a dynamically reconfigurable diffraction grating, and define the antenna beam holographically. The metamaterial is placed adjacent to the broad wall of a rectangular waveguide feed structure that couples all the elements to a radio frequency wave generated by a single transmitter (Figure 2-13).

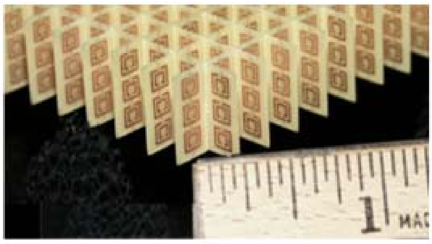

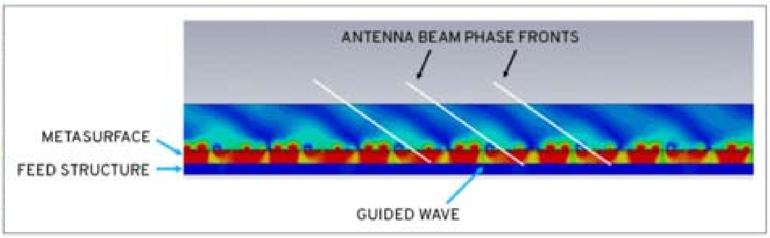

Figure 2-13: Metamaterial periodic structure (Left), Antenna Cross-Section (Right) [52]

The elements are individually tuned by computer to radiate the guided wave, and those that radiate in phase, at a certain scan angle, are tuned to scatter strongly, while the other elements that do not contribute constructively to the overall radiation, are detuned, not to radiate. The bandwidth of the antenna beam is determined by the tuneable range of the elements, each element being tuned by varying the permittivity of Liquid Crystal material.

The antenna can operate in full duplex mode, and this is achieved by interleaving the Tx and Rx elements, and controlling them independently. The polarisation can be dynamically switched between linear and circular, and the beam can be steered 360˚ in Azimuth and from 15˚ onwards in Elevation. The radiation complies with ITU and FCC power spectral density (PSD) masks to minimize adjacent satellite interference, which can result from the beam broadening that occurs with increasing scan angle [52].

The antenna is scalable, and for LEO satellite applications, a 20 cm aperture can provide around Mbps, a Tx EIRP of 33.8 dBW, and a receive gain of 28.6 dBi [50]. In March 2021, Kymeta demonstrated the tracking and acquisition capability of a LEO Kepler satellite, in extremely cold weather. The u8 Antenna (shown in Figure 2-14) operates in the Ku band, is 89.5 cm × 89.5 cm x 12.3 cm and weights 25 Kg. The Rx

Frequency band is 10.7-12.75 GHz, and it presents a G/T Figure of 9-11 dB/K at Broadside and 6-9 dB/K at 35˚ Elevation. The Tx Frequency Range is 13.75-14.5 GHz and the Tx Gain is between 33.5-34.5 dBi at Broadside, and 31-32.5 dBi at 35˚ Elevation. It requires a DC input power between 12-36VDC [53], [54].

Figure 2-14: Kymeta U8 antenna

Kymeta antenna is the very first commercial Flat Panel Antennas for the Non-Geostationary Satellite Orbits, but it's complicated design, increased the unit price considerably. Also, the antenna is heavy and can present high dimensions for some applications.

2.4.2.2 Phasor Phased Array

Phasor Electronically Steerable Antenna presents a Software Defined Antenna Architecture. The entire RF Chain is incorporated in a proprietary microchip (ASIC), which controls the phase and amplitude of several patch antennas. Each microchip with the controlled patches forms a radiating element.

An array of such Elements composes the antenna aperture, which is connected to a core module that provide the power, control and communication to the system. Figure 2-15 presents the configuration of the radiating elements.

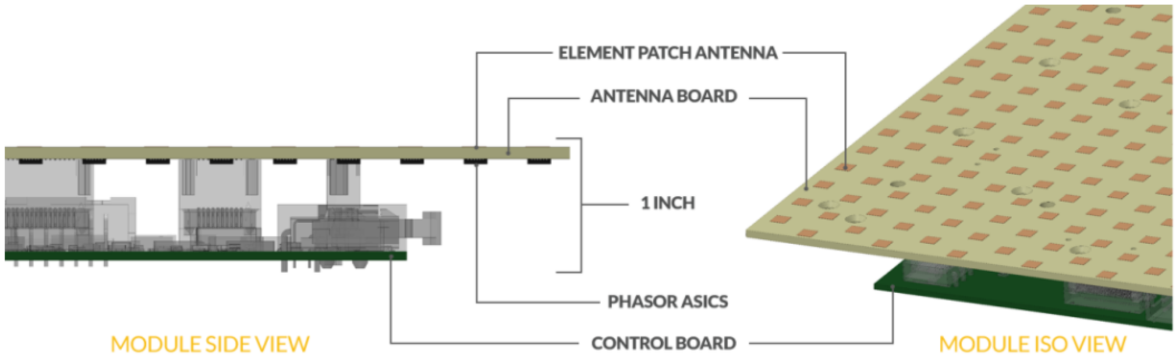

Figure 2-15: Phasor array configuration [55]

The antenna is scalable and capable of delivering a G/T figure of at least 20 dB/K and EIPRs greater than 70 dBW. The launching product is expected to operate over the Ku band (11 GHz-14 GHz). Other technical details have not been released yet by the company [55].

This antenna array is lower in profile than the Kymeta panel, but it represents an active array, where the RF components (incorporated in the microchip) are distributed among the groups of patches. This could anticipate an increase of the unit price, even if the product has not been released on the market yet.

2.4.2.3 Isotropic Phased Array (All Space)

Isotropic Systems has designed and tested a flat panel antenna based on optical beamforming concept. The RF signal is concentrated in a certain direction using lenses. As a consequence, they use less electronic components, resulting in less power consumption and relatively lower costs.

Ku band and Ka band prototypes have been built in 2018-2019 and the first Ka band terminal has been released. The design is targeted for military applications and high-end enterprise and leisure craft such as yachts and super yachts. By scaling the optical beam module, which is 6 cm in diameter and 5 mm tall, derivative products can be created to suit other applications (Figure 2-16). The optical beam module represents the main optical beamformer, where lenses are employed for focusing the energy in certain directions.

Figure 2-16: Isotropic Optical Modules [56]

The antenna can reach a look angle of 20˚ of Elevation, as the RF lenses bend and focus the RF energy. The gain at those extreme angles is said to be around 3 dB better than a standard flat panel ESA. However, the antenna is conformable to specific shapes, that can push the minimum elevation angle even further.

Instead of having to illuminate thousands of antenna elements all the time, one lens and feed are illuminated to generate a beam. The beams from multiple "cells" are then combined to achieve the desired bandwidth, drastically reducing the power consumption. With the dynamic resource allocation, only the resources required are turned on, depending on the link characteristics and the purpose of that specific beam. The number of feeds under each lens can be varied, which tailors the product to a specific application.

To shift the phase of the signal, that is amplified and digitized, solving the time delay problem (squint). By using individual cells, essentially dedicated send or receive modules, the patch antenna elements are separated, thereby eliminating the interference and allowing full-duplex.

Each optical module is 5 cm tall and includes the lens, the feeds, and the printed circuit boards with the amplification and digital beamforming circuitry and functionality. The reduced number of chips, eliminates the need for heatsinks, which highly reduces the weight of the antenna [56] [57].

2.4.2.4 Satixfy Phased Array

Satixfy electronically-steerable multi-beam array antenna presents its proprietary application specific integrated circuit (ASIC) for Digital Beamforming and signal processing, which comprises the Analog to Digital Converters (ADC), Digital to Analog Converters (DAC) and Digital Phase Shifter for True Time Delay to avoid beam squint.

The Prime ASIC chip is responsible for delivering up to 32 independent steerable beams, equalisation and digital pre-distortion for each beamformer chain, beam tracking and beam steering, linear and circular polarisation control.

The Ku band antenna elements are connected to the Prime digital Beamformer through another chip, called ‘Beat’. This chip integrates the Tx and Rx RF Chains: transmit driver and power amplifier, transmit up-converter, receive low noise amplifier, receive down-converter and antenna polarization control, either linear or circular. A single Beat supports four Ku-Band antenna elements operating in half-duplex mode. Figure 2-17 illustrates the Prime and Beat chips configuration in a steerable antenna array.

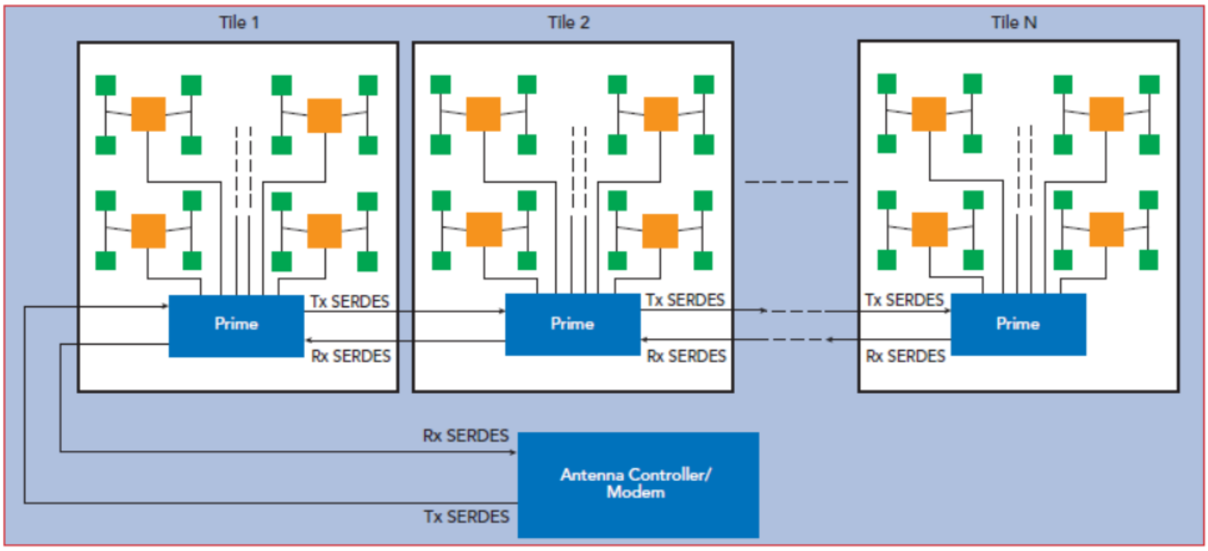

Figure 2-17: The block diagram of a fully integrated steerable multibeam antenna [58]

The fully digital 256-element antenna is a single board design with a shared aperture antenna (Rx and Tx), operating from 11 to 12 GHz for Rx and 13.75 to 14.5 GHz for

Tx. The 256-element ESMA comprises eight Primes daisy-chained and 64 Ku-Band Beats.

The antenna can simultaneously point, track and manage multiple beams with multiple polarizations. Figure 2-18 shows the 256 element antenna. The radiating elements are circular patches, the Tx antenna gain is 28 dBi, and Rx gain is 26.5 dBi. The RF bandwidth is 1 GHz and the Channel bandwidth 880 MHz.

This modular antenna is intended to be used for various applications such as IoT, Broadband Communications for Land, Maritime and Aeronautical Applications, 5G Fixed Wireless Access [58] [59].

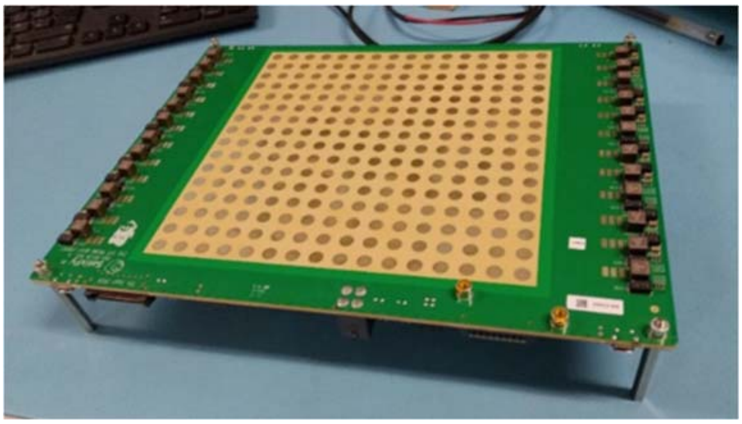

Figure 2-18: 256 elements antenna [58]

2.4.2.5 Thinkom Phased Array

The Thinkom Phased array represents a combination between the mechanically steered and electronically steered antenna arrays. The antenna consists of multiple layers that rotate around a common axis to provide beam steering and polarisation change. Figure 2-19 presents the layered structure of the antenna.

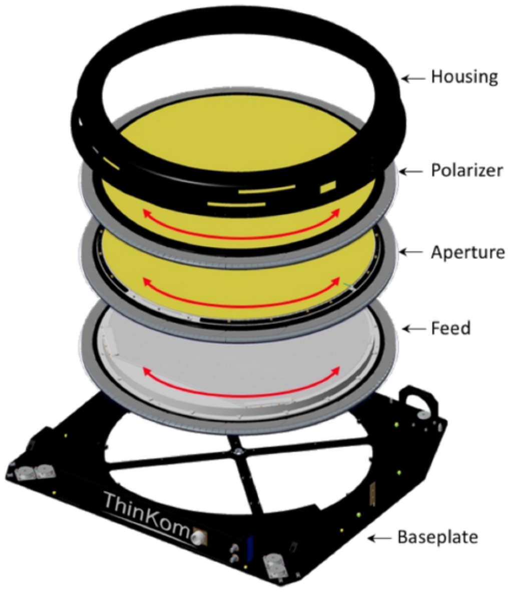

Figure 2-19: The layered structure of the Thinkom phased array antenna [60]

The Aperture platter represents in essence a VICTS antenna (variable inclination continuous transverse stub), which derives from the CTS (continuous transverse stub) antenna type. The Elevation, Azimuth, Polarisation angles and the beam shape vary with the rotation angle of the plates at the operating frequency.

In general, for VICTS antennas, the beam steering is achieved by rotating the feed and the CTS Layer either in tandem or relative to each other. As shown in Figure 2-20, the CTS layer consists of slots and matching stubs.

Figure 2-20 relates to Figure 2-19 through the fact that the CTS layer in Figure 2-20 is represented by the aperture in Figure 2-19. The radiating slots are distributed on the aperture layer, while the slow wave structures are in the feeding layer.

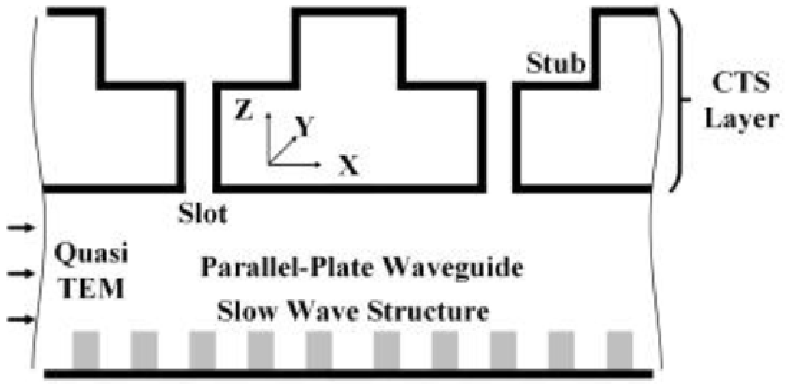

Figure 2-20: Continuous Transverse Stub Layer [61]

The beam scanning in Azimuth is achieved by rotating the aperture and the feed at the same time, and the scanning in Elevation is achieved by rotating the CTS layer relative to the feed. The Thinkom terminals for LEO-MEO satellites operate in the Ku or Ka bands (10.7-12.75 GHz for Rx and 13.75-14.5 GHz for Tx; 17.7-21.2 GHz for Rx and 27.5-31 GHz for Tx), and have an Effective Isotropic Radiated Power between 33.5 dBW and 57.5 dBW, depending on the frequency [60], [61].

2.4.2.6 Starlink Antennas

The Starlink Phased array antenna is about 50 cm in diameter and, as the other antennas described above, it employs chips for the digital beam forming. The antenna transmits in the LHCP (Left Hand Circular Polarisation) in 14 GHz-14.5 GHz band and receives in the RHCP (Right Hand Circular Polarisation) in 10.7 GHz-12.7 GHz range. It has a gain of about 32 dBi and presents a stacked layer architecture (Figure 2-21).

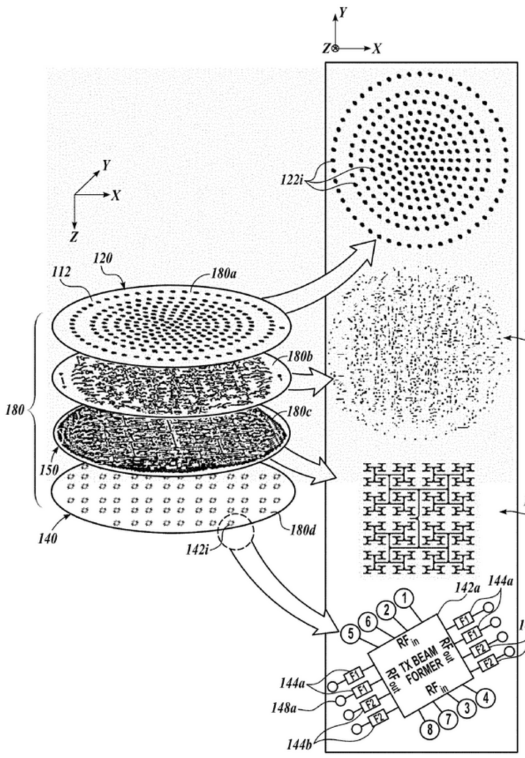

Figure 2-21: The stacked architecture of the Starlink antenna

The antenna contains about 1300 circular patches, which are controlled by about 630 chips. The RF components are contained into the integrated chips [62].

2.4.2.7 Limitations

As described above, the flat panel antennas present relatively high dimensions which agree with the theoretical calculated gain at 14 GHz centre frequency. Kymeta antenna array presents a gain of 28.6 dBi, for a 20 cm aperture. The theoretical gain for a 20cm aperture at 14 GHz is 29.33, assuming 100% efficiency. Phasor antenna array presents a diameter of approximatively 0.7 m, which translates into a theoretical gain of approximately 40 dBi at 14GHz. Isotropic antenna has a diameter of approximatively 30 cm, which means a theoretical gain of about 32.8 dBi. Satixfy antenna has a gain of about 28 dBi and Starlink of 32 dBi. The Starlink antenna is 50 cm in diameter, which translates into 37.3 dBi theoretical gain, if 100% efficiency is considered at 14GHz. The Kymeta antenna appears to have a better efficiency, compared to Starlink antenna, as the reported gain is very close to the theoretical gain.

The existing flat panel antennas employ dedicated integrated circuits (chips) and signal processing for beamforming. The number of elements controlled by the integrated circuits can be in the order of thousands. The active phased array antennas have an individual transmit-receive module for each radiating element (or for a group of radiating elements). This increases the number of the circuits (chips) and given that these are solid-state modules, an efficient cooling system must be employed for keeping all the elements in an operational temperature range.

The power consumption can be another drawback encountered on the antenna arrays that use digital signal processing and digital beamformers. Digital beamforming (DBF) requires many analog to digital converters (ADCs) and mixers. The increased number of components increases power and cost significantly, especially for a large array. The distribution of the high frequency local oscillation (LO) signals while maintaining phase coherence is also a challenge for DBF implementation and adds to the power consumption.

The computational requirement of digital beamforming is a significant contributor to the overall power consumption. The amount of data the Digital Signal Processor (DSP) must process is proportional to the number of elements, number of beams, and instantaneous bandwidth of the signal.

The hardware complexity and also, the signal routing complexity used on these antennas increase substantially. This is computationally demanding, fact that causes significant increase in product price and product dimensions. Beside the complexity added by the digital processing, elements like metamaterials and optical lenses can add extra elaboration to the antenna elements.

For some applications (mobile phones, satellite phones, laptop antenna, IoT devices, etc.) where the physical space is essential, a low-profile antenna is required. On cubesats, for example, where the allocated space for antennas is limited, a low-profile antenna, which occupies as less space as possible, is preferred. For those scenarios, the deployable antennas are frequently used.

2.5 Antennas used in Mobile Devices

The antenna design requirements for mobile terminals are: small sized and built-in antenna, with multiband operation and various standardization and requirements compliance. For example, the smartphone antennas need to support more than 35 frequency bands for 2G, 3G, 3.5G, 4G networks for global coverage and roaming [63]. Figure 2-22 illustrates the frequency ranges allocated in UK for mobile communication services.

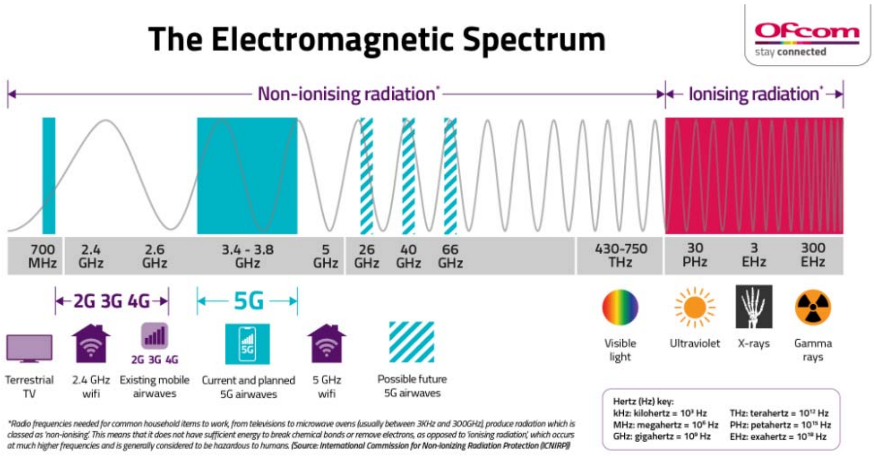

Figure 2-22: Frequency bands allocated for mobile communications in UK [64]

In addition to the multiband antennas dedicated for communication, other antennas for services like Bluetooth, NFC (Near Field Communication), GPS (Global Positioning System), etc. are integrated in the device.

Planar Inverted F Antenna (PIFA) is a very popular antenna used in mobile communications. This is essentially a derivation from the λ/4 rectangular microstrip antenna. Figure 2-23 shows the structure of a PIFA antenna.

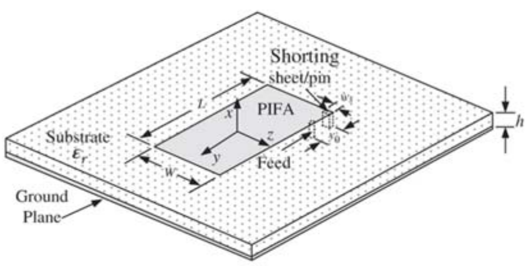

Figure 2-23: Planar Inverted F Antenna (PIFA) design [41]

PIFA antenna presents the following advantages:

- Low backward radiation and implicitly reduced Low Absorption Rate;
- Easy to Design, at low costs;
- Light weight;
- Reliable;

The radiation pattern of a PIFA antenna is similar to the microstrip patch antenna's radiation pattern (broadside radiation). The shorting pin ensures that the current and voltage will have the same distribution as the ones for λ/2 microstrip antenna. By removing the shorting pin and by doubling the dimension of the antenna, a λ/2 microstrip antenna is obtained. This represents a good method for antenna size reduction, with small effects on the antenna gain and bandwidth.

The resonant frequency of the PIFA antenna is determined by the dimensions of the antenna and of the shorting pin:

$$L + W - w_s = \frac{\lambda}{4} + h \tag{2.6}$$

The input impedance of the PIFA is controlled by the distance between the shorting pin and the feeding point. Multiple resonances required in mobile communications can be achieved by introducing U-Slots into the design [41].

Multiband function can be obtained by introducing slots on the patch or by adding parasitic elements. A triple band PIFA antenna is described in [65], and a gain between 1.1 dBi to 2.5 dBi is obtained for the three operational frequency bands.

An Inverted-F Antenna consists of a thin arm, which is connected at one of its ends to a ground plane: (Figure 2-24). The feed is placed between the arm and the ground plane, next to the shorting pin. The length of the Arm should be about λ/4. The input impedance is controlled by the distance between the feed and the shorting pin.

The IFA antenna represents half of the slot antenna structure. Its radiation pattern is similar to the slot antenna pattern. Given that the slot antenna is the complement of a dipole type antenna, according to Babinet's principle, it results that the radiation pattern of an IFA antenna is omnidirectional, as it is for a dipole antenna [41].

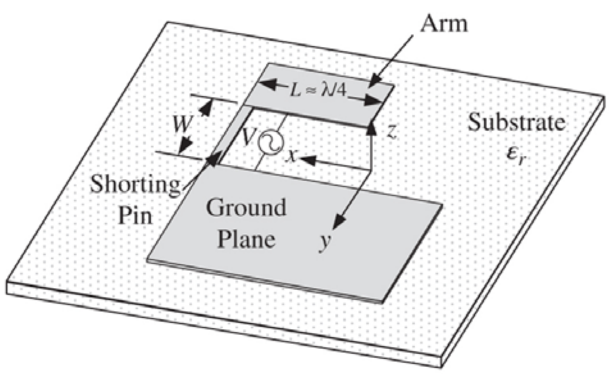

Figure 2-24: Inverted F antenna (IFA) structure [41]

The Inverted F antennas are used as GPS antennas in mobile phones (at 1575.42 MHz and 1227.6 MHz). The GPS received signals are very weak (-153 dBm in theory, but more like -120 dBm in practice) and, therefore a good receiving antenna is needed for reception. The gain of the antenna is around -1 dBi when integrated in the handset [66].

For a wider bandwidth, the chassis of the mobile is taken as the ground plane of the PIFA or IFA antenna. The resonating currents are spread over the chassis, therefore, by the integration of the mobile terminal's housing into the antenna system, the gain and the bandwidth are improved. However, the performance of the antenna is degraded under the effect of the human body, especially the hand.

For this reason, the printed loop antenna is another type of antenna employed in mobile communications. The loop antenna induces small current in the ground plane, therefore the effect of the human body on the overall performance is minimised. Because of the coupling between multiple sections of the loop, a better bandwidth than the PIFA is obtained with this type of antenna [63], [67].

In [67] and [68], two multiband loop antennas are designed for smartphone and LTE standard. Figure 2-25 illustrates the structure of the loop antennas. Both antennas are designed to have multiple resonances in order to cover as many frequency bands as possible.

The length of the loop is about λ/2 at around 900 MHz, but the antennas also resonate at higher modes corresponding to loop lengths of 1λ, 1.5λ, 2λ (at approx. 1.6 GHz, 2.3 GHz and 3 GHz). In both cases, the radiation pattern of the antennas at λ/2 loop length is omnidirectional. The gain over the bands varies between 0.19 dBi to 5.5 dBi and the radiation efficiency between 45% to 82%.

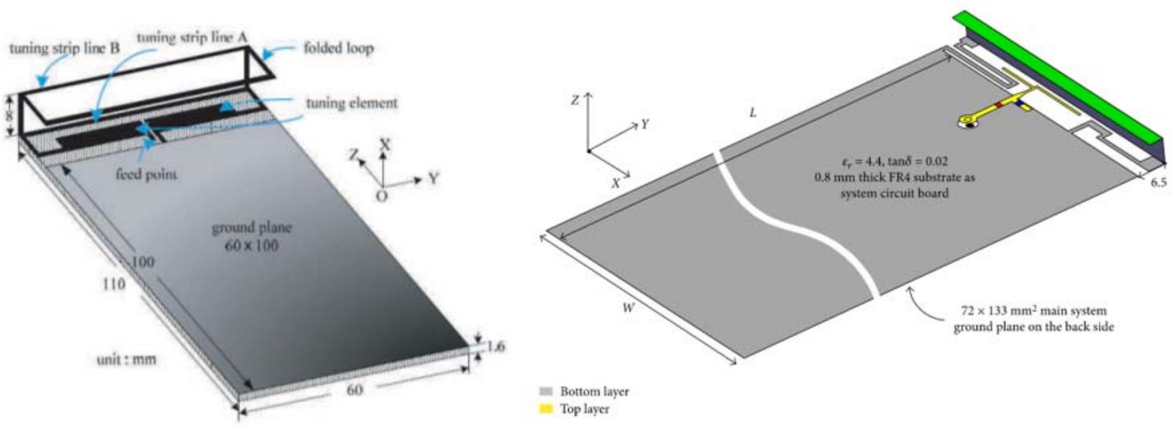

Figure 2-25: Loop antennas designed for smartphones in [67]-left and [68]-right

Printed monopole and dipole antennas are also used in mobile communications because of the omnidirectional features of their radiation patterns. In [69], a multiband antenna based on monopoles is presented, which covers frequencies from 1.4 to 2.64 GHz and from 3.32 to 4.64 GHz. The antenna structure is illustrated in Figure 2-26.

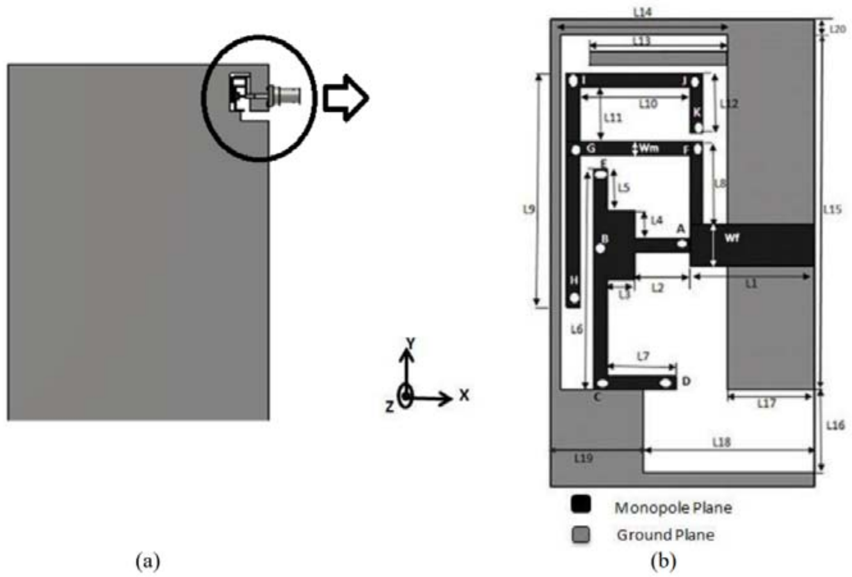

Figure 2-26: 150x80 mm^{2}antenna based on Monopoles: Top view (a) and Detailed view (b) [69]

The antenna gain ranges from 4.25 to 6 dBi over the band, with the efficiency between 70% to 90% [69]. Also, in [70], a broadband planar antenna, based on a spiral monopole is presented. The wide band is achieved through some parasitic patches and the direction of the beam is made broadside by the extension of the ground plane in a U-shape. The final structure is wideband (23.76 to 42.15), with a peak gain of 11.5 dBi and with more than 83% radiation efficiency.

Apart from printed, built in Microstrip antennas, Monopole antennas and Normal Mode Helical antennas are implemented on small mobile terminals. The Helical antenna was usually placed on top of a Monopole antenna (whip antenna) and it became 'active' as soon as the monopole antenna was retracted. The Monopole and Dipole Antennas are simple, lightweight and low-cost structures used on mobile terminals. However, their lengths, for operating frequencies below 1 GHz, proved to be unpractical to be mounted on the mobile terminals [65].

The Normal Mode Helical antenna is a thin, simple structure, which radiates in directions normal to the helical antenna axis. The radiation pattern is similar to that of a short dipole (omnidirectional). To achieve the normal mode of operation, the total dimension of the helix must be much less than the operating wavelength. In general, the helical antenna can be considered as a sequence of small loop antennas interconnected by short dipoles (Figure 2-27). Therefore, the farfield radiated by the helical antenna can be described in terms of E_θ and E_ϕ components of the loop antenna and dipole antenna [41].

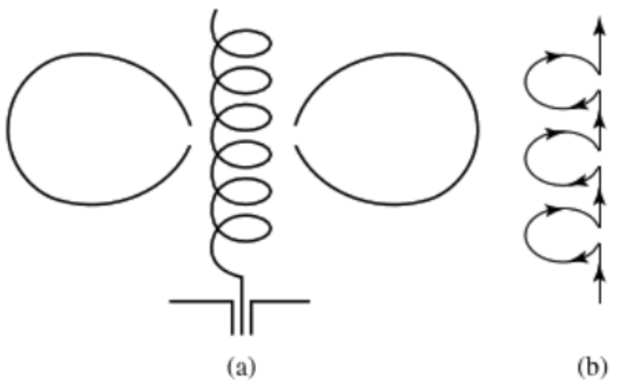

Figure 2-27: Normal Mode Helical Antenna (a) and its equivalent arrangement (b) [65]

As its length must be much less than the operating wavelength, the helix antenna operating in normal mode presents a very narrow bandwidth, and a small radiation efficiency. However, these can be improved if the length of the antenna is increased [65]. In [71], a 3.3 GHz, normal mode, bifilar helical antenna has been implemented for mobile communications. The antenna 10 dB bandwidth is 200 MHz and gain 5.12 dBi. Moreover, in [72] a simulated helical structure made of glass demonstrates that the bandwidth can be increased to approx. 1.4 GHz at 5.3 GHz.

2.6 Antennas used in 5G Communications

5G is the next generation of technology that supports high data rates, more capacity, with low latency and better quality of service. The 3GPP (Third Generation Partnership Project) released the 5G technology standards and presented three fundamental usage scenarios for the 5G technology (see Figure 2-28):

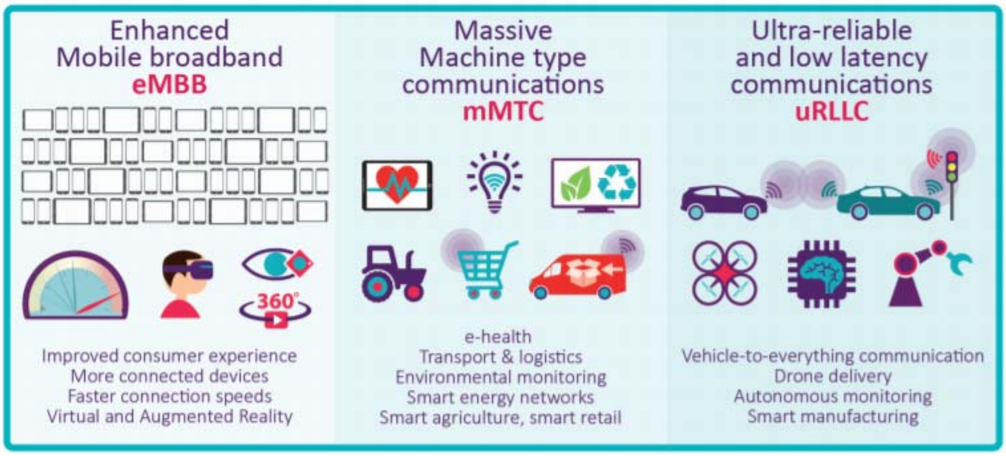

Figure 2-28: Usage Scenarios for 5G Technology [73]

The frequency ranges used for 5G are below 6 GHz and above 6 GHz. Table 2-4 shows the spectrum used on 5G as presented in [74].

Table 2-4: Frequency Ranges for 5G [74], [75]

<table>
<tr><th>Frequency Range (MHz)</th><th>Frequecuency Band</th><th>Frequency Range (MHz)</th><th>Frequency Band</th></tr>
<tr><td>470-698</td><td>n71</td><td>24250-29500</td><td>n257, n258, n261</td></tr>
<tr><td rowspan="2">698-960</td><td rowspan="2">n5, n8, n12, n14, n15, n20, n25, n28, n29, n81-n83, n89, n91-n94</td><td>37000-43500</td><td>n260</td></tr>
<tr><td>45500-47000</td><td>-</td></tr>
<tr><td>1427-1518</td><td>n50, n51, n74-n76, n91-n94</td><td>47200-48200</td><td>-</td></tr>
<tr><td>1710-2025</td><td>n1-n3, n34, n39, n65, n66, n70, n84, n86, n95</td><td>66000-71000</td><td>-</td></tr>
<tr><td>2110-2200</td><td>n65, n66</td><td></td><td></td></tr>
<tr><td>2300-2400</td><td>n30, n40</td><td></td><td></td></tr>
<tr><td>2500-2690</td><td>n7, n38, n41, n90</td><td></td><td></td></tr>
<tr><td>3300-3400</td><td>n77, n78</td><td></td><td></td></tr>
<tr><td>3400-3600</td><td>n48, n77, n78</td><td></td><td></td></tr>
<tr><td>3600-3700</td><td>n48, n77, n78</td><td></td><td></td></tr>
<tr><td>3700-4200</td><td>n77</td><td></td><td></td></tr>
<tr><td>4400-4990</td><td>n80</td><td></td><td></td></tr>
</table>

NR band number	Frequency band	Uplink/Downlink (MHz)	Bandwidth
n257	28 GHz	26500-29500	3 GHz
n258	26 GHz	24250-27500	3.25GHz
n260	39 GHz	37000-40000	3 GHz
n261	28 GHz	27500-28350	850 MHz

The n257 frequency band covers 26.5 GHz to 29.5 GHz in Japan, North America and South Korea. N258 applies to Europe and China and encompasses the 24.25-27.5 GHz. The 28 GHz narrow band (27.5-28.35 GHz) applies to USA.

During the International Telecommunication Union’s (ITU) World Radiocommunication Conference 2019 (WRC-19), further frequency bands have been identified for 5G:

24.25-27.5 GHz (n258-Europe), 37-43.5 GHz, 45.5-47 GHz, 47.2-48.2 and 66-71 GHz [76].

Different spectrum bands are assigned for 5G services in order to cover various demands: the low frequency range will allow 5G to cover wide areas, higher frequencies will ensure enough capacity to support a large number of connected devices, and the mm wave frequencies will provide very large bandwidths and low latency in area of high traffic demand (see Figure 2-29). These three 5G bands enabled in Europe are: 700 MHz, 3.4-3.8 GHz, and 24.25-27.5 GHz.

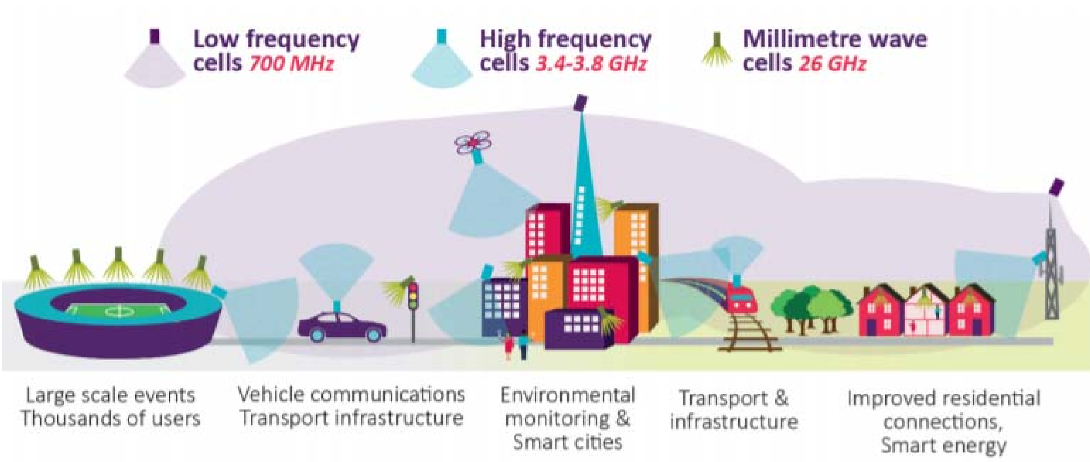

Figure 2-29: 5G frequency bands applications [73]

The current mobile services in the UK operate between 700 MHz and 3.8 GHz (2G, 3G, 4G and 5G). For 5G, higher frequency bands are proposed to be used, and that includes the 26 GHz, 40 GHz, and 66 GHz. The mm wave frequencies can deliver very high speeds and capacity, with very low latency. One disadvantage is that at these frequencies, the signal travelling is affected by the buildings, trees, or any other obstacle that the signal cannot penetrate. This makes these signal frequencies unsuitable for a wide area coverage. Instead, by employing massive MIMO and beamforming technology, the signal will be transmitted only in the direction where the transmission is required, making the transmission more efficient [78].

Because the mm wave frequency can travel only short distances, the cell dimension becomes smaller. As a consequence, the number of base stations increases. It means that the base station can be installed only in certain areas and this generally leads to smaller base station antennas. This helps with the frequency reuse and channel capacity increase. The antennas are also reduced in size and number.

The emerging 5G technology also foresees the integration of the satellite communication system into the 5G ecosystem. Both geostationary and non-geostationary satellite networks have unique attributes that contribute to the satellite-based solutions in 5G deployment. The satellite is able to support high bit rate trunking of video, IoT and other data to a central site. With this technology, small and flat panel antenna terminals come into discussion.

By integrating the use of satellites into the 5G ecosystem, the development of this new concept can be accelerated. This combination will lead to:

- Improved connectivity for different users;
- Direct services to end users and devices (M2M, IoT);
- Temporary Networks;
- Satellite Backhauling for Base Stations;
- Extra backhaul capacity in case of congestion;
- Wide Coverage;

- Seamless Connectivity;
- Emergency Response and Backhaul Communications [79];

The antenna for 5G communication must have high gain, bandwidth and low radiation losses. Single Input Single Output antennas have been implemented for 5G communications. However, for mm wave frequencies, the propagation losses increase, therefore it is desirable to have a multi-element antenna rather than a single element antenna. An antenna with multiple elements has a better gain, but an increased size and complexity [74].

Different types of antennas, suitable for 5G communications, have been specified in literature.

a) *Monopole Antenna*: Different monopole shapes and configurations are presented in [80] and [81], at both mm wave and sub-6 GHz frequencies. Although it is simple to design and fabricate, the monopole antenna presents a low gain and is weather conditions sensitive [74].

b) *Dipole Antenna*: In [82] are compared three dipole antennas, designed with different strip materials. Good results in terms of Bandwidth, VSWR, and radiation efficiency are obtained when Graphene is used as strip material on Teflon substrate. A wideband end-fire dipole LC based antenna is proposed for 5G applications in [83]. The wideband is obtained by using an additional surface structure (director) which resonates and increases the bandwidth. Similarly to the Monopole Antenna, the Dipole Antenna is easy to design and fabricate, but presents low gain and bandwidth and is not suitable for long range communications [74].

c) *Magneto-Electric (ME) Dipole Antenna*: as described in [84] and [85], the magneto-electric dipole consists of a vertically placed, shorted quarter wavelength patch antenna and a planar electric dipole. This is equivalent to a combination between a magnetic and an electric dipole (see Figure 2-30).
In this way, complementary, unidirectional radiation patterns can be generated in both principal planes. Low profile ME dipole antennas have been proposed in [86]-[89] for 5G mm-wave applications. This type of antenna presents a wide bandwidth, low cross-polarisation, and low sidelobes. However, the design and fabrication complexity, high costs and relatively low gain characteristics are some of the antenna disadvantages outlined in [74].

d) Loop Antenna: different loop antennas structures are presented in [90]-[93], for different 5G applications, for both sub 6 GHz frequency band and mm wave frequency band. Multiple resonances are employed in [84] to increase the bandwidth necessary in MIMO technology.

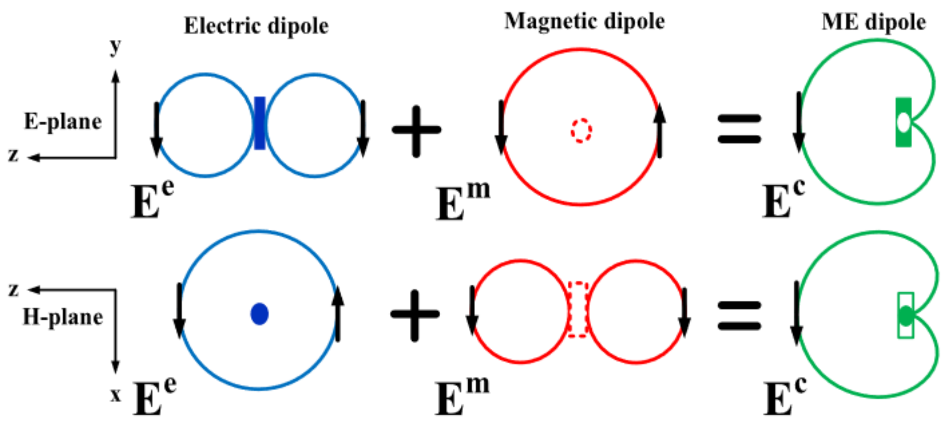

Figure 2-30: Complementary principle of a ME Dipole [86]

However, usually, multi element loop antennas are required in order to increase the gain or bandwidth. Even so, the Loop Antenna is easy to design at relatively low costs [74].

e) *Antipodal Vivaldi Antenna:* this antenna consists of two mirrored exponentially tapered conductors, separated by a substrate (see Figure 2-31).

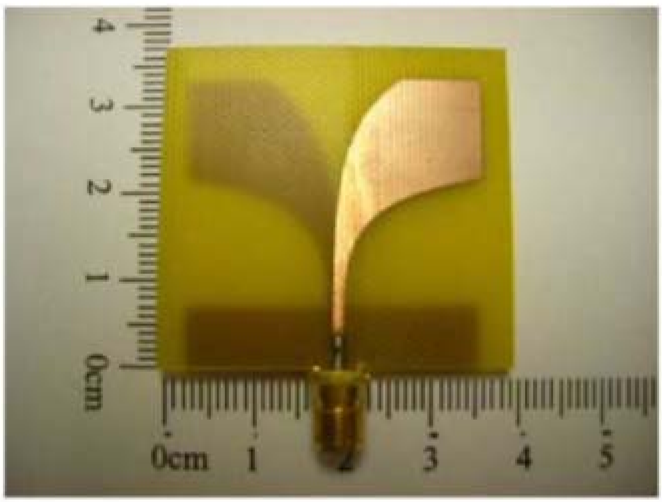

Figure 2-31: Antipodal Vivaldi Antenna [94]

Multiple AVA arrays are proposed for 5G applications in [94]-[100]. Gain, Bandwidth and Front to Back Ratio are improved by adding corrugations to the metal sheets in [95], [96] and [100]. Notch structures on the ground plane are used to reduce the mutual coupling between elements in [97] and parasitic elements (directors) that resonate [98], [100] are used to increase the bandwidth and gain of the structures. Although the radiation pattern given by this type of antenna is stable, it requires more space and it might have lower gain at low frequencies [74].

f) *Fractal Antenna:* this antenna concept consists in repeating of a fractal structure multiple times, using a mathematical iteration. The performance of an antenna array can be improved by using fractal elements. Better array factor properties are obtained because of the recursive nature of the structure, and also, multi-band and multi-beam characteristics are improved [101]. Very wide bandwidths are reported in [102]-[106], with good impedance matching, low profile sizes and stable performance over the band. This makes the fractal antenna suitable for 5G communication applications. The main drawback of the fractal antennas is the design complexity and fractal iteration limitation [74].

g) *Inverted F-Antenna (IFA) and Planar Inverted F-Antenna (PIFA):* the structure of these types of antennas is described in section 2.5. Planar Inverted F antennas have been designed both for mm wave applications and C- band frequency applications [107]-[110]. These are usually implemented on mobile handsets because of their convenient profile size. In most applications, slots are used to achieve a wide band or multi bands [107]-[110]. A reconfigurable PIFA antenna is presented in [107], and PIN diodes are used to switch between the different states of the patch. A total bandwidth of 1.099 GHz is obtained between 3.5 GHz and 4.8 GHz, with a gain of 3.4 dB only. A wider bandwidth, 12.5 GHz, is obtained in [108], where slots are also used in the ground plane. The position of the slots is optimised for maximum gain (6.1 dBi between 24.5 GHz and 37 GHz).

A method used for gain improvement is presented in [109], where a superstrate which acts as a dielectric load is employed to achieve a gain of 8.8 dBi. 3.18 GHz bandwidth (between 27.57 GHz and 30.75 GHz) is also achieved by using slots in the patch. [110] presents a pair of PIFA antennas which can be used for 5G MIMO applications in C-band. The isolation between the two antennas is better than 10 dB.

Inverted F antennas have also been referenced in literature for 5G applications [111-114]. In [111] the wideband characteristic is achieved by using a coupled-meandered feed at one end, and by exciting multiple modes in the C-band frequency (3.27 GHz-6.13 GHz).

[114] presents a dual band Inverted F antenna which uses tuneable inductor and capacitor for choosing the resonant frequency. Good impedance matching and wide bandwidth are reported in [112], where a graphene based Inverted F antenna is presented. An 'all metal' Inverted F antenna can also be used for 5G C-band communications, as presented in [113].

2.7 Introduction to Microstrip Patch Antenna

The Microstrip Antenna is a metallic patch printed on a thin, grounded dielectric material. As shown in Figure 2-32, the patch thickness is very small ($t \ll \lambda_0$) and usually, the substrate thickness is between $0.003\ \lambda_0 \leq h \leq 0.05\ \lambda_0$.

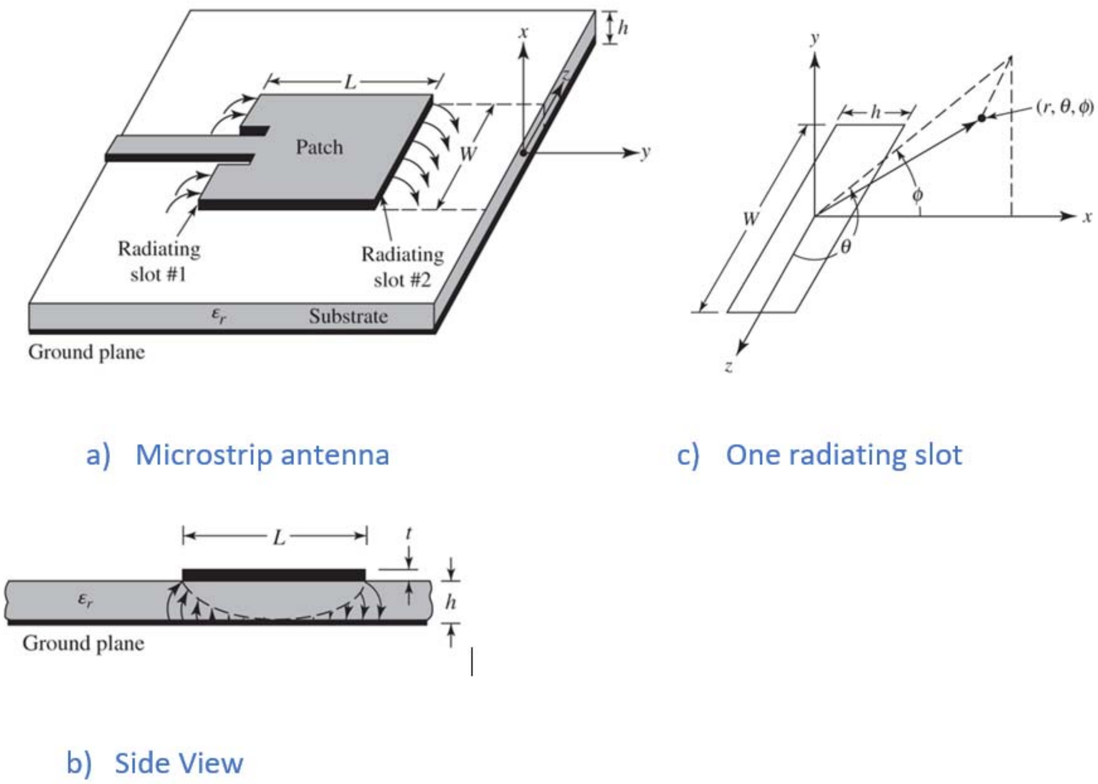

Figure 2-32: Microstrip Antenna Structure and coordinate system [41]

Normally, the Microstrip Patch antenna is broadside radiator, but it can also be an end-fire radiator by conveniently choosing the field configuration in the substrate. The patch can take different shapes like: square, rectangular, circular, triangular, elliptical, etc.

The rectangular patch is one of the most common types of radiators used for a microstrip patch antenna. It is easy to fabricate and analyse and it possesses convenient radiation characteristics. The length of the radiating patch is usually chosen to be between: $\lambda_0/3<L<\lambda_0/2$, where λ_0 is the free-space wavelength.

There are many types of substrates that can be used for the Microstrip Antenna design and their dielectric constants are usually between: $2.2\leq\varepsilon_r\leq12$. A thick substrate and a low dielectric constant value ensure good efficiency, large bandwidth, good radiation into space, but a larger radiating element [115]. This happens because:

$$L=\frac{\lambda_g}{2}=\frac{\lambda_0}{2\sqrt{\varepsilon_r}},\text{(if the fringing effects are ignored)} \tag{2.7}$$

Where

$$\lambda_g=\frac{\lambda_0}{\sqrt{\varepsilon_r}},\text{ is the wavelength through the substrate} \tag{2.8}$$

2.8 Microstrip patch antenna feeding methods

There are various methods of feeding a microstrip patch. The most popular ways are described in [41] and include: microstrip line, coaxial probe, aperture coupling and proximity coupling.

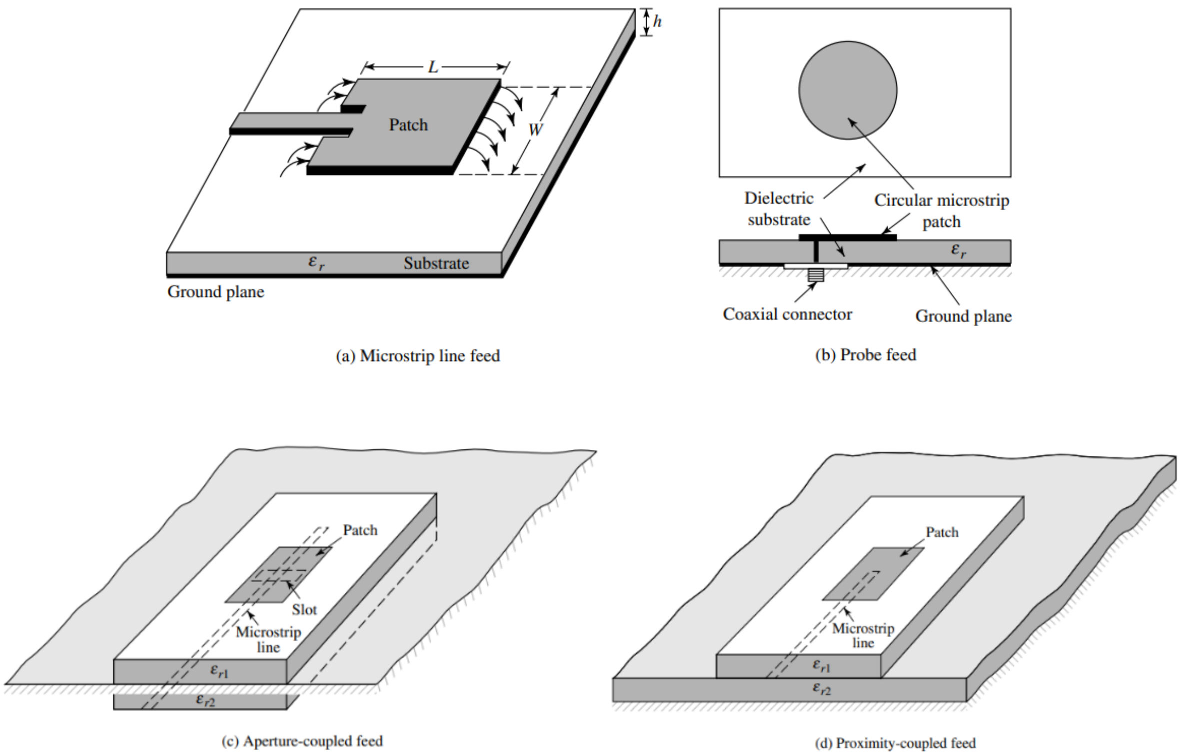

Figure 2-33: Popular feeding methods for Microstrip Patches [41]

The feed line method, Figure 2-33 (a), employs a thin conducting strip whose inset position is used to control the matching. Both the feed line and the patch are etched on the same surface. The feed line is much thinner than the patch, but even so, as the substrate thickness increases, the surface waves and feed spurious radiations increase and affect the bandwidth [116-121].

In the coaxial feed method, Figure 2-33 (b) the inner conductor of the coax is connected to the patch and the outer conductor is connected to the ground plane. Similar to the feed line method, the probe position controls the input impedance. This feeding method is easy to fabricate when the substrate thickness is fairly thin and the spurious radiation is low, but at very high frequencies the probe length corresponds to a large inductance which has to be accounted for in the matching. As indicated in [122], with thick substates, the inductance caused by the probe feed can increase the inductance component of the input impedance, which degrades the impedance matching. In order to compensate for the inductance introduced by the probe, a coupling capacitance needs to be introduced in the system. An annular gap etched in the rectangular patch, concentric with the probe is presented to be a good solution in [122].

The usage of the annular gap capacitor introduces negligible design complexity and fabrication costs. The inner radius r, the gap width g, and the feed position to adjust the value of the gap capacitor Cs can be calculated using the formulas in [122]. However, with thin substrates, the annular gap capacitor does not have a major effect on the amount of reflected power to the source.

For the above feeding methods, the impedance matching is done by selecting the appropriate inset/feeding position. The matching is important because it assures that no reflected power occurs towards the source and that most of the transmitted power excites the antenna.

As described in [116], the patch antenna is excited by a voltage between the patch and ground plane (Figure 2-34). This gives rise to currents below and around the surface of the patch and a vertical Electric Field appears between the patch and ground plane (in the substrate). The electric field components that are parallel to the ground plane are negligible throughout the substrate. The patch resonates when its Length, L, approaches λ/2 and this translates into high current and field amplitudes. As Figure 2-34 shows, the current values at x=0 or x=L is minimum. The patch is an open circuited structure, therefore, the voltage is maximum at x=0 or x=L and the current is minimum.

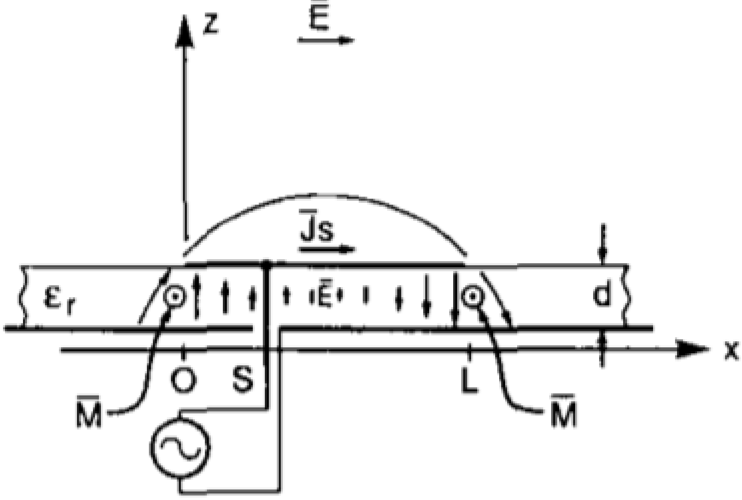

Figure 2-34: Cross-section view of a probe fed antenna, showing the magnetic and electric field distribution in the substrate, the surface current and the magnetic currents at the radiating edges of the patch [116]

Considering Figure 2-34, if the feeding point is at the edge of the patch, the impedance tends to very high values (around 200Ω). If the feeding point is at the centre of the patch, where the current amplitude is maximum, then the impedance is zero (by applying Ohm's law). In general, the feeding coax cable has an impedance of 50Ω, therefore the coax must be attached to the point where the impedance of the patch is also 50Ω (somewhere between the edge and the centre of the patch).

The above two feeding methods are very simple to design and implement, but they suffer from high spurious feed radiation and surface waves, especially if the substrate thickness is high. In general, an increase in substrate thickness increases the bandwidth (as the microstrip antenna is virtually an open resonator), but it also increases the surface waves and spur radiations. Because of the feeds' asymmetries, besides the dominant mode, higher order modes are also excited, and this leads to cross-pol radiation [41], [116-121].

The aperture coupling and proximity coupling feeding methods overcome the asymmetry issue. The aperture coupling method, Figure 2-33(c), uses two substrates separated by a ground plane. The feed line is placed at the bottom of the lower substrate and it is coupled to the radiating patch through a slot in the ground plane. The lower substrate is chosen to have a higher dielectric constant and the top substrate a lower dielectric substrate. In this way, the microstrip feed spuriouses are isolated from the radiating patch and the polarisation purity is preserved. The matching is controlled through the dimensions of the slot and the width of the feed line. If the slot is placed below the middle of the patch, where the Electric field is zero and the Magnetic field is maximum, then the magnetic coupling dominates. This leads to low cross polarised radiation because the excitation of the patch is symmetric. This type of feed is difficult to fabricate and it has narrow bandwidth.

The proximity coupling feed, Figure 2-33 (d), consists of two substrates with the microstrip line, which terminates below the patch, between the substrates. This method allows the patch to be on a relatively thick substrate, which improves the bandwidth, The microstrip feed is on a thin substrate, which reduces the spurious radiations. The Length of the feeding stub and the width-to-line ratio of the patch are used for matching control. This feeding method presents the widest bandwidth (as 13%), it has low spurious radiation and it is fairly easy to implement [41], [116].

2.9 Microstrip Patch Antenna operation principle

There are several methods developed to analyse microstrip antennas. From those, the most used ones are: transmission-line method, cavity method and full wave method.

The complexity of these methods increases from the transmission line to the full wave method. The transmission-line method provides a very good physical approximation, but is not very accurate and the coupling is hard to be modelled. On the other side, the cavity method is more accurate, but at the same time more complex.

The Full wave method delivers very good results when modelling the coupling and it is very accurate, however it does not provide good physical insight and it is very complex to model. Many electromagnetic software use full-wave concept combined with finite element/finite difference technique, so they are suitable for analysis of microstrip antennas including feeds.

2.9.1 Transmission Line Analysis Model

In this analysis method, the substrate is considered to be homogeneous, of infinite dimensions in the plane of the radiating patch. This method does apply only to applications in which the substrate thickness and permittivity are fairly low, the surface waves are negligible, and radiation from feed discontinuities can be ignored. The method is mainly used for matching purposes. Figure 2-35 shows the equivalent transmission line models for a Microstrip fed Patch and Coax fed Patch.

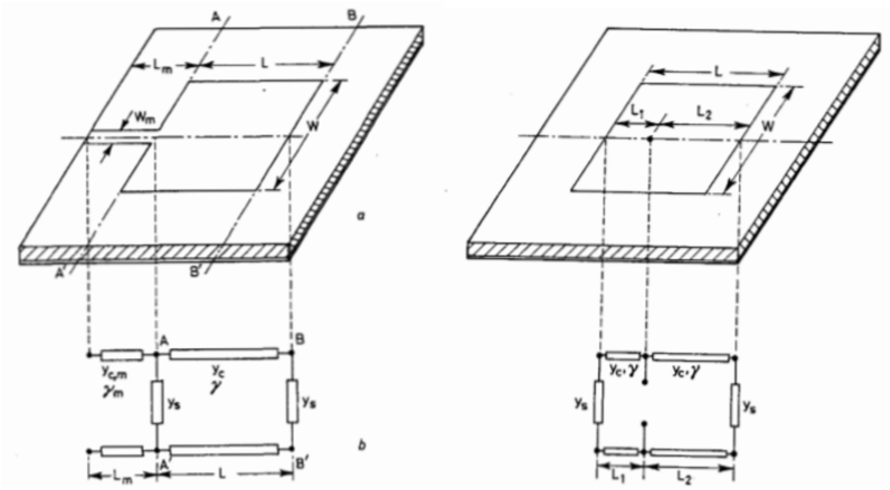

Figure 2-35: Equivalent transmission line models of a Microstrip fed Patch (left) and Coax fed Patch (Right) [123]

$Y_{c,m}$ represents the characteristic admittance of the microstrip feed line, determined by the aspect ratio W_m/h, relative permittivity ε_r and length L_m. γ_m is the microstrip feed line propagation constant and γ is the patch propagation constant. γ_c is the characteristic admittance of the Patch, characterised by W/h ratio, relative permittivity ε_r, and Length L.

The open-ended terminations of the patch are represented by a parallel admittance: $Y_s = G_s + jB_s$. This is because the open-ended microstrip line does not behave as a perfect open circuit. In general, the field lines do not stop at the end of the microstrip line. The fields at the edges of the patches undergo fringing, which means that the microstrip line becomes electrically longer by Δl. This implies an amount of stored energy, but it also triggers the power radiation above the patch and the power trapped along the substrate as surface waves. Figure 2-36 illustrates the fringing fields distribution in a side view of the microstrip patch. The real part of the parallel admittance, G_s, reproduces the radiation and the surface waves, whereas the imaginary part, B_s, accounts for the stored energy by the virtual extra patch length.

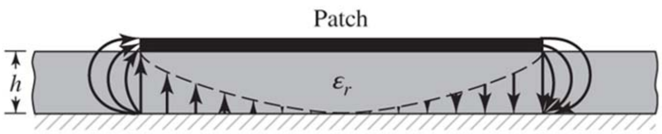

Figure 2-36: The side view of the Microstrip Patch and the Fringing Fields [41]

Referring to Figure 2-33 (a), the amount of fringing in the principal plane X-Y depends on the L/h ratio and ε_r. Fringing fields are reduced when L/h>>1, however its effects must be taken into account because the resonant frequency is highly affected by the fringing field effects.

For a microstrip line, with W/h>>1 and ε_r>>1, most of the field lines reside in the substrate. The fringing, in this case, makes the microstrip line look electrically longer. As the field lines cross both the air and the substrate, an effective dielectric constant is introduced to account for the 2 different mediums (air and dielectric substrate), therefore the effective dielectric constant $1<\varepsilon_{reff}<\varepsilon_r$. If $\varepsilon_r>>1$, then $\varepsilon_{reff}\approx \varepsilon_r$. Also, as the operational frequency increases, most of the field lines reside in the substrate and $\varepsilon_{reff}\approx \varepsilon_r$. Figure 2-37 shows the effective dielectric constant vs frequency for typical substrates for a microstrip line [41], [123].

In general, at high frequencies, the dielectric molecules (dipoles) are not able to fully polarise in one direction before the electric field switches to the other direction. On the contrary, at low frequencies, the molecules fully polarise and the material can response fast enough at these frequencies.

The curves in Figure 2-37 show that on a microstrip line, as the frequency increases, most of the filed lines reside in the substrate, and the electric dielectric constant approaches the value of the dielectric constant of the substrate.

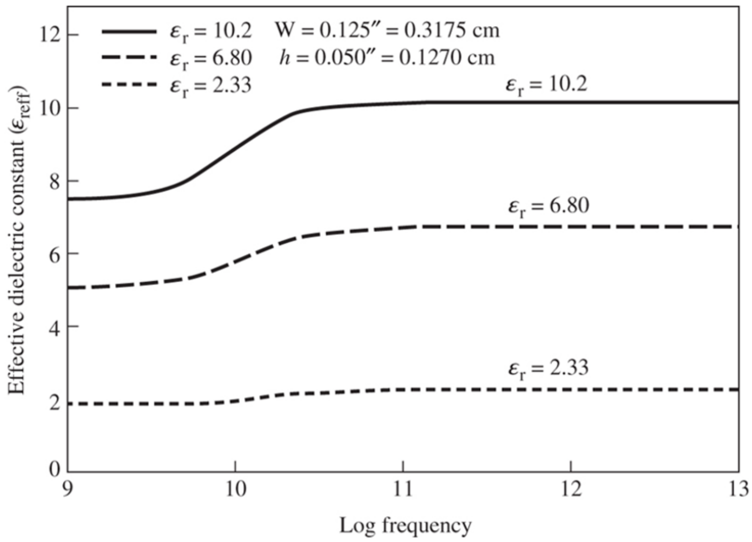

Figure 2-37: Effective dielectric constant behaviour with frequency [41]

The Microstrip Patch length extension (ΔL) caused by the fringing fields is approximately expressed as:

$$\frac{\Delta L}{h} = 0.412\frac{(\varepsilon_{reff}+0.3)(\frac{W}{h}+0.264)}{(\varepsilon_{reff}-0.258)(\frac{W}{h}+0.8)} \tag{2.9}$$

For the dominant mode, TM_{010}, the resonant frequency of the Microstrip Patch is:

$$f_{010} = \frac{1}{2L\sqrt{\mu_0\varepsilon_0}\sqrt{\varepsilon_r}} = \frac{c}{2L\sqrt{\varepsilon_r}}, \tag{2.10}$$

Where $\mu_0 \varepsilon_0$ are the vacuum permeability and permibility respectively and c is the speed of light.

If the effects of the fringing fields are considered, then:

$$f_{fr010} = \frac{c}{2(L+2\Delta L)\sqrt{\varepsilon_{reff}}} \tag{2.11}$$

In summary, if the substrate thickness increases, the fringing fields also increase and the resonant frequency decreases [41].

According to [124], for a slot of width W:

$$G = \frac{W}{120\lambda_0}\left[1 - \frac{1}{24}(k_0 h)^2\right], \text{ where } \frac{\mathrm{h}}{\lambda_0} < \frac{1}{10} \tag{2.12}$$

$$B = \frac{W}{120\lambda_0}\left[1 - 0.636\ln(k_0 h)\right], \text{ where } \frac{\mathrm{h}}{\lambda_0} < \frac{1}{10} \tag{2.13}$$

Figure 2-38 presents the slot conductance vs the slot width:

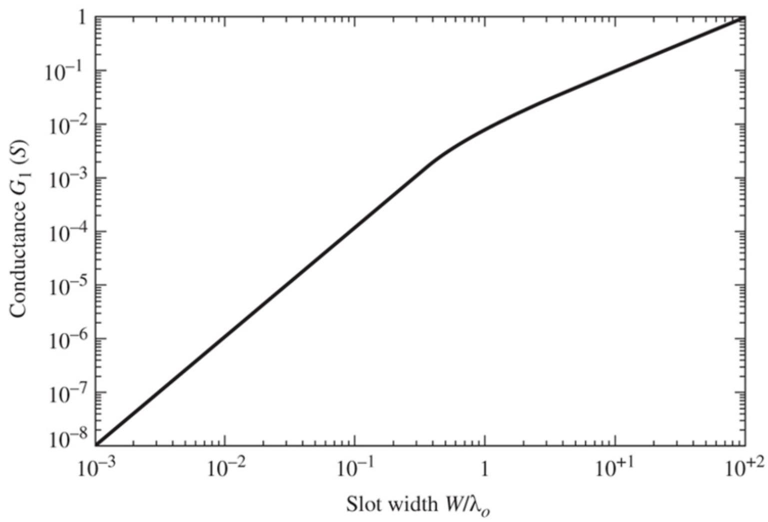

Figure 2-38: Slot conductance vs slot width [41]

An approximate expression for the input impedance of the rectangular microstrip antenna is given in [41] as:

$$R_{in} = 90\frac{\varepsilon_r^2}{\varepsilon_r-1}\frac{L}{W}, \text{where h} \ll \lambda_0 \tag{2.14}$$

The input resistance is not influenced by the substrate thickness. This can be decreased by decreasing the width of the patch. For an inset feed (y_0 mm from the edge of the patch), the input resistance becomes:

$$R_{in}(y = y_0) = R_{in}(y = 0)cos^2(\frac{\pi}{L}y_0) \tag{2.15}$$

2.9.2 Cavity Analysis Model

With this model, the microstrip patch antenna is approximated with a cavity with electric boundary conditions (on top and bottom of the antenna) and magnetic boundary conditions (sides of the microstrip antenna). The electric boundary condition on top and bottom of the antenna mark the presence of the electric conductor in those two planes (the ground plane on the bottom and the patch on top), where the tangential component of the electric field is zero. This approximation can be used for finding the fields within the substrate, the radiation pattern, input impedance and resonant frequency.

However, by treating the microstrip antenna only as a cavity, without any loss in the substrate, the antenna would not radiate, the input impedance would be purely reactive, and therefore the amplitude of the electric and magnetic fields could not be determined. By introducing the Radiation Resistance R_r and Loss Resistance R_L as imaginary poles, the input impedance becomes complex. The antenna loss is taken into account by the effective loss tangent, δ_{eff}, which is the inverse of the quality factor Q (δ_{eff}=1/Q).

This model states that when the patch is energised, attractive and repulsive mechanisms determine the charge distribution on both sides of the radiating patch and on the surface of the ground plane. Figure 2-39 shows the charge arrangement and the current densities created.

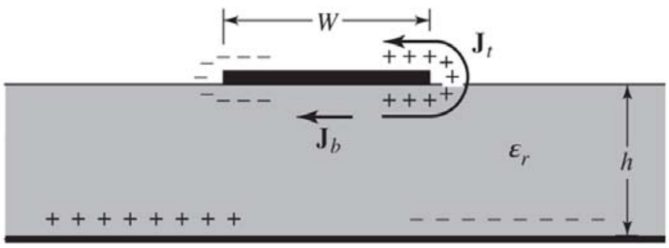

Figure 2-39: Charge distribution on cavity model analysis [41]

The attractive mechanism is between the opposite charges that reside in the substrate, between the lower side of the patch and the top side of the ground plane. This force keeps the charge concentration on the bottom of the patch. The repulsive force is between the same polarity charges at the bottom of the patch. This force pushed some charges around the edges of the patch, on the surface of the patch.

The movement of these charges creates the top and bottom current densities of the patch (J_t and J_b). Between the two forces, the attractive force is dominant and that determines the current flow to remain underneath the patch.

The amount of current flowing on top of the patch decreases with the h/W ratio and at limits, it tends to zero. This allows to consider the tangential magnetic field component negligible and it also allows the modelling of the four side walls as perfect magnetic conducting surfaces.

In reality the tangential magnetic fields are not perfectly zero, but small enough to be neglected. These considerations will provide a good field distribution beneath the patch.

The fields underneath the patch resemble the fringing fields around the edges of the patch (along the length L). Therefore, the fringing fields are responsible for radiation. As shown in Figure 2-36, the fringing fields at the edges of the patch are travelling in the same direction, therefore their effects are adding-up in phase and re-enforce each other, giving rise to radiation.

Along the Width of the patch (W), the current adds up as well, but it cancels out with the equal, reversed current which appear on the ground plane. This explains why the microstrip transmission line does not radiate.

For a microstrip antenna, the convenient voltage distribution along the length of the patch gives rise to the fringing fields, which in turn triggers the radiation. As explained in Section 2.7, a lower value dielectric constant leads to a better radiation, as the field bents further away from the patch.

Because of the small substrate thickness, the waves within the dielectric get reflected at the edge of the patch and the formed standing waves can be represented by cosine and sine functions.

The fringing fields at the edges of the patch are also very small and the electric fields appear to be perpendicular to the surface of the patch. This means that the TM modes will be considered within the cavity.

2.9.2.1 TM Fields within the Cavity

As described in [41], the field configurations (modes) within the cavity can be determined using the vector potential and the boundary conditions.

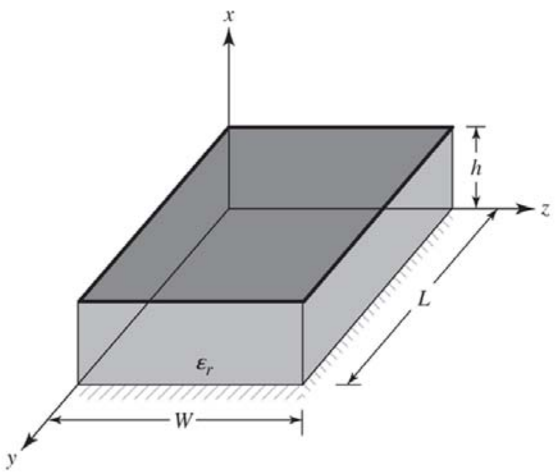

Figure 2-40: Rectangular Microstrip Patch geometry [41]

For a rectangular microstrip patch geometry described in Figure 2-40, the resonant frequencies within the cavity are:

$$(f_r)_{mnp} = \frac{1}{2\pi\sqrt{\mu\varepsilon}}\sqrt{(\frac{m\pi}{h})^2 + (\frac{n\pi}{L})^2 + (\frac{p\pi}{W})^2} \tag{2.16}$$

Where m, n ,p = 0, 1, 2,….are the number of half-cycle field variation along the x, y, z directions [125].

The fields within the cavity can be written as:

$$E_x = -j\frac{(k^2-{k_x}^2)}{\omega\mu\varepsilon}A_{mnp}\cos(k_x x')\cos\left(k_y y'\right)\cos\,(k_z z')\ ; \tag{2.17}$$

$$E_y = -j\frac{k_x k_y}{\omega\mu\varepsilon} A_{mnp} \sin(k_x x') \sin(k_y y') \sin(k_z z') ; \quad (2.18)$$

$$E_z = -j\frac{k_x k_z}{\omega\mu\varepsilon} A_{mnp} \sin(k_x x') \cos(k_y y') \sin(k_z z') ; \quad (2.19)$$

$$H_x = 0; \quad (2.20)$$

$$H_Y = -\frac{k_z}{\mu} A_{mnp} \cos(k_x x') \cos(k_y y') \sin(k_z z'); \quad (2.21)$$

$$H_z = -\frac{k_y}{\mu} A_{mnp} \cos(k_x x') \sin(k_y y') \cos(k_z z'); \quad (2.22)$$

$$\text{Where } k_x = \frac{m\pi}{h};\ k_z = \frac{p\pi}{W};\ k_y = \frac{n\pi}{L} \quad (2.23)$$

are the wavenumbers at mode m, n, p, and x', y', z' are the coordinates along the corresponding axes and the A_{mnp} represents the amplitude coefficients for each mnp mode.

The dominant mode is the mode whose resonant frequency is the lowest. This is mainly determined by the dimensions of the patch.

a) If L>W>h, then the dominant mode is TM_{010}^{x}, with the following resonant frequency:

$$(f_r)_{010} = \frac{1}{2L\sqrt{\mu\varepsilon}} = \frac{c}{2L\sqrt{\varepsilon_r}}, \text{where c is the speed of light in vaccum.} \quad (2.24)$$

b) If L>W>L/2>h, then the second order mode is TM_{001}^{x}, with the following resonant frequency:

$$(f_r)_{001} = \frac{1}{2W\sqrt{\mu\varepsilon}} = \frac{c}{2W\sqrt{\varepsilon_r}}, \text{where c is the speed of light in vaccum.} \quad (2.25)$$

c) If L>L/2>W>h, then the second mode is TM_{020}^{x} (instead of TM_{010}^{x}), with the following resonant frequency:

$$(f_r)_{020} = \frac{1}{L\sqrt{\mu\varepsilon}} = \frac{c}{L\sqrt{\varepsilon_r}}, \text{where c is the speed of light in vaccum.} \tag{2.26}$$

d) If W>L>h, then the dominant mode is $\mathrm{TM}^{\mathrm{x}}_{001}$, with the resonant frequency given in b).

e) If W>W/2>L>h, then the second order mode is $\mathrm{TM}^{\mathrm{x}}_{002}$ and the resonant frequency is:

$$(f_r)_{002} = \frac{1}{W\sqrt{\mu\varepsilon}} = \frac{c}{W\sqrt{\varepsilon_r}}, \text{where c is the speed of light in vaccum.}$$

Considering the field within the cavity described above, the field distributions along the sidewalls of the cavity for different modes is very similar to what is shown in Figure 2-41.

The microstrip patch can be represented by 4 slots, corresponding to the four edges of the antenna, but from these, only 2 slots radiate and produce the radiation pattern of the structure. The slots separated by the length of the patch radiate, while the radiation of the other slots that are separated by the width of the patch cancel along the principal planes.

The distance between the radiating slots is $\frac{\lambda_g}{2}$, where λ_g is the guide wavelength. Having this distance between the slots, it means that the fields at the aperture of the two slots have opposite polarisation, as shown in Figure 2-41, for the $\mathrm{TM}^{\mathrm{x}}_{010}$mode. This allows the addition of those fields in a plane perpendicular to the ground plane and it gives the maximum radiation pattern normal to the patch.

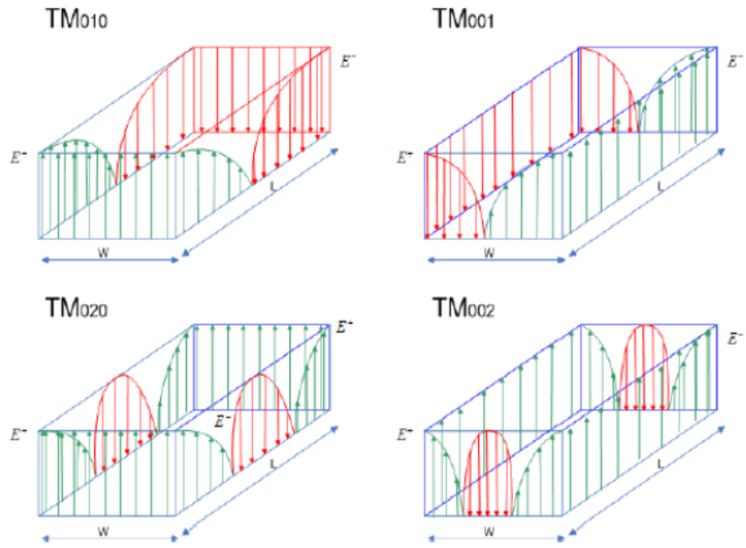

Figure 2-41: TM Modes in a Microstrip Patch Cavity [41], [126]

2.9.2.2 TM_{010} Operating Mode

If the dominant mode is TM_{010}, then the fields within the cavity are:

$$E_x = E_0 \cos\left(\frac{\pi}{L} y'\right) \tag{2.27}$$

$$H_z = H_0 \sin\left(\frac{\pi}{L} y'\right) \tag{2.28}$$

$$E_y = E_z = H_x = H_y = 0 \tag{2.29}$$

$$\text{Where } E_0 = -j\omega A_{010} \; and \;\; H_0 = (\frac{\pi}{\mu L}) A_{010} \tag{2.30}$$

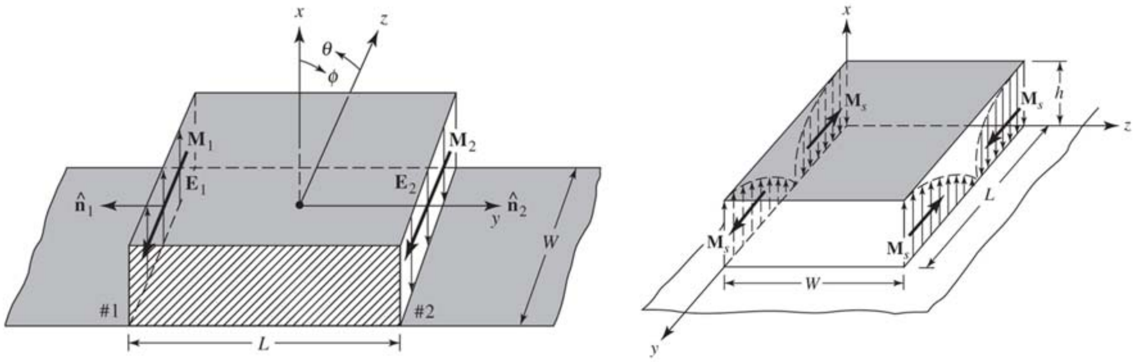

Figure 2-42: Current Densities on Microstrip Patch slots for the first mode [41]

As explained in the previous section, the electric field undergoes a phase reversal along the length of the structure and is uniform along the width of the structure. As illustrated in Figure 2-42, on each slot, there is a magnetic current density, $M_s = -2\hat{n} \times E_a$, where E_a is the E field at the slots.

The magnetic current densities have the same magnitude and phase along the W. The two magnetic current densities are separated by L and they will add in a direction normal to the patch. Figure 2-43 shows the E and H pattern of each slot and of the combination between the two slots. #1 and #2 represent the numbers of the radiating slots that combine to provide the broadside radiation pattern.

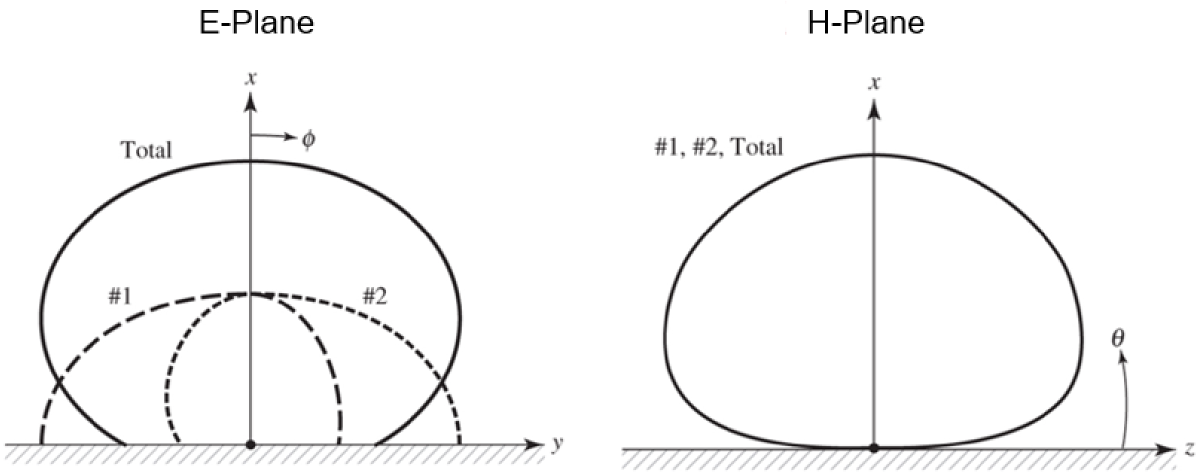

Figure 2-43: E and H pattern cuts of the Microstrip Patch Slot [41]

The other two slots of Length L and height h present two current densities of the same magnitude, but opposite direction, as shown in Figure 2-42. As a consequence, the fields radiated by those slots cancel each other.

The far Electric Fields radiated by one of the end slots of the microstrip antenna are [41]:

$$E_r \approx E_\theta \approx 0 \tag{2.31}$$

$$E_\phi = +j\frac{k_0 h W E_0 e^{-jk_0 r}}{2\pi r}\left\{sin\theta\,\frac{sinX}{X}\frac{sinZ}{Z}\right\} \tag{2.32}$$

$$\text{Where } X = \frac{k_0 h}{2} sin\theta cos\phi, \text{and } Z = \frac{k_0 W}{2} cos\theta \tag{2.33}$$

if $k_0 h \ll 1,$ then

$$E_\phi = +j\frac{V_0 e^{-jk_0 r}}{\pi r}\left\{sin\theta\,\frac{\sin\left(\frac{k_0 W}{2} cos\theta\right)}{cos\theta}\right\} \tag{2.34}$$

$$\text{Where } V_0 = hE_0 \text{ is the voltage across the slot} \tag{2.35}$$

and r is the farfield distance.

Considering that the array factor for two elements of the same magnitude and phase separated by L, along y direction is [41]:

$$(AF)_y = 2\cos\left(\frac{k_0 L}{2}\sin\theta\ sin\phi\right) \tag{2.36}$$

the total electric field for the two slots can be written as [41]:

$$E_{\phi tot} = +j\frac{2V_0 e^{-jk_0 r}}{\pi r}\left\{sin\theta\frac{\sin\left(\frac{k_0 W}{2}cos\theta\right)}{cos\theta}\right\}\cos\left(\frac{k_0 L}{2}sin\theta\ sin\phi\right) \tag{2.37}$$

In Figure 2-44, the broadside radiation pattern is shown for a microstrip patch antenna operating in the TM_{010} mode.

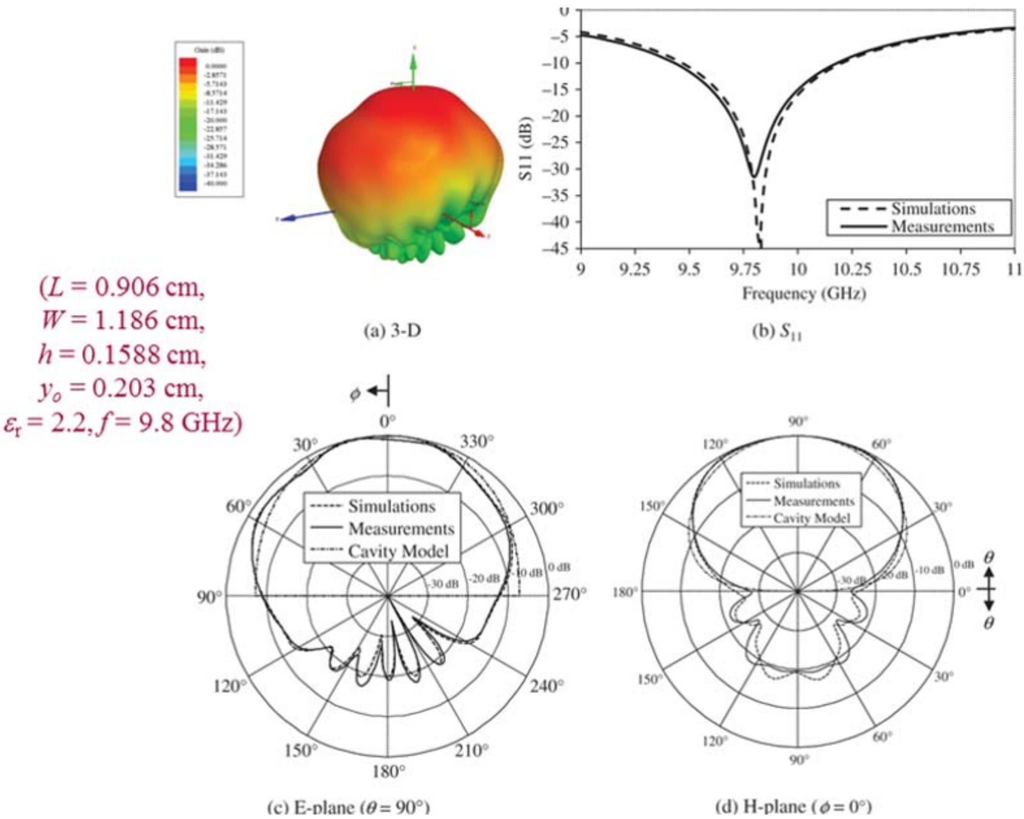

Figure 2-44: TM010 Mode Radiation Pattern [41]

2.9.2.3 TM_{020} Operating Mode

The second mode can be excited at the desired resonant frequency if the patch dimensions are selected as explained in Section 2.9.2.1:

If L>L/2>W>h, then

$$(f_r)_{020} = \frac{1}{L\sqrt{\mu\varepsilon}} = \frac{c}{L\sqrt{\varepsilon_r}}, \text{where c is the speed of light in vaccum.} \quad (2.38)$$

Such a patch has been built in CST, in order to evaluate the radiation pattern and to prove its operational concept. Figure 2-41 shows the field distribution inside the cavity and it illustrates the differences between the second mode and the first mode.

Similar to Figure 2-42, the current densities distribution for the Microstrip Patch operating in the second mode are illustrated in Figure 2-45. This helps to understand and estimate the radiation pattern for the second operational mode.

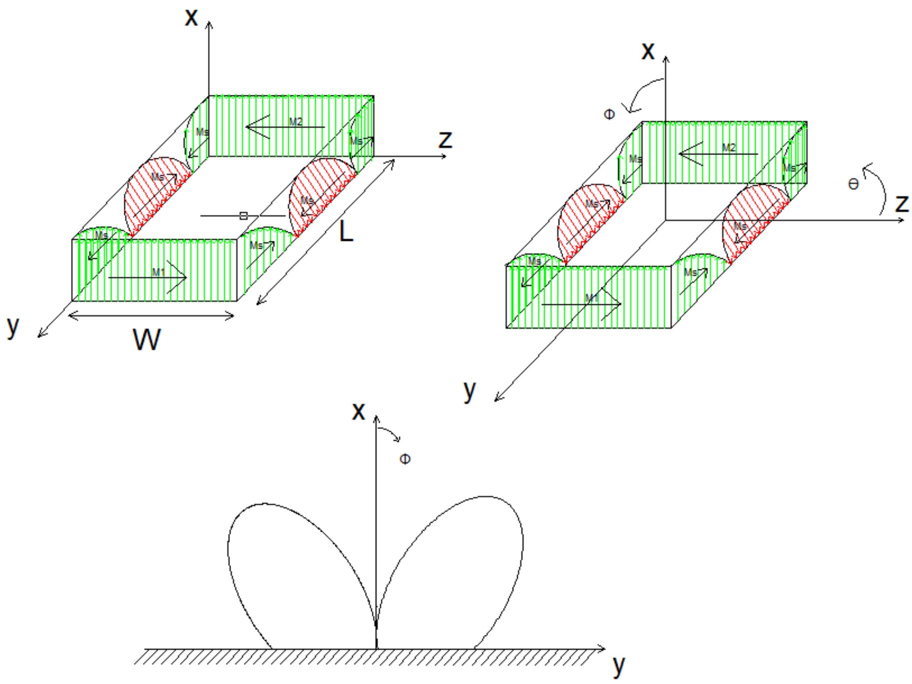

Figure 2-45: Current Densities on Microstrip Patch slots for the second mode

As in the previous section, the fields within the dielectric substrate can be found more accurately if treating the structure as a cavity with electric walls above and below and magnetic walls along the perimeter of the patch. Referring to Figure 4-1, which shows the considered coordinates of a simulated patch operating in the second mode, the electric and magnetic fields within the cavity are:

$$E_z = -j\frac{1}{\omega\mu\varepsilon}\left(\frac{\partial^2}{\partial z^2} + k^2\right)A_z \;; \tag{2.39}$$

$$H_z = 0 \;; \tag{2.40}$$

$$E_x = -j\frac{1}{\omega\mu\varepsilon}\frac{\partial^2 A_z}{\partial z \partial x} \;; \tag{2.41}$$

$$H_x = \frac{1}{\mu}\frac{\partial A_z}{\partial y} \;; \tag{2.42}$$

$$E_y = -j\frac{1}{\omega\mu\varepsilon}\frac{\partial^2 A_z}{\partial z \partial y} \;; \tag{2.43}$$

$$H_y = -\frac{1}{\mu}\frac{\partial A_z}{\partial x} \;; \tag{2.44}$$

where, A_z is the vector potential and after applying the boundary conditions, the final form of the vector potential within the cavity is:

$$A_z = A_{mnp}\cos(k_x x')\cos(k_y y')\cos(k_z z') \tag{2.45}$$

The primed coordinates x', y', z' are used to represent the fields within the cavity and A_{mnp} is the amplitude coefficient of each mnp mode.

$$k_x = \frac{n\pi}{L};\; k_z = \frac{m\pi}{h};\; k_y = \frac{p\pi}{W} \;; \tag{2.46}$$

Where m, n, p are half cycle field variations along z, x, y directions.

Knowing that $k_x{}^2 + k_y{}^2 + k_z{}^2 = k_r{}^2 = \omega_r{}^2\mu\varepsilon$ (2.47) and using the formulas from [41], it results that the resonant frequency

$$(f_{res})_{npm} = \frac{1}{2\pi\sqrt{\mu\varepsilon}}\sqrt{(\frac{n\pi}{L})^2 + (\frac{p\pi}{W})^2 + (\frac{m\pi}{h})^2} = \frac{c}{2\pi\sqrt{\epsilon_r}}\sqrt{(\frac{n\pi}{L})^2 + (\frac{p\pi}{W})^2 + (\frac{m\pi}{h})^2} \quad (2.48)$$

Where h, L, W are the substrate thickness, patch length and patch width, μ is the substrate permeability, ε_r is the substrate permittivity, and c is the speed of light in vacuum [55].

By introducing (2.45) in (2.39) to (2.44) and by calculating the partial derivatives of vector potential, it results that:

$$E_z = -j\frac{(k^2 - {k_z}^2)}{\omega\mu\varepsilon}A_{mnp}\cos(k_x x')\cos(k_y y')\cos(k_z z')\ ; \quad (2.49)$$

$$E_y = -j\frac{k_z k_y}{\omega\mu\varepsilon}A_{mnp}\cos(k_x x')\sin(k_y y')\sin(k_z z')\ ; \quad (2.50)$$

$$E_x = -j\frac{k_z k_x}{\omega\mu\varepsilon}A_{mnp}\sin(k_x x')\cos(k_y y')\sin(k_z z')\ ; \quad (2.51)$$

$$H_z = 0; \quad (2.52)$$

$$H_y = -\frac{k_x}{\mu}A_{mnp}\sin(k_x x')\cos(k_y y')\cos(k_z z'); \quad (2.53)$$

$$H_x = -\frac{k_y}{\mu}A_{mnp}\cos(k_x x')\sin(k_y y')\cos(k_z z'); \quad (2.54)$$

For TM_{020} (m=0 , n=2 , p=0), equations (2.49)-(2.54) become:

$$E_z = E_0\cos(\frac{2\pi}{L}x') \quad (2.55)$$

$$H_y = H_0\sin(\frac{2\pi}{L}x') \quad (2.56)$$

$$E_y = E_x = H_z = H_x = 0; \quad (2.57)$$

2.10 Circularly polarised microstrip patch

This section presents some methods for obtaining circular polarisation on the rectangular microstrip patch. It also discusses the necessity of employing the circular polarisation, especially for the LEO-MEO satellite applications.

2.10.1 Circular polarisation benefits

Either as a transmitter or a receiver, the ground station antenna plays an important role in any type of communication including satellite communications. The azimuth, elevation and polarisation angles must be accurately adjusted on the ground antenna in order to achieve the highest throughput [127].

The polarisation of an electromagnetic wave is normally defined by the electric field vector whose extremity can vary only in one direction or in more than one direction. A wave can be described as linearly polarised, circularly polarised or elliptically polarised, and it denotes the position of the electric field vectors relative to a defined plane. For the linear polarisation, the E-field vectors are either positioned horizontally or vertically relative to a plane, from where the name of ‘horizontal polarisation’ and ‘vertical polarisation’ originate.

The circular polarisation, results from two perpendicular, linear polarisations placed 90˚ out of phase. If the two linear electric fields have equal vectors in amplitude, then, the polarisation is purely circular. In this case, the tip of the E-field vector rotates as it propagates, and it defines a circular path in the plane normal to the direction of propagation. The direction of rotation can be left hand or right hand producing the left-hand circularly polarisation (LHCP) or right-hand circularly polarisation (RHCP), as the wave propagates away from the observer. This sense of rotation depends on the position of the 90˚ out of phase polarisation: if leads or lags the other wave.

The elliptical polarisation is a particular type of circular polarisation. If the amplitudes of the two E-field vectors are not equal and/or the phase difference between the two waves is not 90˚, then the resultant vector tip defines an elliptical shape in the direction of propagation [128].

The polarisation of the receiving antenna must be aligned to the polarisation of the incoming wave for maximum power transfer. A linearly/circularly polarised antenna is able to receive a circularly/linearly polarised wave, but at a power loss of 3 dB. This is because the linear antenna will respond only to one of the linear components of the circularly polarised wave, and therefore, the received power is halved, compared to the transmitted power.

In satellite communications, the horizontal polarisation is defined as the polarisation where the E-field vector is parallel to the equatorial plane and the vertical polarisation as the polarisation where the E-field vector is parallel to the Earth's polar axis [129].

As the LEO and MEO satellites orbit the Earth at high speeds, the ground station antenna must be able to track the moving satellites which can become visible at different azimuth angles on each pass. The circular polarisation is conveniently used in these situations because the polarisation losses due to antennas misalignment do not occur as with the linear polarisation.

The ionospheric effects have a great impact on linearly polarised waves. The linear polarisation is rotated (Faraday rotation) because of the strong magnetic fields in the Ionosphere and polarisation mismatch occurs between transmitting and receiving antennas. This phenomenon does not affect the circular polarisation because the vectors rotation occurs equally for both wave components [128].

The multipath propagation for a circularly polarised wave is greatly reduced by filtering. When a circularly polarised wave hits a conductive surface, the reflected wave is inversely polarised. Therefore, if the transmitted wave is left-hand polarised, then the multipath propagations will be right-hand polarised, and therefore filtered at the receiving side.

The Circular Polarisation purity is quantified by the cross-pol discrimination (XPD). This is, in essence, the co-polar minus the cross-polar logarithmic values:

$$XPD = 20log\frac{Co{-}pol}{Cross{-}pol}\ (dB) \tag{2.58}$$

Another way of expressing the cross-pol discrimination is by the Voltage Axial Ratio (VAR). VAR is the ratio of the major axis to minor axis of the ellipse that the resulting vector defines in the direction of propagation.

Ideally, for circular polarisation, this value is equal to 1 (linear value), and the XPD is infinite. However, in reality, the ratio is greater than one, and therefore, the E-Field vector describes an ellipse. The relationship between the XPD and VAR is:

$$XPD = 20log\frac{r+1}{r-1}\ (dB), \text{where r is the Axial Ratio} \tag{2.59}$$

2.10.2 Methods for obtaining circular polarisation on a rectangular Microstrip Patch

As described in the previous section, circular polarisation is desired in applications where one or both components of the communication link move. Circular polarisation allows the data transmission regardless the orientation of the transmitter or receiver [130].

Circular polarisation radiation is realised by exciting two orthogonal modes of equal amplitudes [131]. This involves the insertion of small perturbing elements into the microstrip structure, at appropriate locations, with respect to the feed [132].

Different types of perturbation methods have been reported in literature to generate circular polarisation on a single fed Microstrip Patch: truncated corners [133], stubs [134], slits [132], notches [135], [166]. Figure 2-46 illustrates some of the perturbation methods reported in literature.

The bandwidth of a circularly polarised microstrip patch is obtained after overlapping the 10 dB impedance bandwidth and the 3 dB axial ratio bandwidth [131].

In [133], the circular polarisation is obtained by truncating two opposite corners of a rectangular microstrip patch. The impedance and axial-ratio bandwidths are improved by implementing a U-slot.

Another similar way of obtaining circular polarisation is presented in [132]. Asymmetrical slits are implemented on all four corners of the rectangular patch. The reported impedance and axial ratio bandwidths are small.

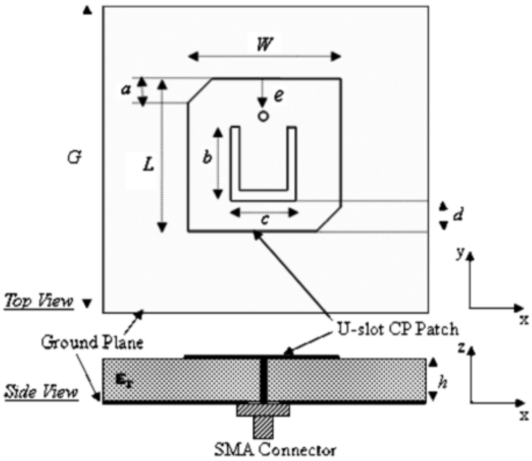

133

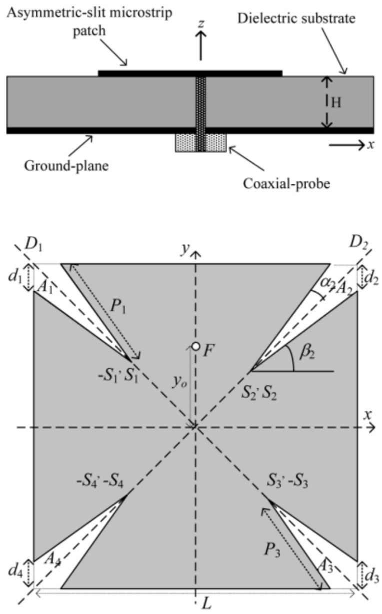

132

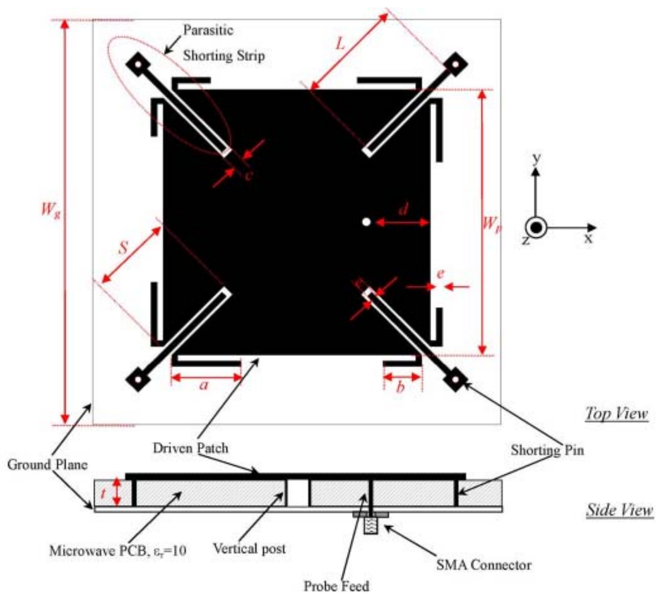

134

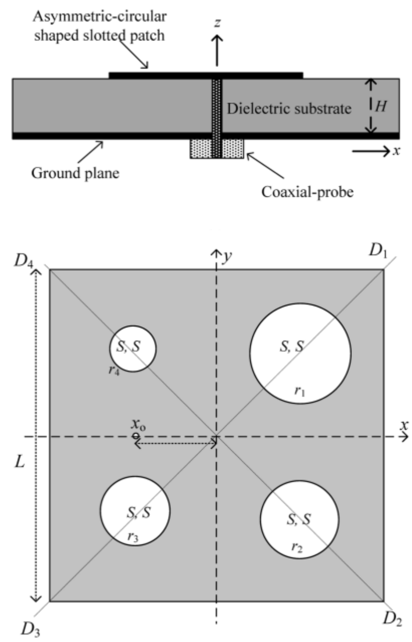

135

Figure 2-46: Perturbation methods reported in literature for achieving circular polarisation

Parasitic elements are implemented instead in [134], on all four corners of the patch. The elements are shorted to the ground plane, for size reduction and capacitive and inducting loading. The reported impedance and axial ratio are again, small.

In [135], circular, asymmetric, slots are employed along the diagonal directions of the rectangular patch. The size of the antenna is reduced by implementing four symmetric slits along the orthogonal directions of the asymmetric circular slots, which reduce the resonant frequency of the structure. As in all the other methods, this method also provides small impedance and axial-ratio bandwidths.

Dual fed microstrip patches with 90˚ phase shifted signals have been also reported in literature, to generate Circular Polarisation with high axial ratio bandwidth. This comes at the expense of increased size of ground plane and a more sophisticated feeding network [131].

In [41], Balanis obtains circular polarisation on a rectangular patch by placing the feed along the diagonal line of the element. The same results can be obtained for a square patch by cutting diagonal slots on patch.

2.11 Reflect-array Antennas Theory

A reflectarray represents a hybrid antenna that combines the advantages of a conventional printed antenna array consisting of hundreds of elements and a spatially placed feed antenna illuminating the elements, Figure 2-47, [136]. The printed elements are designed so that they reflect the incident field with certain phase shifts in order to collimate the beam to a certain direction. In this way, the reflectarray eliminates the bulkiness of conventional parabolic antennas and the lossy feed networks of printed arrays.

The elements of the reflectarray are designed to introduce phase shifts meeting the following two important conditions:

- The phase shift from each element at a point in space is spatial phase delay (because each element of the reflectarray is illuminated at a different location by the feed, introducing a phase delay between the feed and each patch);

- The phase shifts are progressive phase shift (a progressive phase shift must be introduced between elements if it is intended to get the reflected energy from each element collimated into a beam and to squint that beam to a certain direction) [137].

To achieve this, different phase tuning approaches have been reported in literature: variable size elements [137-140, 145], delay lines [138, 141-144], rotation angles [136-137], use of solid-state elements [137], use of tuneable dielectric materials [138-157].

The microstrip patch is a highly resonant element, which according to the transmission line theory, it can be approximated with a parallel RLC circuit: the metallic patches behave as parallel capacitors with the adjacent elements, the ground can be associated with a parallel inductor and the dielectric substrate loss can be modelled as a parallel resistor.

For the variable size elements tuning approach, the length of the microstrip patch should be half a wavelength in the dielectric and a small deviation from that value produces a wide range of phase shift in the reflected wave. Figure 2-47 illustrates the concept of a typical reflectarray, where the source is positioned far enough from the patches such that the incident wave to the elements can be approximated to a plane wave. Ideally, one single reflecting element should be capable of providing a 360˚

phase shift while sweeping the Length of the patch. In reality, this value is affected by the substrate thickness, separation between elements, the angle of incidence of the feed, and a phase shift of about 300-330˚ is achieved. However, in [136] this phase shift range has been considered sufficient for the reflectarray design.

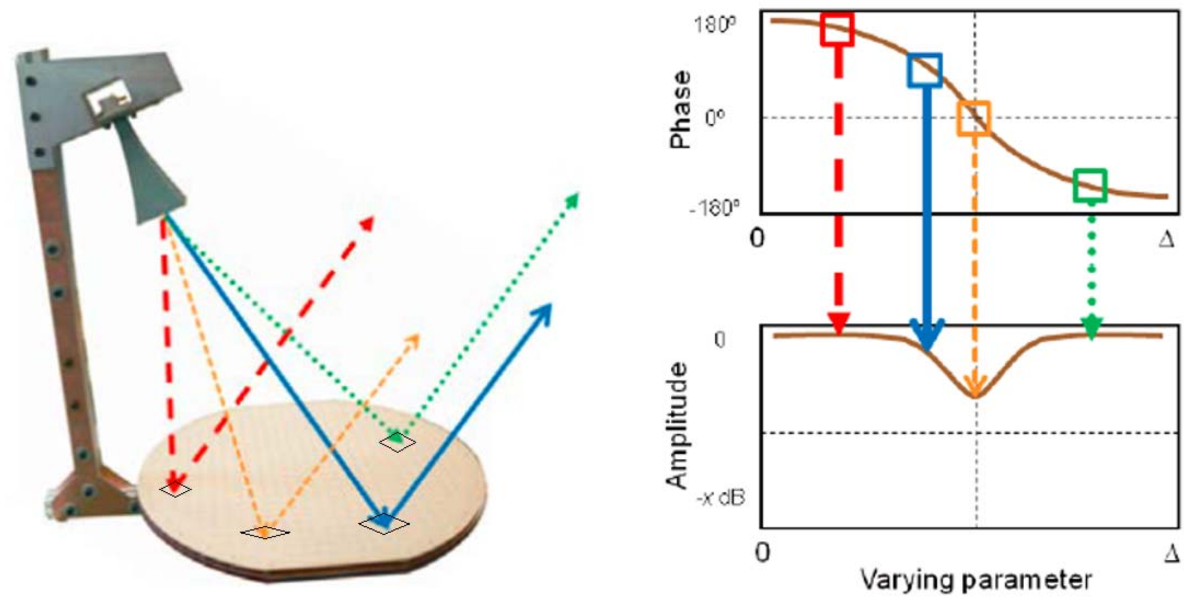

Figure 2-47: The reflectarray concept and the phase and amplitude of the reflection coefficient of the reflecting elements [136]

A typical S-curve that shows the reflected phase change versus the patch length for variable size reflectarray is showed in Figure 2-47. It can be observed that the S-curve crosses 0˚, which represents the resonance of the reflectarray element, i.e. the orange reflected wave. All the other reflecting elements present different lengths, which exhibit different phases on the reflected waves. The Slope of the S-curve, while it crosses the

0˚ is bandwidth representative. The more gradual slope, the wider the bandwidth of the element. The elements with the dimensions close to the resonance provide the largest variation in phase range, but they also exhibit the highest loss, as the amplitude of the reflection coefficient shows in Figure 2-47. At resonance, the electrical current flow on the element reaches its maximum, which leads to maximum loss.

Similar to the antenna arrays theory, in order to collimate the beam in a particular/desired direction, a progressive phase value is assigned to each element in the reflectarray. However, one also has to take into account the feed position with respect to each element in the antenna. The incident electromagnetic fields from the feed will have a certain phase at the reflectarray surface, proportional to the distance between the feed and the reflectarray elements. This is the **spatial phase delay**.

In a typical reflectarray antenna structure, the reflectarray is in the farfield of the feed antenna and its surface is perpendicular to the incident radiation. All the elements of the reflectarray are illuminated at an offset angle with respect to the centre of the reflectarray, therefore different path-delays exist at different points on the surface of the reflectarray.

Each element will then reflect the incoming field with a specific delay and the reflected energy will combine in phase constructively or destructively, giving rise to a non-coherent pattern. In order to collimate the beam, the phasing elements of the reflectarray must compensate for this path-delay.

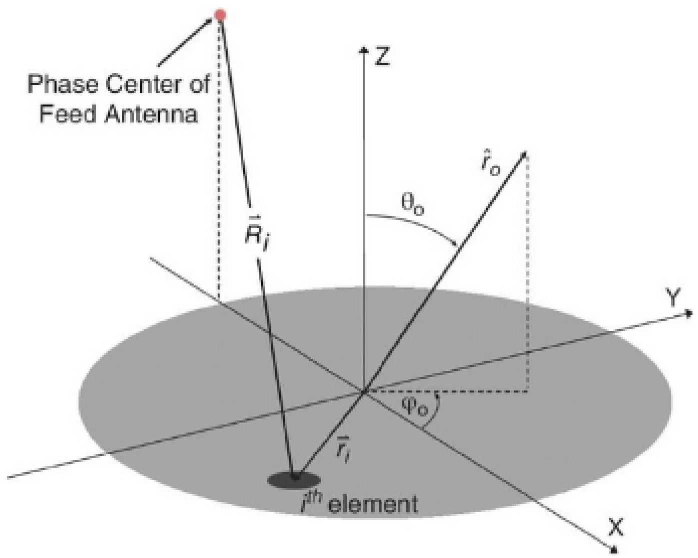

Figure 2-48: The geometrical parameters of a planar reflectarray Antenna [137]

According to Figure 2-48, the spatial phase delay can be written as:

$$\Phi_{spd} = -\beta_0\, R_i \tag{2.60}$$

Where R_i is the distance from the feed to the ith element and β_0 is the wavenumber equal to $2\pi/\lambda_0$. If each element in the reflectarray will exhibit such a phase, therefore compensate for this spatial delay, then the reflected beam will collimate in the broadside direction (Z-direction).

To point the beam in any other direction than broadside (θ=0, Φ=0), each element must generate a certain phase, referred to in [137] as the **progressive phase shift**:

$$\Phi_{pp} = -\beta_0\, r_i \cdot r_0 \tag{2.61}$$

Where $\mathrm{r_i}$ is the position unit vector of the ith element and $\mathrm{r_0}$ is the beam direction unit vector, as it is illustrated in Figure 2-48. The dot product between the two-unit vectors represents the cosine of the angle between the two vectors.

If the position vector of the ith element is written using the spherical angles θ and ϕ, then the progressive phase becomes:

$$\Phi_{pp} = -\beta_0 \, (x_i \sin\theta_0 \cos\varphi_0 + y_i \sin\theta_0 \sin\varphi_0) \tag{2.62}$$

It results that the total phase that the unit cell must account for is the **spatial phase delay plus the progressive phase shift**:

$$\Phi_{total} = -\Phi_{spd} + \Phi_{pp} = \beta_0 \, (R_i - \sin\theta_0 (x_i \cos\varphi_0 + y_i \sin\varphi_0)) \tag{2.63}$$

If the position of the feed is known, then

$$R_i = \sqrt{(x - x_i)^2 + (y - y_i)^2 + (z - z_i)^2} \tag{2.64}$$

where x_i, y_i, z_i are the position coordinates of the elements in the reflectarray and x,y,z are the position coordinates of the feed [158].

Otherwise, if the feed incident angles are known instead, then

$$R_i = \sin\theta_i(x_i\cos\varphi_i + y_i\sin\varphi_i) \tag{2.65}$$

Where θ_i, φ_i represent the feed incident angle [159].

When employing patches or similar elements in a reflectarray, several methods used to increase the element bandwidth are presented in [140] and these include: increasing the substrate thickness (but using low dielectric constants), use substrates with high dielectric constant in order to decrease the substrate's thickness, increase the inductance of the patch by cutting slots into it, add reactive components to reduce the VSWR.

In [139], it is concluded that the length-phase slope increases as the substrate permittivity increases, which leads to bandwidth reduction. The phase curve illustrates the element phase stability with respect to frequency variation.

The main issue encountered with this phase shifting method is the nonlinear variation in phase with frequency. A first consequence of this issue is the narrow bandwidth of reflectarrays with variable size patch element.

In [137], the reflection coefficients of the reflectarray elements, as a function of patch length, at different incident angles are presented, and shown in Figure 2-49:

As it can be observed, at 40˚ incidence angle, the resonant length changes, but not considerably, the slope of the S-curve increases slightly, and the amplitude of the reflection coefficient drops (more loss). Given this, one can say that by changing the frequency, a slight variation of the incident angle can be achieved [160].

For the components excited at a certain incident angle, the reradiated component will be directed in the same direction as the element's pattern, while the reflected components will be directed away from the beam, at the specular angle. Figure 2-50 illustrates this.

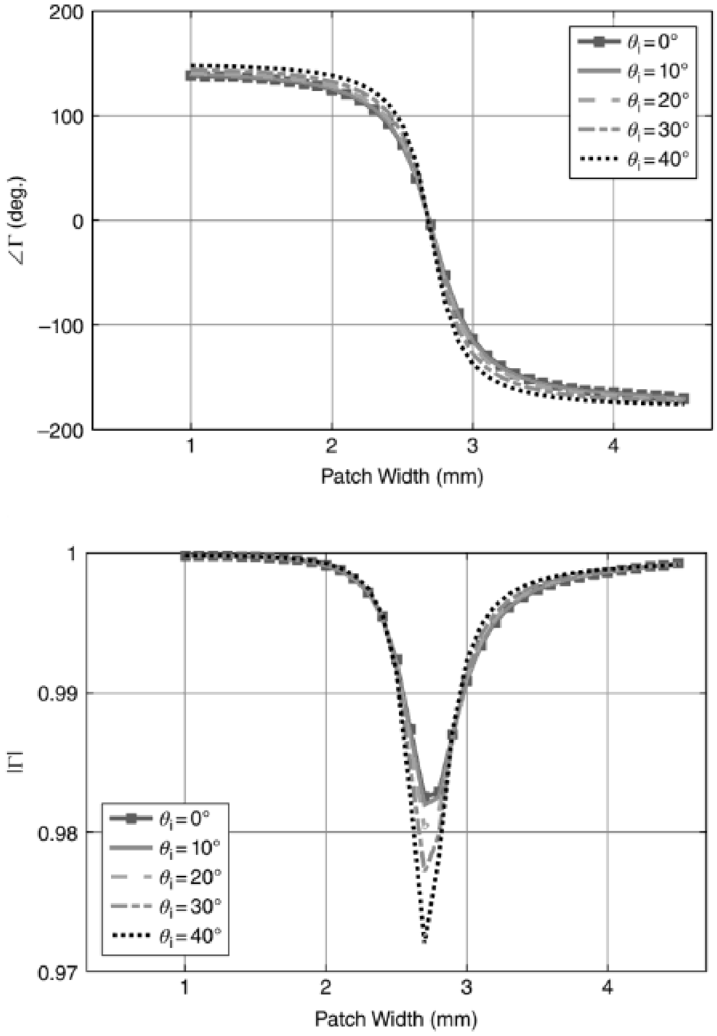

Figure 2-49: Reflection coefficients of the variable size square patch reflect-array element as a function of the patch length, for different angles of incidence [140]

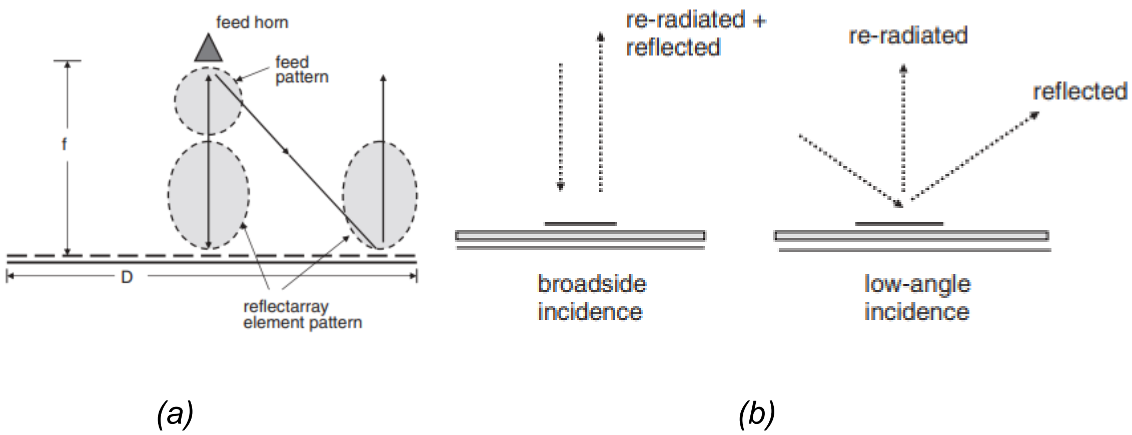

Figure 2-50: Reflectarray element pattern (a), reradiated and reflected waves of a reflectarray element (b) [160]

3. Antenna requirements analysis

Based on the background provided in the previous chapter, a set of requirements for the designed antenna are determined in the following sections. This is done based on a scenario in which a link between the antenna and a LEO satellite is made. This scenario imposes a tighter gain requirement in comparison to other scenarios (as point to point links on Earth, 5G on Earth, IoT, etc.), as the free space path loss between Earth and LEO satellites is high, plus that other losses need also to be considered (as atmospherical losses, polarisation losses, misalignment losses, etc.).

3.1 Link Budget Calculation

In this section, a link budget calculation will indicate the power level received by a satellite from the ground. In this scenario, the satellite altitude is considered to be 550 km and the uplink frequency 30 GHz, as in the SpaceX constellation described in the previous section.

The Power Received at the satellite can be calculated with the following formula:

$$P_r = EIRP + G_R - Losses \tag{3.1}$$

Where $EIRP$ is the Effective Isotropic Radiated Power, G_R is the gain of the receiving antenna, and $Losses$ constitute the total loss that the signal encounters from the Transmitting antenna to the Receiving antenna.

$$Losses = FSPL + RFL + AML + AA + PL \tag{3.2}$$

Where FSPL is the Free Space Path Loss, RFL is Receiver Feeder Loss, AML accounts for the Antenna Misalignment Losses, AA is the Atmospheric and Ionospheric Loss and PL is the Polarisation Loss.

The FSPL can be calculated using the following formula (considering isotropic transmitting and receiving antennas):

$$FSPL = 20\log\left(\frac{4\pi}{\lambda}d\right) \tag{3.3}$$

Where λ is the wavelength, and d is the distance to the satellite. Similar to SpaceX constellation, the satellite altitude is considered to be 550 km. For 30 GHz, the wavelength is 10 mm, and by replacing the values in the FSPL formula, it results:

$$FSPL = 20\log\left(\frac{4\pi}{10*10^{-6}} * 550\right) = 176.78\ dB \tag{3.4}$$

For all the other losses (RFL+AML+AA+PL), an approximate 6 dB value is considered. The Effective Isotropic Radiated Power represents the power that leaves the transmitting antenna.

$$EIRP = P_T + G_T \tag{3.5}$$

Where P_T is the power at the antenna input and G_T is the gain of the antenna. If the power at the antenna input is considered 1W (0 dB or 30 dBm) and the gain of the antenna 15 dB, then the Effective Isotropic Radiated Power becomes:

$$EIRP = 30\ dBm + 15\ dB = 45\ dBm \tag{3.6}$$

In [24], the Rx antenna gain, at the satellite, used for the gateway uplink budget for SpaceX is 40.9 dBi. Having these values, it results that the Power Received at the satellite is:

$$P_r = 45\ dBm + 40.9\ dBi - 176.78\ dB = -90.88\ dBm \tag{3.7}$$

In the above scenario, it was considered the case when the satellite was right above the transmitting antenna, and the distance between the antenna and satellite was minimum. It must be considered that as the satellite moves away from the antenna, the distance between them increases. As a consequence, the FSPL value changes. In order to see the effect of those changes on the link budget, some extra calculations will be presented below.

In the SpaceX constellation, the satellites orbit at 550 km altitude, with 22 satellites per plane. The circumference of the Earth is:

$$Circumference = 2 * \pi * R = 2 * \pi * 6372 = 40016.16\ km \tag{3.8}$$

As illustrated in Figure 3-1, the geocentric semi-angle from the centre of the Earth is:

$$\theta = \arcsin\left(\sin(\alpha) * \frac{R_E + h}{R_E}\right) - \alpha \tag{3.9}$$

The formula above has been determined assuming that RE ≈ OG, as RE>>D/2, h<<RE and θ<<α. For simplicity and clarity, the geometry in Figure 3-1 has not been scaled to illustrate the assumptions above.

By replacing with the values given in Figure 2-5, it results that:

$$\theta = \arcsin\left(\sin(56.55) * \frac{6372+550}{6372}\right) - 56.55 = 8.46^\circ = 0.14758\ rad. \tag{3.10}$$

Having θ, the diameter of the field of view of each Starlink Satellite, orbiting at 550 km above the surface of the Earth, is:

$$D = 2\theta R_E = 2 * 0.14758 * 6372 = 1880\ km \tag{3.11}$$

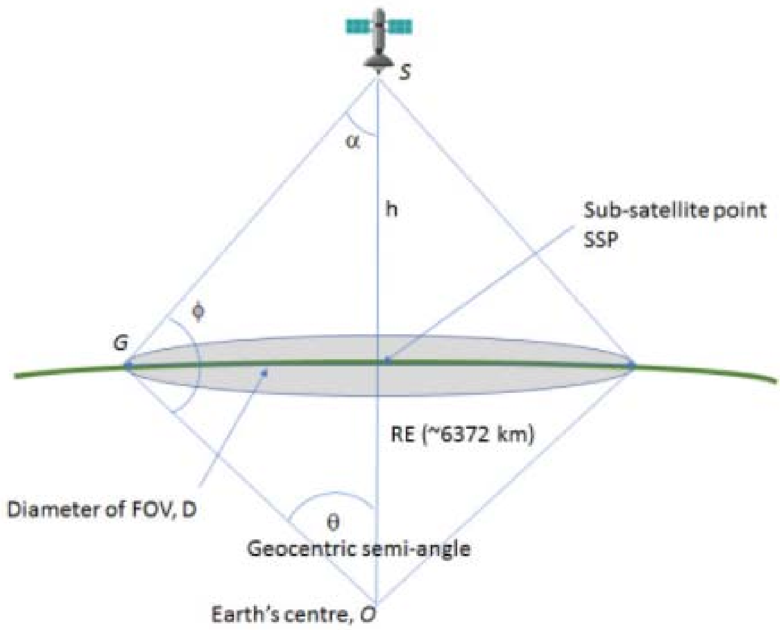

Figure 3-1: Field of View Geometry, where h<<RE and θ<<α

The diameter of the field of view of the Starlink satellites obtained from the above calculations, appears to agree with the value declared in [25], regarding the area that a satellite can cover (970 km radius).

Knowing these values, it results that the number of LEO satellites, with this coverage, necessary to surround the Earth is:

$$\frac{40016.16\ km}{1880\ km} = 21.28 \sim 22\ satellites \tag{3.12}$$

Only one orbit plane is used in this case as this represents the worst scenario. As the number of satellites per plane or the number of planes increases, the tracking requirements relax.

This means that the satellites footprints do not overlap or the overlapping area is very small. As the number of the satellites in constellation increases, the satellites footprints can overlap within 3 dB of the footprint (i.e. half of the footprint area).

For the above scenario, the satellites orbit at 550 km altitude, with 22 satellites per plane. It results that the satellite orbits at 6922 km from the centre of the Earth (Earth radius is 6372 km). The circumference of this circle can be calculated as:

$$Circumference = 2 * \pi * R = 2 * \pi * 6922 = 43492.2\ km \qquad (3.13)$$

By dividing the $Circumference$ to the number of satellites in one plane it results the arc length:

$$Arc = \frac{43492.2\ km}{22} = 1976.91 \qquad (3.14)$$

The corresponding angle to this arc length is:

$$1976.91 = 2 * \pi * 6922 * \frac{Angle}{360} \qquad (3.15)$$

$$Angle = 16.37°$$

It means that the angular distance between two consecutive satellites is about 16.4˚, from the centre of the Earth. From the surface of the Earth, because the satellite footprints do not overlap, the ground antenna needs to track the satellite for about 70˚, on this particular constellation and satellite position. When the ground antenna lies between two satellites, the angle becomes about 92˚, as shown later, in Figure 3-3.

Figure 3-2 illustrates the angle between two satellite, from the centre of the Earth, and the corresponding angle between satellites seen by the ground antenna. When SAT. 1 is positioned at the zenith point relative to the ground antenna, the other consecutive satellite, SAT. 2, is already visible to the antenna, at about 20˚ elevation.

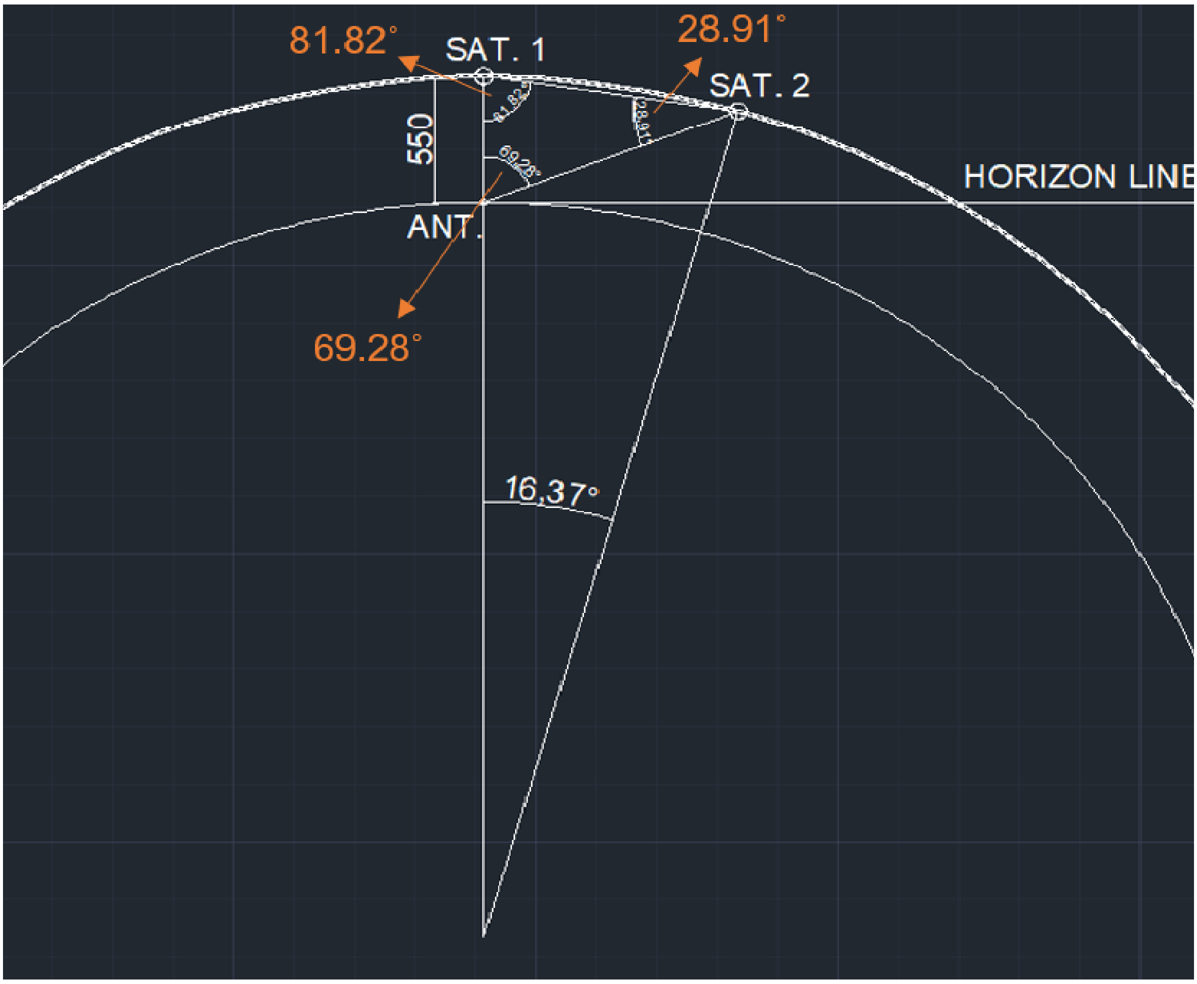

Figure 3-2: Distance between satellites from the Centre of the Earth

This is, obviously, different, if the constellation density is higher, if more than 22 satellites are placed in one orbital plane. For example, for 58 satellites per plane, at 550 km altitude, as SpaceX intends to launch, the angle between satellites is 6.2˚ only, from the centre of the Earth, and about 37˚-40˚ from the surface of the Earth. As the number of satellites in the orbit increases, the angular distance between the satellites seen by the ground antenna decreases. Having a higher number of satellites in orbit, it means that satellites antennas footprints overlap, therefore the ground antenna will need to track the satellite for approximately 40˚ only.

In Figure 3-2, the distance between the antenna and SAT. 2 can be calculated using the sine law:

$$\frac{550}{\sin(28.91)} = \frac{x}{\sin(81.82)} \qquad (3.16)$$

$$x = 1126\ km$$

With this distance, the FSPL changes to 183 dB, therefore, the power received by the satellite will be about 6.2 dB lower. This distance is, again, subject to the number of the satellites per plane. As the satellites are closer to each other, the variations in path loss and in power received at the satellite will be smaller, especially if inter-satellite links are employed.

3.2 Beam Scanning speeds

In order to calculate the orbital speed of a LEO satellite which orbits at 550 km, the Newton second law must be applied on the satellite:

$$F_{sat} = ma \qquad (3.17)$$

Where m is the satellite mass and a is the acceleration due to gravity. The orbiting satellites present a constant horizontal speed and acceleration due to gravity.

The relation above can be written as:

$$\frac{GMm}{r^2} = \frac{mv^2}{r} \tag{3.18}$$

Where G is the gravitational constant, M is the mass of the Earth, v is the orbital speed of the satellite, and r is the distance from the centre of the Earth to the satellite. The relationship becomes:

$$GM = rv^2 \tag{3.19}$$

$$6.67408 \times 10^{-11} \times 5.972 \times 10^{24} = (6372 + 550) \times 10^3 \times v^2 \tag{3.20}$$

v =7588.2 m/s

Having the value of the orbital speed, from the centre of the Earth, the orbiting period can be calculated:

$$\frac{2\times\pi\times(6372+550)\times10^3}{7588.2} = 5731\, sec = 95.5\, mins \tag{3.21}$$

The calculated velocity above is the linear orbital velocity, but in order to determine the necessary tracking speed of the ground antenna, the apparent velocity must be determined. This velocity depends on the distance between the antenna on the surface of the Earth and the satellite. As the satellite approaches the zenith of the ground antenna (the overhead pass), the speed of the satellite will appear to be higher. As the satellite passes the zenith and moves away from the ground antenna, its speed will appear to be lower. This happens due to the position of the satellite velocity vector relative to the ground antenna's line of sight. At zenith, the satellite's velocity vector is exactly perpendicular to the ground antenna's line of sight and the speed of the satellite is maximum. At low elevation angle, the distance between the ground antenna and satellite is maximum, resulting in the lowest apparent angular velocity [165].

The apparent angular velocity can be calculated as per [165]:

$$v_{app} = \frac{\sqrt{GM/r}}{d} \tag{3.22}$$

where d is the distance from the ground antenna to the satellite.

After replacing all the values in the above relationship, it results that:

$$v_{app} = \frac{7588.2\ m/s}{550\times10^3\ m} = \frac{0.0137\ rad}{s} = 0.79°/s \tag{3.23}$$

Therefore, when the distance between the ground antenna and the satellite is 550 km, the tracking velocity is 0.79˚/s. To calculate the angular speed when the distance between the satellite and the ground antenna is $1126\ Km$, the same formula as above must be used:

$$v_{app} = \frac{7588.2\ m/s}{1126\times10^3\ m} = \frac{0.00673\ rad}{s} = 0.38°/s \tag{3.24}$$

Hence, based on Figure 3-2, the tracking speed, that the Ground station antenna needs to follow the satellite, varies between $0.79°/s$ and $0.38°/s$. The values obtained appear to match the expected angular speeds for these altitudes, as described in the graph presented in [161] and [165].

3.3 The required Ground Antenna Beamwidth

In order to determine the necessary ground antenna half-power beamwidth, based on the number of satellites in one orbital plane, some observations must be highlighted.

Figure 3-3 shows the Ground tracking antenna in 2 different situations: one is the same as illustrated in Figure 3-2, marked in red, in which Satellite 1 is at the zenith of the antenna. The second position of the satellites relative to the tracking antenna is illustrated in green. In this situation, the first satellite moved away from the antenna and the second satellite moved towards the antenna, such that the ground station is now placed between the two satellites.

In the first position, when Satellite 1 is perpendicular to the antenna, the angle between the lines of sight of the antenna to the satellites is 69.3˚. However, for the second position, this angle changes to 92.2˚ and this is the highest angle that can occur between the lines of sight, for this orbit (assuming 22 satellite in one plane, spaced 16.37˚ from the centre of the Earth).

Similar to the explanation provided in Section 3.2, because of the angular speed vector, to get from position one (red) into position two (green), the first satellite must move 46.1˚ away from the tracking antenna, whereas the second satellite must move only 23.2˚ towards the tracking antenna. Therefore, the tracking angle required from the ground antenna is 46.1˚, which represents the worst case, where the number of satellites per plane is 22 satellites.

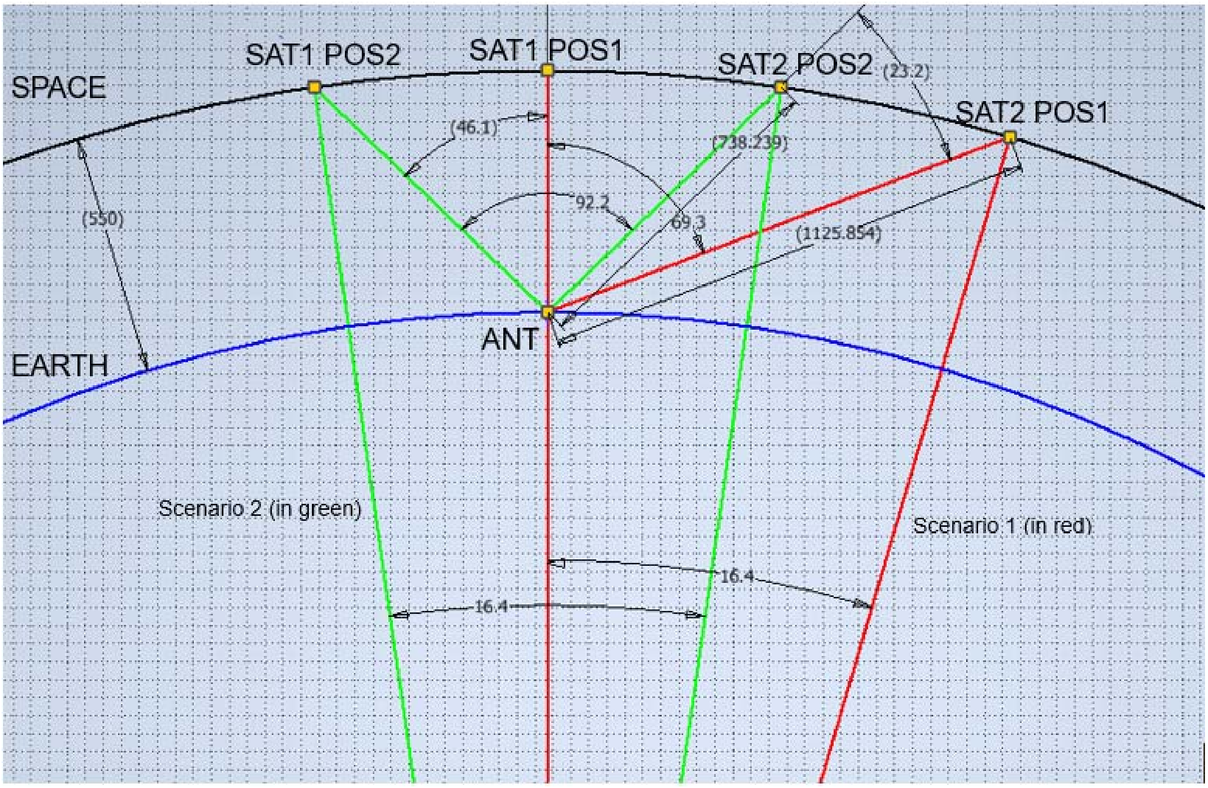

Figure 3-3: The angle between the Lines of Sight of the tracking antenna to two orbiting satellites, in two different situations, assuming 22 satellites per orbit.

As explained by Balanis in [39], the beamwidth of an antenna describes its resolution capabilities to differentiate between two adjacent radiating sources, in our case two adjacent satellites. If the two adjacent satellites are separated by angular distances equal or greater than the half beamwidth angle of the antenna, then the two sources can be distinguished, otherwise, the angular distance between the two will be flatten.

As a consequence, for the first situation, the tracking antenna must not have a beamwidth greater than 69.3˚ and for the second situation, not greater than 92.2˚, otherwise the antenna will not distinguish between the two satellites. Using the formula provided in [39] for determining the gain of a planar antenna knowing the half power beamwidth in the principal planes:

$$Gain\ (dB) \approx 10\ x \log\left(\frac{30000}{\Theta_{1deg}\Theta_{2deg}}\right) \qquad (3.25)$$

it results that 69.3˚ beamwidth translates into an antenna gain of 7.95 dB and 92.2˚ into 5.47 dB. The angles on the denominator represent the half power beamwidths in the principal planes. In the calculations, it has been considered the same beamwidth value in both principal planes.

Those values will be different if the number of satellites per plane increases. For example, if the number of satellites increases to 58, then the tracking antenna must not present a beamwidth higher than 37˚, which means an antenna gain of 13.4 dB. This might change if other inclined orbits, populated with satellites appear and if the intersatellite links are employed.

4. Study of the Microstrip Antenna operating in TM020 Mode

As it has been shown in Section 2.9.2, when the first operating mode is excited, the rectangular microstrip patch presents a broadside radiation pattern. The first operating mode represents the dominant mode, i.e. the lowest operating frequency of the antenna. The broadside beam feature has been extensively referred in literature, and used in applications where broadside and wide beamwidths are required. However, if the second operating mode is excited, the radiation pattern becomes symmetrically split around the zenith, and this could be used for directivity enhancement.

The antenna will be exploited in order to obtain the antenna gain required in the scenario described in Chapter 3. So far, this mode has not been referenced in many applications. The second operating mode of a patch antenna, TM020, is analysed in this chapter, where a patch antenna is designed and simulated in CST.

4. 1 Simulations of the Microstrip Patch antenna operating in TM020 mode

To verify the second operational mode theory, a microstrip patch has been modelled and simulated in CST. Figure 4-1 illustrates the dimensions of a Microstrip Patch antenna which operates in TM020 mode, at 30 GHz. The patch is fed by a coaxial probe, whose position point (y0) has been chosen to minimise the reflected power back to the source.

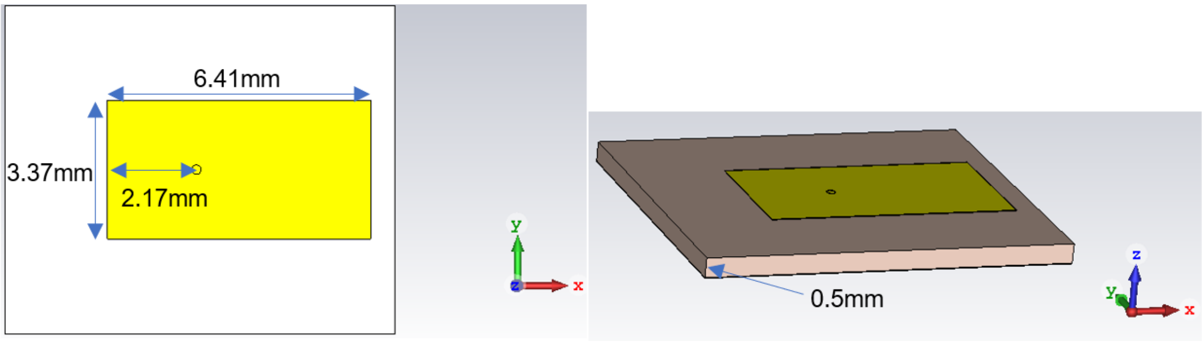

Figure 4-1: Microstrip Patch Antenna dimensions for TM020 operating mode

Using the coax impedance calculator facility of CST Studio, the coax feed dimensions have been calculated, resulting in a line impedance of 48.85Ohm. The internal conducting pin of the coax has a diameter of 0.23 mm, and the dielectric around the pin has a diameter of 0.77 mm, with a dielectric constant of 2.2.

A parameter sweep, where the position of the feeding point was varied relative to the edge of the patch (y0 = 2.17mm), helped finding the optimum position of the feeding point.

As it can be observed, in Figure 4-2 (a), the curve corresponding to y0=2.166 mm from the edge of the patch, shows the lowest reflection point when the antenna is resonating. As explained in [162], ideally, at resonance, the impedance, at an arbitrary distance from the edge of the patch, is purely resistive.

The Length of the patch has been slightly trimmed down to 6.41 mm to have the resonance centred to 30GHz. The 10 dB bandwidth is 974 MHz. It has also been observed that by offsetting the metallic patch from the centre of the dielectric substrate, the resonance increases and the return loss improves - Figure 4-2 (b). The metallic patch is shifted in +x direction, by 0.95mm, bringing it very close to the edge of the dielectric substrate (0.6mm).

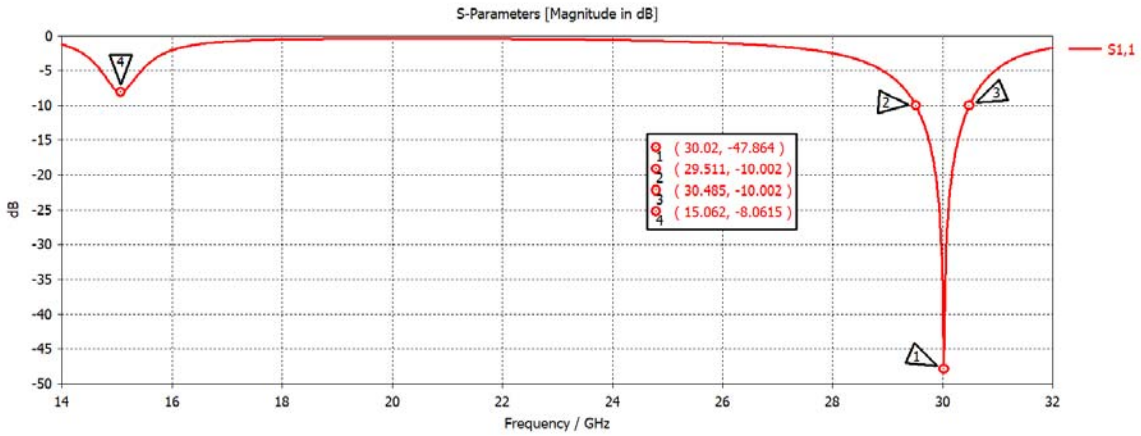

(a)

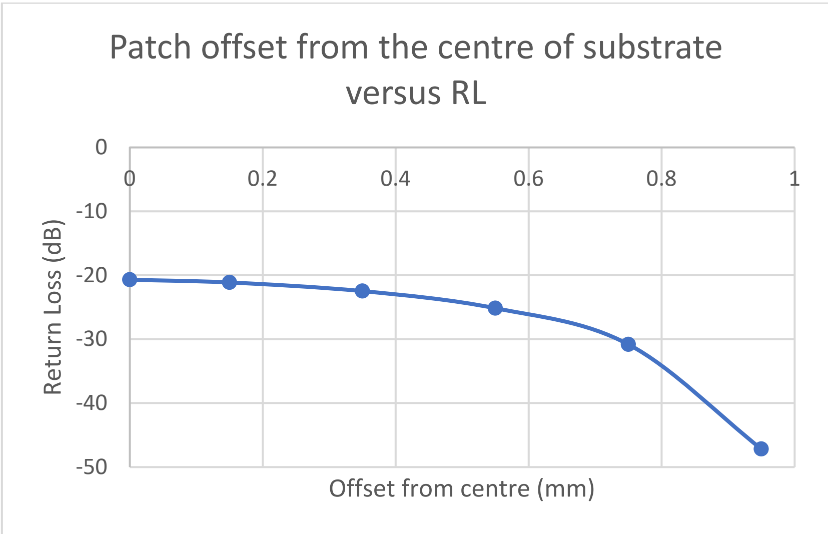

(b)

Figure 4-2: Return loss Curve showing (a) the optimum position of the feed at 30 GHz and (b) patch offset from the centre of the dielectric substrate vs. Return Loss

The width of the grounded substrate has been swept with frequency and it was observed that the gain of the structure gradually improved while the substrate width increased up to 11 mm. The gain starts to slowly degrade above that width.

Figure 4-3 below, shows the return loss variation with the grounded substrate width and E-Theta pattern cuts corresponding to each substrate width. As it can be observed, the best Return Loss and Gain corresponds to 11 mm substrate width. The Gain drops by 0.8 dB when the width is reduced to 7 mm or increased to 18 mm.

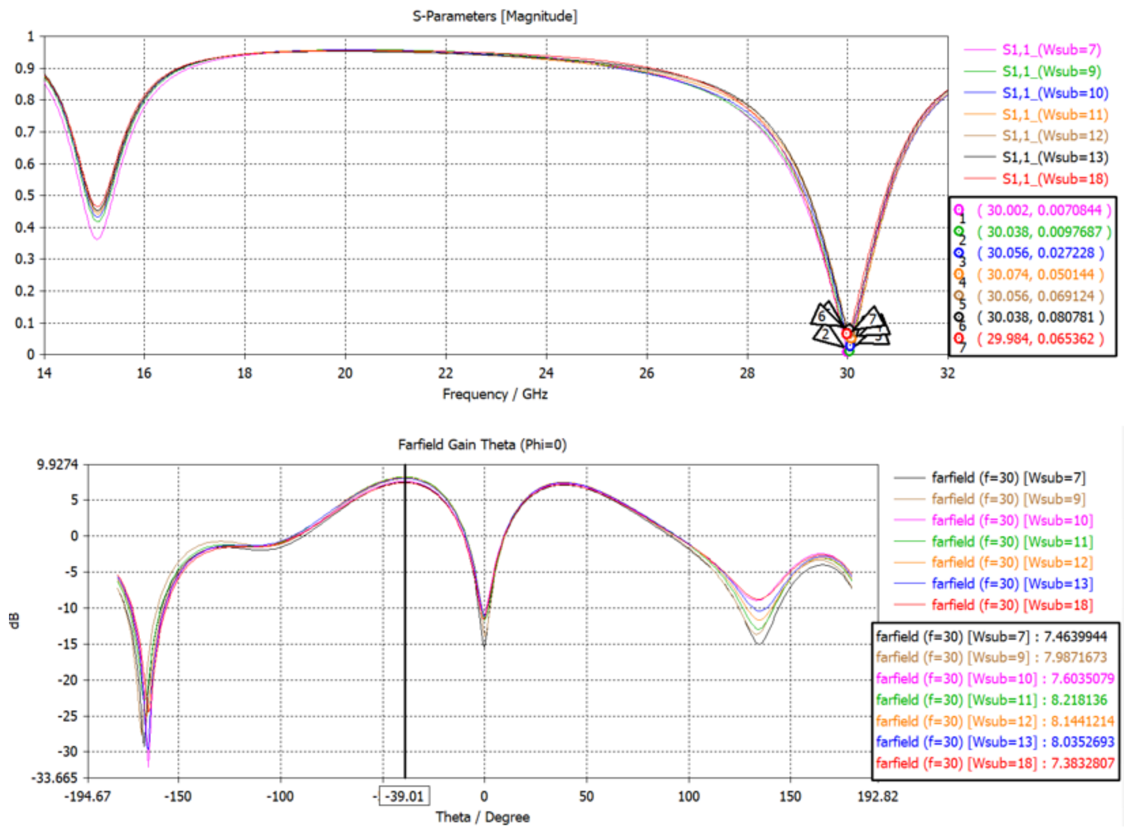

Figure 4-3: S11 when the substrate width is varied between 7 and 18 mm (top) and E-Theta pattern cuts for different substrate widths (bottom)

Besides the second mode strong appearance at 30 GHz, one can also observe the first mode around 15 GHz, but with a higher reflection coefficient. Using the formulas provided in Section 2.9.2.3, and taking into account the fringing fields that make the patch look slightly longer (approx. 6.7 mm), then the resonant frequencies can be calculated. It will be observed that the resulting values coincide with the values given by the Return Loss curve.

The radiation pattern of the structure from Figure 4-1 is presented in Figure 4-4. The polarisation is linear (vertical), and the E-theta component is illustrated below.

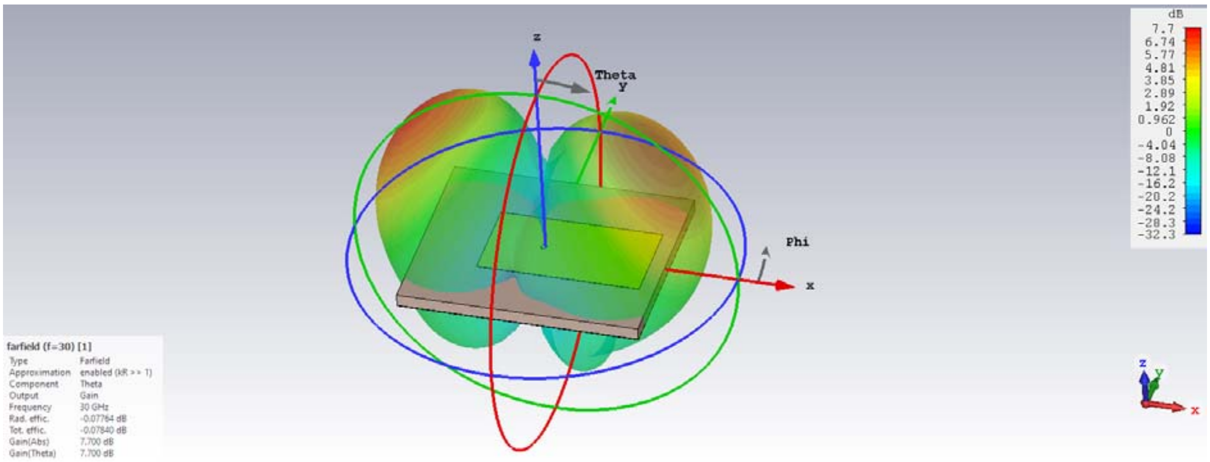

Figure 4-4: The Farfield Gain Pattern of the structure

Generally, the microstrip patch is designed as a broadside radiator, by properly choosing the field configuration beneath the patch. However, an end-fire radiation pattern can be obtained by selecting the appropriate modes. As explained in section 2.9.2.3, the second mode is obtained by appropriately selecting the dimensions of the patch. This produces two phase reversal of the electric filed under the patch, along the length (X-axis).

The E-theta Cut in Figure 4-5 shows some extra details on the obtained farfield. Compared to TM010 mode, the second mode produces two symmetrical beams on each side of the Z axis. The main lobe direction is about 39˚ on each side and the 3 dB beamwidth is about 47.7˚.

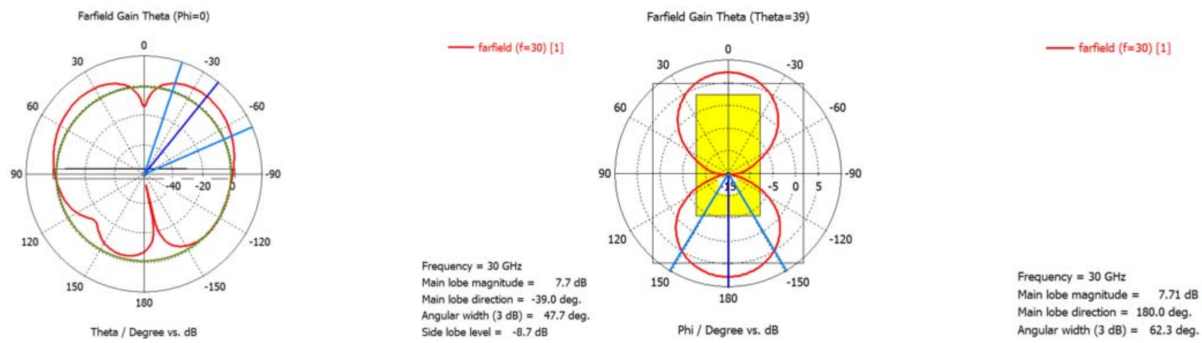

Figure 4-5: E-Theta and E-Phi Pattern cuts

As shown in Figure 4-4, the simulated radiation efficiency of the patch is -0.07764 dB which translates into approximately 98% efficiency. Figure 4-6 illustrates the simulated surface currents, which also provides an insight on the magnetic field distribution.

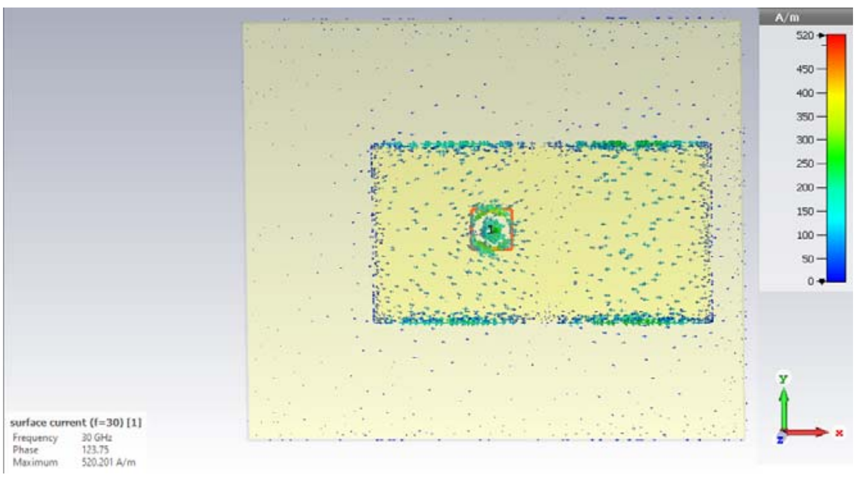

Figure 4-6: Surface current distribution of the antenna operating in TM020 mode

The dominant TM_{010} mode (the mode with the lowest cutoff frequency, in which the length of the patch is longer than the width) has the following resonant frequency:

$$f_{010} = \frac{c}{2L\sqrt{\varepsilon_r}} = 15.06 \text{ GHz} \qquad (3.52)$$

knowing that $c = \frac{1}{\sqrt{\mu_0 \varepsilon_0}}$, and $\mu\varepsilon = \mu_0 \mu_r \varepsilon_0 \varepsilon_r$ (3.53)

and this corresponds to the first resonance frequency observed in Figure 4-2.

If the Width of the patch is higher than the length, then TM001 becomes the dominant mode. The dominant modes show in which direction is the electric field lines vary and how many variations occur on the patch's dimension. For example, TM010 mode shows that a variation of the electric field lines occurs in the X direction.

The first mode radiation pattern is illustrated below, in Figure 4-7. As it can be observed, the radiation pattern is broadside, similar to the pattern shown in Figure 2-44.

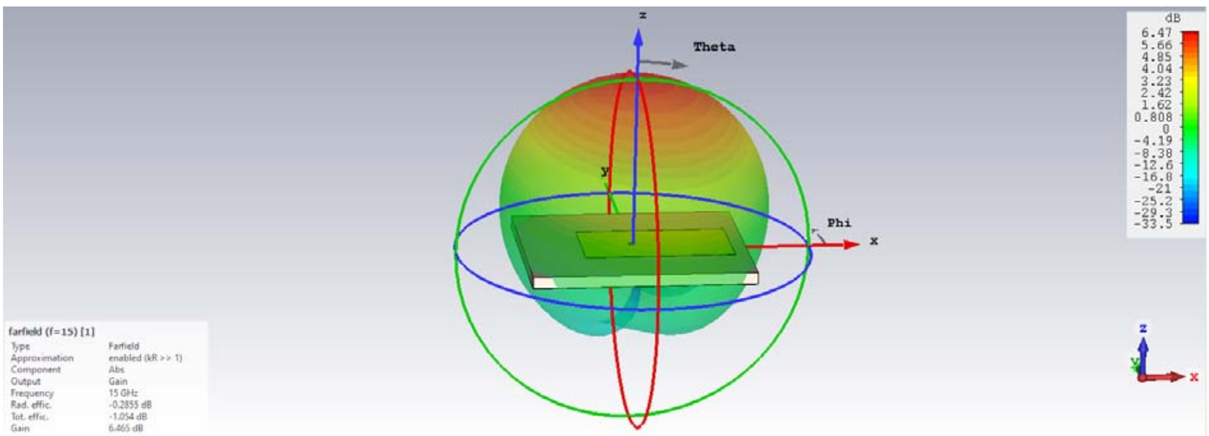

Figure 4-7: First mode radiation pattern at 15 GHz

Figure 4-7 shows that the new patch operates in the second mode TM020, which means that there are two variations of the field along the length of the patch, i.e. in the X direction.

$$f_{020} = \frac{c}{L\sqrt{\varepsilon_r}} \simeq 30 \text{ GHz} \qquad (3.54)$$

(taking into consideration that the fringing fields make the patch look slightly longer)

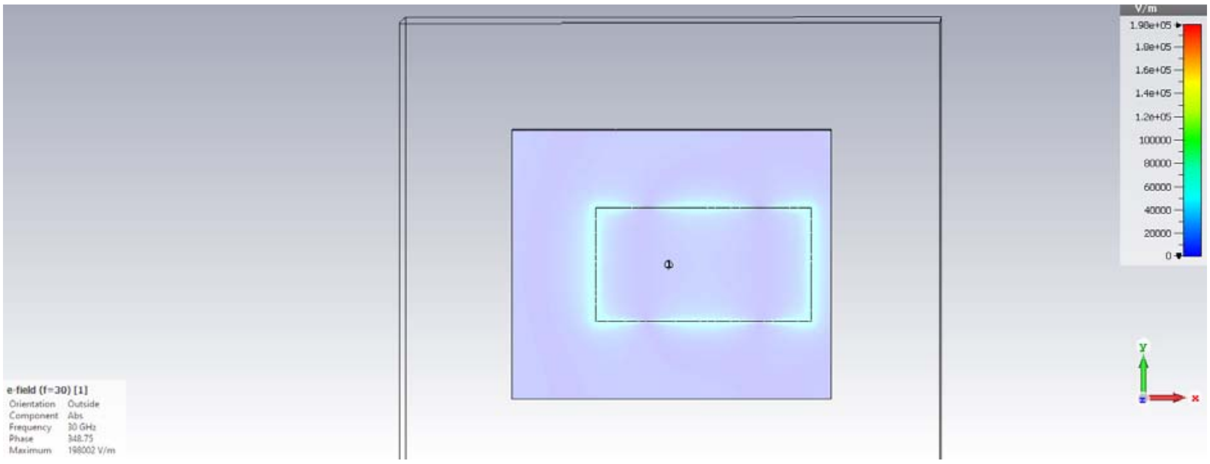

Figure 4-8: E-Field distribution of the second mode operating patch

Figure 4-8 shows the Field variation along the X axis. The field distribution along the patch and the farfield radiation pattern presented above, matches the experiments and theory presented in [162].

The simulated radiation efficiency of the patch antenna shown in Figure 4-7 is -0.2855 dB, which translates into approximately 93% efficiency. Figure 4-9 below illustrates the surface current distribution of the patch antenna operating in the first mode and it also gives an insight on the magnetic field distribution.

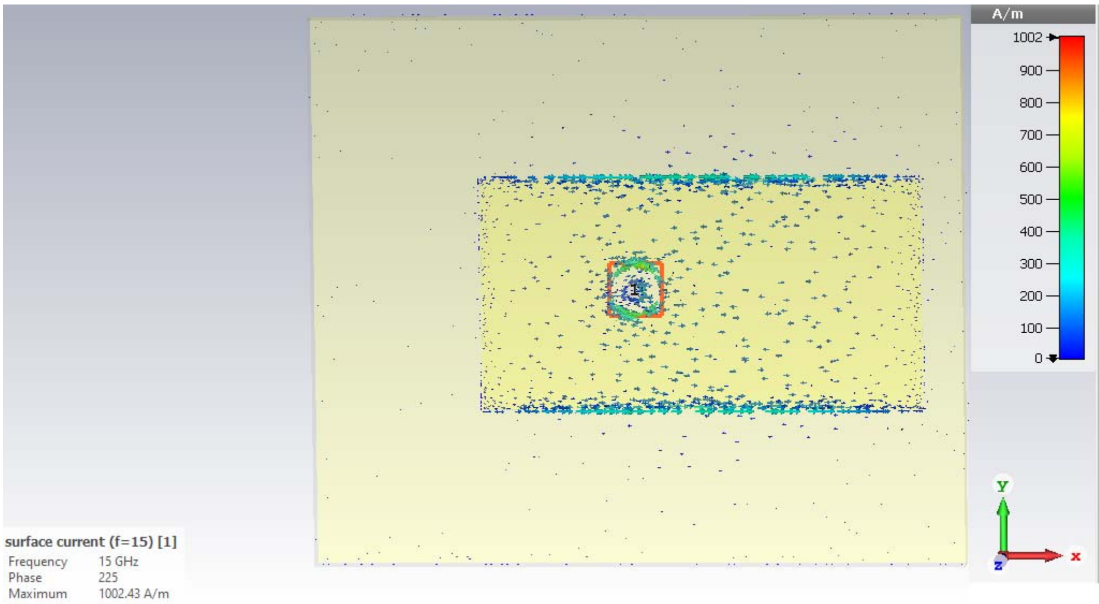

Figure 4-9: Surface current distribution of the patch antenna operating in TM010 mode

4. 2 Simulations of the Circularly Polarised Microstrip Patch Antenna

The Microstrip Patch simulated in Figure 4-4 has been converted into a circularly polarised patch by truncating two opposite corners. This determines the E-Field vector decomposition into two perpendicular vector components: one of them exciting the edges along the Length and the other vector exciting the edges along the Width. This coupling process creates two orthogonal modes, 90˚ out of phase, which provides the circular polarisation of the patch: TM020 mode along the Length of the Patch and TM010 mode along the Width of the Patch. Because in the TM010 mode the patch presents a nearly hemispherical radiation pattern, the combination between the two modes generated by the dimensions of the antenna, gives the TM020 circular mode. The width of the patch, the feeding point and the corners cuts dimensions have been varied in order to obtain the desired resonant frequency. The minimum cross polarisation has been obtained with the opposite patch corners trimmed by approximately 0.78mm in the x and y directions.

Figure 4-10 illustrates the new dimensions of the circularly polarised Microstrip Patch:

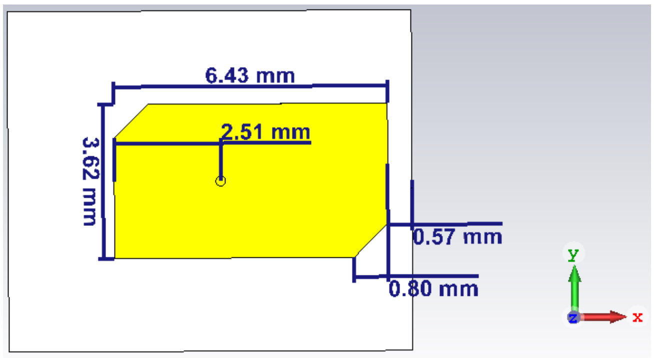

Figure 4-10: Dimensions of the circularly polarised microstrip patch

The LHCP (cross-polarisation) and RHCP (co-polarisation) radiation patterns are illustrated in Figure 4-11. As the polarisation cannot be purely circular, a small amount of the opposite polarisation (LHCP) is expected to be also generated. The maximum LHCP gain generated is -1.96 dB, while the maximum gain obtained from RHCP is 7.15 dB. In the simulations below, the patch is RHCP polarised, however, for the LHCP polarisation the other two opposite corners of the patch must be truncated.

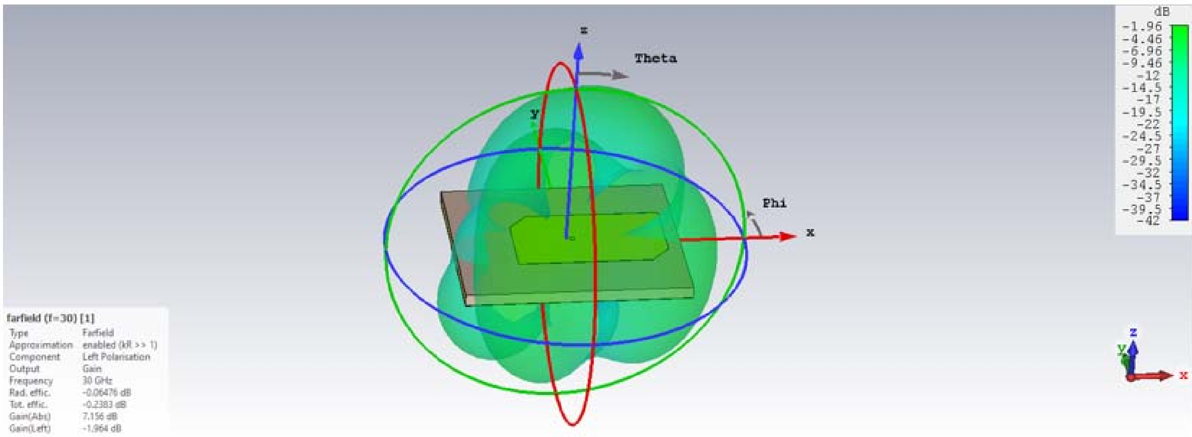

a) LHCP polarisation

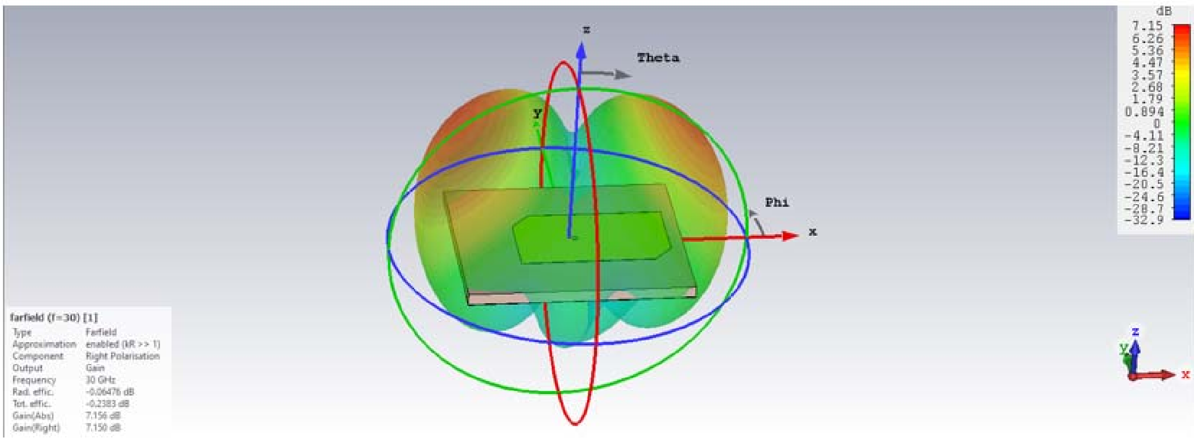

b) RHCP polarisation

Figure 4-11: LHCP and RHCP polarisation patterns

Figure 4-12 illustrates the LHCP and RHCP pattern cuts and Figure 4-13 presents the patch return loss and the axial ratio curve. The axial ratio curve indicates the cross-pol discrimination in the direction where the maximum gain is achieved, i.e. θ= -40˚ and φ = 0˚, over the frequency range. As explained in the previous section, to determine the bandwidth of a circularly polarised structure, both the return loss and the cross-pol discrimination performance of the unit must be considered. The overall performance is obtained by overlapping the 10 dB impedance bandwidth and the 3 dB axial ratio curve bandwidth.

From the S11 curve in Figure 4-13, the 10 dB impedance bandwidth can be calculated:

Impedance BW: ((32-29.362)/31.236) = 8.44%.

The axial ratio 3 dB bandwidth can be also calculated:

AR BW: ((30.389-29.763)/30.076) = 2.08%.

By overlapping the two curves, it can be observed that the overall performance BW is dictated by the axial ratio bandwidth: 2.08%.

The bandwidth extends from 29.763 GHz to 30.389 GHz, where the return loss is between 15 dB and 11 dB, with 14 dB at 30 GHz. In terms of polarisation discrimination, the axial ratio values vary between 0.41 dB and 3 dB, with 0.89 dB at 30 GHz.

Figure 4-14 illustrates the axial ratio vs Theta, when Phi=0˚, for 29 GHz, 30 GHz, 31 GHz and 32 GHz. The best axial ratio values are obtained at 30 GHz. At Theta=-40˚, the axial ratio is 0.89 dB, which is in agreement with the plot in Figure 4-13. At the other frequencies, the axial ratio values are above 3 dB, which suggest that the field is not circularly polarised anymore, but linearly polarised.

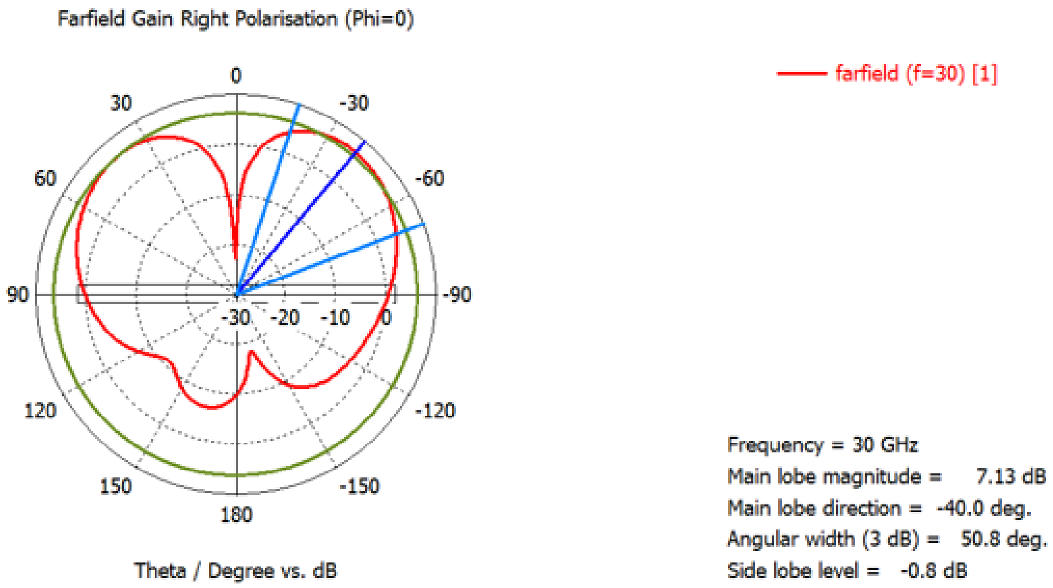

a) RHCP radiation pattern cut

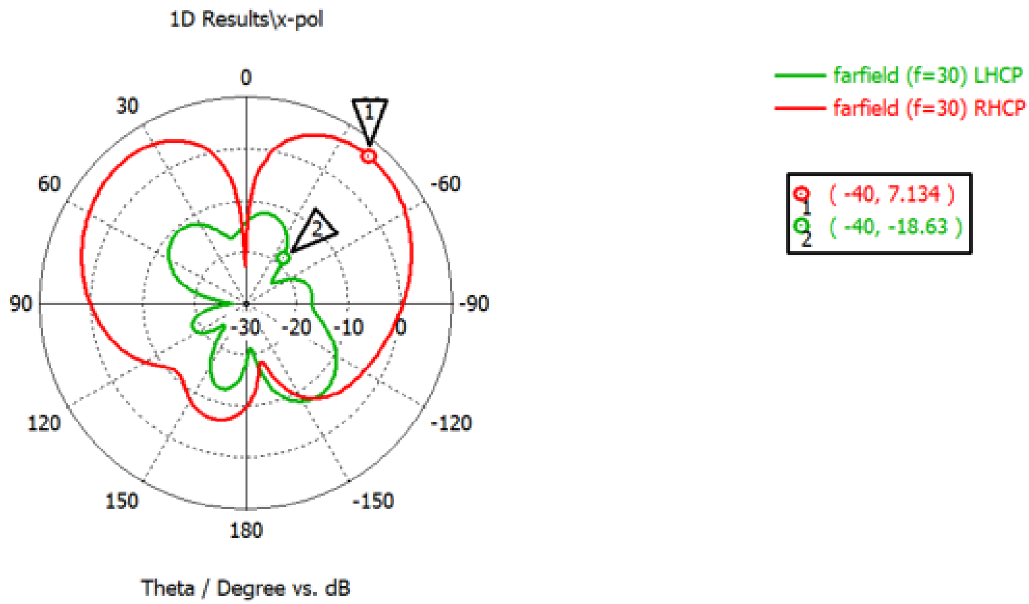

b) LHCP and RHCP radiation pattern cuts

Figure 4-12: RHCP and LHCP Pattern Cuts

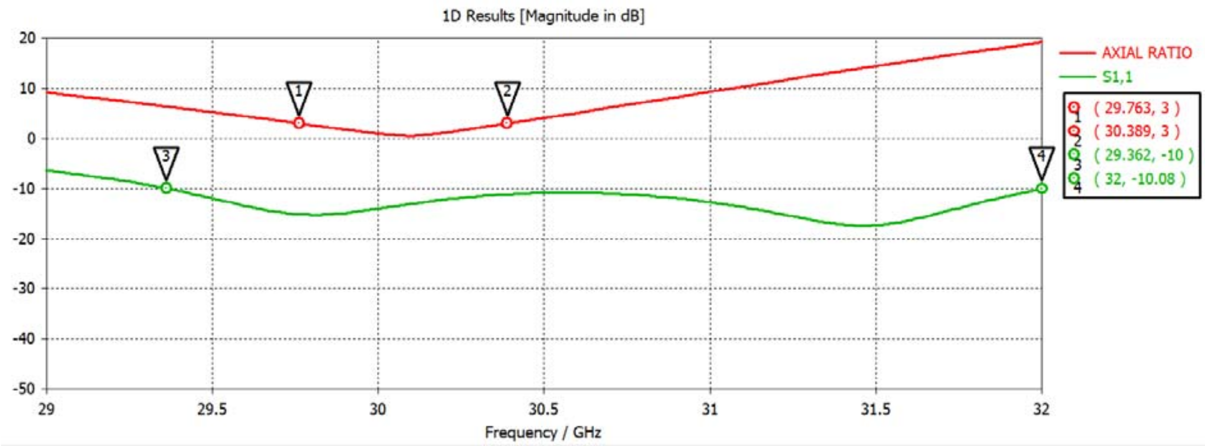

Figure 4-13: S11 and Axial Ratio (axial ratio over frequency at Theta = -40 and Phi=0)

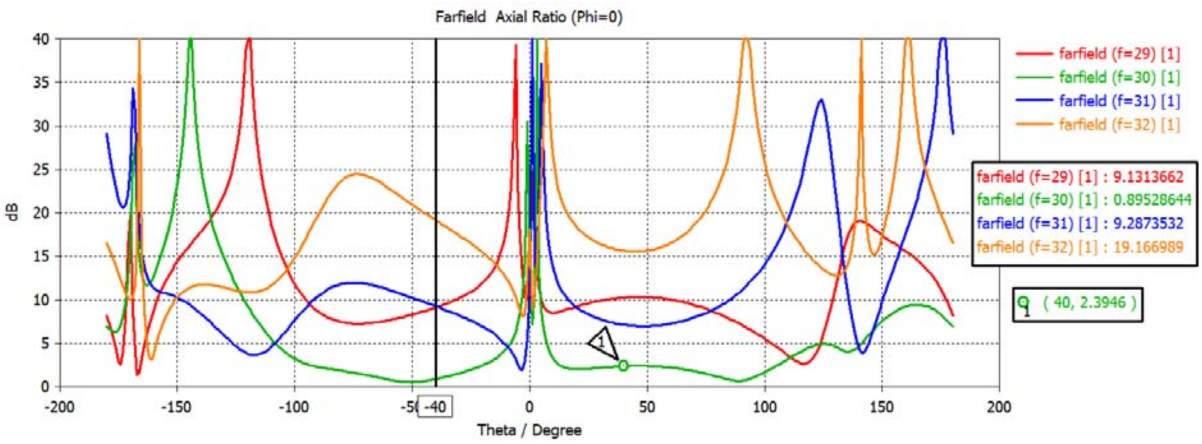

Figure 4-14: Axial Ratio vs Theta at Phi=0°

In the next chapter, the behaviour of the circularly polarised microstrip patch in the presence of a reflective substrate is analysed. The simulation results will show that due to the radiation pattern shape of the feed (two symmetrical beams), the resultant pattern will always have a high cross-polar component. The RHCP beam lobe becomes LHCP after hitting the reflective substrate, and combines with the RHCP beam lobe launched in air. This and other experiments will be discussed in the next chapter.

5. Antenna Arrays Using Second Mode of Microstrip Patch Antenna

The microstrip patch operating in the second mode can be used to develop a low-profile, higher gain antenna, by attaching a reflective surface to redirect one of the two symmetrical beams, produced as a result of the second mode excitation. Furthermore, for beam steering capability, this structure can be arranged in an array configuration. The gain of the resulting radiation pattern can be further improved if *extra* resonating, reflective patches are placed on the reflective surface. This approach resembles the principle of operation of a reflectarray antenna, as described in Section 2.11. This Chapter describes the results of different simulations relating to the microstrip patch antenna operating in the second mode in presence of reflective surfaces and then any of their extensions to array configurations. In this chapter, it will be demonstrated that the antenna gain and beam scanning angle requirement determined in Chapter 3 can be met using patch antennas operating in the second mode, TM020.

5.1 Linearly polarised microstrip patch in presence of a reflective surface

As shown in Chapter 4, the microstrip patch operating in TM020 mode presents two symmetrical lobes about the broadside axis (z-axis) providing a maximum gain of about 7.7 dBi at the operating frequency of 30 GHz. Figures 4-4 and 4-5 showed the radiation pattern and pattern cuts of the antenna.

The gain of the antenna can be improved if a grounded substrate is placed perpendicularly, in -z direction, under the antenna substrate as illustrated in Figure 5-1. The feeding patch antenna is rotated 90˚ along the y axis and placed on the new grounded substrate. The overall effect is that the lower beam produced by the patch shown in Figure 4-4 hits the reflecting substrate and the resulted, reflected beam combines with the higher beam, giving rise to a more directive beam. The dimensions of the reflective substrate have been arbitrary chosen as 28 mm (in length) x 8 mm (in width). The substrate dielectric material is Rogers 5880 LZ with a thickness of 0.5 mm and a permittivity of 2. In this configuration, the lower beam of the patch antenna hits the grounded substrate and reflects back into the air, where it recombines with the top beam. By adding the reflective substrate, it is predicted that the increase in gain would be of maximum 3 dB [163] plus the added advantage of a single beam radiation from the structure.

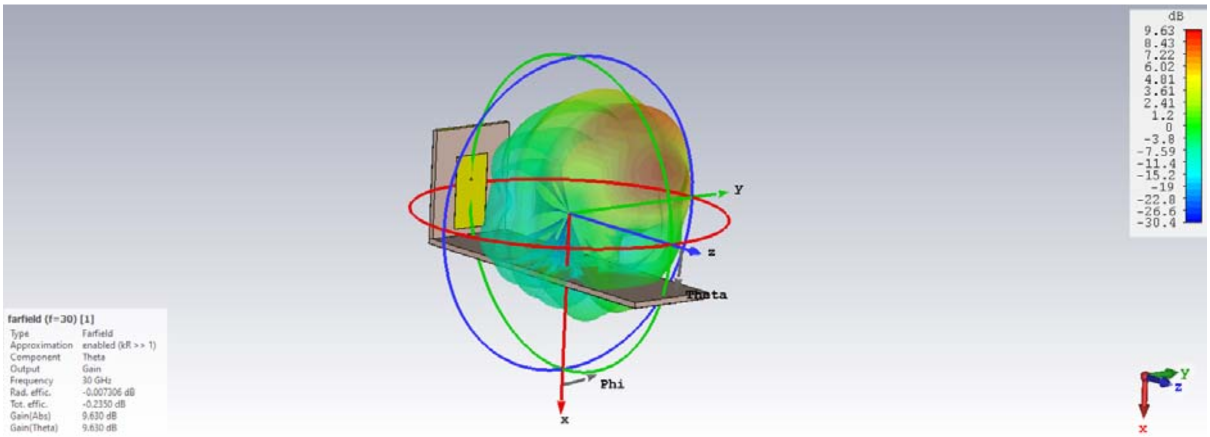

Figure 5-1: Radiation pattern of the microstrip patch antenna rotated 90˚ along the y axis and placed on the reflective substrate

As can be observed from the simulated radiation pattern, Figure 5-1, the gain increases only by approximately 2 dB, to 9.63 dBi. This is because of the short width of the reflective substrate not supporting the entire reflection of the lower beam in its width. Figure 5-2 illustrates the E-Theta pattern cut. It indicates that the reflected beam and the beam which travels in space are not combining totally, to give a single, more directive beam. Indeed, the reflected beam scatters at the edges of the narrow reflective substrate. Markers 1 and 2 in the Figure 5-2 illustrates the two uncollimated beams, as they are shown in Figure 5-1.

The reflecting grounded substrate also influences the return loss of the antenna. As shown in Figure 5-3, the return loss at the antenna resonance decreases to approximately -13.6 dB and the resonant frequency shifts to 30.15 GHz. However, the 10 dB bandwidth of the structure is almost the same as that of the single patch antenna operating in the second mode. As explained in [41], the effect of the location of the ground plane is visible in the input impedance. The input impedance varies with the height at which the antenna is located relative to the ground plane and its' phase and magnitude also depend on the angle of incidence to the ground plane.

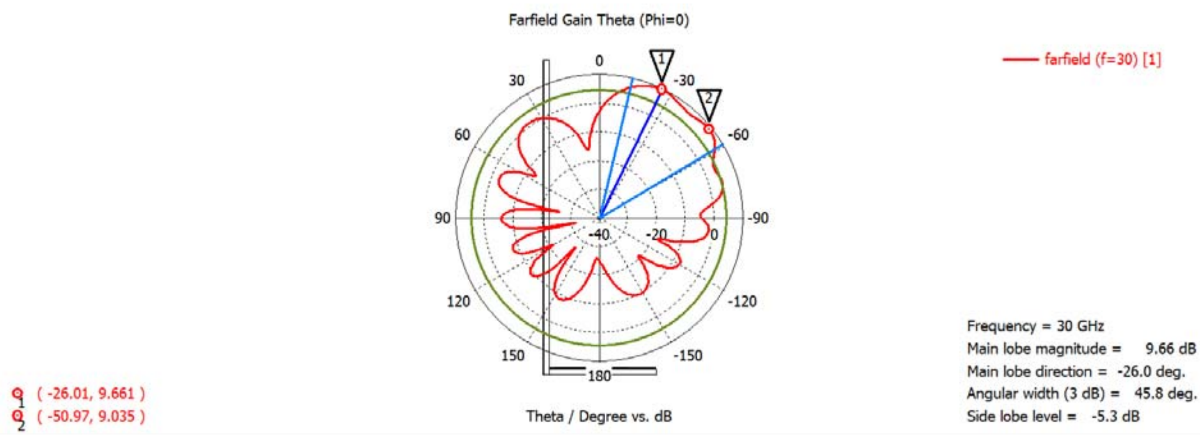

Figure 5-2: E-Theta radiation pattern cut of the patch antenna with reflective substrate showing the two uncollimated beams

The effects of the width on the gain and return loss of the antenna structure are simulated and shown in Figure 5-4 & 5-5.

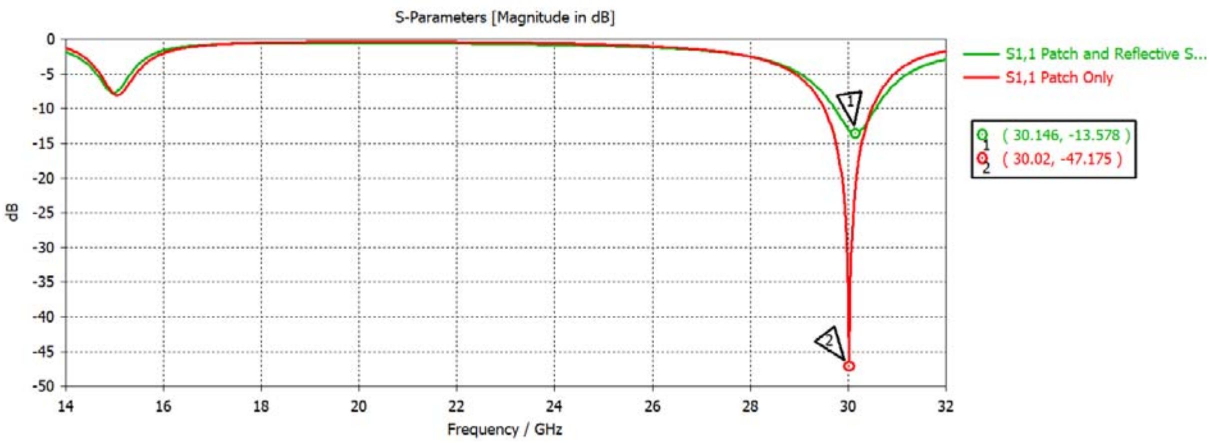

Figure 5-3: The effect of the reflective substrate on the return loss S11 (mag.)

Figure 5-4 shows as the reflecting substrate width increases from 8 mm to 21 mm, the gain reaches its peak, 10.6 dBi (which is 1 dB higher than the previous gain), for a width of the substrate of about 18 mm. In this case, the two symmetrical beams of the microstrip patch antenna (in the second mode) can be assumed to combine nicely into one single beam (thanks to less energy scattering at the edges of the grounded substrate). However, the return loss, S11 illustrated in Figure 5-5, varies slightly as the substrate width is increased. Further, the structure resonant frequency changes with the width but not considerably.

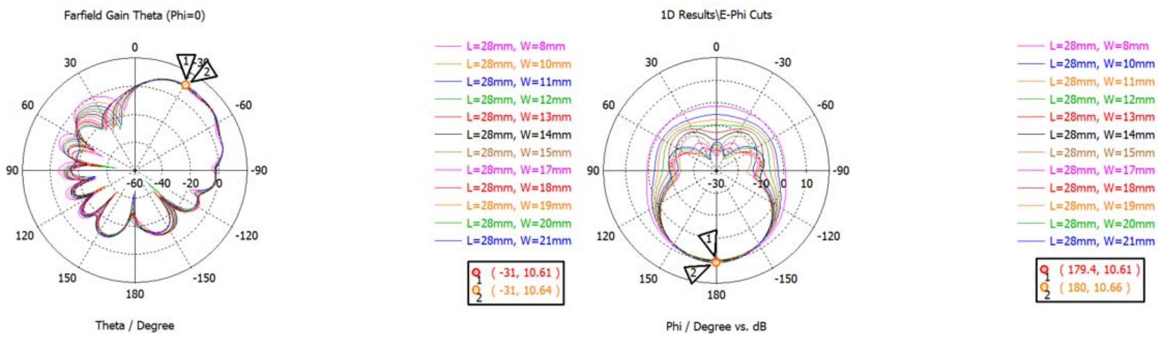

Figure 5-4: Gain variation with the width of the reflective substrate at 30 GHz, when the reflective substrate width is varied from 8mm to 21mm

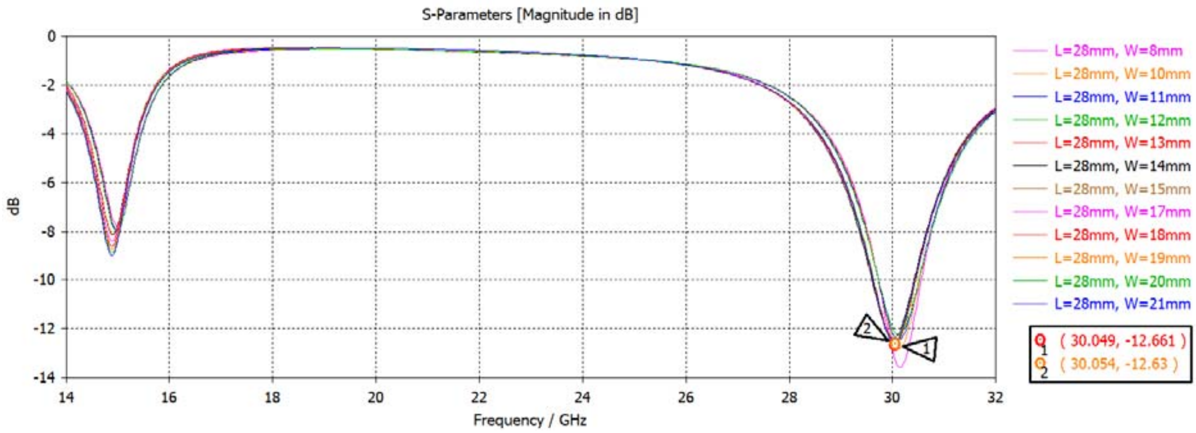

Figure 5-5: Return loss variation with the width of the reflective substrate, when the reflective substrate width is varied from 8mm to 21mm

The effects of the length of the reflective substrate have also been studied, keeping its width at 18 mm. The highest gain obtained for the structure is when the length is about 17 mm, but this gain is very slightly higher than the previous case gain, see Figure 5-6. Figure 5-7 shows the return loss variation with the length of the grounded substrate, but again it is very small in comparison to the previous case return loss.

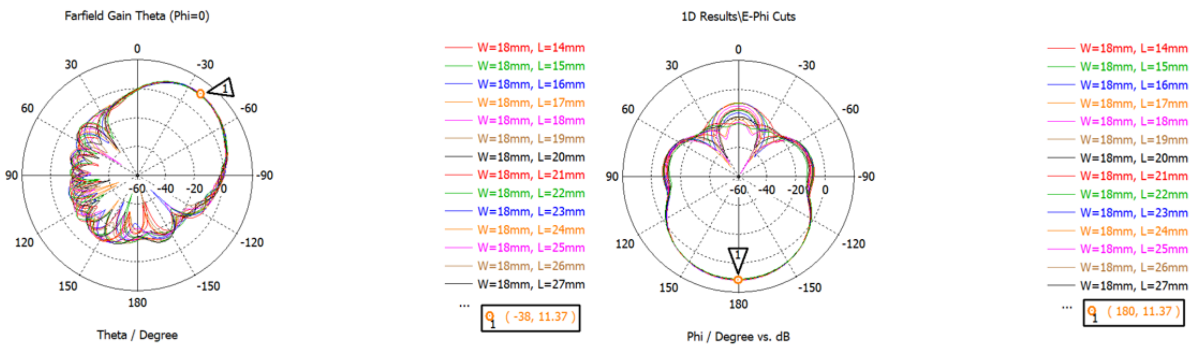

Figure 5-6: Gain variation of the antenna structure with the length of the grounded substrate, when the length of the grounded substrate is varied between 14mm to 27mm

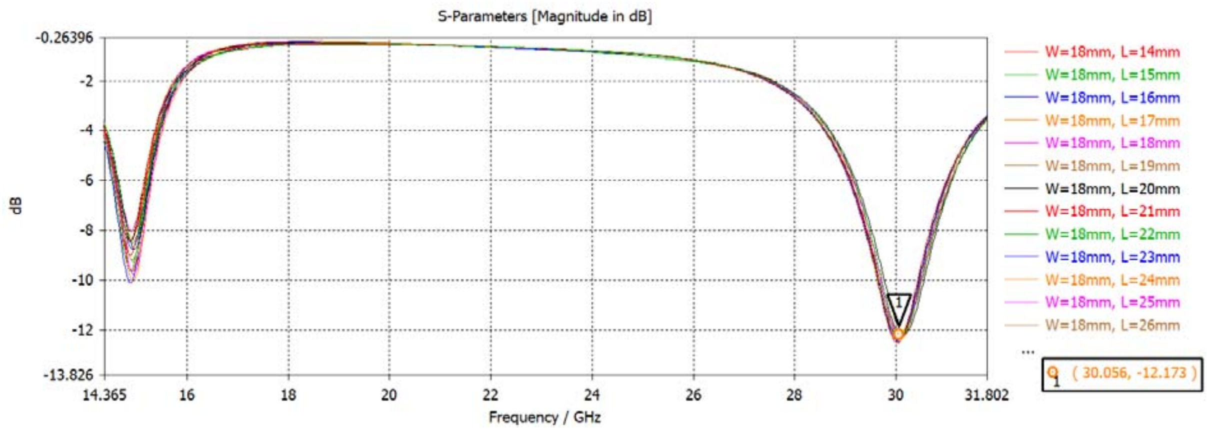

Figure 5-7: Return Loss variation with the length of the grounded substrate, when the length of the grounded substrate is varied between 14mm to 27mm

The variation of the grounded substrate dimensions has been done while keeping the width of the microstrip patch antenna set to 8 mm. As shown in Figure 5-8, by increasing the width of the microstrip patch antenna to match the width of the reflecting substrate (18 mm), the 3 dB BW in Phi direction increased considerably from 56˚ to 72˚, however, the gain remained unchanged.

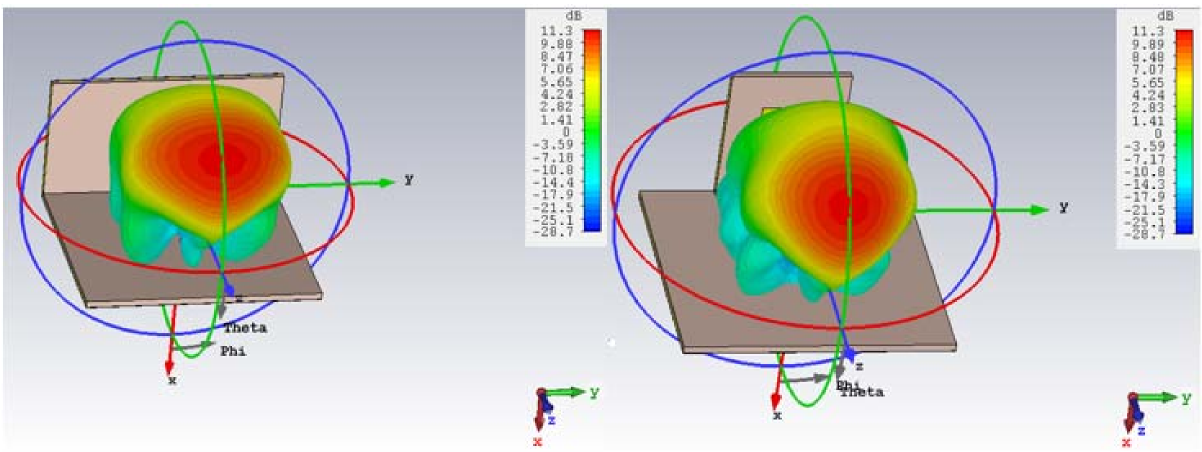

Figure 5-8: E-Theta gain when the width of the feed's substrate matches the width of the reflecting substrate

5.2 Patch Antenna Array with Reflective Grounded Substrate

To improve the gain of the antenna structure a second element can be utilised as in antenna arrays, assuming initially in the y-direction. To this end, the reflective substrate width is taken as 18 mm and its length as 17 mm. The width of the patch antennas feeding the reflecting ground plane is always chosen to match the width of the reflective substrate.

Initially, the patch antennas are assumed to be separated by a distance of approximately 10 mm (from centre to centre), as illustrated in Figure 5-10. This is done to mitigate the occurrence of unwanted lobes, but also to reduce the interaction or coupling between consecutive antennas. The patch antennas behave like a 2-element array that their radiation combined impinges on the reflective substrate.

Some relevant formulas used in the antenna array theory are presented below. These formulas will be applied in the subsequent subsections.

The array factor represents a function which describes the radiation pattern of an antenna array. It is a measure of how the radiation pattern of a single antenna element is changed by adding more antennas to form an array.

As described in Section 2.4.2, the array factor for two isotropic elements, fed by sources having the same magnitude and phase, separated by a distance d (centre to centre), along the Y axis is:

$$AF_Y = 2\cos\left[\frac{1}{2}(k_0 d sin\theta sin\phi + \beta)\right] \tag{5.1}$$

Where $\mathrm{k_0}$ is the wavenumber in free space $= \frac{2\pi}{\lambda_0}$, and β is the progressive phase between the array elements

For an array of N isotropic elements along the Y axis, the array factor becomes:

$$AF_Y = \frac{1}{N}\left[\frac{\sin(\frac{N}{2}(k_0 d sin\theta sin\phi+\beta))}{\sin(\frac{1}{2}(k_0 d sin\theta sin\phi+\beta))}\right] \quad (5.2)$$

Once the Array Factor is determined, the radiation pattern of the antenna array can be determined by multiplying (if linear) or adding (if logarithmic) the radiation pattern of one element, placed at the origin of the coordinate system, with the Array Factor.

5.2.1 Two-Element Antenna Array

As explained in the previous section, a two-element array is formed by repeating the antenna element determined in Section 4-2, and shown in Figure 4-8 (left-hand side). The two elements are initially placed at a distance of 10 mm apart measuring from centre to centre. For the sake of comparisons to follow, first the radiation pattern of one of the elements in the array is presented, Figure 5-9. The width of the reflecting substrate is 18 mm and the length 17 mm. As it can be observed in the figure, the total efficiency of the antenna is -0.2965 dB, which translates into 93% efficiency. The radiation pattern of the array with two elements with 10 mm inter patch spacing is shown in Figure 5-10. The antenna elements have been excited assuming 0° progress phase.

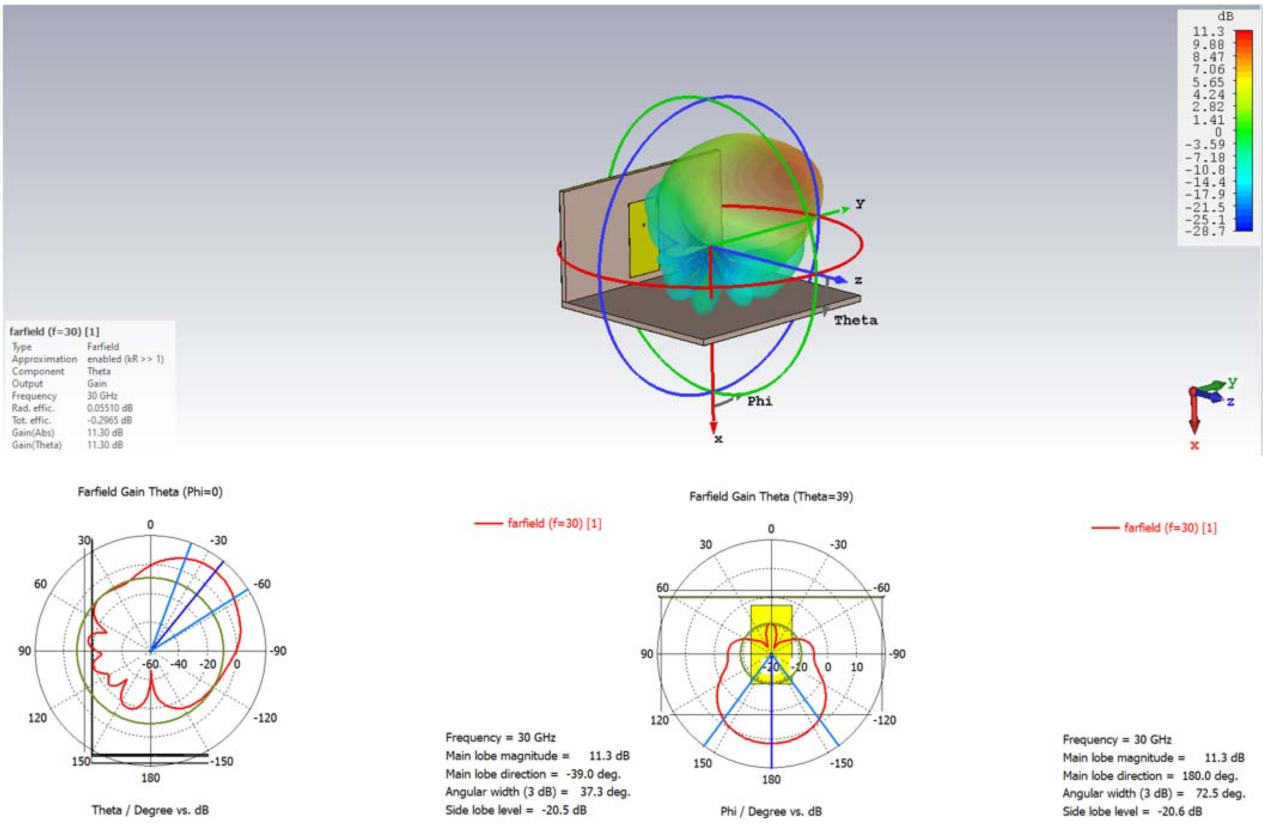

Figure 5-9: Radiation pattern of one-element (of the array)

As expected, the addition of the second element in the y-direction has increased the gain by about 3 dB (14.5-11.3) to 14.5 dB. The sidelobes levels are low (1 dB), but they inevitably occur because the distance between the elements is greater than λ/2. E-Phi cuts vividly show that the directivity has improved reducing the -3 dB beam width from 72˚, Figure 5-9, to 43˚, Figure 5-10.

To help further with the understanding of the behaviour of the antenna array, the E-field vector propagation and radiation pattern cut in the XZ-plane is also illustrated in Figure 5-11. The antenna total efficiency is -0.2427 dB, which translates into 94% efficiency.

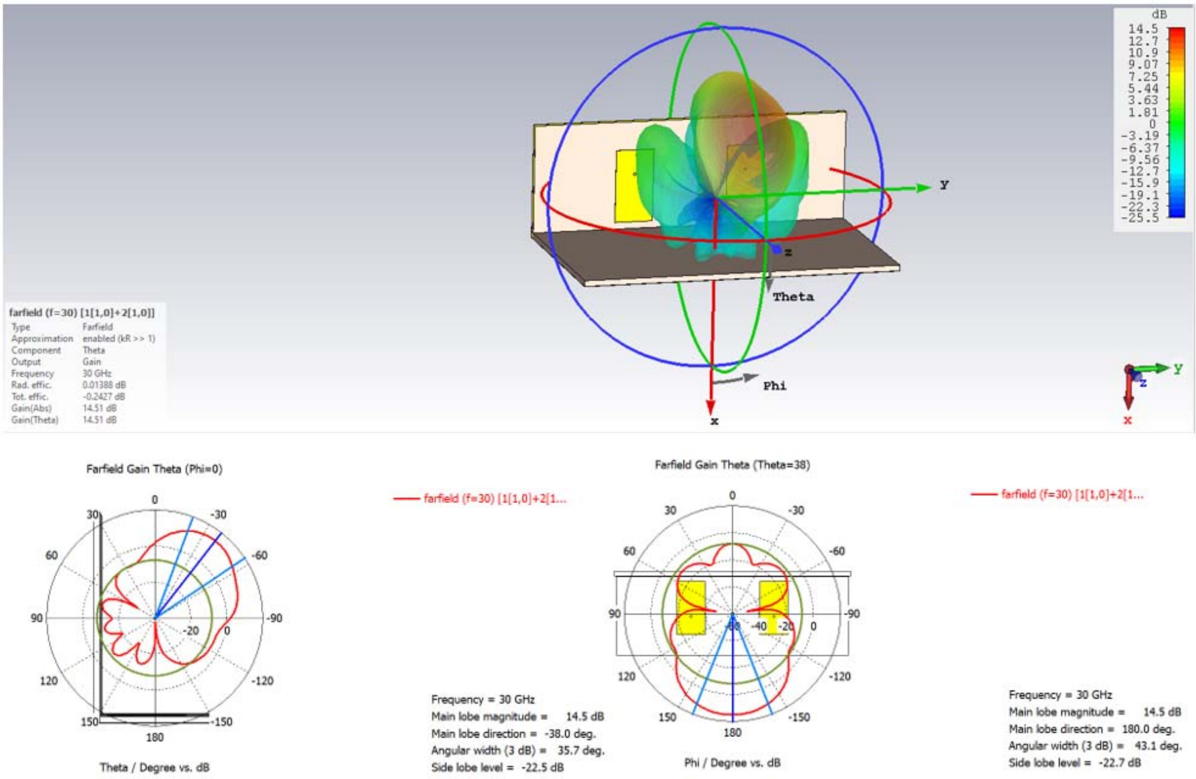

Figure 5-10: Radiation pattern and cuts for two-element array with 10 mm distance between elements

If desired, the sidelobe levels can be reduced from the present levels by shortening the distance between the elements. However, this increases the coupling between the antenna elements, which may adversely affect the radiation pattern and the input impedance of the array. Figure 5-12 illustrates the coupling between the two patches when the first patch is fed. The isolation between the patches has been measured for several inter patch spacings (5 mm, 8 mm, 10 mm, 13 mm) and illustrated below, in Figure 5-13.

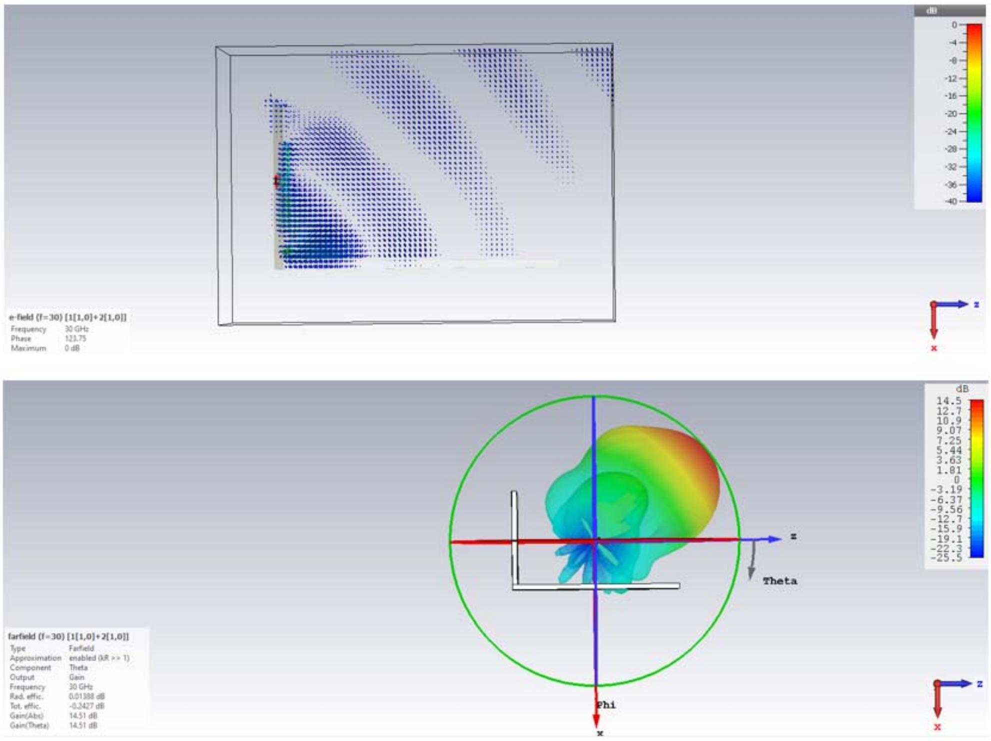

Figure 5-11: E-field distribution and formed beam (side-view)

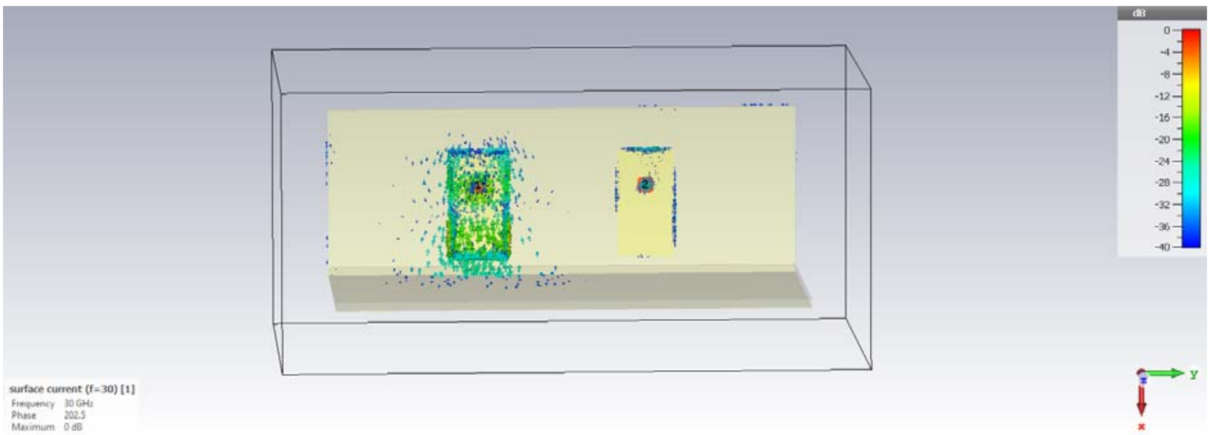

Figure 5-12: Coupling illustration between the two feeding patches

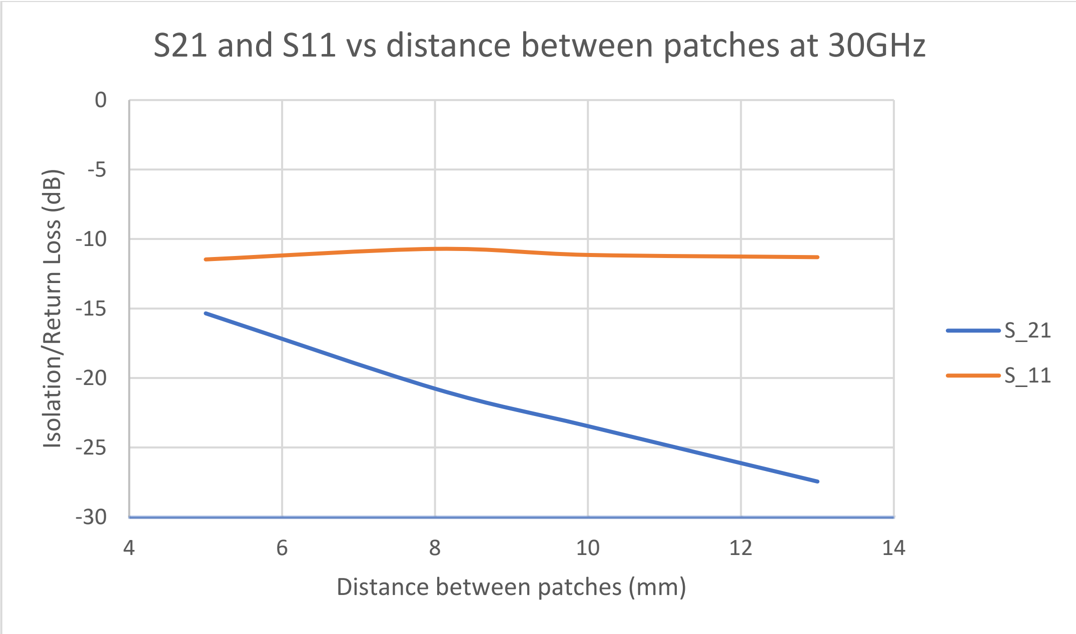

Figure 5-13: S21 and S11 vs distance between patches at 30 GHz

The highest coupling between the elements occurs at the resonant frequencies, i.e., at about 15 GHz (which corresponds to the first mode of operation of the patch) and at 30 GHz (corresponding to the second mode of operation of the patch). At 30 GHz, as shown in Figure 5-13, the coupling between elements drops by 12 dB when the distance between elements varies between 5 mm and 13 mm. The Return loss curve does not vary as much as the Insertion loss, however it slowly improves as the distance between patches increases.

As suggested in Section 2.4.2, the derivation of the Array Factor (AF) is based on assuming isotropic radiators. The AF depends on the distance between the elements, the operating wavelength, and the axis along which the elements are located. In other words, the AF pattern does not take into account the actual radiation pattern of the elements of an array. To obtain the overall radiation pattern of an array, its AF (considered as a common factor) needs to be multiplied (or logarithmically added) by the element radiation pattern [41].

Considering the case under study in this work, the AF of a two-element array with 10 mm inter spacing is shown in Figure 5-14. The pattern has been obtained in Matlab where two generic elements have been placed along the y-axis. The upper part of Figure 5-14 shows the Array Factor Pattern, with the Phi and Theta cuts.

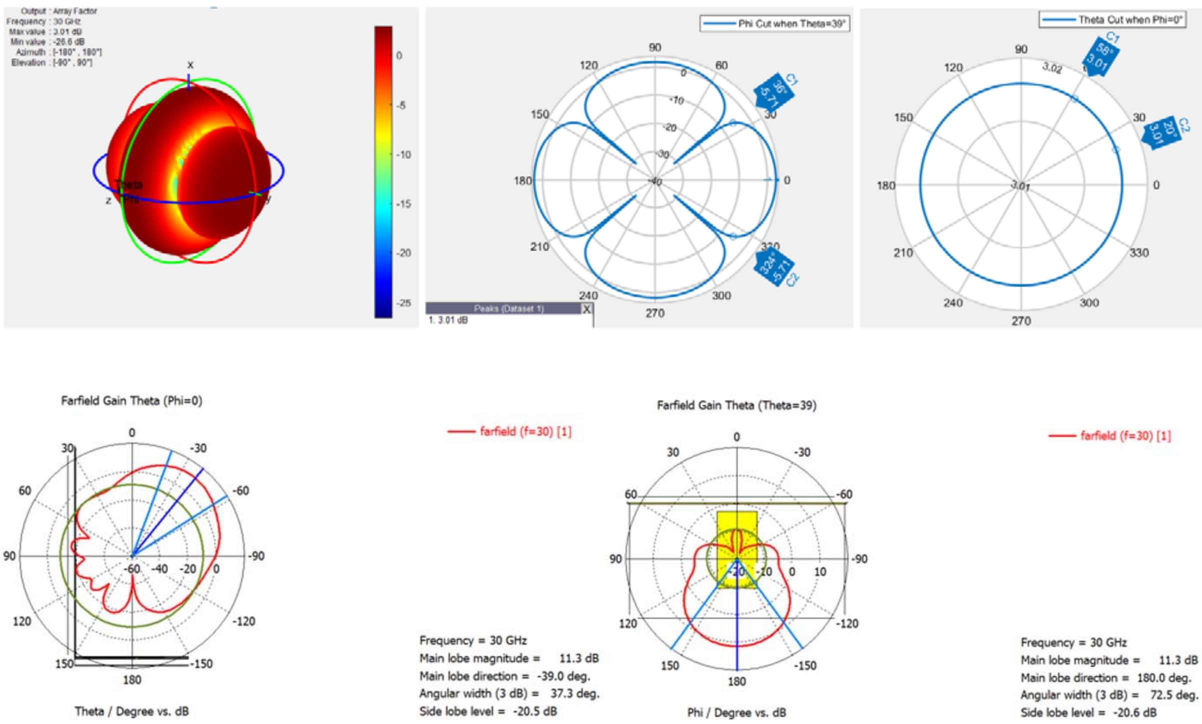

Figure 5-14: Array Factor of a 2-element array with 10 mm spacing between consecutive elements fed in phase with the associated pattern cuts (top) and the Array Element Pattern cut from Figure 5-9 (bottom)

By aligning the E-Phi cut in Figure 5-9 to the Phi pattern cut in Figure 5-14, it can be observed that the width of the beam (E-Phi) in Figure 5-9, overlaps the beam in Figure 5-14 along Phi=0˚. The E-Phi 3 dB BW in Figure 5-9 expands between 143.75˚ and

216.25˚, which corresponds to 36˚ and 324˚ in the Phi pattern cut in Figure 5-14. For Phi=0˚ pattern cut, the 3 dB beamwidth extends between -20.35˚ and -57.65˚ in Figure 5-9, which corresponds to 20.35˚ and 57.65˚ in Figure 5-14.

The addition of the two patterns represents the pattern presented in Figure 5-10. The two-element Array Factor pattern presents a maximum of 3 dB, which explains the increase of the resultant pattern by 3 dB. The sidelobes that appear next to the main lobe are due to the presence of the nulls in the Array Factor Pattern and also because of the width of the main lobe in Figure 5-9 which is covers a part of the Array Factor lobes lying along the 0˚-180˚ axis.

5.2.2 Four-Element Antenna Array

Similar to the previous case, but this time the radiation pattern of a four-element array attached vertically to the reflective grounded substrate as shown in Figure 5-15 in which the radiating elements are patch antennas operating in the second mode is analysed. Figure 5-15 shows the array radiation pattern, the E-theta, and the E-phi pattern cuts at 30 GHz centre frequency. The total efficiency of the antenna is approximately 95%.

In comparison to the previous two-element array (4-10), addition of the two more radiating elements has increased the gain by about 3 dB to 17.9 dB and of course, the beam has become more directive over the y-direction. Indeed, as expected, the 3 dB E-Phi beamwidth has decreased and the 3 dB E-Theta beamwidth remained the same.

It can be observed in Figure 5-15 that there are minor side lobes next to the main lobe in the radiation pattern, which can also be predicted from the plot of the AF pattern for this antenna structure, as illustrated in Figure 5-16 obtained by a Matlab program.

From Figure 5-16, the AF maximum value is 6 dB, which is as expected of a four-element array (ie: 3 dB for the first two and another 3 dB due to the equivalent sum of two set of two radiators). If the distance between array elements increases, the number of the sidelobes will rise and this can be verified using the AF expression.

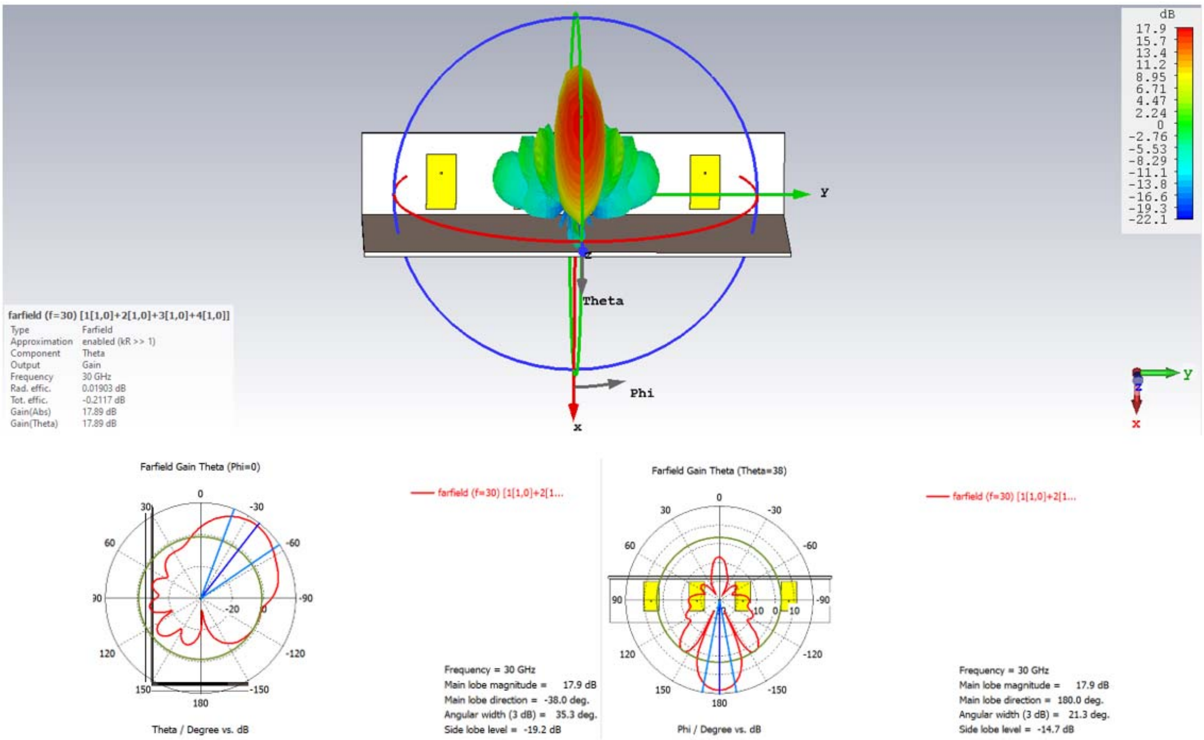

Figure 5-15: Radiation pattern and E-theta and E-Phi pattern cuts for four-element array with 10 mm distance between consecutive elements

By adding the radiation patterns in Figure 5-16 (top) with the radiation pattern of one element from Figure 5-9 or from Figure 5-16 (bottom), it results the pattern shown in

Figure 5-15. As it can be observed, as the number of elements increases, the Array Factor Pattern produces narrower main lobes, but also a higher number of narrow sidelobes. These in combination with the wide beam of the element pattern, produce an overall pattern with more sidelobes, compared to the two element Array Factor described in the previous section.

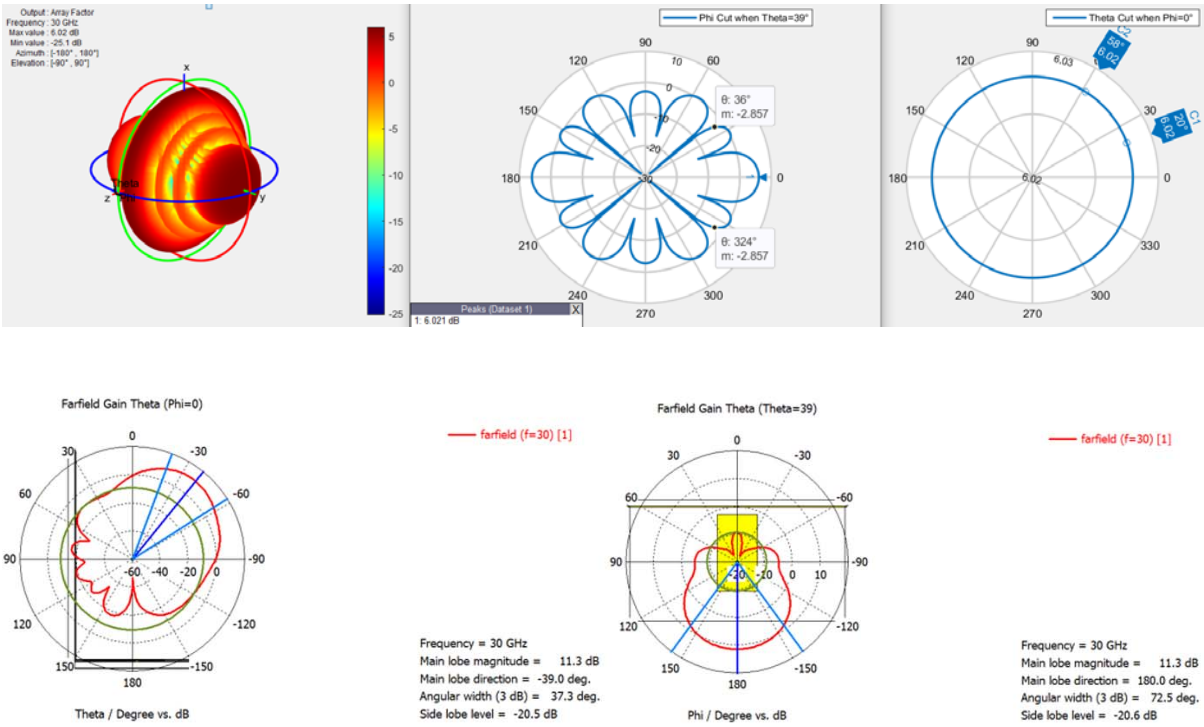

Figure 5-16: Array Factor of a 4-element array with 10 mm spacing between consecutive elements fed in phase and the associated pattern cuts

5.3 Beam Scanning

For the antenna array presented in Figure 5-15, the beam can be moved in the Z-Y plane (Azimuth) by simply introducing a progressive phase at the input of the feeding patches.

As shown in the AF formula, the total phase shift in an antenna array is comprised of the spatial phase delay plus the progressive phase at the input of each element in the array. Therefore, by imposing a progressive phase shift at the input of each feed in the Figure above, the beam will shift in Azimuth.

Figure 5-17 illustrates the beam shift in the Z-Y plane, for different progressive phases imposed at the input of the patches. The progressive phases used at the input of the patches are: 0°, 30°, 60°, 90°, 120°, 150°, 180°.

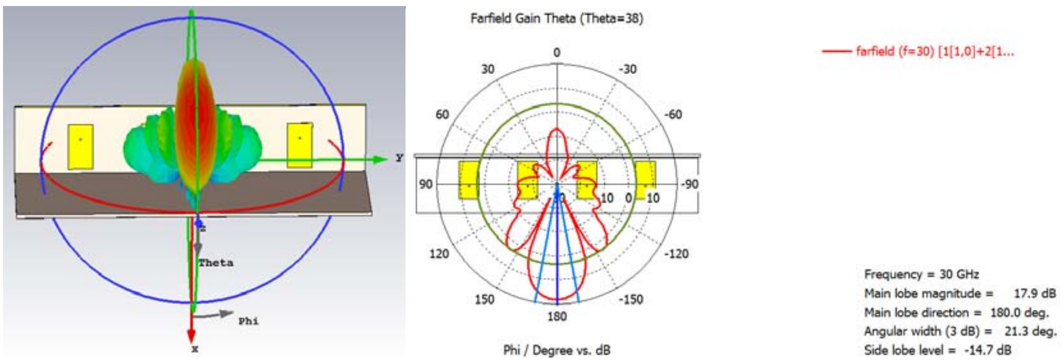

(a)

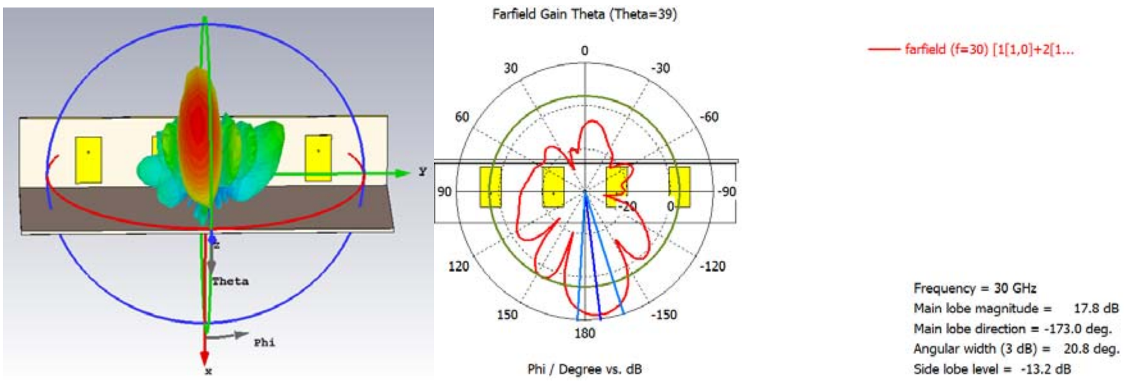

(b)

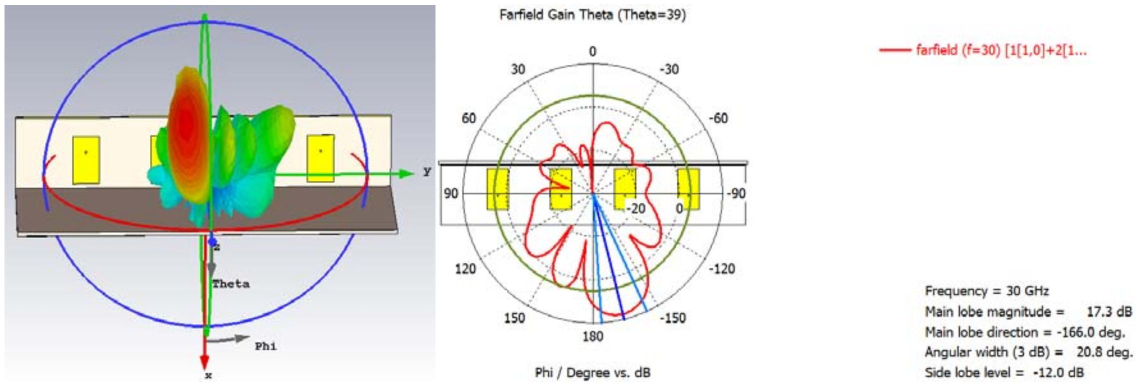
Farfield Gain Theta (Theta=39)
farfield (f=30) [1[1,0]+2[1...
Frequency = 30 GHz
Main lobe magnitude = 17.3 dB
Main lobe direction = -166.0 deg.
Angular width (3 dB) = 20.8 deg.
Side lobe level = -12.0 dB
Phi / Degree vs. dB
Theta
Phi

(c)

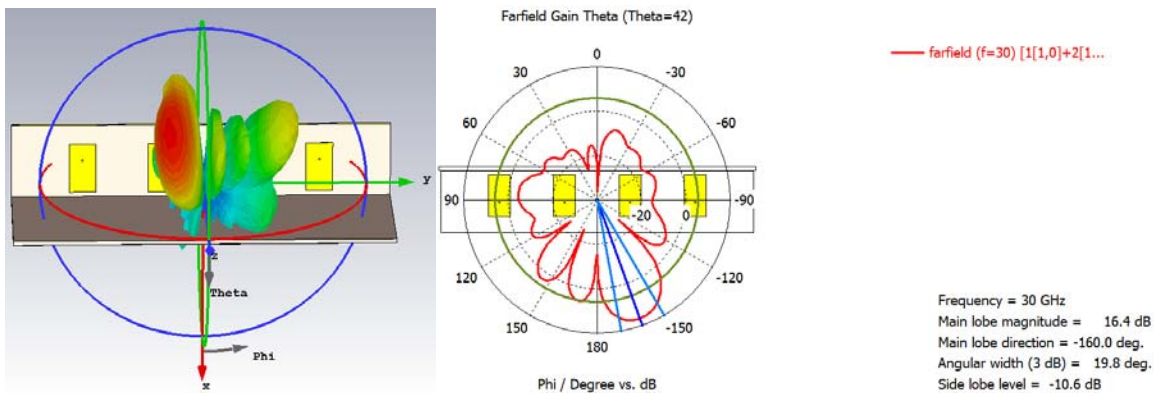
Farfield Gain Theta (Theta=42)
farfield (f=30) [1[1,0]+2[1...
Frequency = 30 GHz
Main lobe magnitude = 16.4 dB
Main lobe direction = -160.0 deg.
Angular width (3 dB) = 19.8 deg.
Side lobe level = -10.6 dB
Phi / Degree vs. dB
Theta
Phi

(d)

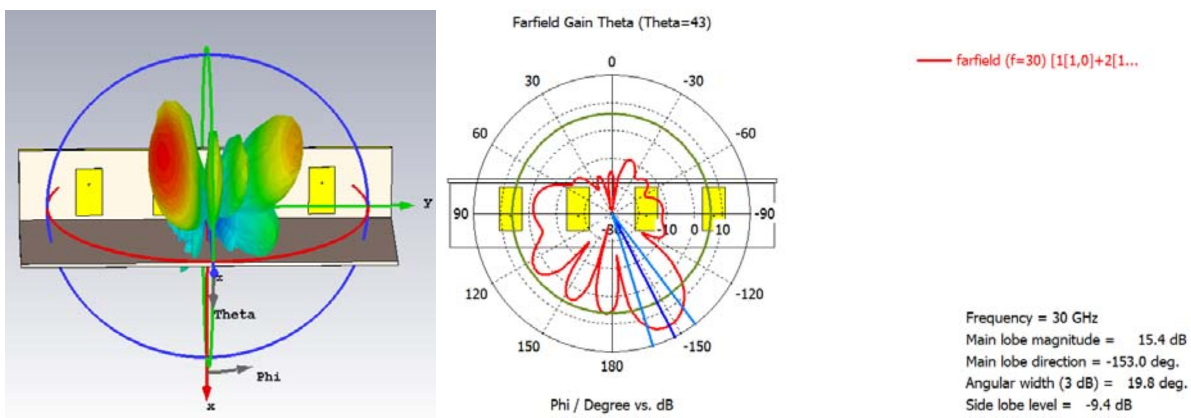
Farfield Gain Theta (Theta=43)
farfield (f=30) [1[1,0]+2[1...
Frequency = 30 GHz
Main lobe magnitude = 15.4 dB
Main lobe direction = -153.0 deg.
Angular width (3 dB) = 19.8 deg.
Side lobe level = -9.4 dB
Phi / Degree vs. dB
Theta
Phi

(e)

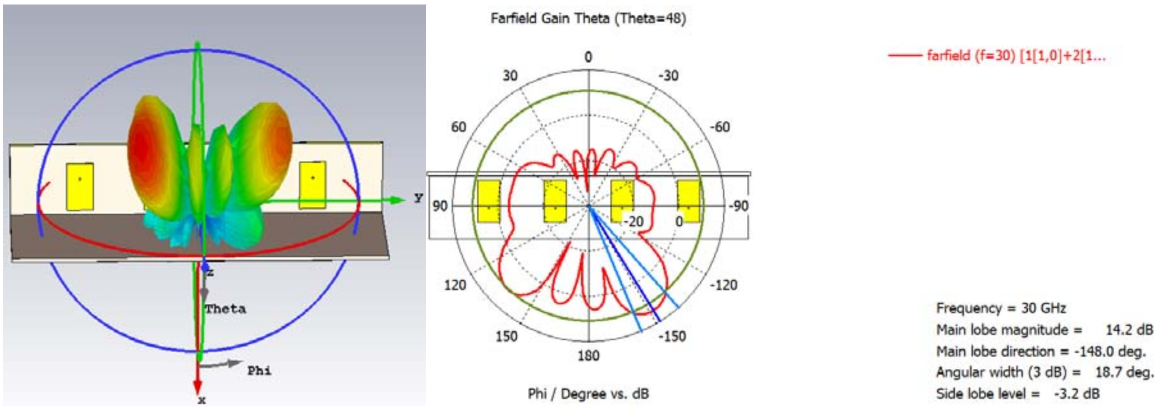

(f)

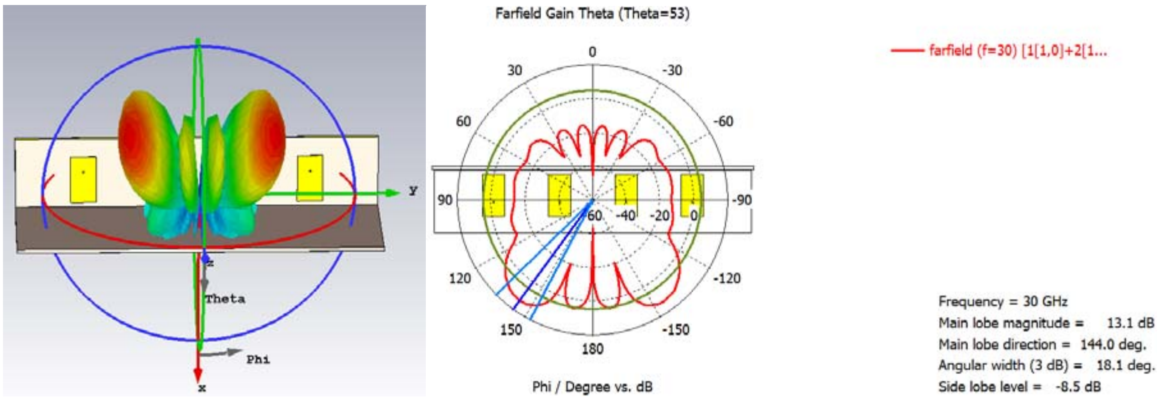

(g)

Figure 5-17: Beam shifting in Azimuth for (a) 0°, (b) 30°, (c) 60°, (d) 90°, (e) 120°, (f) 150°, (g) 180° progressive phase input

As it can be observed, the main lobe magnitude decreases rapidly, as the beam is scanned. At 150° progressive phase, the main lobe decreases by approximately 3.7 dB, giving a steering range of 32˚ on each side of the structure (64˚ in total). The grating lobe becomes more prominent as the progressive phase increases to 150˚.

The absolute side-lobe level is 11.8 dB, and as the progressive phase input increases further to 180˚, the side-lobe level expands until it becomes a grating lobe. The grating lobe occurs because the distance between the feeding patches is > λ/2. However, at distances < λ, the feeds start to couple to each other and their interaction reduce the overall gain of the structure.

Table 5-1 presents the pattern cuts values at different progressive phase on the input of the patches.

Table 5-1: Beam Shifting Results when the distance between the feeding patches is 10 mm

Progressive Phase (deg)	0	30	60	90	120	150	180
Phi Lobe Magnitude (dB)	17.9	17.8	17.3	16.4	15.4	14.2	13.1
Phi Lobe Direction (deg)	180	-173	-166	-160	-153	-148	-144
Phi 3 dB BW (deg)	21.3	20.8	20.8	19.8	19.8	18.7	18.1
Phi Side Lobes (deg)	-14.7	-13.2	-12	-10.6	-9.4	-3.2	-8.5
Theta Lobe Magnitude (dB)	17.9	17.8	17.3	16.4	15.4	14.2	13.1
Theta Lobe Direction (deg)	-38	-38	-39	-39	-41	-46	-51
Theta 3 dB BW (deg)	35.3	34.3	31.3	27.6	25.4	25.2	26.3
Theta Side Lobes (dB)	-19.2	-19.4	-19.6	-19.7	-19.3	-18.1	-14.9

The effect of the progressive phase (imposed at the input of the feeding patches) on the array factor pattern is shown below, in Figure 5-18.

For simplicity, only two progressive phase angles have been considered: 60˚ and 180˚. Compared to Figure 5-16, where the progressive phase angle is 0˚, the Array Factor Pattern at 60˚ progressive phase shows that the lobe at Theta= 90˚ increases and widens considerably.

This determines the occurrence of the high sidelobe observed in Figure 5-17, at around Phi=50˚. Also, the lobe at Theta=0˚ in the Array Factor plots swings towards Theta= 330˚. From here the main lobe scanning in Azimuth, shown in Figure 5-17.

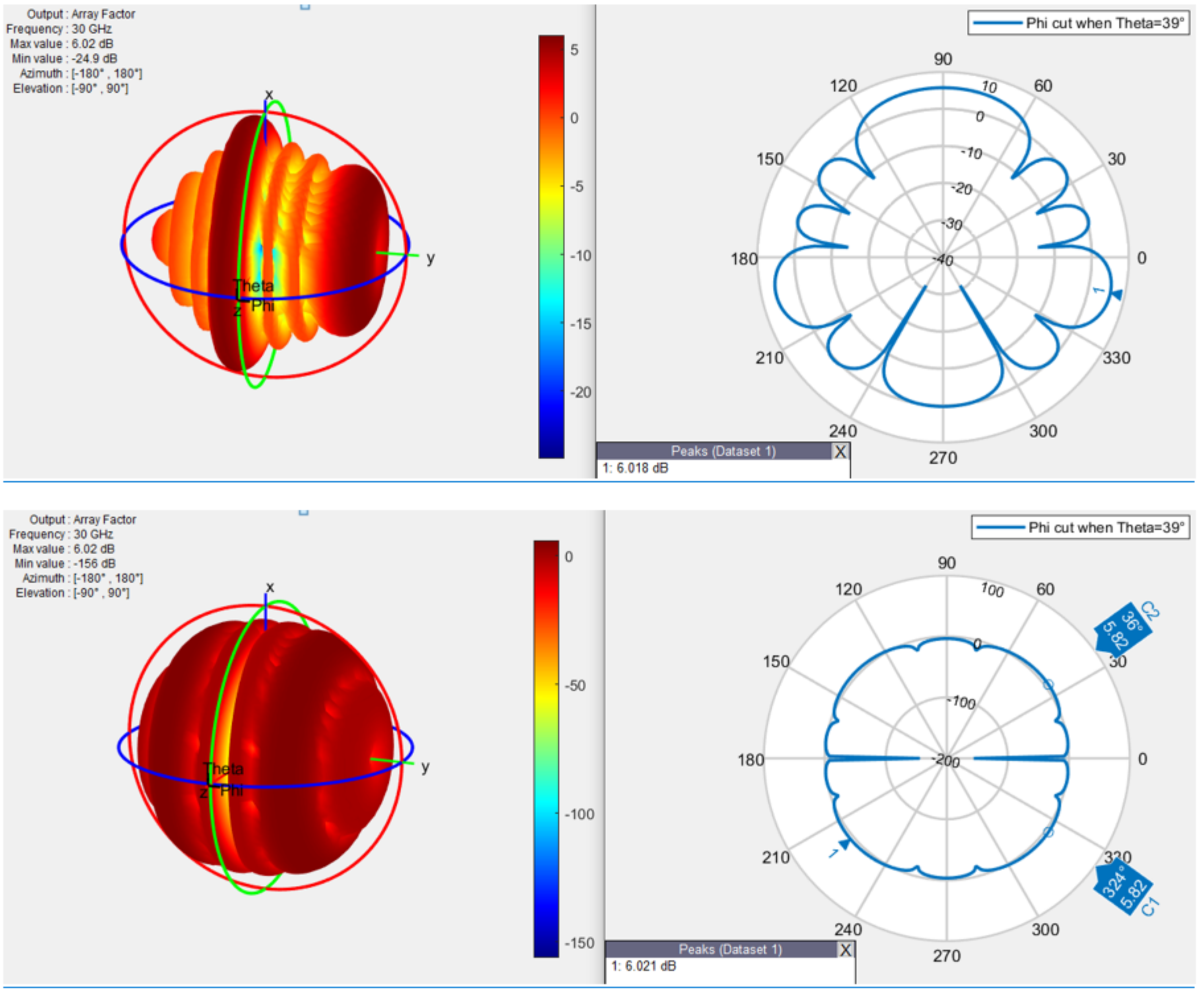

Figure 5-18: Array Factor pattern at 60˚ progressive phase angle (top) and 180˚ (bottom)

When the progressive phase increases to 180˚, the Array Factor pattern appears to be like two major lobes (Figure 5-18 bottom). As it can be observed, the 3 dB beam of the unit element pattern overlaps the trough of AF patten, at Theta=0˚ and it covers areas from both lobes the Array Factor, between 36˚ and 324˚. From here the two main lobes observed in Figure 5-17. The peak of the unit element pattern combines with the trough of the AF pattern, and half-power of the peak adds to 5.82 dB from the AF pattern. Because the maximum of the two patterns do not fall at the same angles, the resultant pattern presents lower levels. If the distance between the patches is increased to 13 mm, then the AF peaks fall within the 3 dB beamwidth of the unit element, and the resultant radiation pattern presents a higher level (15 dBi compared to 13 dBi). This is shown in Figure 5-19.

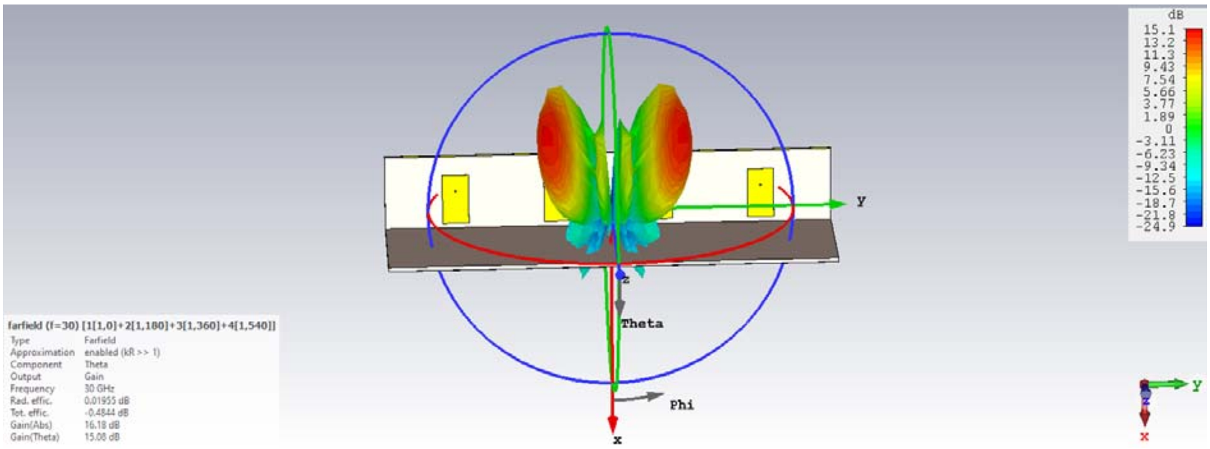

Figure 5-19: The radiation E-Theta pattern for 180° progressive phase when the distance between the patches is set to 13 mm

Table 5-2 presents the Beam Shifting Results when the distance between the feeding patches is 13 mm.

Table 5-2: Beam Shifting Results when the distance between the feeding patches is 13 mm

Progressive Phase (deg)	0	30	60	90	120	150	180
Phi Lobe Magnitude (dB)	17	16.9	16.8	16.4	16	15.7	15.1
Phi Lobe Direction (deg)	180	-174	-169	-163	-158	-154	-150
Phi 3 dB BW (deg)	16	16	15.6	16.6	15.6	15.2	14.9
Phi Side Lobes (deg)	-12.5	-11.7	-11	-10.6	-4.7	-1.5	-9.9
Theta Lobe Magnitude (dB)	17	16.9	16.8	16.4	16	15.7	15.1
Theta Lobe Direction (deg)	-38	-38	-38	-38	-41	-43	-46
Theta 3 dB BW (deg)	36.2	34.4	30.8	27.2	25.3	23.4	22.3
Theta Side Lobes (dB)	-24.3	-19	-20.3	-20.3	-19.6	-19	-17

Compared to the results in Table 5-1, the values in Table 5-2 show that the main lobe magnitude decreases slower when the distance between feeds is set to 13 mm. However, the beam appears to shift more in azimuth when the distance is set to 10 mm.

5.4 Circularly polarised microstrip patch attached to a reflective surface

In Chapter 2 the circular polarisation has been obtained on the microstrip patch antenna by cutting out the two opposite edges of the patch. An axial ratio of 0.89 dB was obtained at 30 GHz, on Theta =-40˚ and Phi=0˚, which correspond to the maximum gain point on the pattern. This axial ratio corresponds to 25.82 dB cross-pol discrimination.

Similar to the linear polarisation analysis performed in Section 4.2, the circularly polarised patch is studied in the presence of a reflective substrate. Initially, the patch is attached to a 28 mm long reflective substrate, as shown in Figure 5-20.

As in the previous study, the substrate dielectric material used is Rogers 5880 LZ, with 2.0 permittivity. It is anticipated for the lower beam of the patch to hit the grounded substrate, which reflects it back in the air and where it recombines with the top beam.

Normally, by adding the reflective substrate, it is expected that the gain increases by approximately 2.5-3 dB [163]. As shown in Chapter 2, the gain of the RHCP polarised patch is 7.15 dBi, therefore, the addition of the substrate should increase the RHCP gain to approximately 10 dBi.

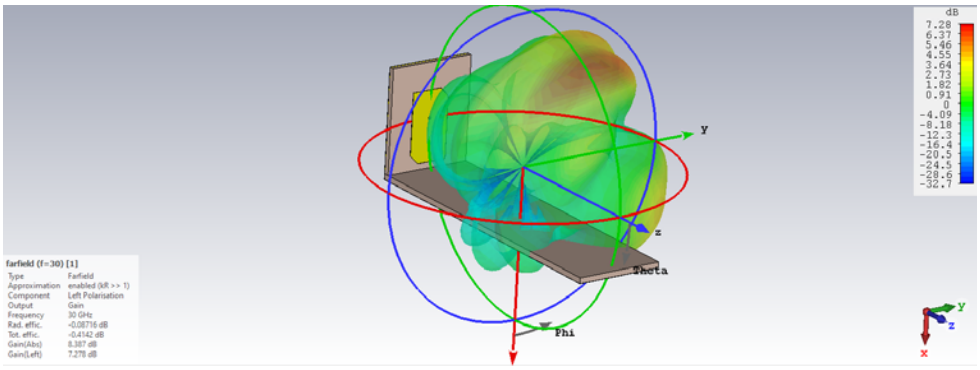

a)

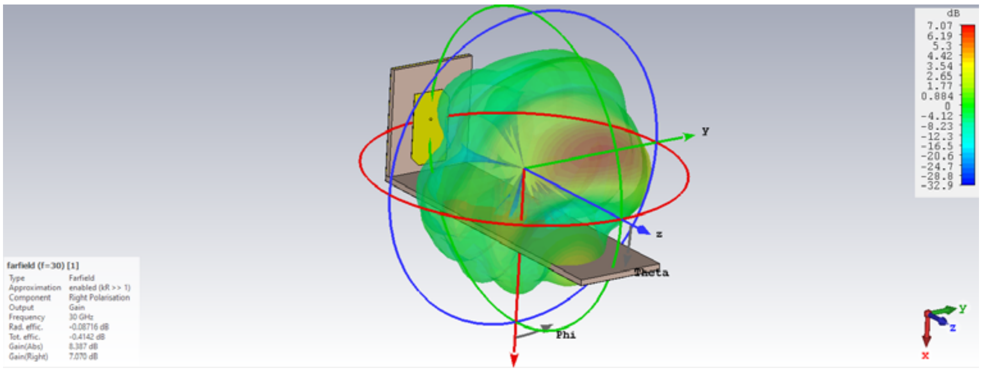

(b)

Figure 5-20: Radiation patterns of a circularly polarised patch attached to a 28 mm long reflective substrate a) LHCP, b) RHCP

However, the radiation pattern illustrated in Figure 5-20 shows that the reflective substrate is too narrow and that the beam to be reflected gets scattered at the edges of the substrate. The width of the reflective substrate has been increased to investigate further.

The gain of the structure vs the substrate width (when the substrate length is set to 28 mm) is shown in Figure 5-21. The RHCP gain increases only to approximately 8.6 dBi, when the substrate width is 22 mm. This is because when a circularly polarised beam hits a reflecting surface, the polarisation of the reflected beam is reversed. As a result, half of the beam that hits the reflecting substrate becomes LHCP polarised. The other half of the beam, which was launched in air, did not reverse in polarisation and remained RHCP polarised. In conclusion, the overall effect of the reflecting surface is the cancellation of the circular polarisation of the combined beams with effect to generation of a linear polarisation. The obtained LHCP polarised gain is approximately 0.5 dB higher than the RHCP polarised gain as a result of the reflective grounded substrate.

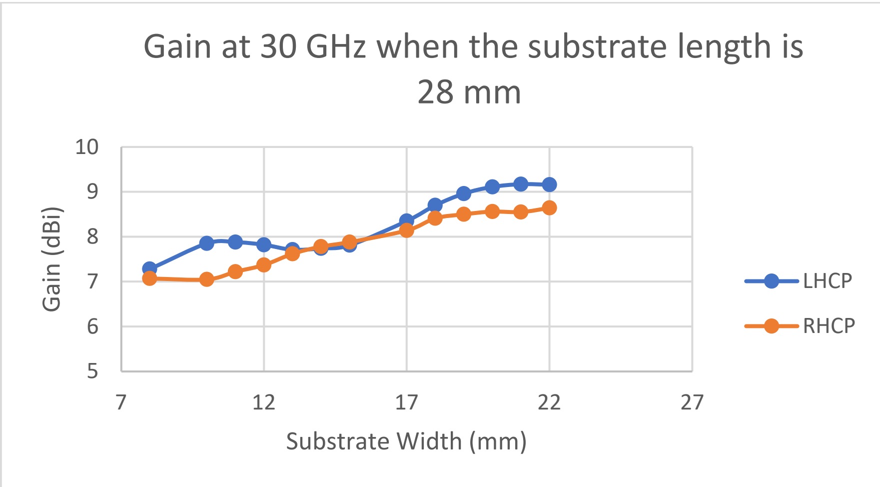

Figure 5-21: Gain variation with the substrate width, when the substrate length is set to 28 mm

Figure 5-22 shows the gain variation with the substrate length, when the substrate width is set to 22 mm. The highest RHCP gain (8.56 dBi) is obtained with a 26 mm long substrate.

Figure 5-23 below, shows the radiation patterns of both the RHCP and LHCP polarisations, when the substrate length is 26 mm and the substrate width is 22 mm. As it can be observed, both the LHCP and RHCP patterns are fully supported by the reflective substrate. The Phi=0˚ and Theta= 0˚ LHCP and RHCP pattern cuts are illustrated in Figure 5-24.

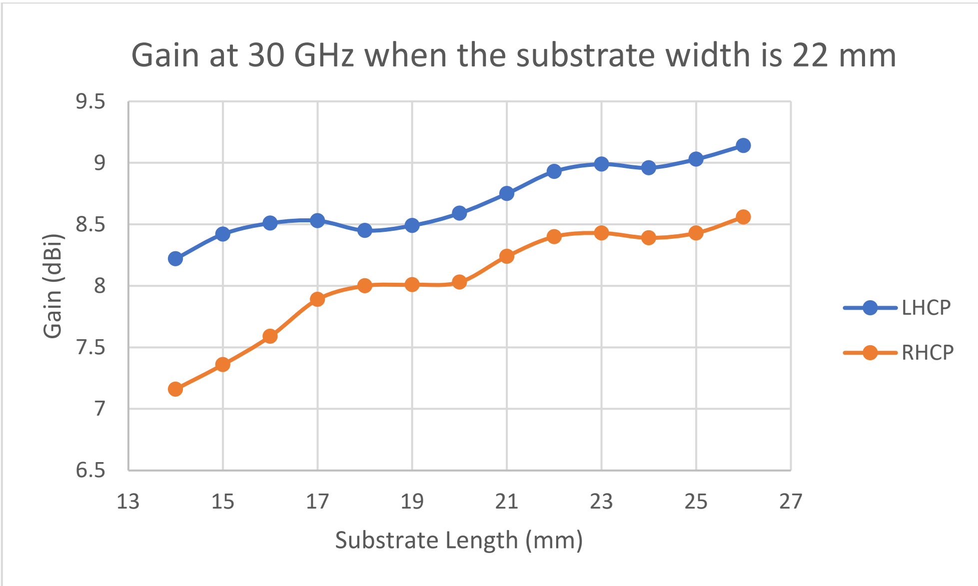

Figure 5-22: Gain variation with the substrate length, when the substrate width is set to 22 mm

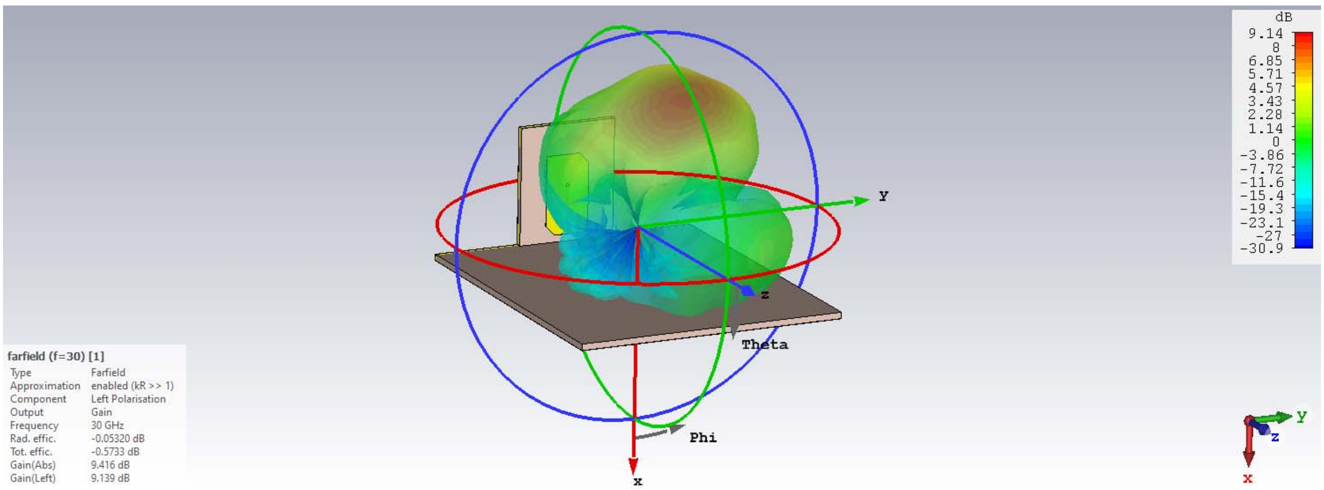

a) LHCP

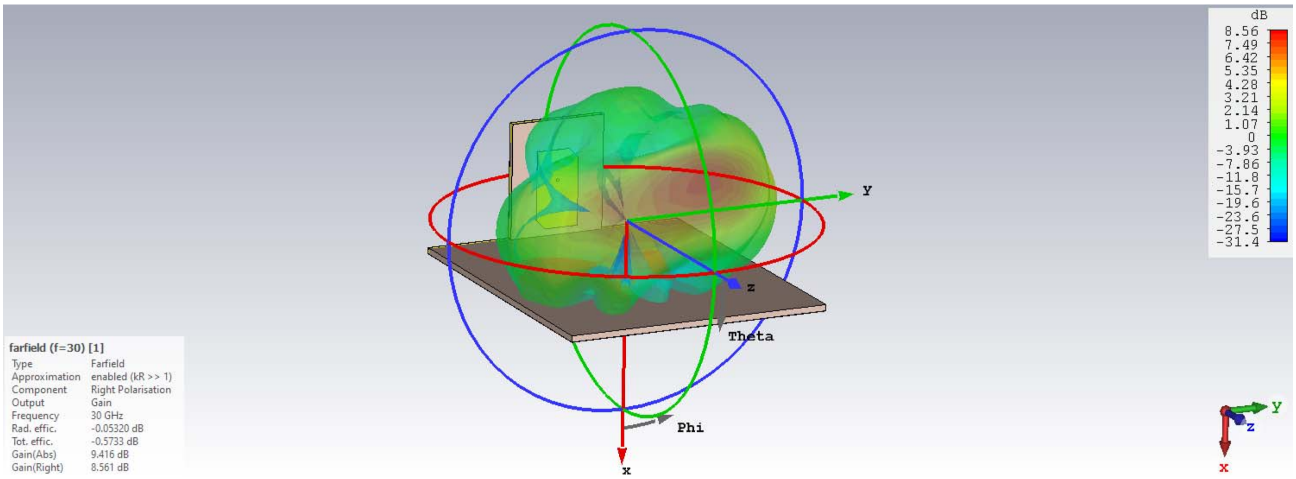

b) RHCP

Figure 5-23: LHCP(a) and RHCP(b) radiation patterns of a circularly polarised patch attached to a 22 mm x 26 mm substrate

Both Figures 5-23 and 5-24 suggest that the LHCP beam, which points to approximately Theta=50˚, has been obtained from the combination between the cross polarisation of the RHCP beam, which was launched in air and the resulted LHCP polarisation from the RHCP beam, which hit the substrate.

The same can be said about the RHCP beam: it points at approximately 29˚ and it represents a combination between the RHCP beam, which was launched in the air and the cross polar of the LHCP beam which resulted from the RHCP beam hitting the substrate.

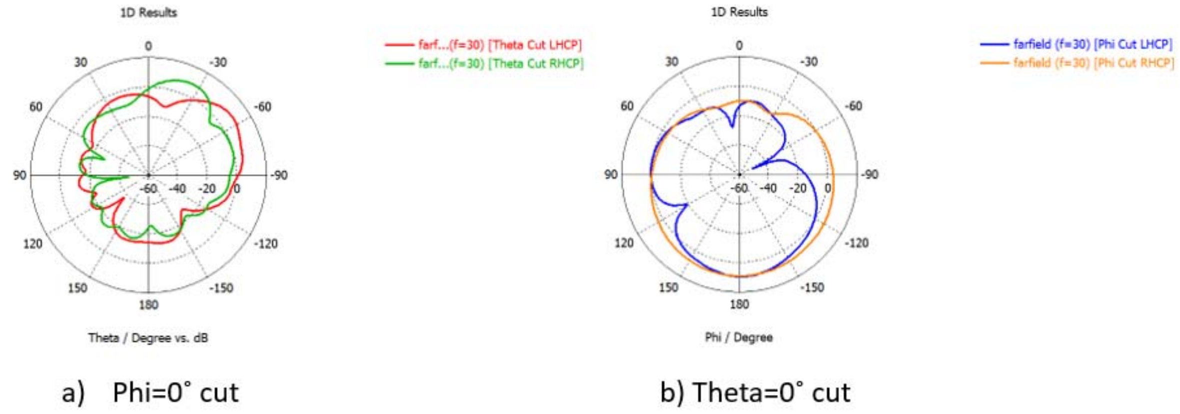

Figure 5-24: LHCP and RHCP pattern cuts

As the cross polar discrimination between the LHCP and RHCP is very low, it is expected for the axial ratio value to be very high. Figure 5-25 illustrates the axial ratio values over Theta at 30 GHz, when Phi=0˚.

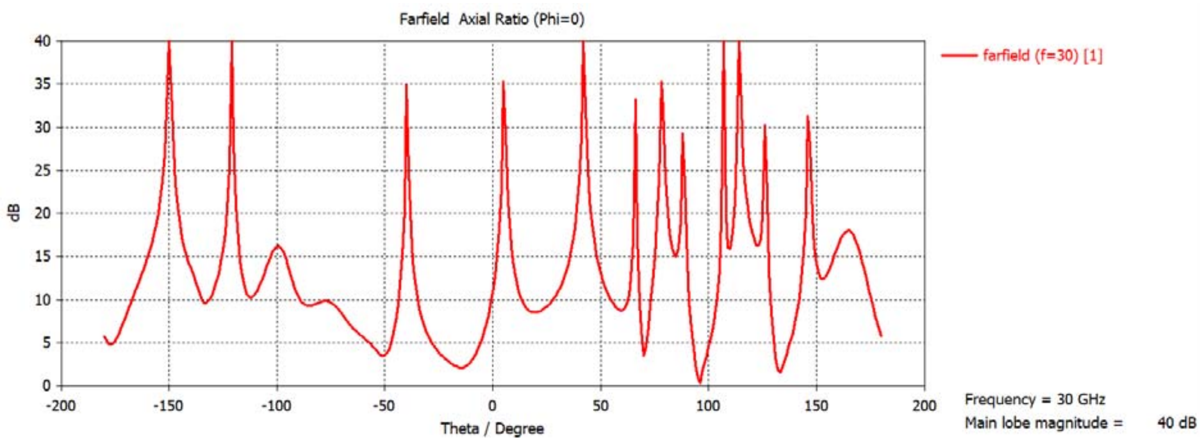

Figure 5-25: Farfield axial ratio, at Phi=0˚

If two such structures are attached together, as an array of two elements, both the LHCP and RHCP polarisations will result in more directive beams. This is illustrated in Figure 5-26.

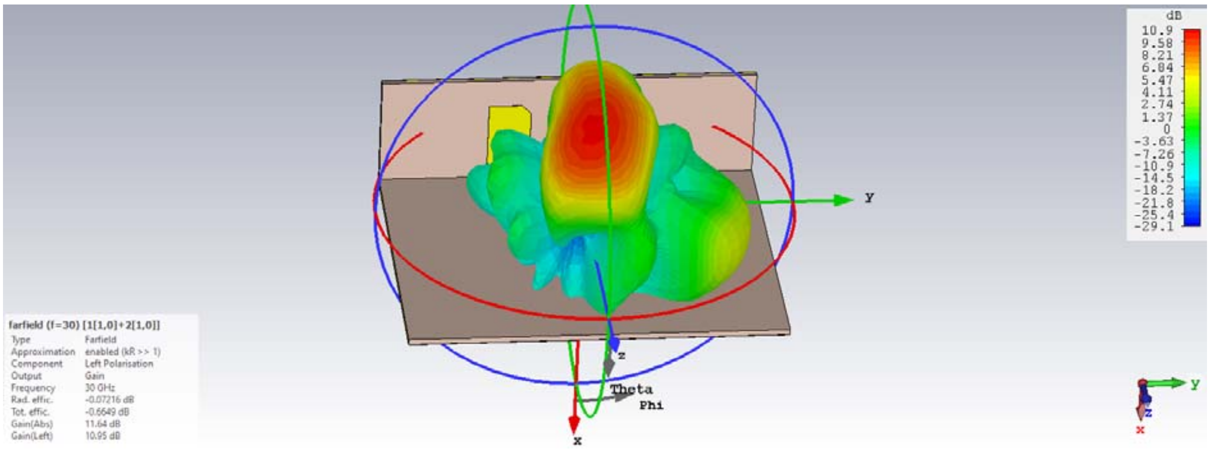

a)

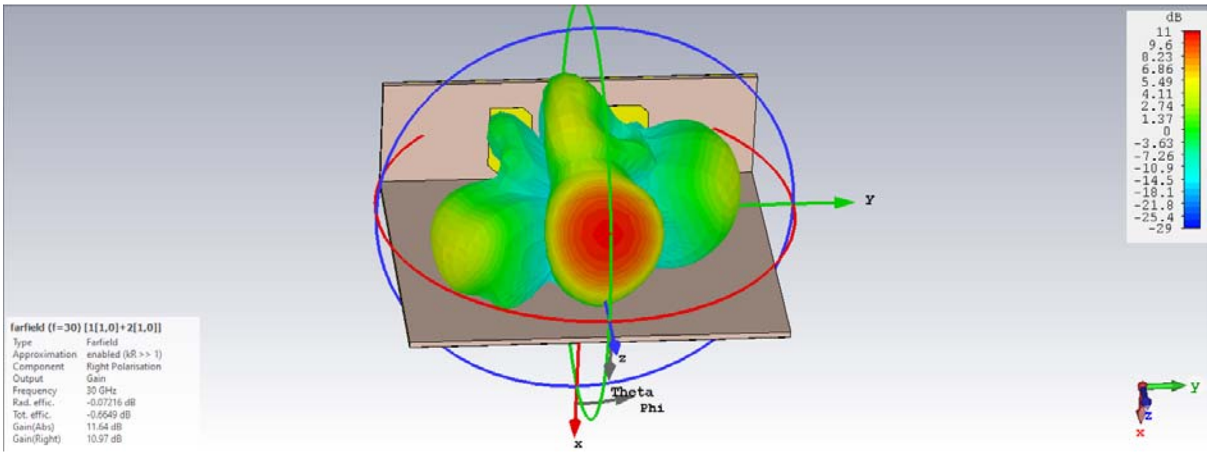

b)

Figure 5-26: a) LHCP and b) RHCP patterns for an array of two circularly polarised patches with reflective substrate

As it can be observed from Figure 5-26, the cross polar discrimination between LHCP and RHCP is very low, therefore it is expected for the axial ratio to be high. This is shown in Figure 5-27, for a Theta cut, when Phi=0˚, at 30 GHz.

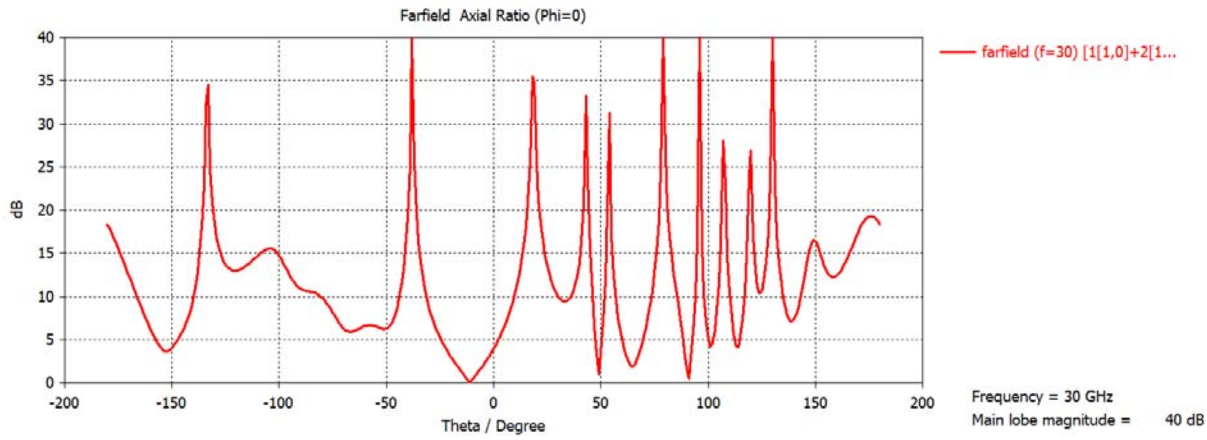

Figure 5-27: Far field Axial Ratio for the two elements array

To summarise, in this section it has been demonstrated that the presence of the reflecting substrate does not improve the gain of the circularly polarised microstrip patch. The overall effect of the reflecting substrate is to convert the circularly polarised field into a linearly polarised field. The RHCP gain is small, because approximately half of the energy is transferred on the opposite polarisation, due to the presence of the reflecting substrate. Due to reciprocity theorem of the antennas, the same effect is expected even if the antenna is transmitting or receiving. The antenna's radiation pattern and receiving pattern are identical.

As this is not the desired effect for this particular structure, it is concluded that it is more advantageous to use the reflective substrate in combination with the linearly polarised patches. As it has been demonstrated in the previous section, the linearly polarised patch in combination with the reflective substrate increases the gain by approximately 3 dB.

6. Investigations of the effect of the reflecting patches on the antenna gain

The gain of the linear structure analysed in Chapter 5 proved sufficient for complying the gain requirement defined in Chapter 3, however, this can be further improved by adding reflecting patches on the reflecting substrate. This improves the gain and the beam angle scanning range. The reflecting patches are illuminated by the lower beam of the feeding patches, and they reflect the incident beam with a different phase, depending on whether the patches are resonant or not. The reflected beam presents a different phase compared to the phase of the top beam which has not been reflected by the substrate. The new phase is determined by the distance between the reflecting patches and the feed (differential space delay) added to the phase introduced by each reflecting patch (progressive phase). This concept is very similar to the way a reflect-array antenna works. It is important to specify that on a reflectarray antenna, the amplitude distribution on each element is dictated by the primary feed, therefore only the phase can be controlled at the printed elements [136]. The concept of a reflectarray antenna was explained in the Chapter 2.

6.1 Directing patches design

To enhance the design of the ordinary flat reflector consisting the ground conductor and the overlay substrate, as shown in the previous chapter, e.g. Figure 5-15, a set of the directing patches is implemented on the substrate (covering the ground-plane) (in other words, the patch rests on the top layer substrate: Roger RT5580LZ ($\varepsilon_r =$

$2.0, \mathrm{tg\ loss} = 0.0021)$ and the whole structure is backed by a ground plane). The ground plane increases the antenna gain by 3 dB [163].

After several simulations using the CST Microwave Studio, the dimensions of the unit cell resonant at 30 GHz have been determined, as illustrated in Figure 6-1. Using the standard formulas, the resonant length of the patch can be approximated as:

$$\mathrm{L} = \frac{\mathrm{c}}{2*\mathrm{fres}*\sqrt{\varepsilon_r}} = \frac{3*10^8}{2*30*10^9*\sqrt{2}} = 3.5\ \mathrm{mm} \tag{6.1}$$

while the width of the patch can be approximated as 0.7*L = 2.45 mm. However, when simulating the patch with the calculated dimensions, at 30 GHz, the phase of the reflected wave is different from 0˚ (-38˚), which means that the patch is not resonant.

The dimensions of the resonant patch resulted to be L=2.83 mm, and W=3.5 mm, and as shown in Figure 6-1 a), the phase of the reflected coefficient at 30 GHz is very close to 0˚, which means that the patch is resonating. The substrate's dimensions are: 5 mm x 5 mm x 0.5 mm.

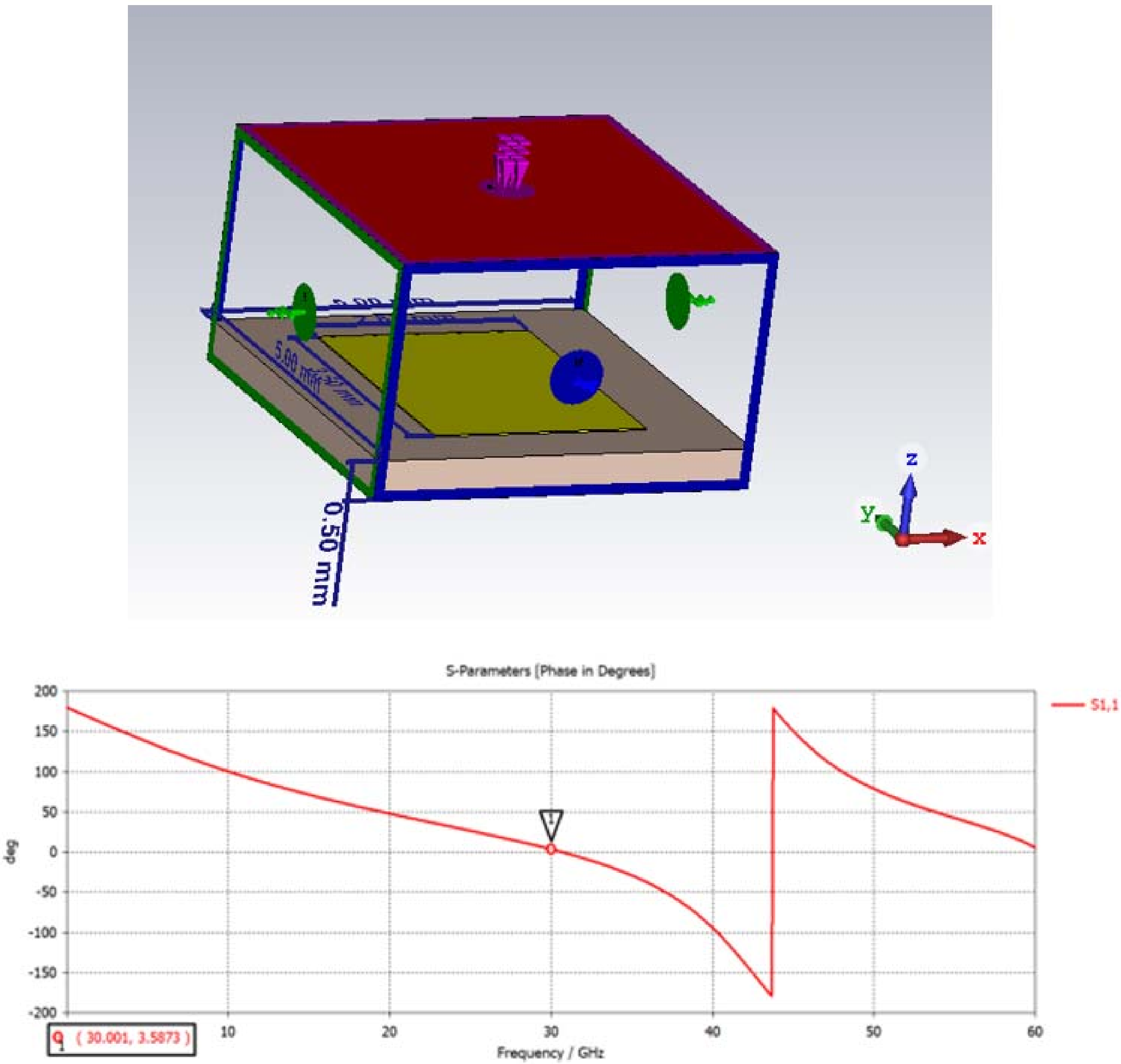
0.50 mm
5.00 mm
z
y
x
S-Parameters [Phase in Degrees]
S1,1
deg
200
150
100
50
0
-50
-100
-150
-200
10
20
30
40
50
60
Frequency / GHz
(30.001, 3.5873)

a)

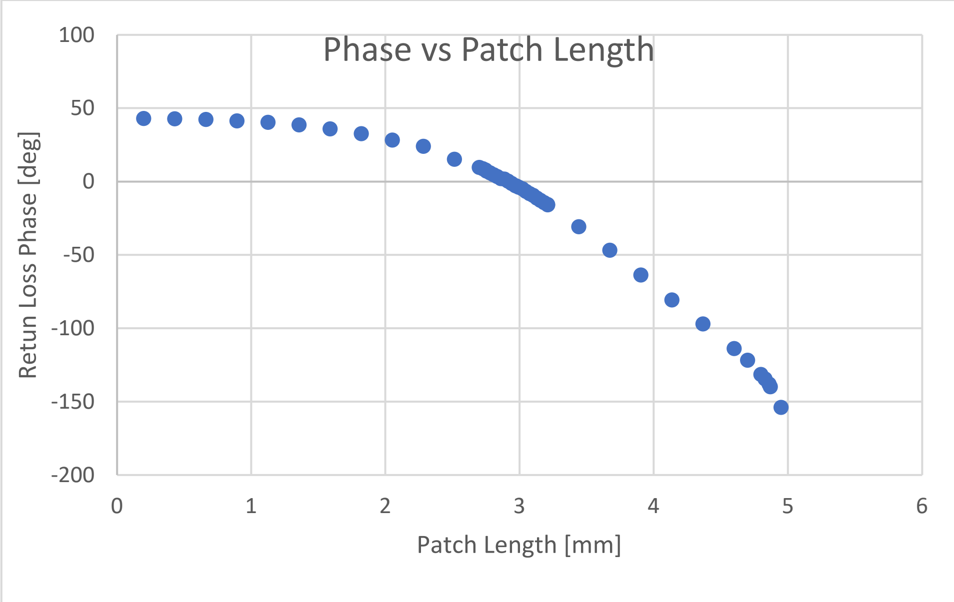

b)

Figure 6-1: a) Directive patch-structure and return loss phase; b) Directive patch-phase versus patch length i.e. the S-curve;

Figure 6-1 b) shows the S-curve obtained by exciting the unit cell (at different lengths) using a waveguide port. The phase of the S11 parameters is obtained and mapped against the corresponding patch length. The unit cell has been excited by a waveguide port in order to determine the resonant length of the patch. For this, the electric boundary condition has been set along the width of the patch and the magnetic boundary condition along the length of the patch, as shown in Figure 6-1 a). This approach is known as ‘parallel plate waveguide simulator’ or ‘H wall waveguide’. The incoming wave hits the tested element at broadside and then gets scattered back (at broadside), with a certain amplitude and phase. The back scattered wave consists of three components: one is the re-radiated component due to resonance of the patch, the second is the specular reflected component due to the ground plane and the third is the scattered component created by the non-resonant structures of the patch and delay lines. As the substrate thickness is 0.5 mm, which is << $0.1*\lambda_0$, then it is correct to assume that only the first two components are dominant [160]. The resonant elements will completely re-radiate the incident energy (at broadside), while the non-resonant elements will present both components in the back-scattered energy: the re-radiated and reflected energy. The reflected energy will be dominant [160].

It is also important to take into consideration the incident angle of the incoming wave. The H wall waveguide simulator takes into account only the broadside incidence case, however, in a real case scenario, the reflectarray elements will be illuminated at different incident angles.

To analyse these cases, a physical waveguide model must be constructed, with the patch under test placed at the end of the waveguide. By varying the H-plane (or the long dimension of the waveguide), a certain incidence angle is obtained, given the formula in [160]:

$$\sin(\theta i) = \pi/(ka) \qquad (6.2)$$

Where a is the long dimension of the waveguide

Figure 6-2 illustrates the radiation pattern of the reflecting element shown in Figure 6-1 (a), with 2.83 mm length and 3.5 mm width. The patch has been excited using a microstrip line placed very close to the patch, along the width, but without actually touching it.

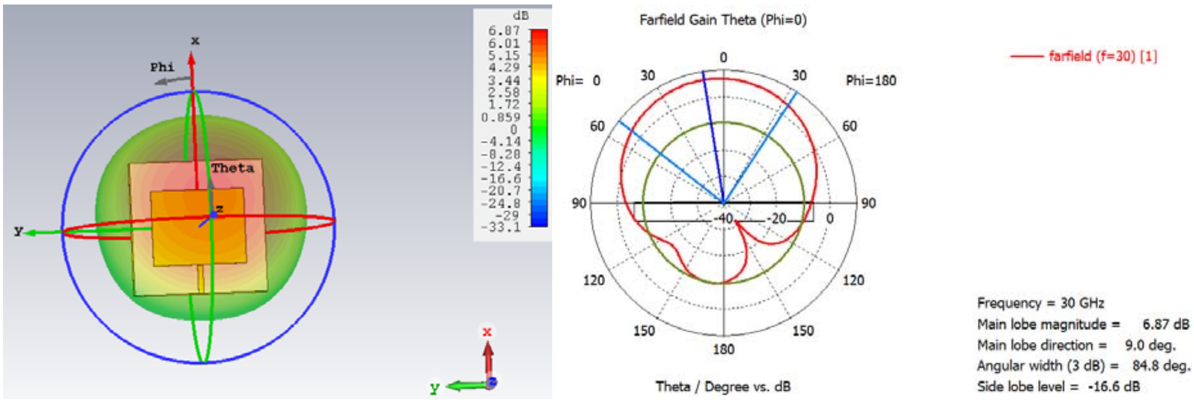

Figure 6-2: The radiation pattern of the reflecting element and the E-Theta pattern cut

It is convenient to map the phase generated by the reflecting patch to the length of the patch, as shown in Figure 6-1. In this way, depending on the amount of differential space delay occurred between the feed and the reflecting patches, the convenient length of the patch can be chosen to compensate for the necessary phase. The phase curve of the reflecting patch is shown in Figure 6-1 b), and it can be seen that the patch can only compensate for phases ranging between 42.9° and -154°. For phases outside this range, there will be phase errors introduced by this limitation. As explained in [139], reduced phase range produces phase error on the surface of the reflectarray, which leads to gain reduction.

The return loss phase shown in Figure 6-1 suggests that the designed patch is nearly resonant at 30 GHz, and that it introduces approximately 3.5873˚ of phase shift. As expected, it has been observed that for 0˚ phase shift, S11 shifts to the left (lower frequencies), and the length of the patch increases - see formula (6.1)

At absolute resonance, the S11 Phase curve shows 0˚ phase shift and the Length of the patch is approximately 2.9 mm. There is no phase shift because the Patch can be modelled with parallel RLC elements, which, at resonance, behaves as an open circuit. The open-circuit introduces reflections to the source that have the same phase as the incident waves.

6.2 Simulations of the structure containing the parasitic patches

By introducing the radiating or parasitic patches on the reflecting substrate, it was expected to obtain a higher gain compared to case when no patches were present on the substrate. The reflected wave from the parasitic patches combines in phase with the first beam of the feeding patches, improving the directivity of the antenna.

Starting from the four elements array illustrated in Figure 5-15, a set of two radiating patches have been added on the reflective substrate, being separated by 5 mm ($\lambda_0/2$). The length of the reflecting substrate is 17 mm and the distance between the feeding patches is 10 mm. The dimensions of the directing patches are, as explained in the subsection above: L=2.83 mm and W=3.5 mm. The performance of structure is then obtained using CST software.

Figure 6-3 illustrates the structure, the 3D radiation pattern and pattern cuts in two principal planes.

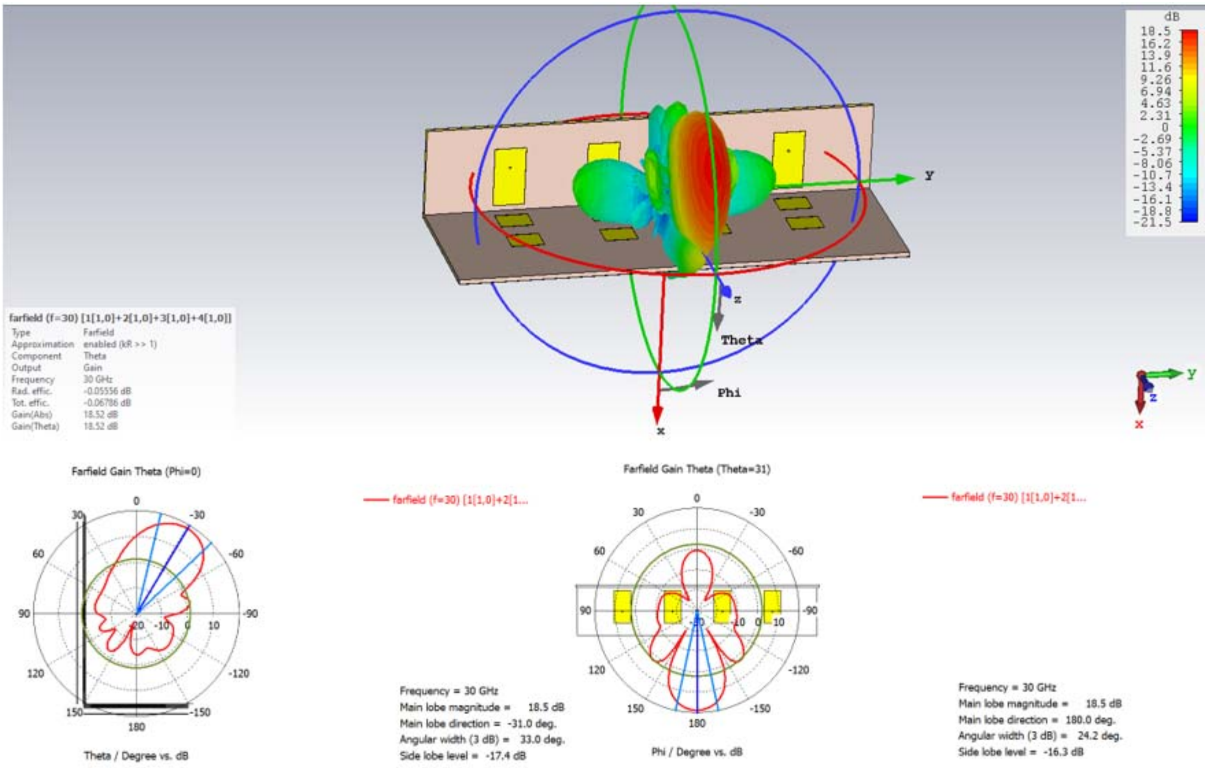

Figure 6-3: Antenna structure with radiating patches added and pattern cuts.

As it can be observed, the gain has improved only by approximately 0.6 dB. Compared to the pattern in Figure 5-15, where the reflecting patches were not present, the number of sidelobes decreased around Phi, but some of them became overprominent. Also, the main lobe direction decreased towards the Z axis, to 31˚, from 38˚, and the 3 dB beamwidth decreased to 33˚ from 35.3˚. This comparison between the two cases is shown in Figure 6-4.

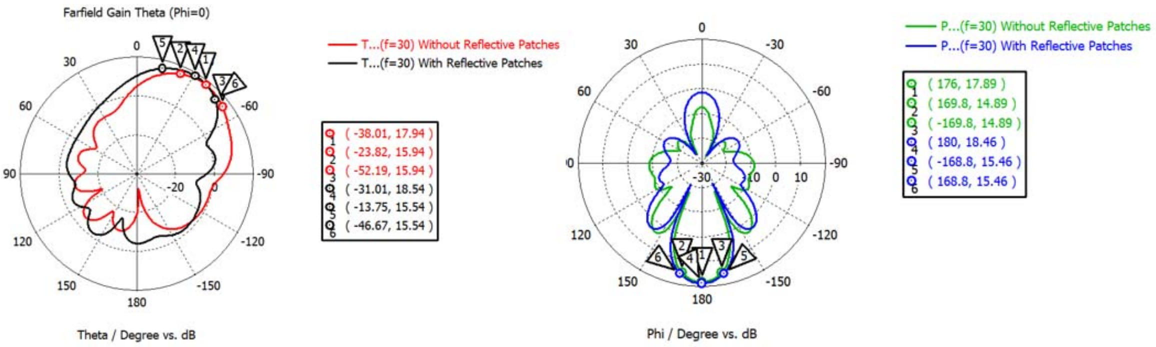

Figure 6-4: E-Theta and Phi Cuts with and without the reflective patches

A third row of patches has been added, and it has been observed that their contribution to the radiation pattern is minimal. Moreover, there is an increase of the sidelobe level observed around 70˚, possibly due to the effect of the spatial phase delay.

The farfield range of the feeding patch starts at a distance of approximately 31 mm away from it and the two sets of the reflecting patches lie at 2.58 mm and 7.53 mm distance from the feeding patches. It results that the reflecting patches are in the nearfield of the feeding patches, and therefore the electromagnetic field incident on each reflecting element cannot be approximated by a plane wave. Instead, the reflecting elements are illuminated by the nearfield. In the nearfield, the relationship between E and H fields is complex and the strengths of the field components vary. There is also a reactive component of the radiated field, which represents the energy stored close to the antenna, and this can be represented by reactive elements (capacitors and inductors). This reactive field induces a current on the reflective elements, however, because the feeding patch is a voltage radiator (due to the presence of the fringing E-fields) and its ground plane cancels the current on the surface of the patch, then it is correct to assume that the H-field component of the nearfield is small compared to the E-field component, which is dominant.

Given the radiation pattern of the feeding patch, as shown in Figure 4-5, with the two symmetrical lobes pointing at θ= +/- 39˚, it is acceptable to say that the first set of reflecting patches is illuminated at an approximate angle of 40˚. As a result, the reflecting elements will re-radiate part of the incoming energy and it will reflect most of it, as illustrated in Figure 2-50, from Section 2.11. The reflected energy will not see the peak of the reflecting patches' beam. If the specular angle is around 40˚, then the reflected field will only be reinforced by 2.7 dB, as shown in Figure 6-2. On the other hand, the re-radiated energy will see the maximum gain of the reflecting elements, but because the patch is not fully resonant, then the amount of the re-radiated energy is small.

The first two sets of reflecting patches are in the reactive nearfield of the feeding patch (which ends at 8.58 mm), and they appear to be illuminated at approximately the same time, as the side view in Figure 5-11 illustrates.

An animation of the E-Field distribution over the reflecting patches show that the last patches get excited later than the first patches and that their radiation is slightly out of phase. Figure 6-5 shows a screenshot of the E-field animation from which it can be observed that the last patches get illuminated less, compared to the first patches that are closer to the feeds.

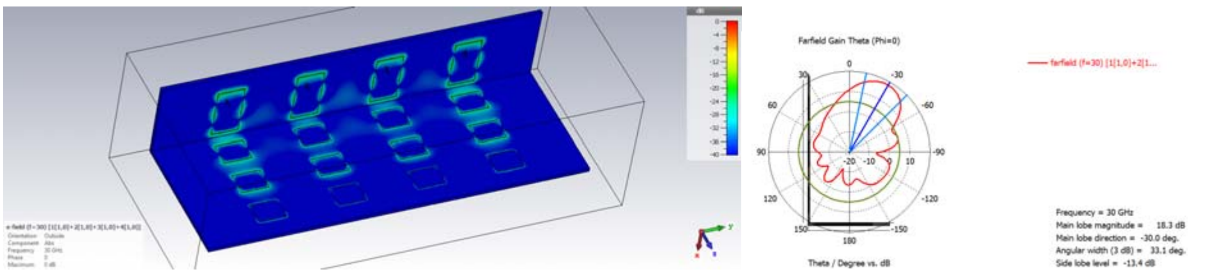

Figure 6-5: E-field distribution contour and Phi=0 pattern cut

The input return loss and the isolation between the feeding ports of the structure in Figure 6-3, is shown in Figure 6-6. The 10 dB input impedance bandwidth is 0.695 GHz.

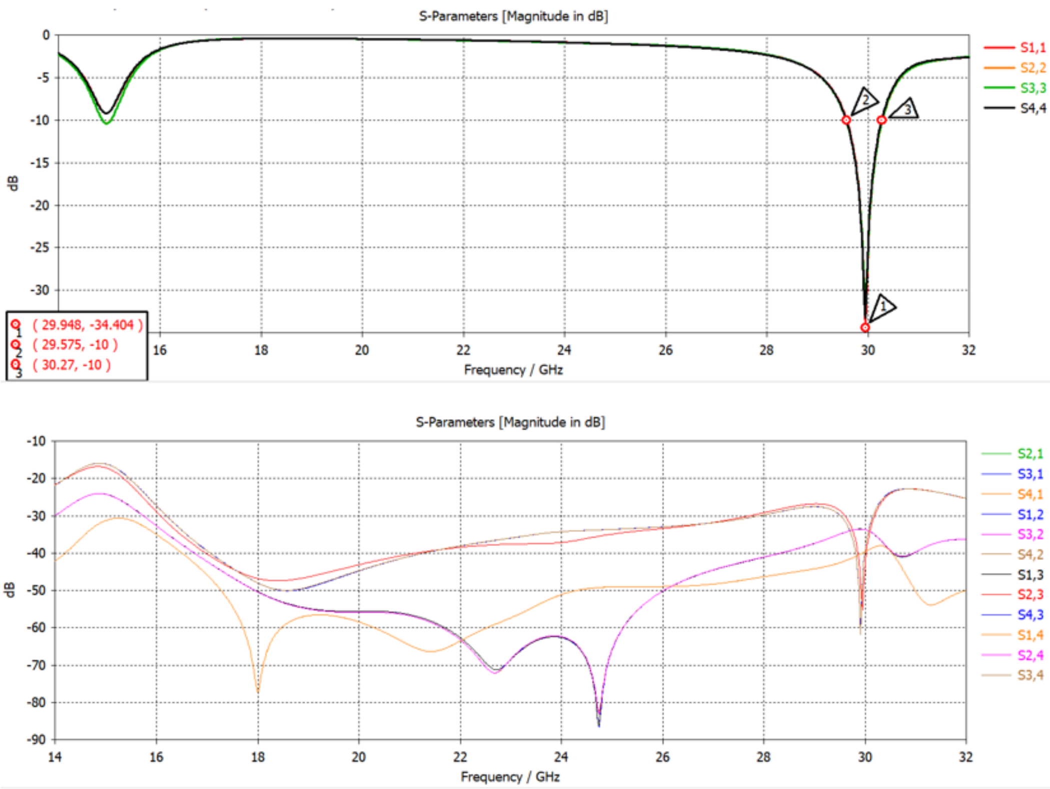

Figure 6-6: The S-parameters of the Structure containing the reflecting patches

The input frequency has been varied within the 3 dB beam peak drop in order to check the operating bandwidth of the structure shown in Figure 6-3. Figure 6-7 illustrates the beam degradation as the frequency is swept between 23 GHz and 32 GHz.

As it can be observed, the main lobe direction changes in Theta direction as a result of a modified radiation pattern of the feed at different frequencies and also as a result of different phases introduced by the reflecting patches at different frequencies. At 23

GHz, the gain dropped to 16.5 dBi, while at 32 GHz, the gain dropped to 16.1 dB (from 18.5 dB at 30 GHz).

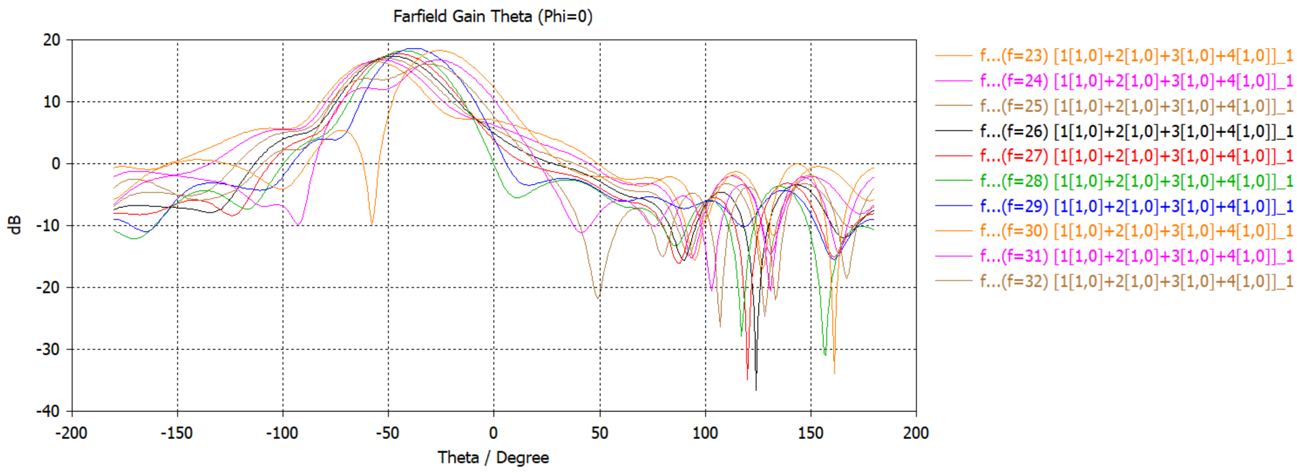

Figure 6-7: Beam degradation with frequency variation between 23GHz and 32GHz

6.2.1 Simulation results when the distance between feeds is increased to 13 mm

To check if an increase in the distance between the feeding patches results in any gain improvement to the structure shown in Figure 6-3, the structure is simulated with the feeding patches separated by 13 mm. This distance has been chosen due to the Array Factor pattern that is produced. The main lobe and the sidelobes are narrower, which provides more directivity to the array pattern. The length of the reflecting substrate containing the reflecting patches has been kept to 17 mm, as before. It was anticipated to see less coupling between the feeding patches, at the expense of higher sidelobes levels, as the E-Theta cut is showing in Figure 6-8. It has been found that at 30 GHz, the highest coupling between the feeds was -33 dB, when the distance between the feeds was 10 mm, and -39 dB when the distance between the feeds was 13 mm. Therefore, the isolation between the feeding patches increased by 6 dB, only by increasing the space between them by 3 mm. Figure 6-8 illustrates the E-Theta and E-Phi pattern cuts for the two cases.

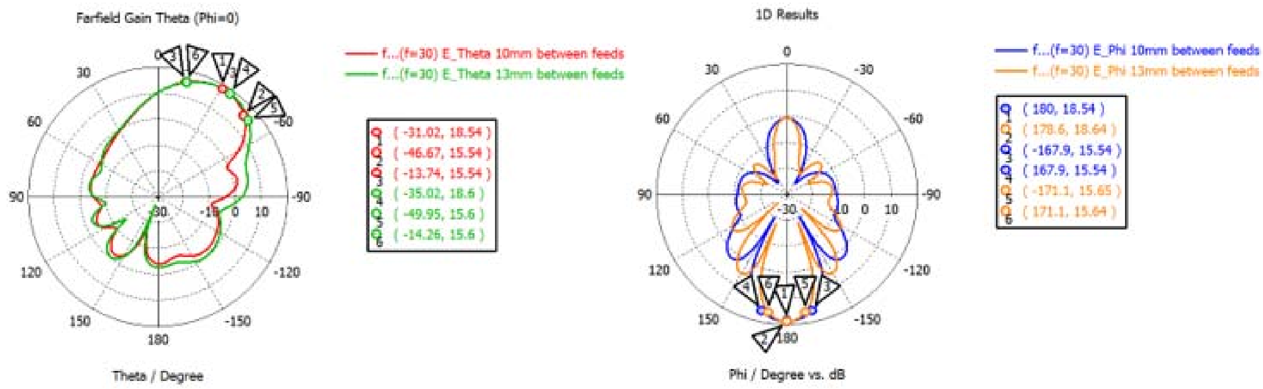

Figure 6-8: E-Theta and E-Phi pattern cuts when the distance between feeds is 10 mm and 13 mm

In Chapter 5, Table 5-2, it has been demonstrated that a maximum gain of 17 dBi can be obtained when the distance between the feeding patches is set to 13 mm and with no reflecting patches present on the reflecting substrate. As a continuation to that, Figure 6-8 shows that the presence of the reflecting patches on that structure increases the gain of the structure by 1.6 dB, from 17 dBi to 18.6 dBi.

Similarly, Figure 5-15, demonstrated that a maximum gain of 17.9 dBi can be obtained when the distance between the feeding patches is set to 10 mm and no reflecting patches are present on the reflecting substrate. As a continuation to that, Figure 6-8 shows that the presence of the reflecting patches on that structure, increased the gain by 0.6 dB only, from 17.9 dBi to 18.5 dBi.

This demonstrates that a higher distance between the feeding patches, reduces the coupling between the elements and improves the overall gain of the antenna.

Table 6-1 shows the beam swing for the two cases discussed above (i.e. when the distance between feeds is 10 mm and 13 mm, with the reflecting patches on the substrate).

Table 6-1: Beam swing capability of the antenna having the feeds spaced by 10 mm and 13 mm (the reflective substrate length is kept to 17 mm in both cases).

10mm between feeds (reflecting patches present on the 17mm reflective substrate)							
Progressive Phase (deg)	0	30	60	90	120	150	180
Phi Lobe Magnitude (dB)	18.5	18.3	17.9	17	16	14.6	13
Phi Lobe Direction (deg)	180	-172	-165	-157	-152	-147	-143
Phi 3dB BW (deg)	24.2	24.2	21.7	22.4	21	20	18.8
Phi Sidelobes (dB)	-16.3	-13.8	-11.8	-10.3	-9.2	-5.7	-8
Theta Lobe Magnitude (dB)	18.5	18.3	17.9	17	16	14.6	13
Theta Lobe Direction (deg)	-31	-32	-33	-35	-39	-43	-48
Theta 3dB BW (deg)	33	31.9	29.6	27.2	25.4	24.1	22.2
Theta Sidelobes (dB)	-17.3	-17.4	-19.3	-21.9	-19.3	-14.9	-11.7
13mm between feeds (reflecting patches present on the 17mm reflective substrate)							
Progressive Phase (deg)	0	30	60	90	120	150	180
Phi Lobe Magnitude (dB)	18.6	18.5	18.1	17.8	17.1	16	14.9
Phi Lobe Direction (deg)	180	-174	-167	-161	-156	-152	-148
Phi 3dB BW (deg)	17.9	18.5	18.7	18	17.6	17.3	16.4
Phi Sidelobes (dB)	-13.7	-12.5	-11.6	-10.8	-9.4	-3.9	-8.5
Theta Lobe Magnitude (dB)	18.6	18.5	18.1	17.8	17.1	16	14.9
Theta Lobe Direction (deg)	-33	-32	-32	-34	-36	-38	-42
Theta 3dB BW (deg)	35.5	32.8	28.3	25.2	23.1	21.5	20.3
Theta Sidelobes (dB)	-19.1	-19.8	-21	-21.9	-19.4	-15.9	-13.5

As it can be observed from the table above, between the two cases, the sidelobe levels increased with the distance between the feeds, however, during the beam swing, the main lobe magnitude decreased at a lower rate when the distance was kept to 13 mm (for example, for 120˚ progressive phase, 17.1 dBi of gain (for 13 mm between the feeds) vs 16 dBi of gain (for 10 mm between the feeds). On the other hand, even if the gain decreases quicker in the latter case, the beam appears to swing a higher range than with 13 mm distance between the feeds (-152˚ vs -156˚). This is a consequence of the array factor pattern change as the distance between the patches changes. As the distance between the elements decreases, some of the lobes of the array factor pattern widen, therefore resulting in more beam swing. Figure 6-9 below summarises the results in Table 6-1 and illustrates the tendency of the main lobe magnitude versus the beam swing angle, as explained above.

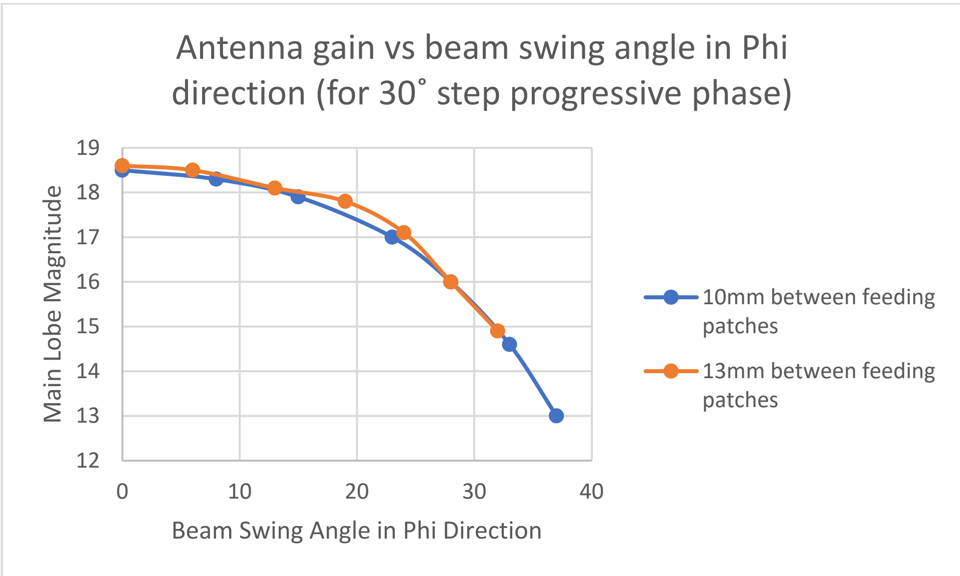

Figure 6-9: Beam swing angle in Phi direction versus the main lobe magnitude for 10 mm and 13 mm distance between the feeds.

Figure 6-10 below shows for the array element, that the presence of the reflective patches on the reflective substrate improved the gain and the radiation beamwidth. The array element without the reflective patches and its radiation pattern are illustrated in Figure 5-9 but shown in Figure 6-10 as well for comparison.

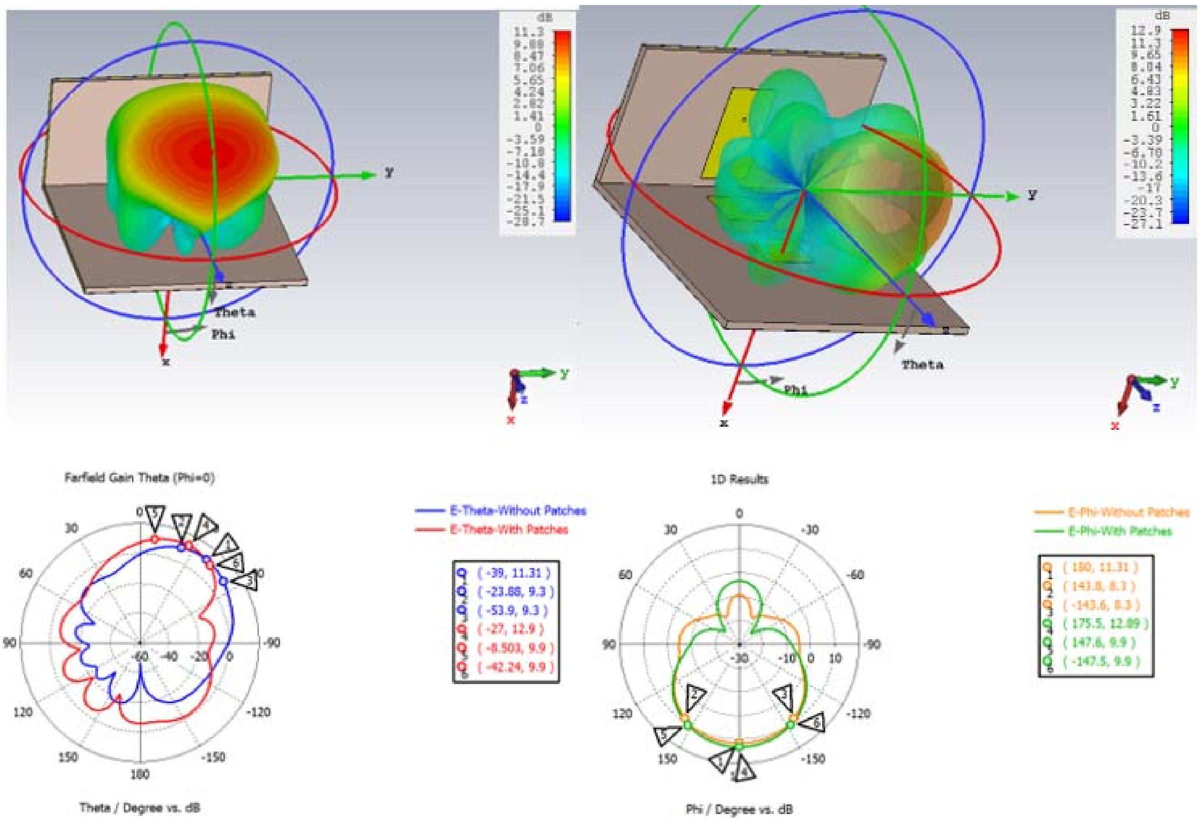

Figure 6-10: The Array Element with and without Reflective Patches and pattern cuts

6.2.2 Simulation results when the length of the reflective substrate is increased to 28 mm

In the previous subsection, it has been analysed the effect of the feeding patches separation, in the presence of the reflective patches, on the main lobe magnitude and the beam swing capability of the antenna.

In this subsection, it is desired to investigate the effect of the reflective substrate's length, in the presence of the reflective patches, on the radiation pattern. In the previous simulations, the length of the reflective substrate was kept to 17 mm. For this investigation, the length is increased from 17 mm to 28 mm (approximately 2 x λ).

Figure 6-11 shows the simulation results of the antenna having 13 mm distance between the feeds and a 28 mm long reflective substrate. Compared to the performance obtained with a 17 mm long substrate, the gain has increased only by approximately 0.2 dB, i.e. from 18.6 dBi to 18.9 dBi. The E-Theta 3 dB BW became narrower, from 35.4˚ to 28.9˚, but wider in the Phi direction from 17.8˚to 23.1˚. The total efficiency of the antenna is approximately 88%.

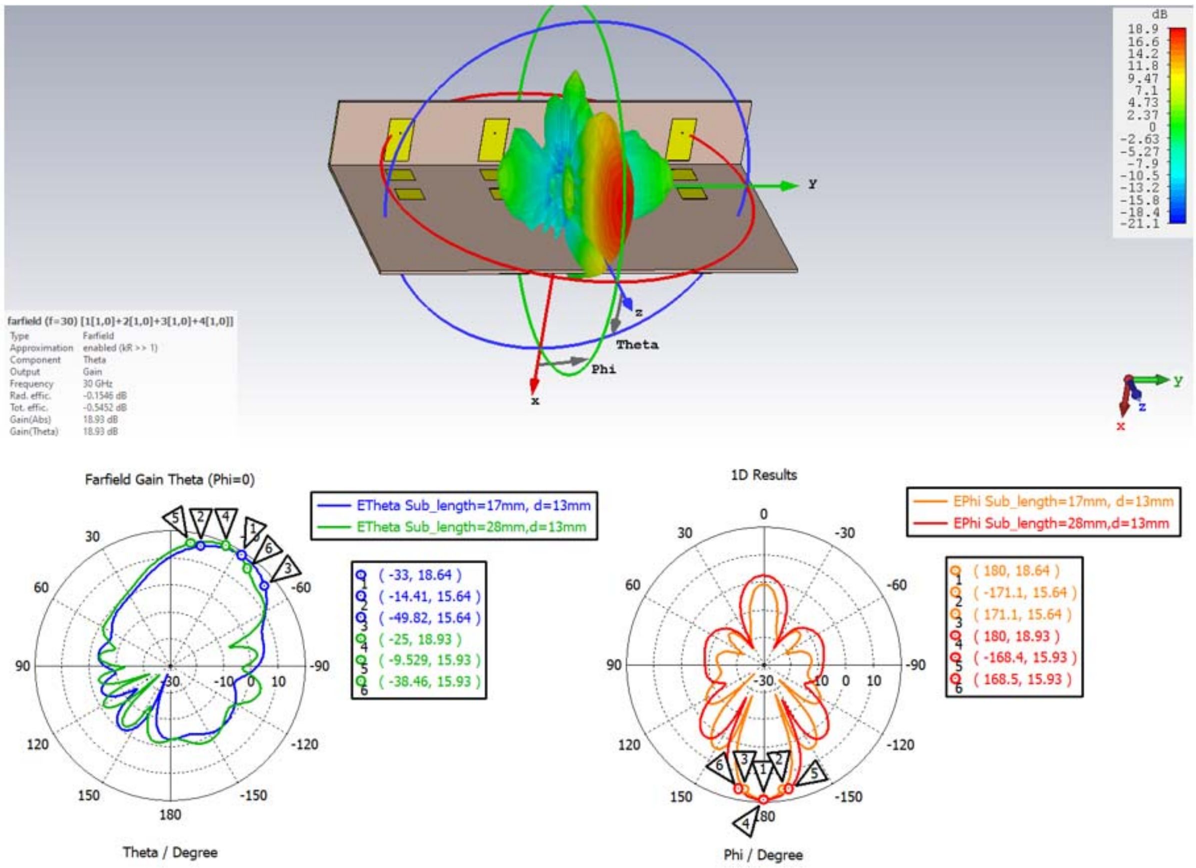

Figure 6-11: Structure with 13 mm between the feeding patches, with reflective patches and 28 mm reflective substrate

Similarly, Figure 6-12 shows the simulation results of the antenna having 10 mm distance between the feeds, but a 28 mm long reflective substrate. In this case, the gain has increased only by 0.3 dB i.e. from 18.5 dBi to 18.8 dBi. As in the previous case, the E-Theta 3 dB BW became narrower from 32.94˚ to 27.64˚, but in Phi direction, the BW increased from 27.64˚ to 29.4˚. The total efficiency of the antenna is approximately 69%.

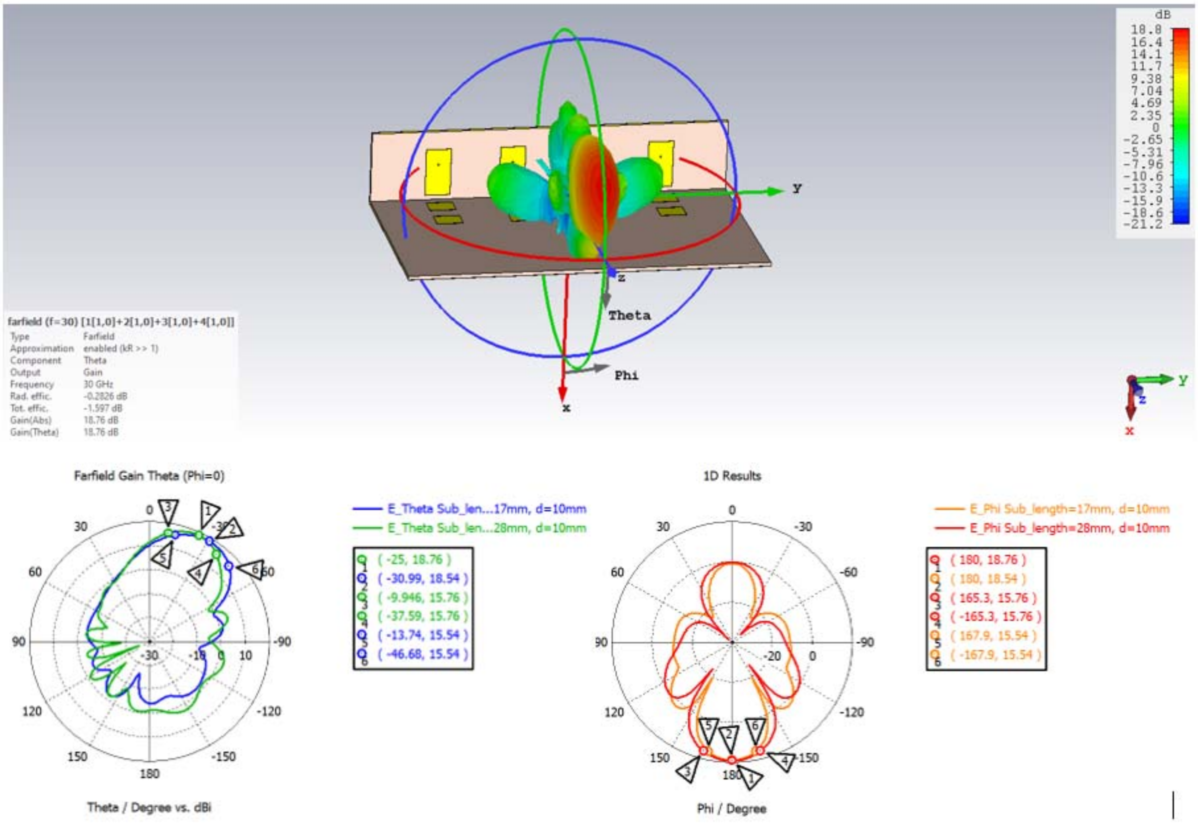

Figure 6-12: Structure with 10 mm between the feeding patches, with reflective patches and 28 mm reflective substrate

In both cases described above, the increase in length of the reflective substrate improved the gain only by approximately 0.2-0.3 dB. This small gain improvement can be due to the surface waves which may scatter from the edges of the reflective substrate or may reflect back from the end of the reflective substrate and get radiated by the reflecting patches. By increasing the length of the reflective substrate, the phase of the scattered/reflected waves changes, and this may contribute to the slight improvement of the antenna gain.

To check the contribution of the radiating patches to the radiation pattern, the structures from Figures 6-11 and 6-12 have been also simulated without the reflecting patches. For the structure with 10 mm between the feeding patches, the simulation results are presented in Figure 6-13, and compared to the simulation results of the structure containing the reflective patches.

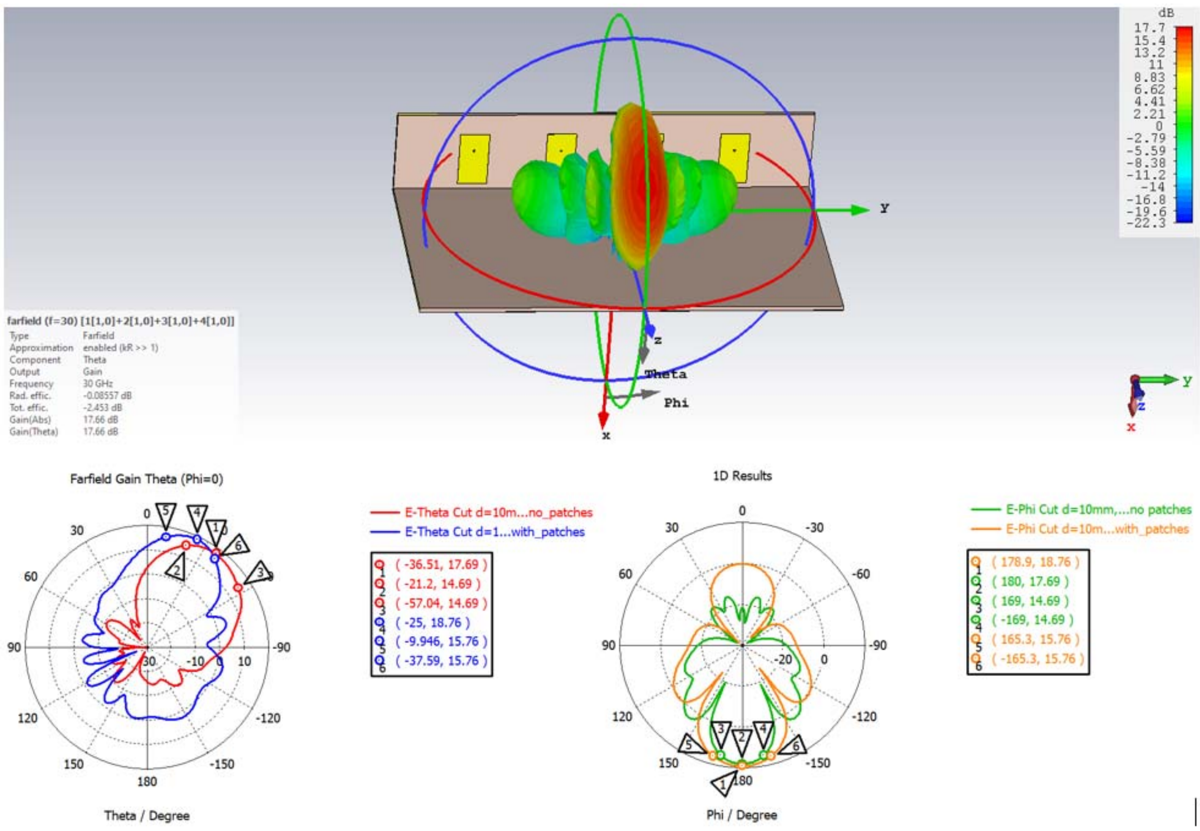

Figure 6-13: Structure with 10 mm between the feeding patches, with no reflective patches and 28 mm reflective substrate

As it can be observed in Figure 6-13, the presence of the radiating patches improves the gain by 1 dB, from 17.7 dBi 18.7 dBi, and the E-Theta 3 dB beamwidth decreases from 35.8˚ to 27.6˚. However, the presence of the patches increases the E-Phi 3 dB beamwidth from 22˚ to 27.2˚.

Similarly, for the structure with 13 mm between the feeding patches, the simulation results are presented in Figure 6-14, which are also compared to the simulation results of the structure including the patches. In this case, the reflecting patches improved the gain by 2.33 dB, from 16.6 dBi to 18.9 dBi. Similar to the previous case, the E-theta 3 dB beamwidth decreased from 44˚ to 29˚ and E-Phi 3 dB beamwidth increased from 18˚ to 27.3˚.

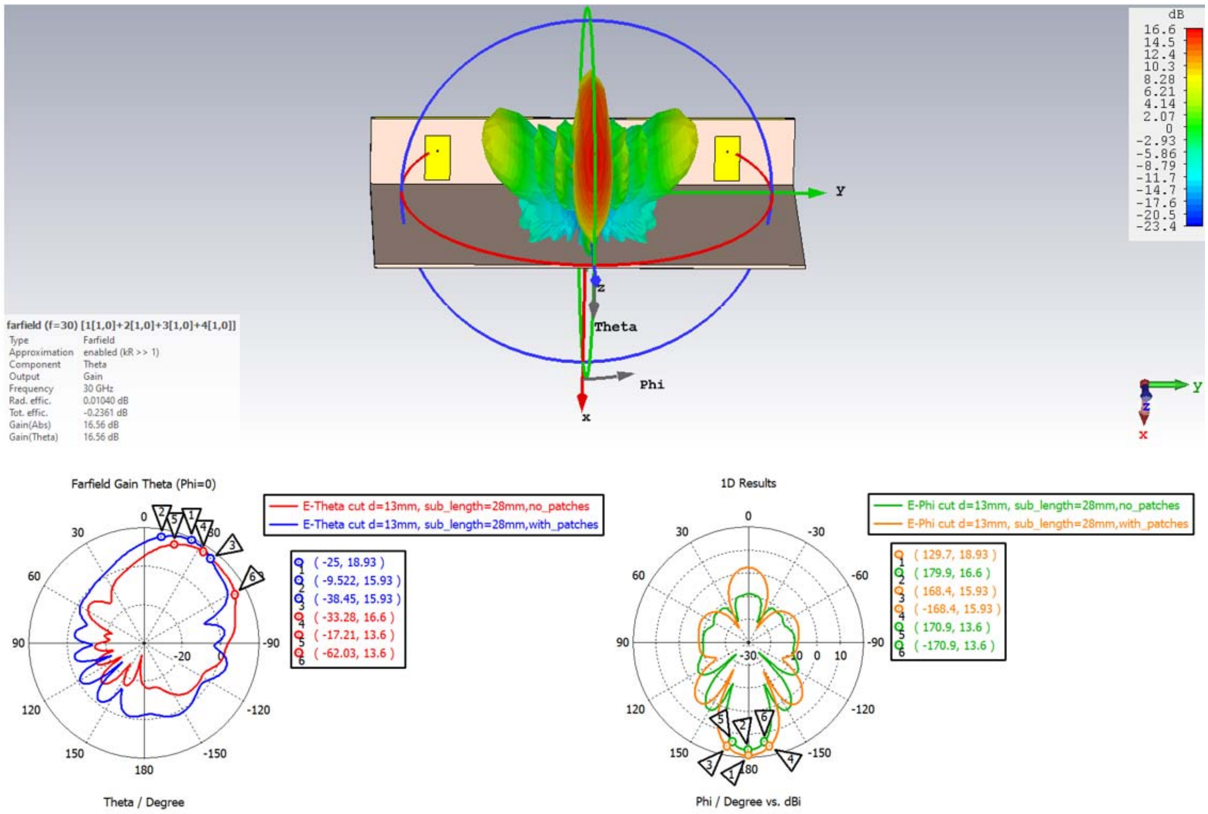

Figure 6-14: Structure with 13 mm between the feeding patches, with no reflective patches and 28 mm reflective substrate

Up to this point, the two structures, presenting 10 mm and 13 mm separation between the feeding patches and a 28 mm long substrate, provide more or less the same gain, i.e. 18.7 dBi and 18.9 dBi. In order to decide which antenna performs better, the beam swing capability of the two needs to be analysed.

In the next subsection, the beam scanning capability in Phi direction for the two antennas is analysed, similar to the analysis done in Section 6.2.1.

6.2.3 Beam swing capability of the structures having 10 mm and 13 mm spaced feeding patches and 28 mm reflective substrate with reflecting patches

The structures shown in Figures 6-11 and 6-12 have been simulated with different progressive phases at the input of the patches. The simulation results are summarised in Table 6-2.

As the beam is steered, the main lobe magnitude decreases more rapidly when the distance between the patches is 10 mm. For example, at 120˚ progressive phase, the main lobe decreases by approximately 2.5 dB, and gives a steering range of 32˚ on each side of the structure (64˚ in total).

However, for 13 mm between patches, the main lobe magnitude decreases only by about 2 dB, for the same progressive phase, but it gives a steering range of 27˚ only on each side (54˚ in total). Shortly said, the structure in Figure 6-12 achieves with 120° progressive phase what the structure in Figure 6-11 achieves at 150° progressive phase, however at the expense of having a lower gain.

Based on the results presented in Table 6-2, Figure 6-15 summarises the beam swing angle versus gain, as explained above.

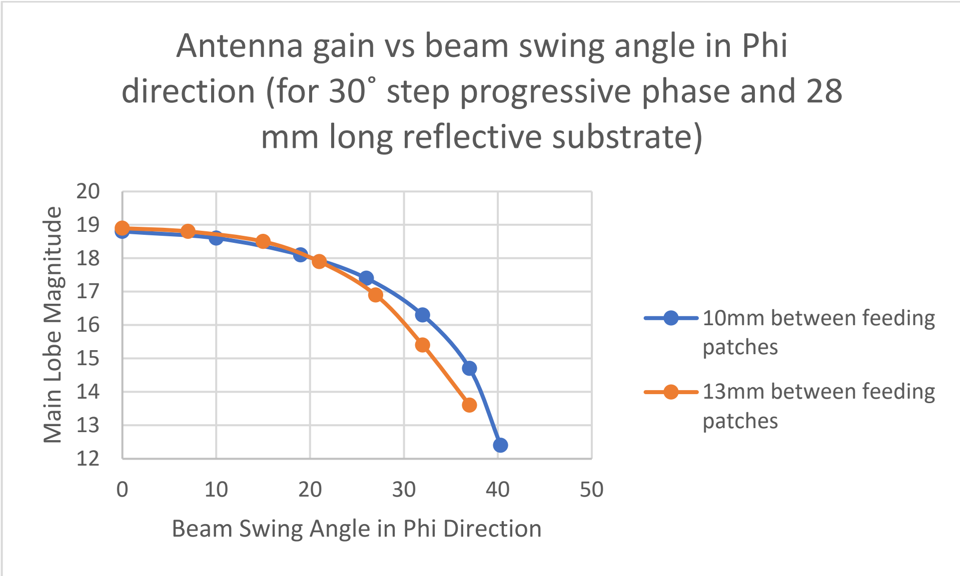

Figure 6-15: Antenna gain vs beam swing angle for a 28 mm long reflective substrate antenna

If judging by the steering capability of the two cases, for the first case (13 mm distance between feeds) with 140˚ progressive phase, where the beam drops by 3 dB (to 15.9 dB), the beam steers 62˚ in total. For the second case (10 mm between the feeds), a progressive phase of 130˚ makes the beam to drop by 3 dB (to 15.8 dB) and a beam steer angle of 66˚ is obtained.

The beam swing and the radiation patterns are illustrated in Figure 6-16, for the case when the distance between patches is 13 mm. The progressive phases used at the input of the patches are: 0°, 30°, 60°, 90°, 120°, 150°, 180°

Table 6-2: Beam swing capability of the antennas having 10 mm and 13 mm distance between the feeds and a 28 mm reflective substrate

10mm between feeds (reflecting patches present on the 28mm reflective substrate)							
Progressive Phase (deg)	0	30	60	90	120	150	180
Phi Lobe Magnitude (dB)	18.8	18.6	18.1	17.4	16.3	14.7	12.4
Phi Lobe Direction (deg)	180	-170	-161	-154	-148	-143	-139.7
Phi 3dB BW (deg)	29.4	27.7	27.8	25.5	24.1	22.9	21
Phi Sidelobes (dB)	-18.4	-14	-12	-10.5	-9.7	-7.8	-8.5
Theta Lobe Magnitude (dB)	18.8	18.6	18.1	17.4	16.3	14.7	12.4
Theta Lobe Direction (deg)	-25	-25	-27	-30	-33	-37	-41
Theta 3dB BW (deg)	27.6	26.6	24.4	22.5	21.1	20.5	19
Theta Sidelobes (dB)	-14.9	-16.7	-17.2	-17.9	-18.3	-13.3	-9.5

13mm between feeds (reflecting patches present on the 28mm reflective substrate)							
Progressive Phase (deg)	0	30	60	90	120	150	180
Phi Lobe Magnitude (dB)	18.9	18.8	18.5	17.9	16.9	15.4	13.6
Phi Lobe Direction (deg)	180	-173	-165	-159	-153	-148	-143
Phi 3dB BW (deg)	23	21.7	21.4	21.2	20.7	20.3	19.6
Phi Sidelobes (dB)	-14.9	-13.1	-12	-11.2	-10.3	-5	-8.3
Theta Lobe Magnitude (dB)	18.9	18.8	18.5	17.9	16.9	15.4	13.6
Theta Lobe Direction (deg)	-25	-25	-26	-27	-29	-31	-35
Theta 3dB BW (deg)	29	26.8	23.3	20.3	18.4	17.5	16.3
Theta Sidelobes (dB)	-15.1	-18.2	-18.3	-18.6	-18.2	-13.8	-10.7

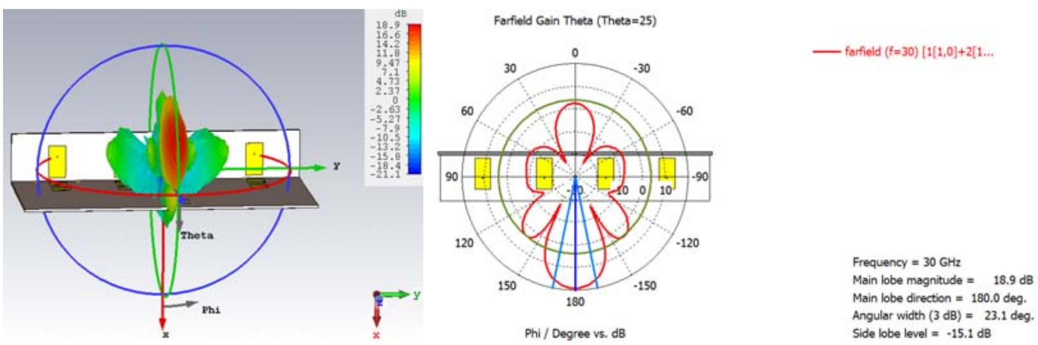

(a)

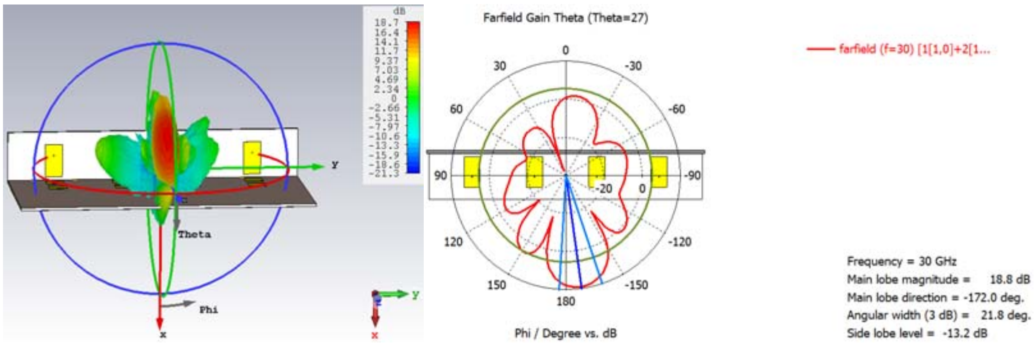
Farfield Gain Theta (Theta=27)
farfield (f=30) [1[1,0]+2[1...
Phi / Degree vs. dB
Frequency = 30 GHz
Main lobe magnitude = 18.8 dB
Main lobe direction = -172.0 deg.
Angular width (3 dB) = 21.8 deg.
Side lobe level = -13.2 dB

(b)

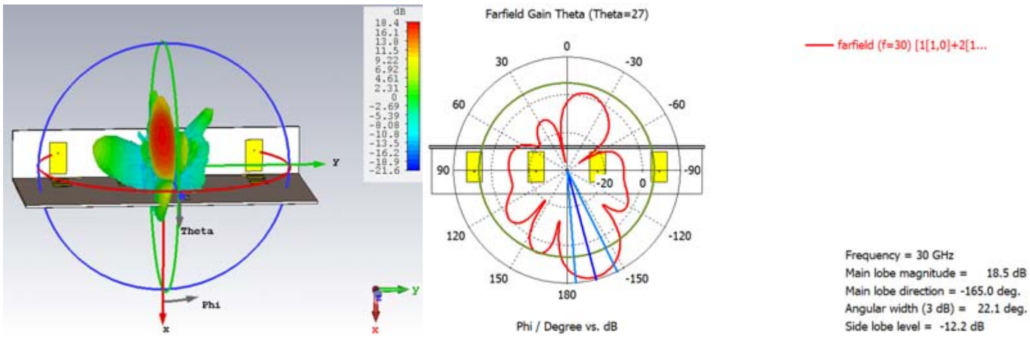
Farfield Gain Theta (Theta=27)
farfield (f=30) [1[1,0]+2[1...
Phi / Degree vs. dB
Frequency = 30 GHz
Main lobe magnitude = 18.5 dB
Main lobe direction = -165.0 deg.
Angular width (3 dB) = 22.1 deg.
Side lobe level = -12.2 dB

(c)

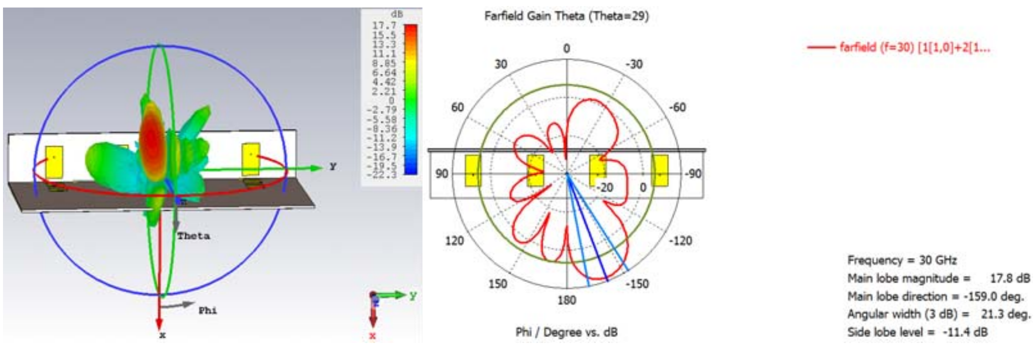
Farfield Gain Theta (Theta=29)
farfield (f=30) [1[1,0]+2[1...
Phi / Degree vs. dB
Frequency = 30 GHz
Main lobe magnitude = 17.8 dB
Main lobe direction = -159.0 deg.
Angular width (3 dB) = 21.3 deg.
Side lobe level = -11.4 dB

(d)

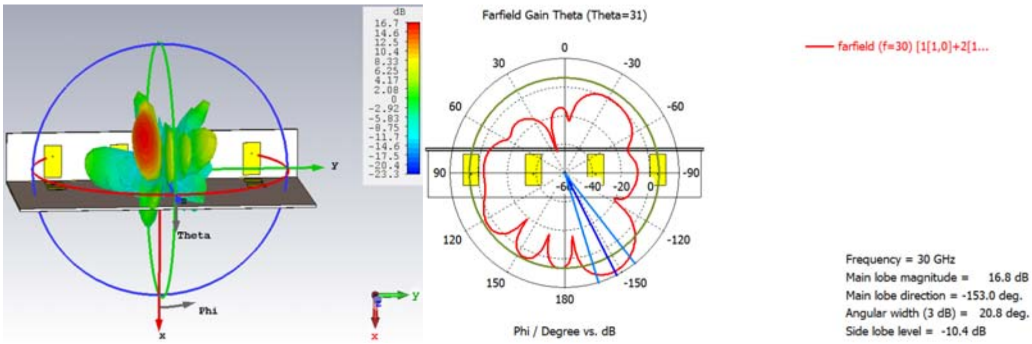

(e)

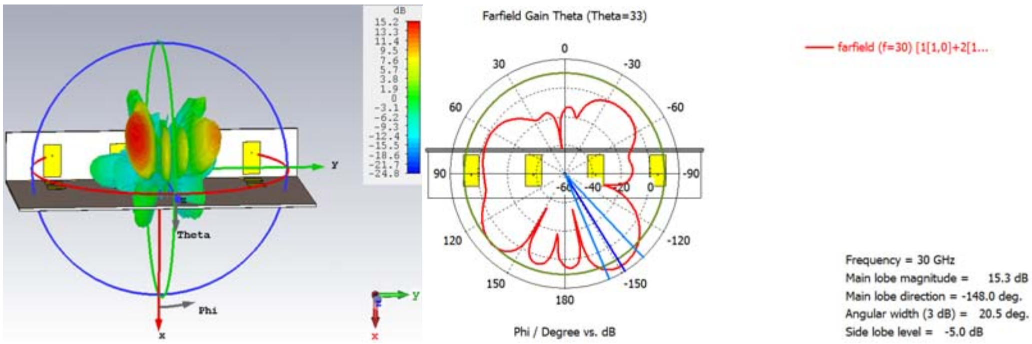

(f)

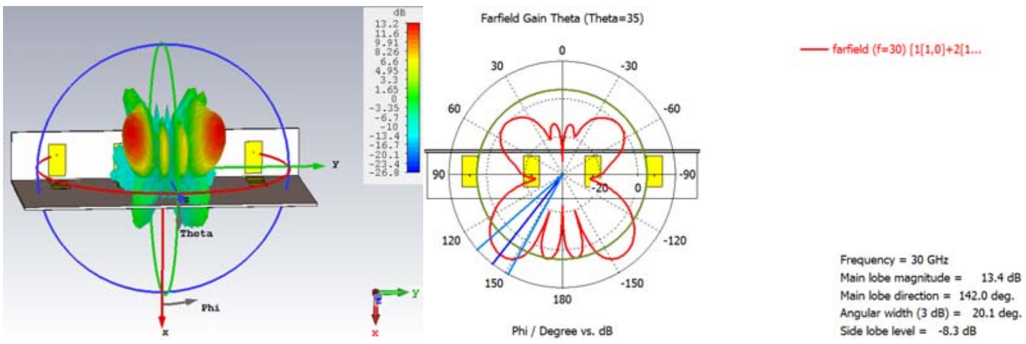

(g)

Figure 6-16: Beam swing in azimuth when progressive phase is introduced (0°, 30°, 60°, 90°, 120°, 150°, 180° and 13 mm between patches)

6.2.4 Investigations on beam steering capability in elevation

In the previous section, it has been shown that by imposing progressive phase shift at the input of the feeding patches, the beam can be steered more than 54˚ in Azimuth (27˚ on each side for a 2 dB drop in gain). It is desirable to obtain the same steering range in Elevation, ideally. In this section, this possibility will be explored by adding one extra row of feeding patches, above the existing ones.

The structure presented previously was comprised of four feeding patches attached to a radiating substrate which was populated with radiating patches, as shown in Figure 6-16. It provided a radiation pattern with a maximum gain of 18.9 dB and a relative sidelobe level of –15 dB in Theta Direction. The beam can be steered to more than 54˚ in the ZY plane, but at the expense of the gain loss and higher sidelobes levels. For example, for a 3 dB lower gain (15.9 dB), and a relative sidelobe level of -7.9 dB, the beam could be steered ± 31˚, using a progressive phase shift of ± 140˚.

To sweep the beam in the other principal plane (XZ plane), a second set of feeds must be introduced on top of the existing ones, to form a 2D array, capable of steering the beam two dimensionally.

Figure 6-17 shows the antenna structure containing the 2 sets of 4 feeding patches. The vertical distance between the patches is 9.5 mm and the horizontal distance is 13 mm.

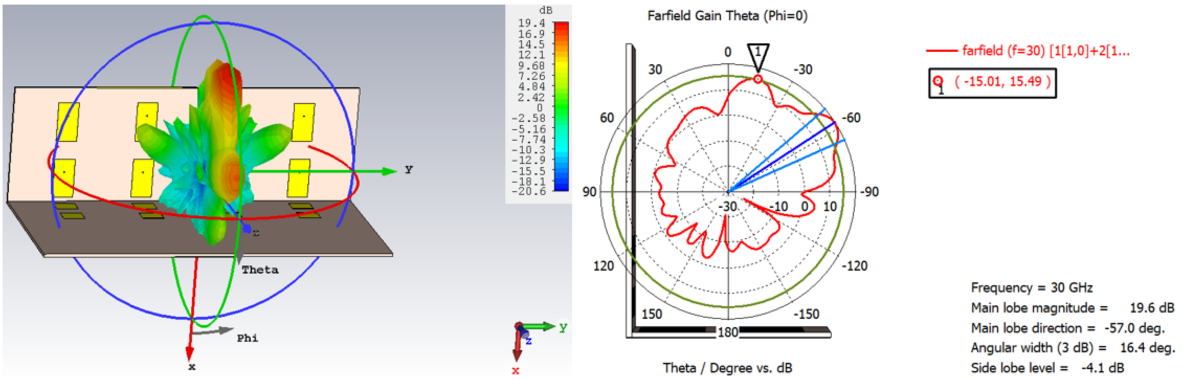

Figure 6-17: 8 feeding patches structure, with 13 mm horizontal distance and 9.5 mm vertical distance

The radiation pattern shown in Figure 6-17 indicates two uncollimated lobes: one produced by the initial set of feeds, and the other lobe produced by the top set of the feeding patches. The E-theta pattern cut shows the direction of the two beams: one pointing to -15˚ and the other to about -57˚ relative to the horizon line (θ=0˚).

The radiation pattern of only one array element containing two vertical patches, with reflective substrate and patches is presented below, in Figure 6-18. As it can be observed, the two uncollimated beams are pointing towards the same direction as above: -15˚ and -57˚. Figure 6-19 shows the radiation pattern produced by each feeding patch, separately.

The top pattern is produced by the lower feed and this is collimated into a single beam pointing towards -27˚, with 26.8˚ 3 dB beamwidth. The lower pattern shown in Figure 6-19 is produced by the top feed and it consists of two separated beams, pointing towards -34˚ and -60˚ respectively. The two patterns combine in phase in such a way that it results the two separated beams at -15˚ and -57˚.

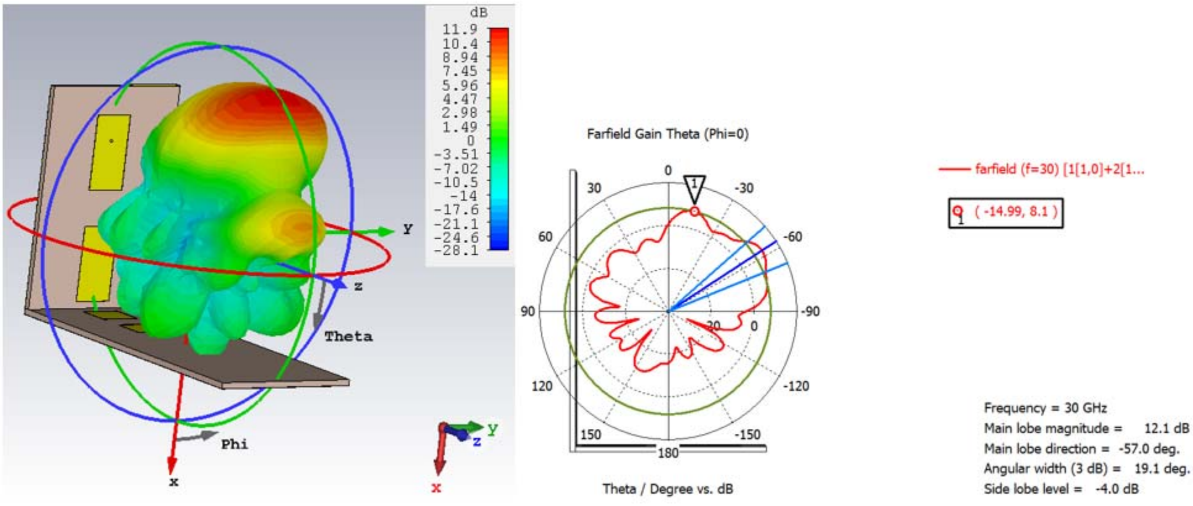

Figure 6-18: One element array radiation pattern and E-Theta cut

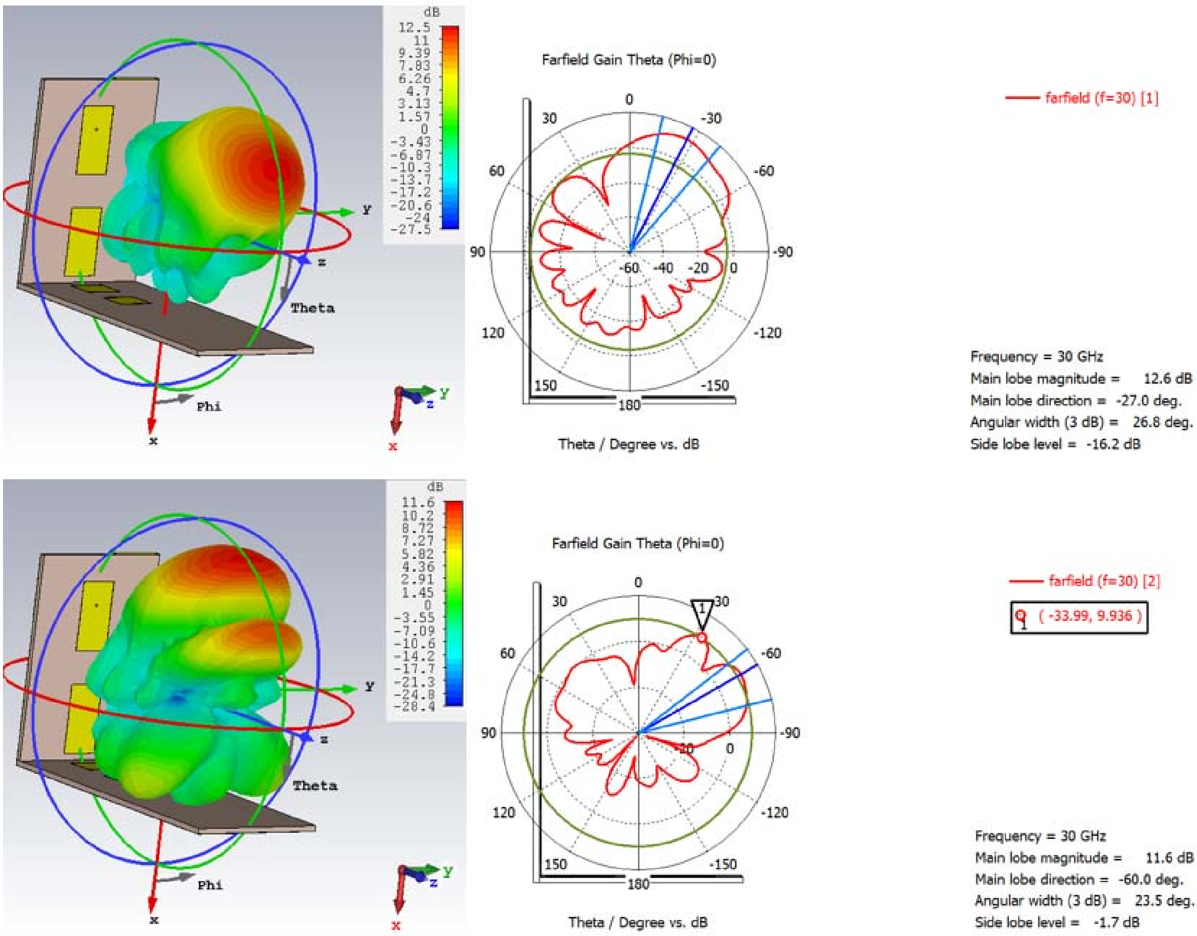

Figure 6-19: Radiation pattern produced by each feeding patch: top pattern produced by the bottom feed and the bottom pattern produced by the top feed

Ideally, the two beams shown in Figure 6-18 should combine into a single beam, but they are not. The two angles should combine in phase as well.

One method of controlling the collimation of the two beams is through the distance between the vertical patches. In Figure 6-17, the distance between the vertical patches is 9.5 mm. Table 6-3 presents the simulation results of the structure in Figure 6-17, for different distances between the vertical patches.

Table 6-3: Distance between vertical patches vs lobes levels

Distance (mm)	Lobe 1 gain (dBi)	Lobe 1 direction (deg)	Lobe 2 gain (dBi)	Lobe 2 direction (deg)
9.5	15.5	-15	19.5	-57
10	14.95	-14	19.8	-56
10.5	14.47	-13	19.9	-55
11	14.09	-12	19.6	-53
11.5	13.78	-12	19.3	-50
12	13.45	-12	19.2	-48
12.5	13.2	-12	19.1	-46
13	13	-12	19.1	-44

As it can be observed, as the distance between the vertical patches increases, the small beam decreases very slowly in gain and the main beam increases in gain up to a point. At 10.5 mm separation between the patches, the sidelobe level decreases only to 14.47 dB and the main lobe increases to 19.9 dB. The radiation pattern and pattern cut are illustrated in Figure 6-20.

The second method of controlling the collimation of the two beams should be through the use of radiating patches. By changing the dimensions of the patches, the phase of the reflected wave changes. It has been observed that by decreasing the length of the reflective patches, the level of the lower beam in Figure 6-18 decreases, and the gain of the main beam increases. Patch length versus beam levels are presented in Figure

6-21.The relative level of the sidelobe decreased to 10.4 dB when the reflective patches were removed. This suggests that the sidelobe was not produced by the reflective patches, but by the top feeding patches. Without the reflective patches, the gain increased to 20.5 dB, and the 3 dB beamwidth was 18.3˚. The presence of the patches increased the gain only to 20.6 dB.

As the length of the reflective patches decreased, the main lobe level increased up to 20.6 dB, obtained with 2.6 mm patches. As the length continued to decrease, the main lobe level remained at 20.6 dB, however, the sidelobe level continued to decrease to 10.65 dB, obtained with 2.0 mm patches.

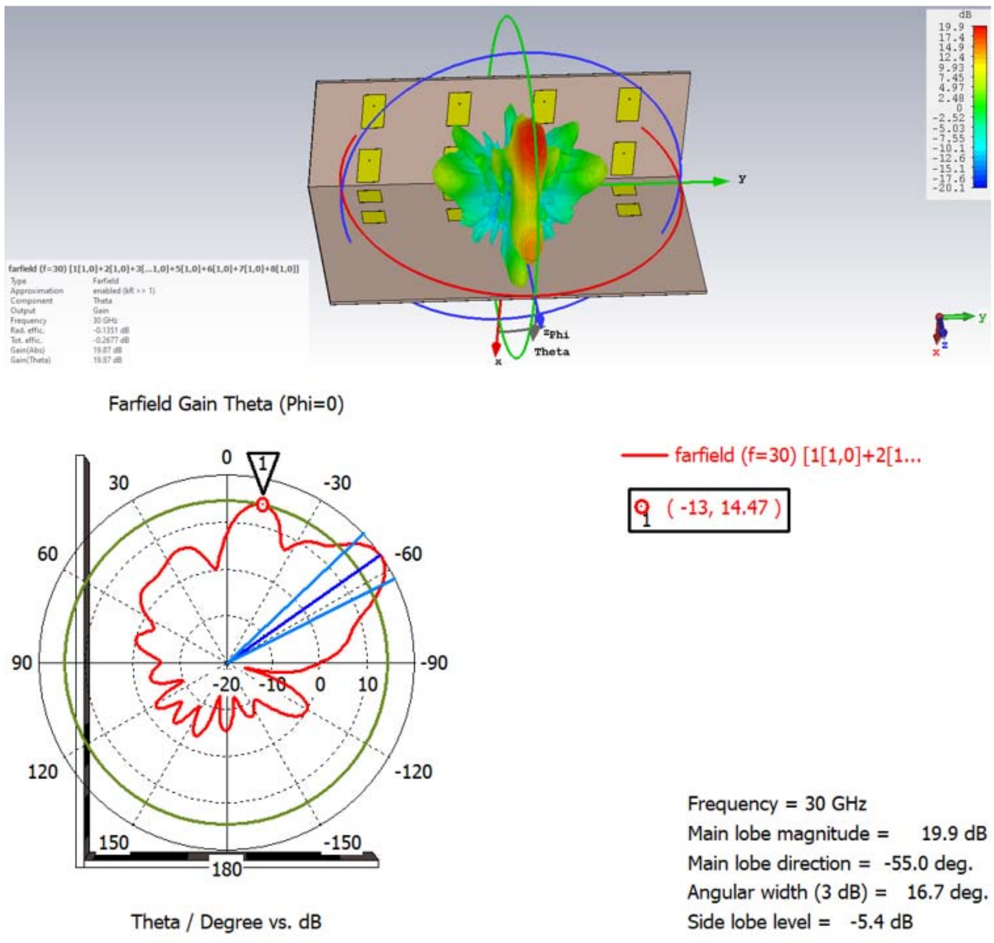

Figure 6-20: 10.5 mm distance between vertical patches, radiation pattern and E-Theta pattern cut

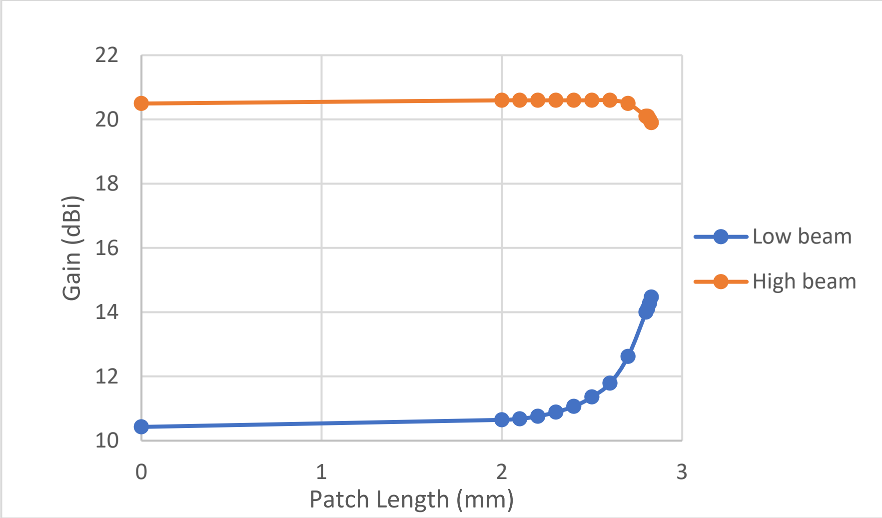

Figure 6-21: Patch Length versus beams gain

The array element containing two vertical patches spaced by 10.5 mm (with 2.83 mm reflective patches) is presented in Figure 6-22, together with the radiation pattern and the E-theta pattern cut.

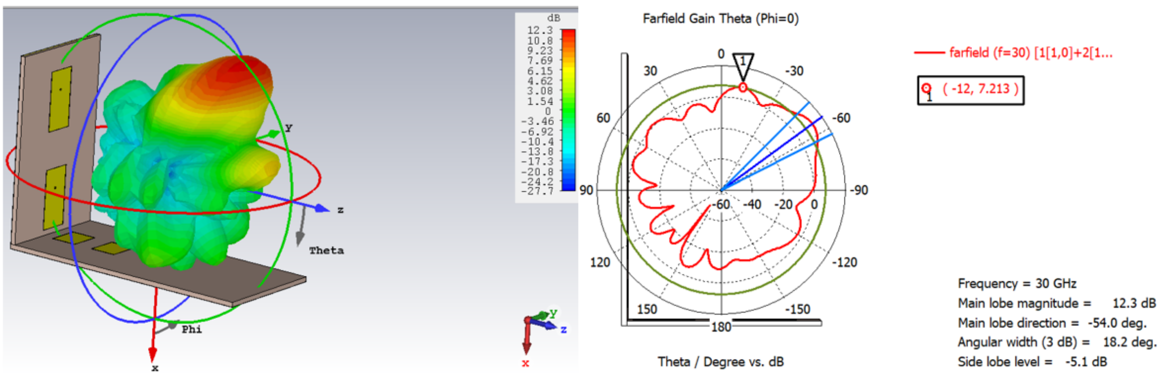

Figure 6-22: Array element with 10.5 mm distance between the vertical patches

Compared to the pattern in Figure 6-18 (where the distance between vertical patches was 9.5 mm and with 2.83 reflective patches), with 10.5 mm between the patches, the minor lobe relative level decreased from 8.1 dB to 7.2 dB and the main lobe magnitude increased fractionally from 12.1 dB to 12.3 dB.

The radiation pattern of the array element combined with the radiation pattern of the array factor produces the final radiation pattern of the structure. The pattern cuts of the array factor are shown in Figure 6-23. By looking at the Array Factor pattern, it can be observed that the Theta pattern cut represents a perfect 6 dB circle, therefore, both the lower and higher-level lobes will increase in value by the same amount, i.e. 6 dB, therefore it is impossible to fully reduce the sidelobe level.

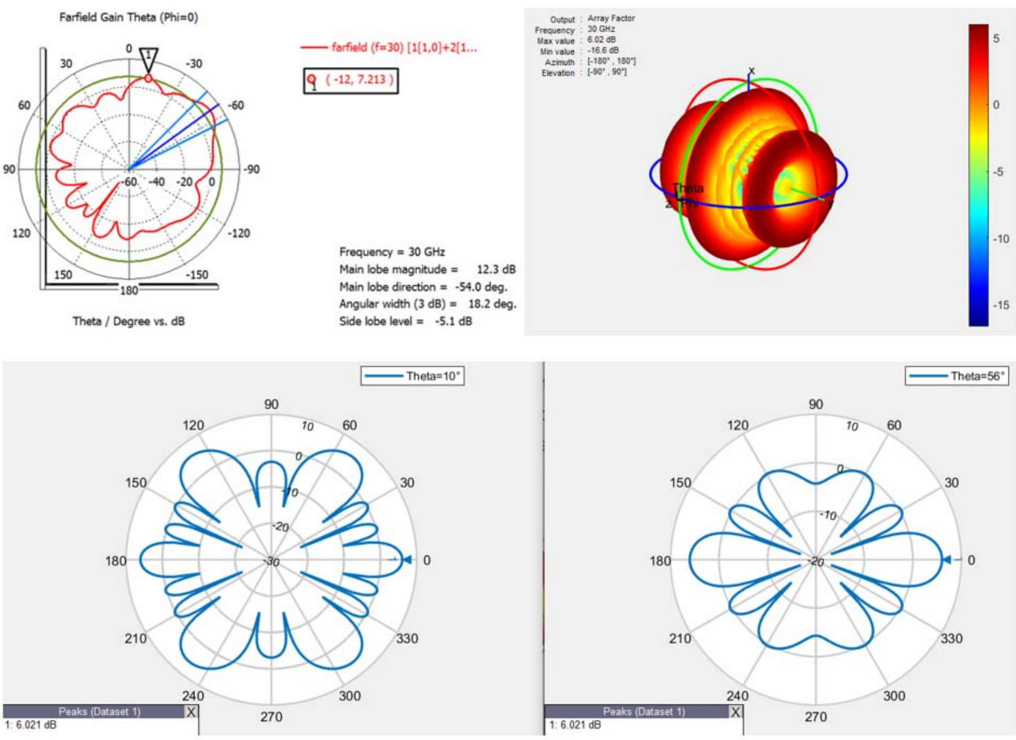

Figure 6-23: Array Factor Pattern and the Azimuth (Phi) cuts at 10˚ and 56˚ elevation (Theta) angles

The higher gain beam can be steered in the XZ direction by introducing a progressive phase between the vertical patches. This is exemplified with the structure containing 2.2 mm reflective patches, below, in Figure 6-24.

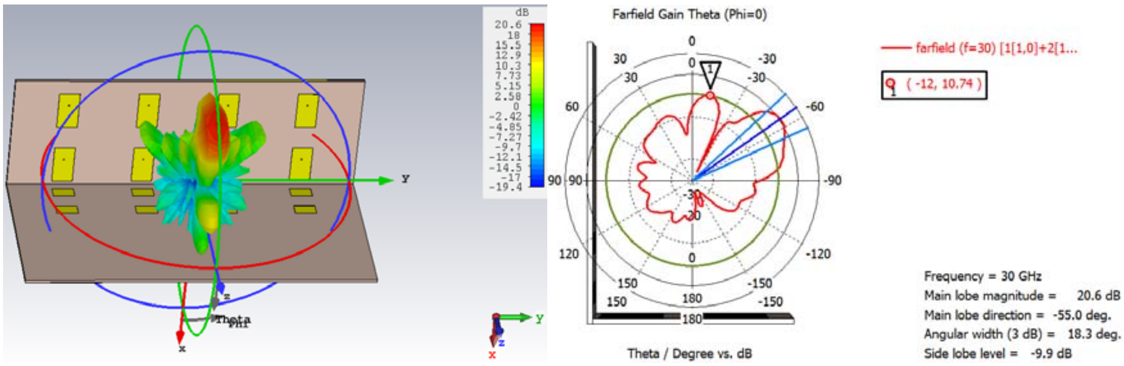

(a)

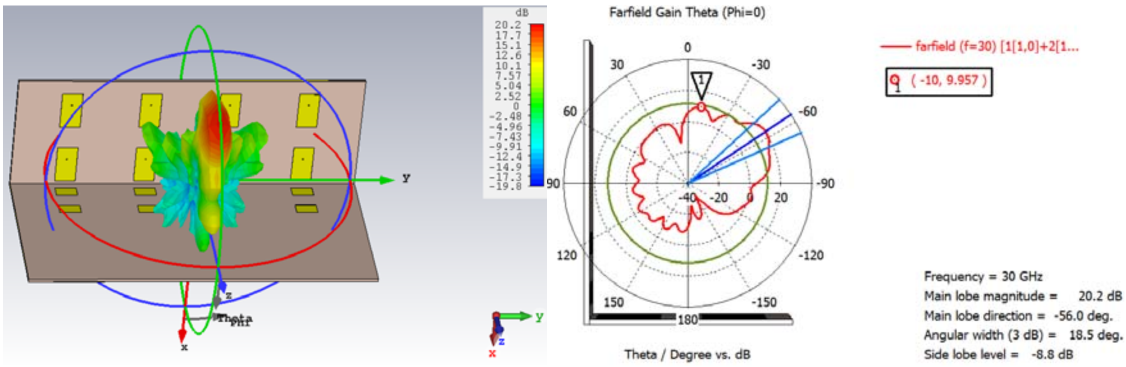

(b)

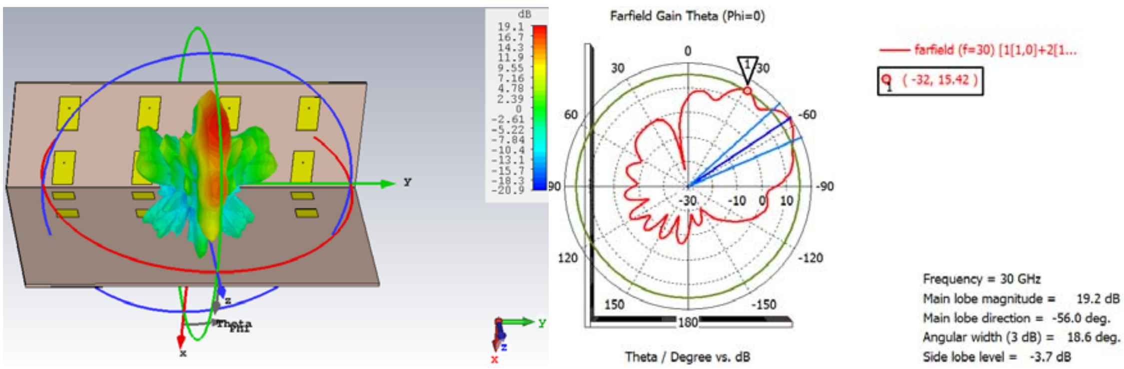

(c)

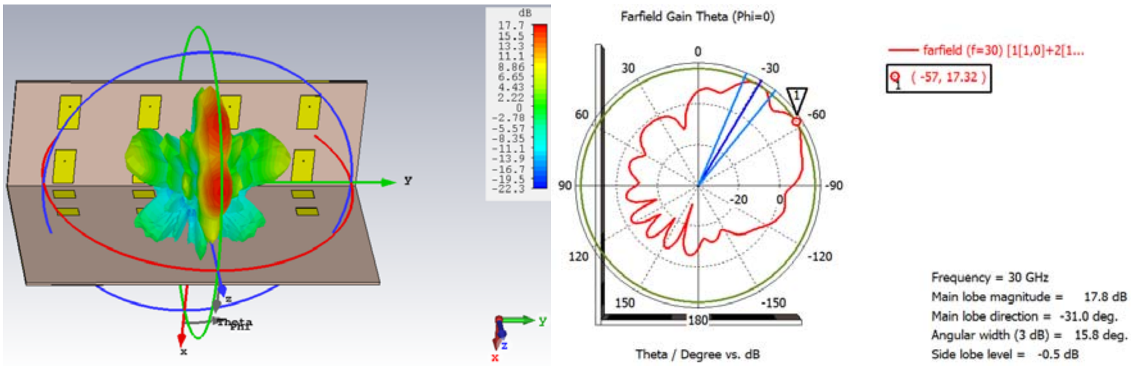

(d)

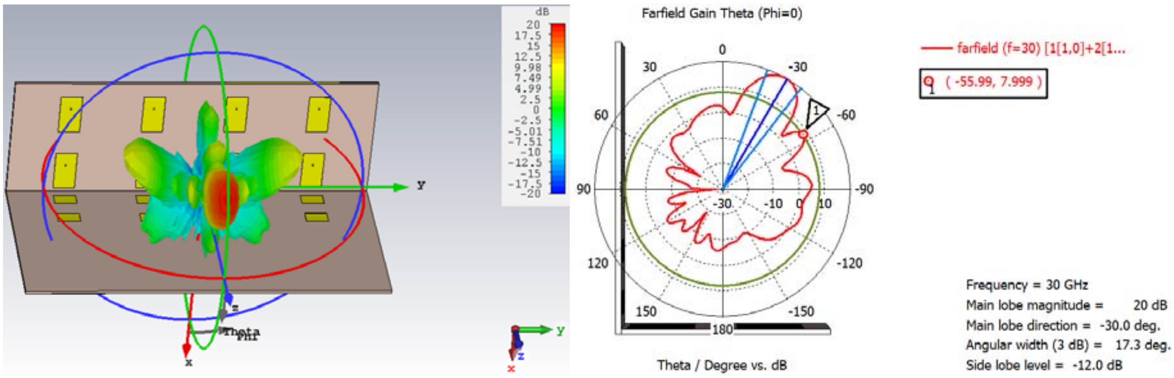

(e)

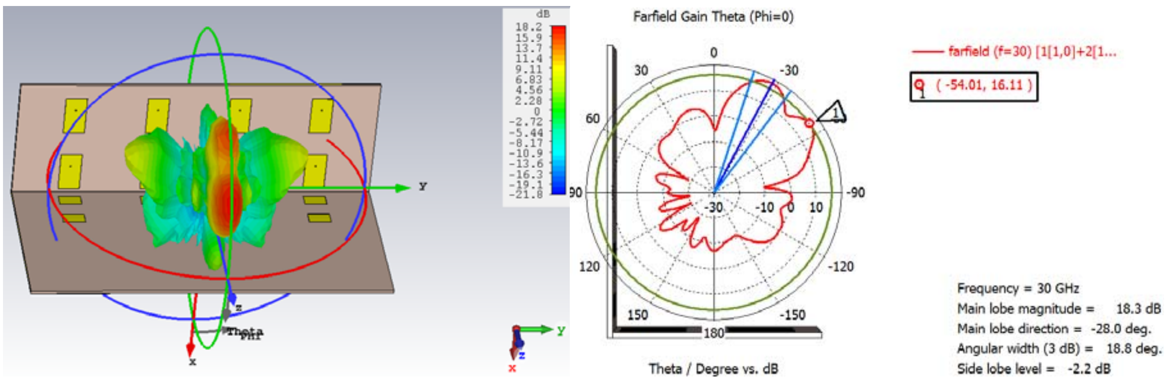

(f)

Figure 6-24: Beam shifting in elevation with 0˚,30˚,60˚,90˚,180˚ and 240˚ phase shift between the vertical patches.

It was observed that by introducing the phase difference between the vertical patches, the beam jumped between 28˚ and 55˚, for 240˚ and 0˚ phase shift respectively and there was not a smooth beam travelling between the two angles.

The length of the reflective patches has been chosen to provide the lowest sidelobe level at 0˚ progressive phase input at the feeding patches, however, when the progressive phase is increased, the sidelobe increases until it becomes the main lobe and the main lobe decreases until it becomes a sidelobe.

Introducing the phase progress the input of the patches is equivalent to having different size reflective patches, therefore the sidelobe level will increase or decrease accordingly.

The 2.83 mm reflective patches were suitable for the lower set of the feeding patches, however, not optimal for the feeding patches set above them. 2.2 mm patches appeared to be a good compromise for the two sets of the feeding patches, however, that changed when the progressive phase was introduced.

In consequence, due to the radiation pattern of the array element and the array factor pattern, the lower sidelobe cannot be eliminated completely. As the progressive phase is changed between the vertical patches, the main beam jumps between the angle of the low sidelobe and the angle of the main lobe, without having a smooth transition between the two angles.

7. Antenna testing

This chapter concerns with evaluation of the scaled (around 10 GHz) version of the 30 GHz antennas designed and analysed in the previous chapters. They are built and measured in an appropriate industrial anechoic chamber. The scaling is done for the sake of simplicity in fabrication, cost issues, and the availability of an industrial measurement facility. Where possible, the results of the scaled versions are compared to the simulation results at mm-waves presented in Chapters 6 and 5, and based on these a set of conclusions are made.

A set of 5 antennas were built in total:

- One single antenna patch operating in the second mode;
- One single patch attached to a reflecting substrate which will show the effect of the ground on the radiation pattern;
- Two and four antenna patch arrays with the reflecting substrate attached;
- Four antenna patch arrays with reflecting substrate and reflect array to show enhancement in the gain;
- Four antenna patch arrays with reflecting substrate and reflect array plus phase shifters to show the beam steering.

The antennas were built at the University of Essex and tested in the Surrey Satellite Technology (SSTL) anechoic chamber by the author of this thesis. The chamber presents an HF907 double ridged waveguide horn reference antenna, which operates between 800 MHz and 18 GHz. As a result, the four-feeding patch antenna array was scaled to operate from 30 GHz to 10 GHz. This is equivalent to a size increase of order 3 (if keeping the same dielectric constant for the substrates).

7.1 Feeding Patch Antenna

The scaled patch was simulated and the results at 10 GHz were found very similar in nature to the results obtained in the previous chapters at 30 GHz.

It was observed that the scaled SMA connector did not match the dimensions of a commercial one. The factors that determine the impedance of a coaxial cable are: pin diameter, dielectric diameter and dielectric constant.

A commercial SMA connector type that operates at 10 GHz was modelled and considered in the simulations. For example, the Huber and Suhner 50Ohm SMA connector 23"SMA-50-0-13/111"NE operates up to 18 GHz and can be used as an input connector for the microstrip patch. Thus, the Pin diameter must increase to 1.28 mm, and the dielectric (PTFE) diameter to 4.1 mm. This gives an impedance of 48.2Ω.

By changing the dimensions of the SMA connector, and the length of the central conductor, the resonant frequency of the whole antenna drifts, therefore the feeding patch length has been trimmed from 19.23 to 19.03 mm and the feeding point moved from 6.5 mm to 6.3 mm, to bring the resonant frequency closer to 10 GHz.

The built feeding patch and the anechoic chamber set-up for measurement are illustrated in Figure 7-1.

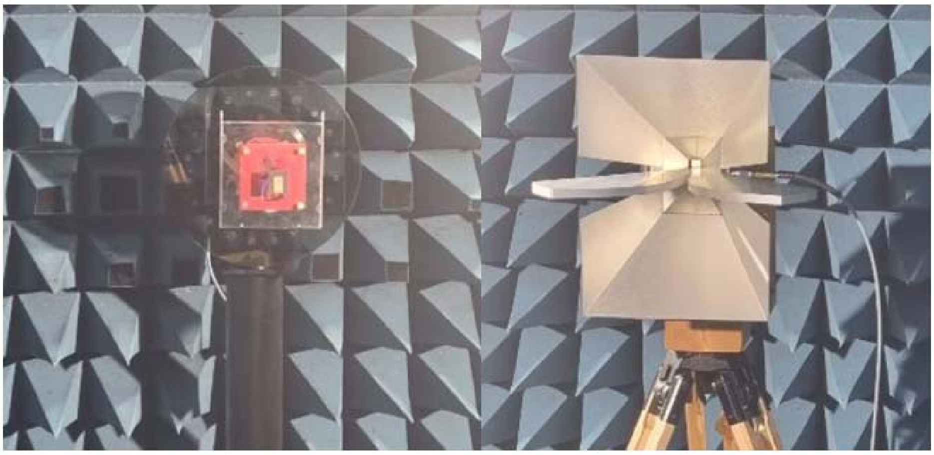

Figure 7-1: The microstrip patch antenna under test and the reference horn antenna

Figure 7-2 illustrates the simulated versus measured return Loss of the patch antenna. The labels in the figure indicate the resonant frequencies and the 10 dB bandwidths. As it can be observed, the measured frequency is shifted by approximately 100 MHz, which is due to built tolerances. The 10 dB bandwidth is approximately the same (approximately 3.2%) in both cases.

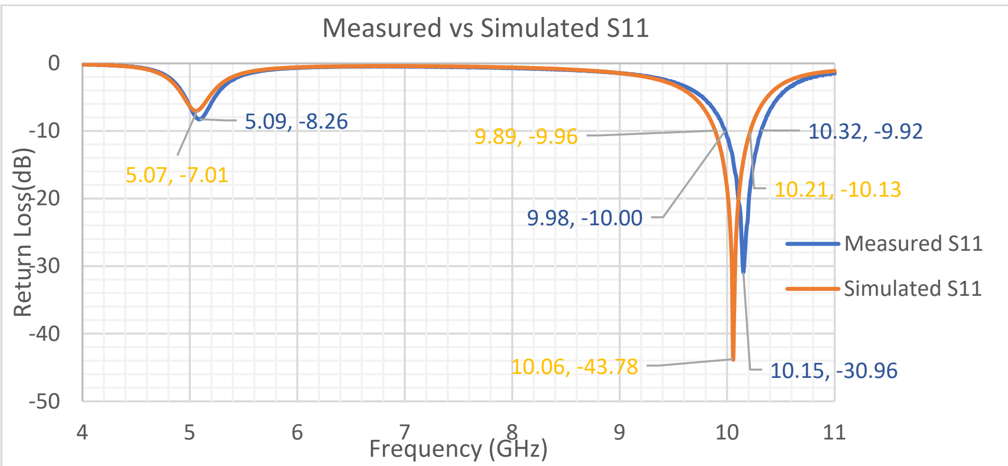

Figure 7-2: S11 Simulated versus S11 Measured of the patch antenna operating in 2^{nd} mode

The associated phase is illustrated in Figure 7-3. The S11 magnitude and the phase at 10.15 GHz translate to an impedance of (47.26+j0.2873) Ω. This conversion has been made using an online reflection coefficient to impedance converter. The absolute value is close to the impedance of the SMA connector. That shows that the impedance is not purely resistive and that it presents a small reactive component. The reactive elements cause the voltage and current to be out of phase to some degree. Some power is stored in the reactive components and not dissipated as heat.

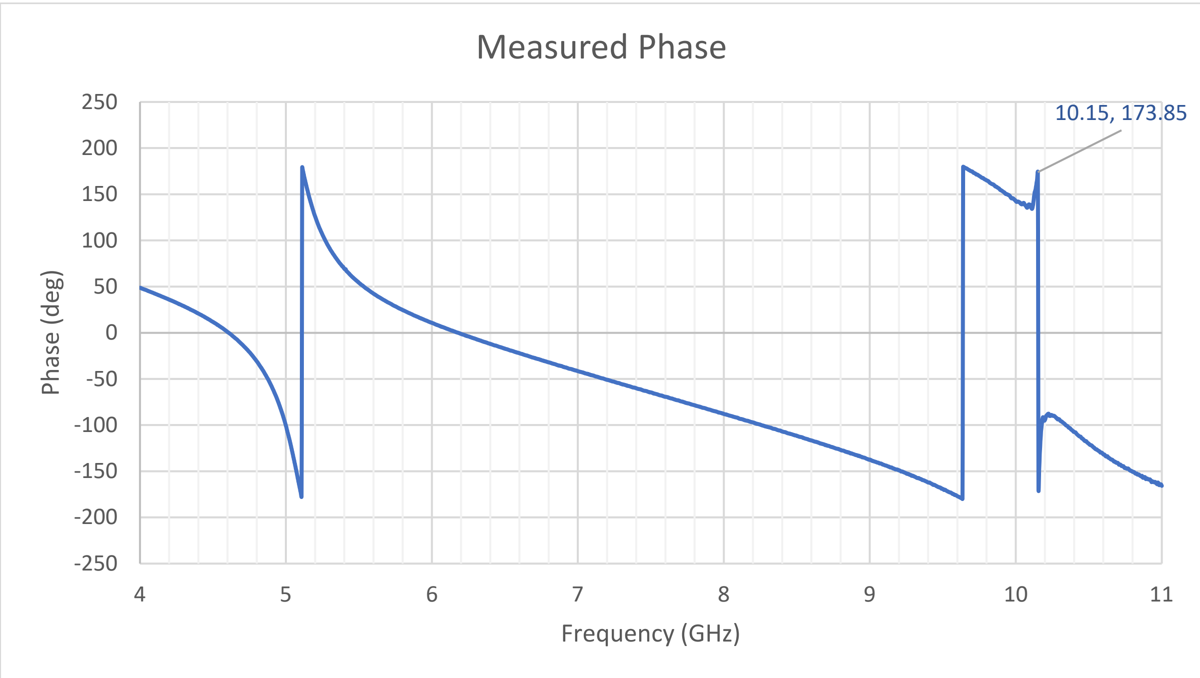

Figure 7-3: The phase of the measured S11 of the single patch antenna operating in 2^{nd} mode

The E-Theta patterns and pattern cuts are compared in Figure 7-4. The two cuts are very similar, and the gain difference is within 0.5 dB. The measured cross-polarisation level is higher than the simulated level. The high cross polarisation level, especially in the diagonal planes, is due to feed point asymmetry, as explained in [164].

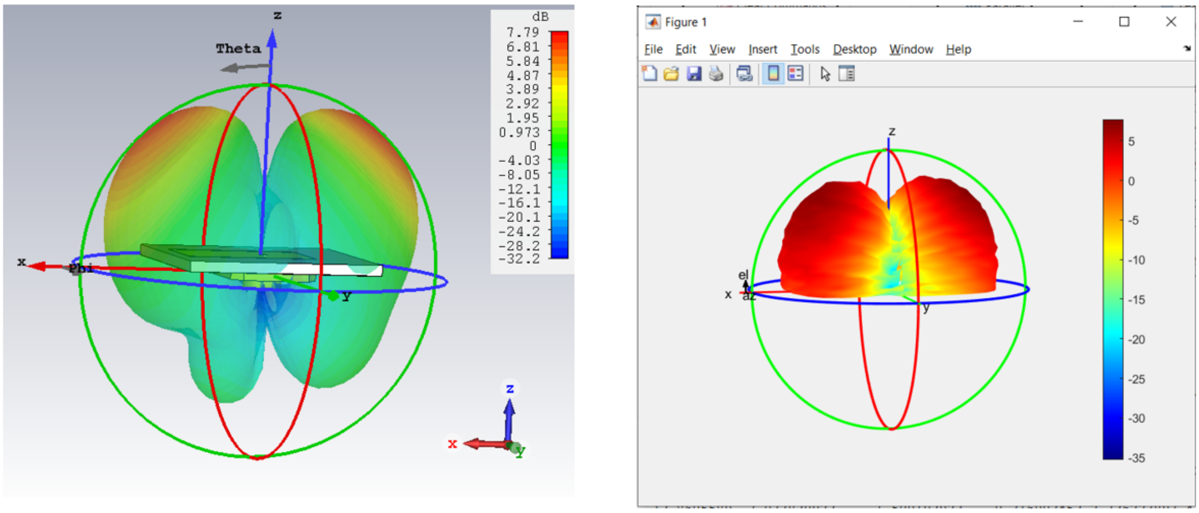

Simulation

Measurement

(a)

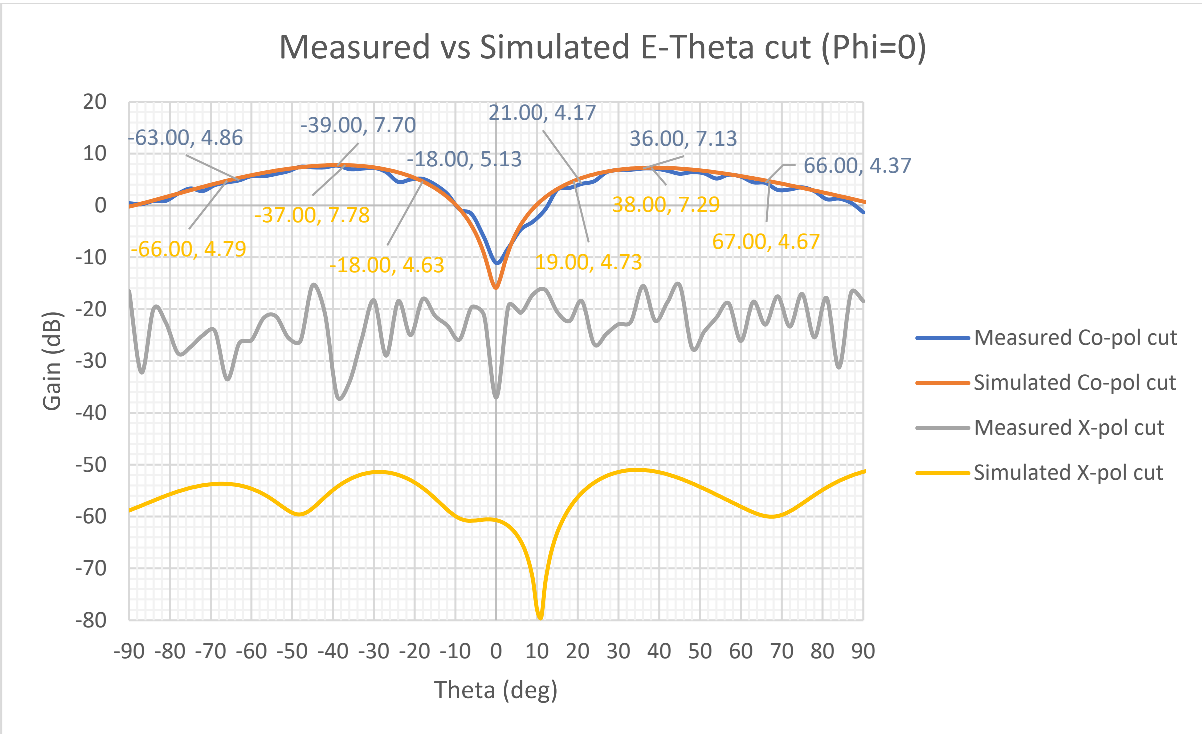

(b)

Figure 7-4: Simulated versus measured co-pol patterns (a) and Co-pol and X-pol cuts of a single feeding patch antenna (b)

The small ripples in the measured pattern curve could be the result of the reflections that occurred due to measurement set-up, i.e. due to the presence of the feeding network at the back of the antenna. It must also be taken into account that a limited number of measurement points were used (to avoid the increase of the sweeping time) and that the curves resulted from the interpolation of the points.

Figure 7-5 illustrates the 3 dB gain drop across the bandwidth, i.e.: between 9.584 GHz and 10.562 GHz (approximately the 3 dB BW). As it can be observed, the shapes of the patterns remain more or less the same, at all frequencies.

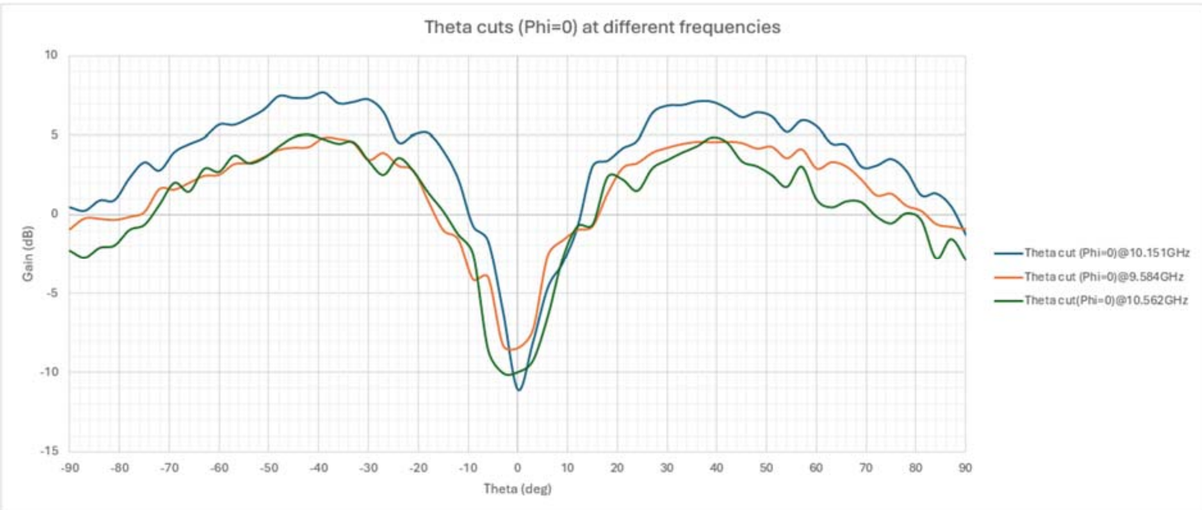

Figure 7-5: Pattern changes with frequency for single patch antenna operating in 2nd mode

7.2 One patch antenna attached to a reflecting substrate

The scaled single patch antenna presented in the previous section is added to the scaled reflecting substrate, as described in Chapter 5. In Chapters 5 and 6, the reflecting substrates material was Rogers RT5880LZ, which has a dielectric constant of 2.0. Because of the lead-time and price of this dielectric material, in this chapter, for all the antennas, RT5880LZ was replaced with RT5880, which has a dielectric constant of 2.2. The simulations showed no significant change in return loss, gain and the radiation pattern due to this change at 10 GHz. No changes on the design of the feeding patches were necessary due to the reflecting substrate dielectric change. All the measurements are compared to the simulations reflecting the new substrate (RT5880).

The experimental patch antenna attached to the reflecting substrate and the chamber set-up for measurement are illustrated in Figure 7-6.

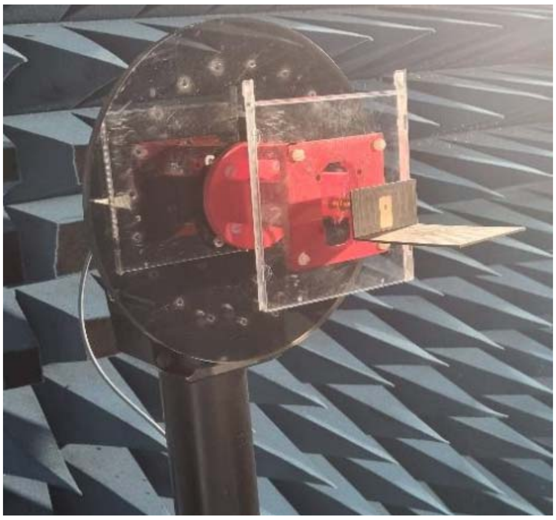

Figure 7-6: Patch antenna with reflecting substrate test setup

The measured vs simulated return losses of the antenna is shown in Figure 7-7. The measured resonant frequency is shifted to the right by approximately 100 MHz and the 10 dB fractional bandwidth is approximately 3.3%. Considering the associated S11 phase, shown in Figure 7-8, it can be inferred that the impedance of the antenna is

(45.7-2.518j) Ω. This has been deducted using an online tool for converting the reflection coefficient (given the module and phase) to impedance.

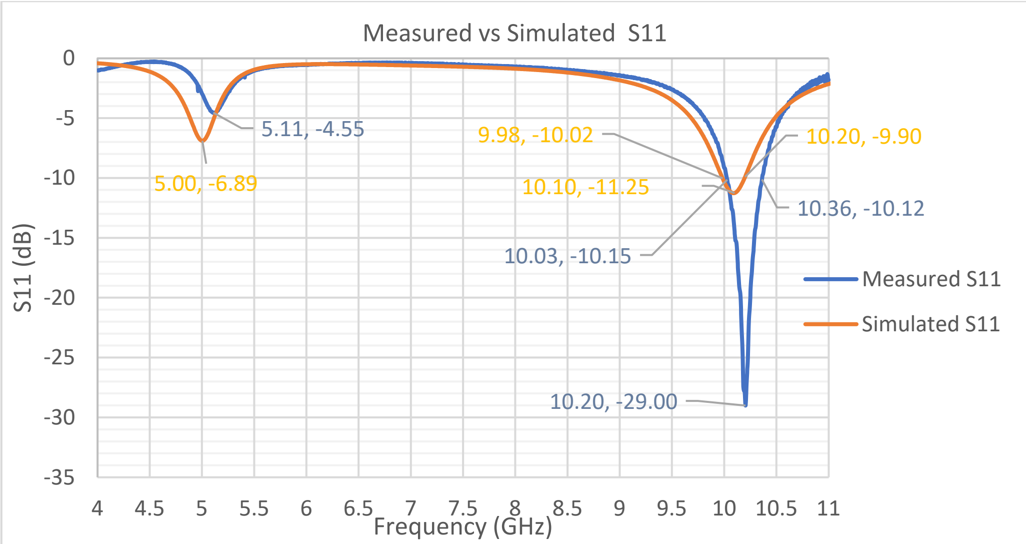

Figure 7-7: S11 Simulated versus S11 Measured of a single patch antenna operating in 2nd mode with reflecting substrate (Figure 6-6)

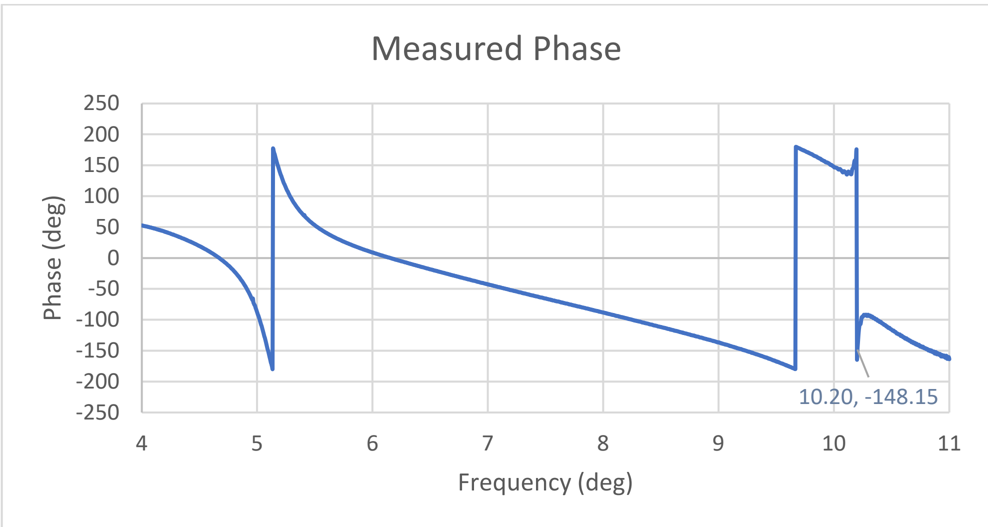

Figure 7-8: The phase of the measured S11 relating to Figure 7-7

The radiation pattern, E-Theta, E-Phi pattern-cuts in co and cross-polar are presented in Figure 7-9. The simulated and measured radiation patterns look very similar.

The E-Theta pattern cut shows that the measured beamwidth is narrower compared to the simulated one (43˚ vs. 27˚), but, the E-Phi cuts show that the measured beam is slightly wider in that direction (95˚ vs 80˚) compared to the simulation.

This aligns with the gain values, as the measured gain is higher than the simulated gain by approximately 1 dB. This could be due to measurement tolerances or build tolerances.

The higher-level cross polarisation shown both in the measured Theta and Phi pattern cuts could be caused by the feed asymmetry and also by the reflections due to measurement setup. Compared to the simulations, the measured antenna presents a higher feed asymmetry, which could be due to the build tolerances. That is visible in S11 measurements, where the resonance is shifted in frequency.

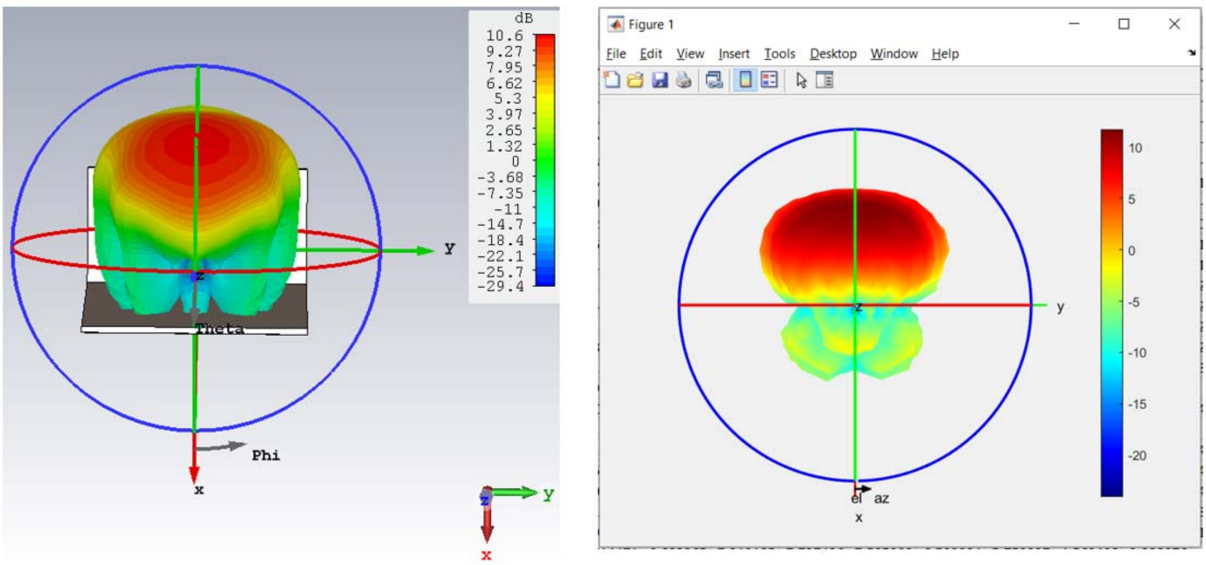

Simulation Measurement

(a)

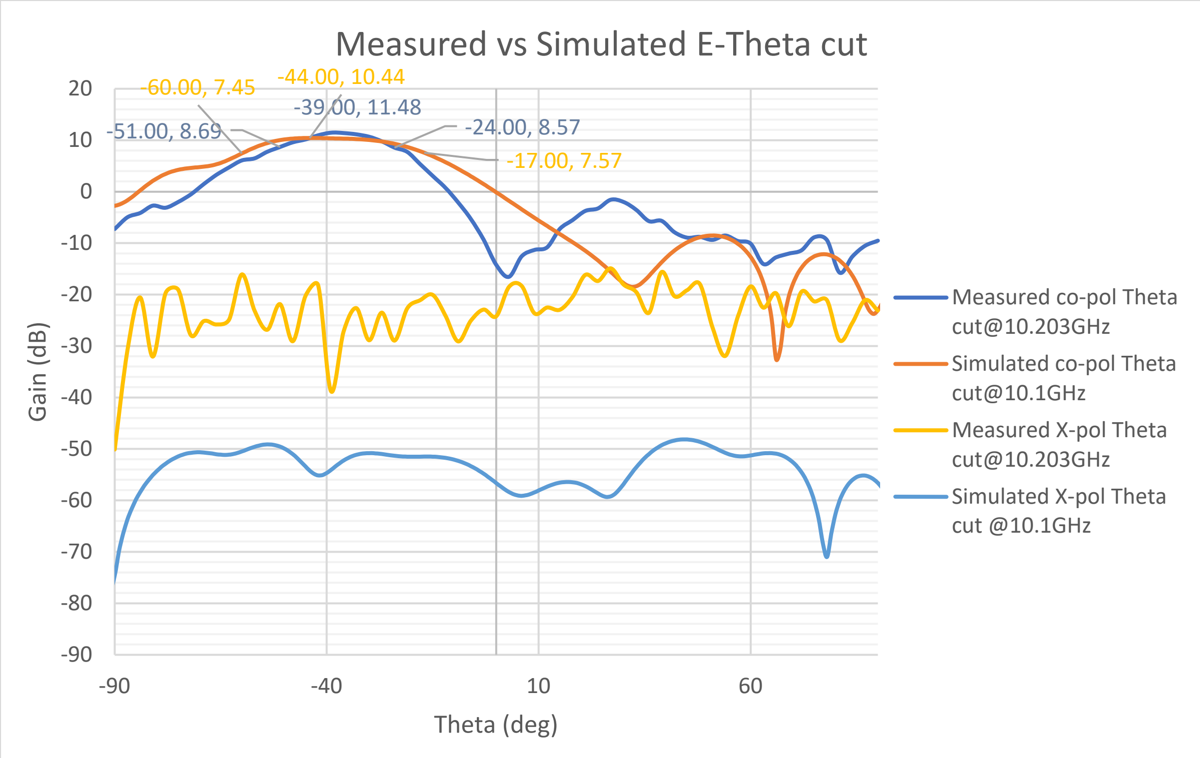

(b)

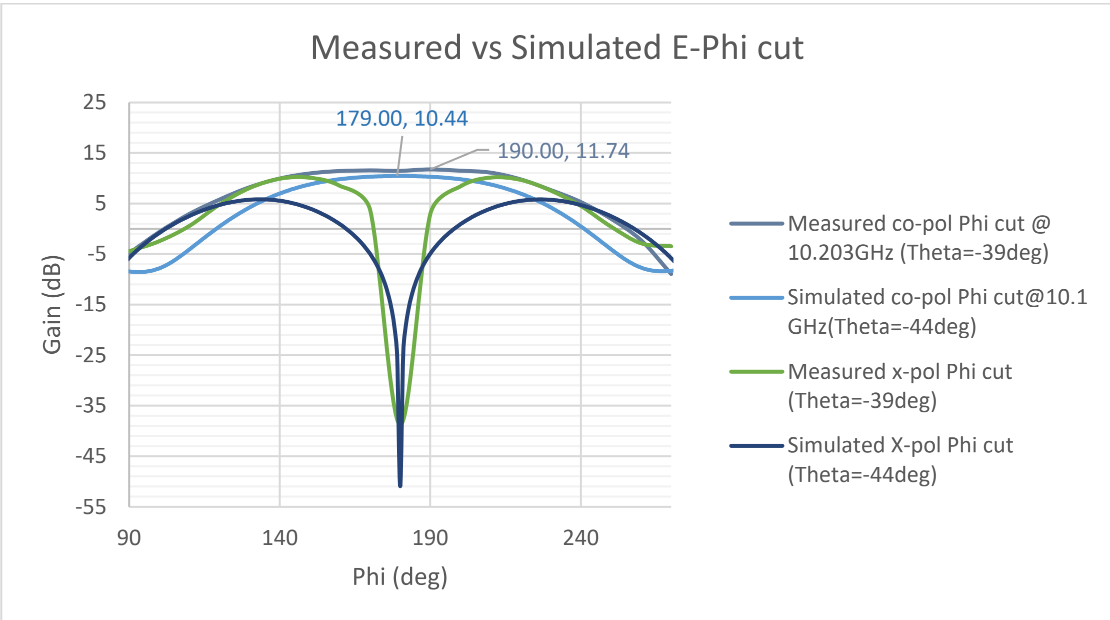

(c)

Figure 7-9: Simulated versus Measured co-pol patterns (a) and Co-pol and X-pol Theta cuts (b) and Phi cuts (c) of the patch antenna operating in 2nd mode at proximity of the reflecting substrate

The drop in gain (~3 dB at Theta = -39˚) over frequency is illustrated in Figure 7-10. At 10.55 GHz, the sidelobe at Theta = 20˚ becomes more prominent and comes closer to the main lobe.

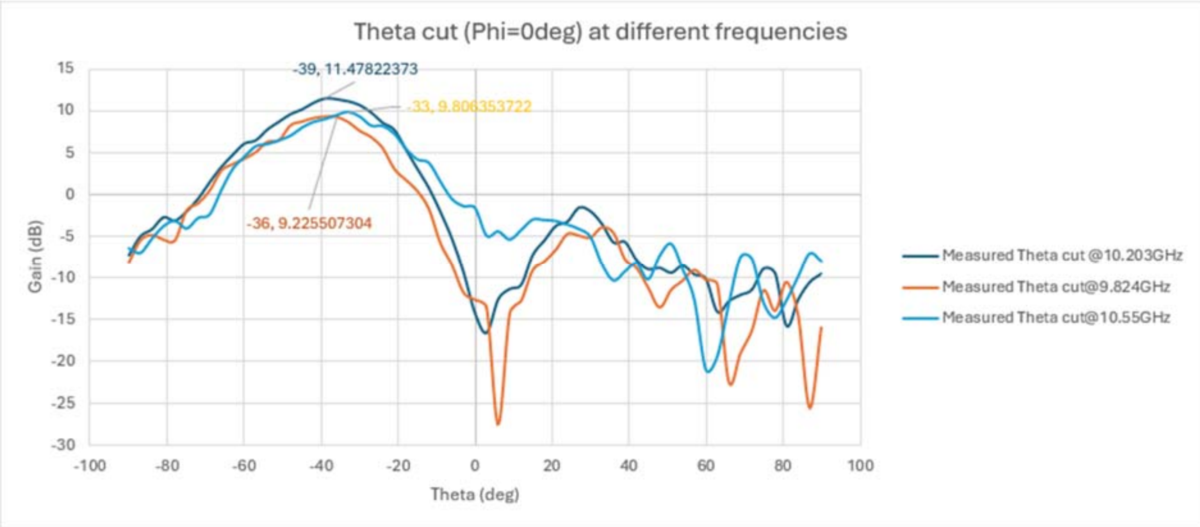

(a)

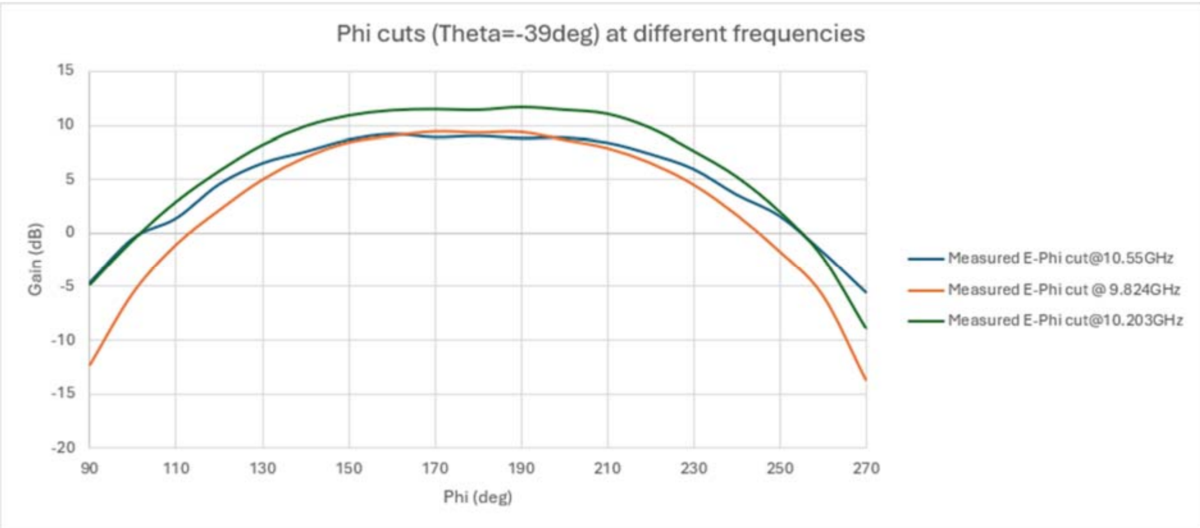

(b)

Figure 7-10: Pattern changes with frequency (a) Theta cut (b)Phi relating to the antenna in Figure 7-6

7.3 Two patch antennas array attached to a reflecting substrate

The measurement set-up of two patch antenna array (where each patch operating in 2^{nd} mode) attached to a reflecting substrate is shown in Figure 7-11. Port 2 from the Vector Network Analyser has been split through a 2-way splitter to provide the power to each patch equally. At the input of each patch, a phase shifter (PTS-A3A8-18-15*f) ensured that the relative phase between the two patches was zero.

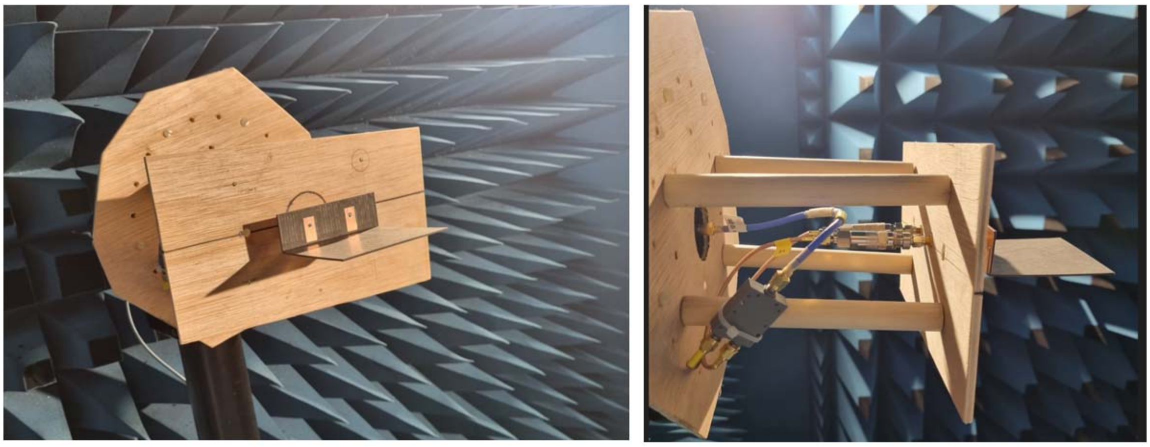

Figure 7-11: Two patch antennas with reflecting substrate test setup

Initially, individual tests performed on each patch to show the asymmetry in fabrication, connector location and coupling effects between the two patch elements in the array.

The measured vs simulated return losses of the invidual patches in the array is shown in Figure 7-12. As with the previous single element antennas, the resonance was shifted to the higher frequencies by approximately 70 MHz for the first patch and 40 MHz for the second patch. The 10 dB fractional bandwidth was approximately 3.4% on the first patch and 3.3% on the second patch. The corresponding measured phases of the S11 and S22 are illustrated in Figure 7-13, resulting an input impedance of (47.39-0.3742j)Ω for Patch#1 and (45.26-1.458j)Ω for Patch#2.

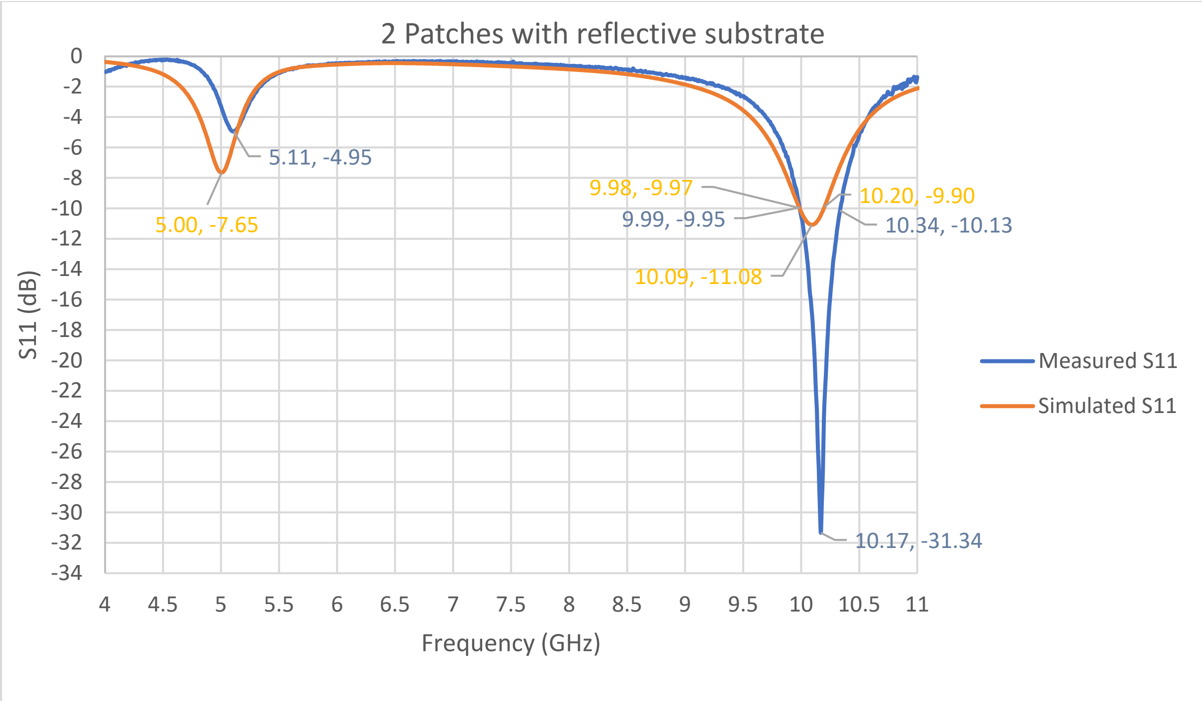

(a)

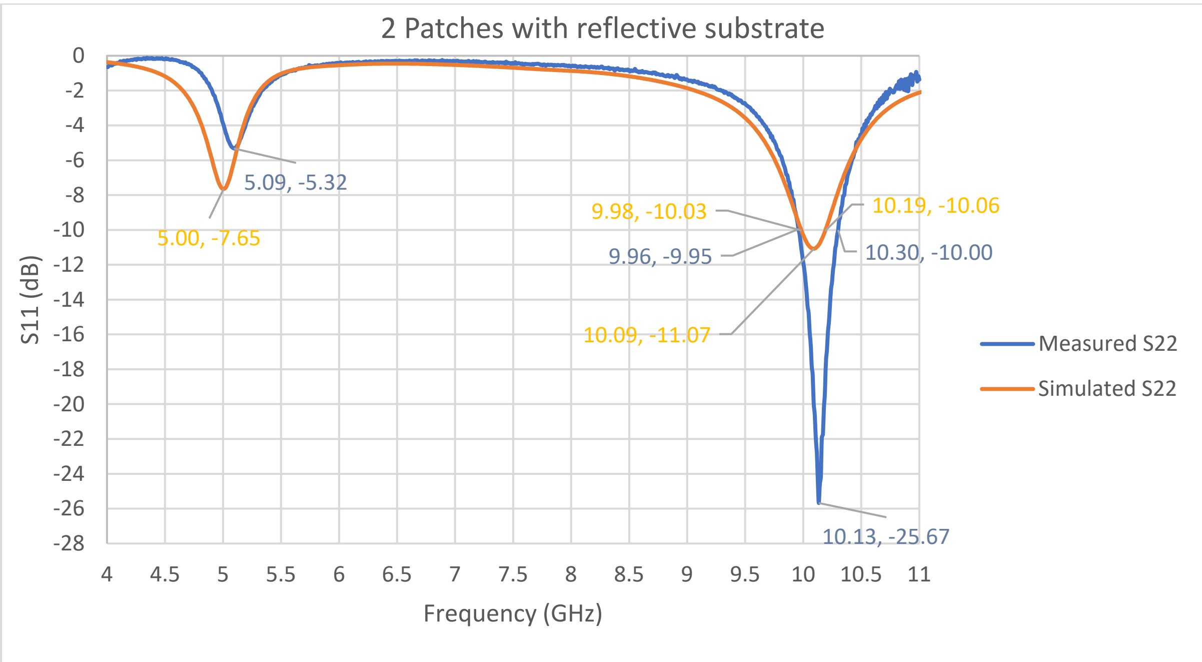

(b)

Figure 7-12: The measured vs simulated return loss (a) Patch #1 (b) Patch #2

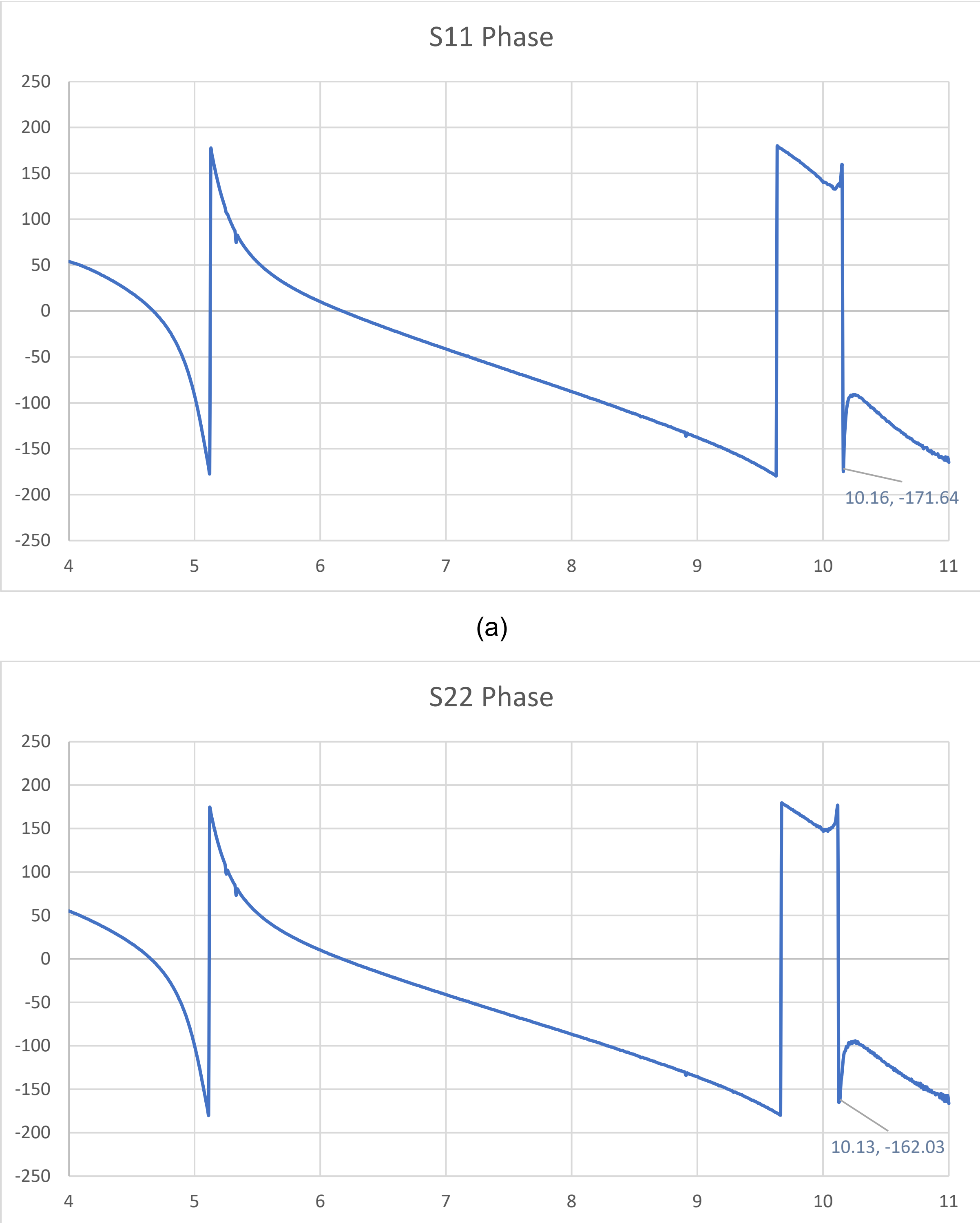

(a)

(b)

Figure 7-13: The phase of the measured S11 (a) and S22 (b) relating to Figure 7-12

Figure 7-14 presents the S11 of the antenna array (as a whole), ie: the S11 into the 2-way splitter. All the subsequent measurements (pattern cuts) for this antenna have been taken at 10.1 GHz. The S11 measurements shown in Figure 7-13 have been taken with the antenna pointing to the absorbing material (instead of pointing to the reference horn antenna), and the measurements were taken straight at each port of the patch antenna. In Figure 7-14, the measurement was taken with the splitter introduced in the feeding network, and with the antenna pointing to the reference horn antenna. As a consequence, the measurement appears slightly noisy due to the reflections occurring from the reference antenna.

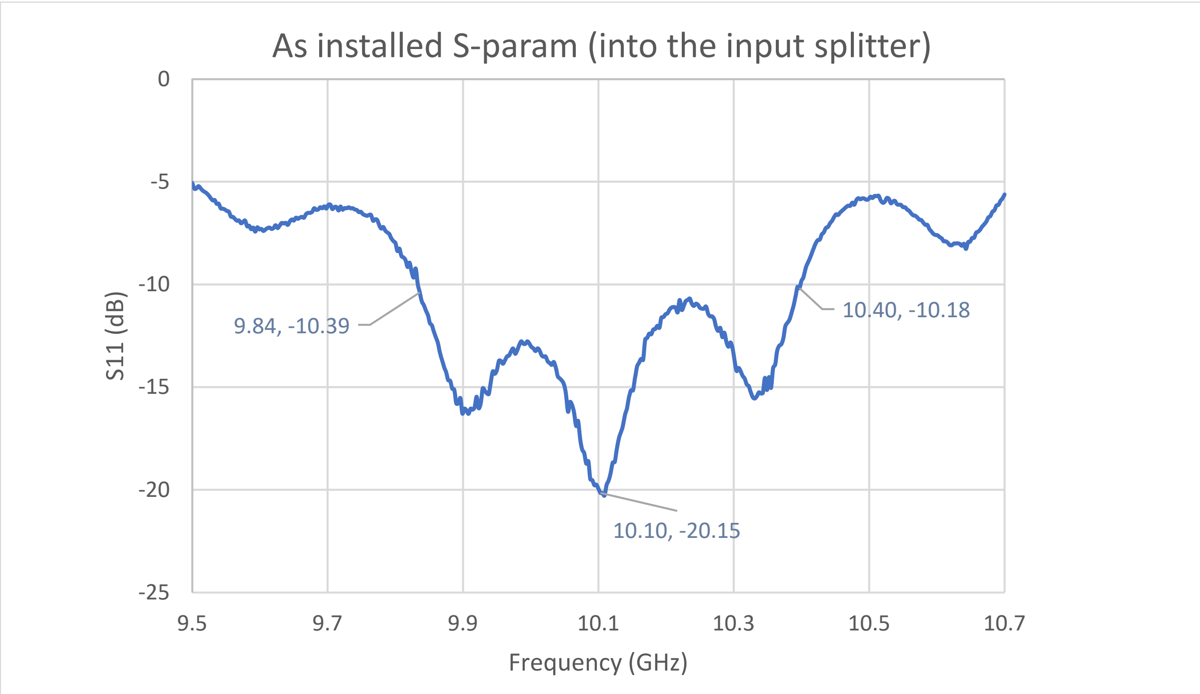

Figure 7-14: S11 of the two element array looking into the two-way power splitter

The radiation patterns, Theta and Phi cuts of the co- and cross-polarisation are presented in Figure 7-15. The measured and simulated patterns look very similar, however, the E-Theta cuts show that the measured pattern has a narrower beamwidth compared to the simulations. The measured gain is higher by approximately 0.5 dB compared to the simulations. The E-Phi cuts shows that measured and simulated beamwidths in Phi direction are similar (~38˚), but the measured cut is slightly shifted to the right. This could suggest that there was a small misalignment in the measurement setup (in Azimuth direction) between the reference antenna and the antenna under test.

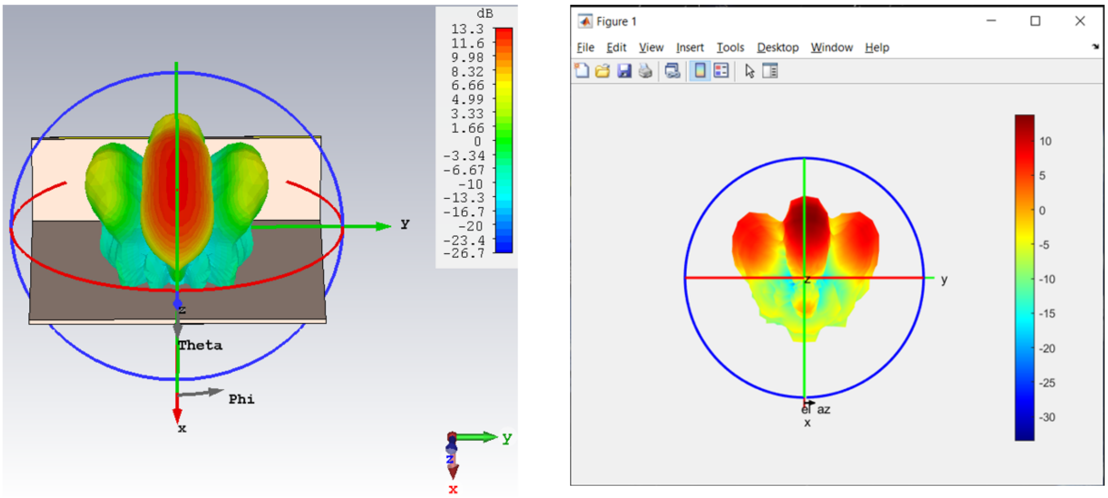

Simulation

Measurement

(a)

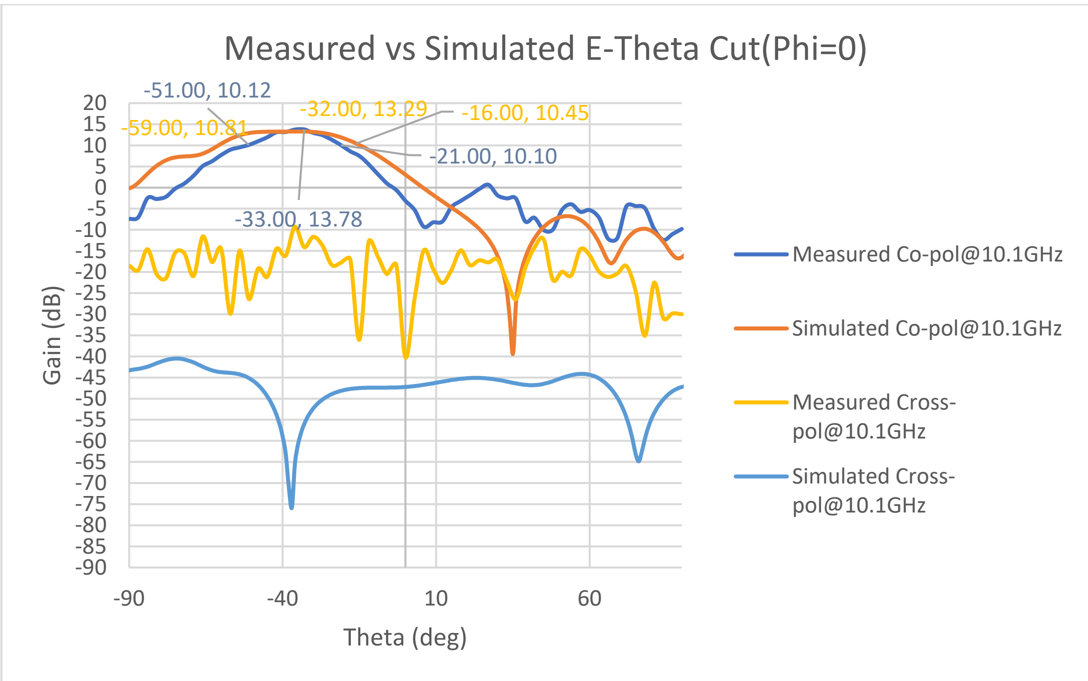

(b)

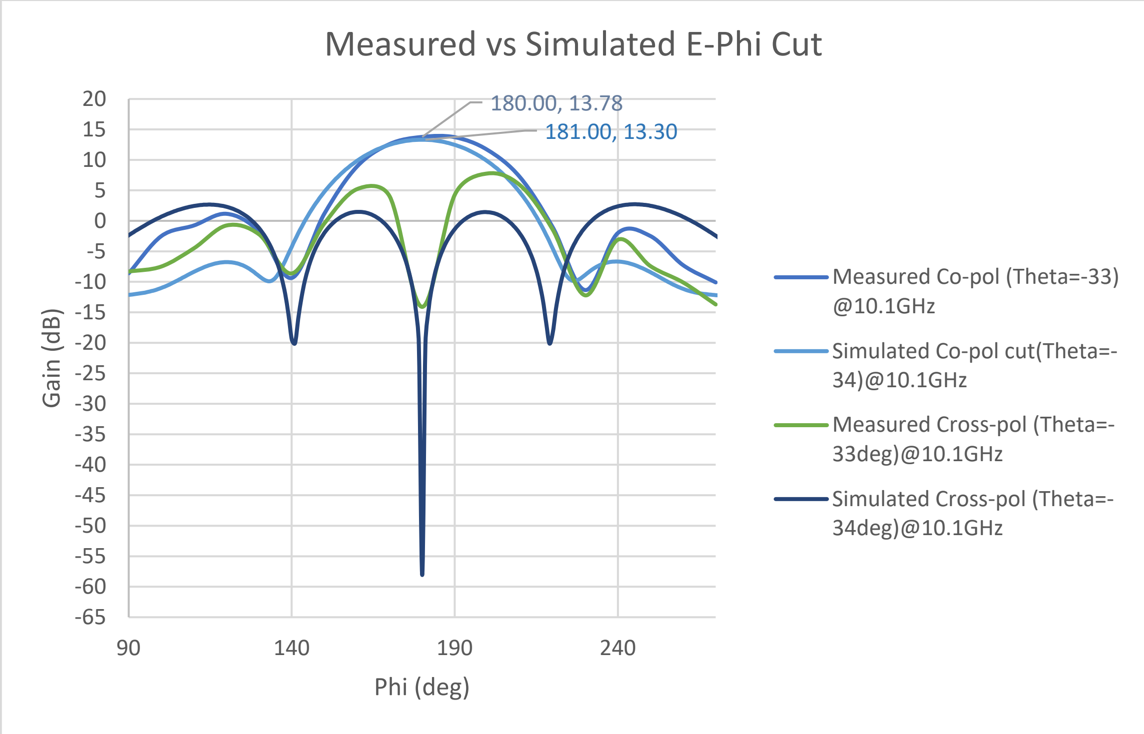

(c)

Figure 7-15: Simulated versus measured co-pol patterns (a) and Co-pol and Cross-pol Theta cuts (b) and Phi cuts (c) of two element patch antenna array (each operating in the 2nd mode) in the proximity of a reflecting substrate

As in the previous measurements, the measured cross-pol levels are higher than those from simulations, and that could be explained by the feeding asymmetry of each patch and the reflections that occur from behind of the antenna under test, where the feeding network was kept. The build tolerances could also be the reason for measuring a different shape X-pol pattern.

The gain drop (~3 dB) over frequency is shown in Figure 7-16.

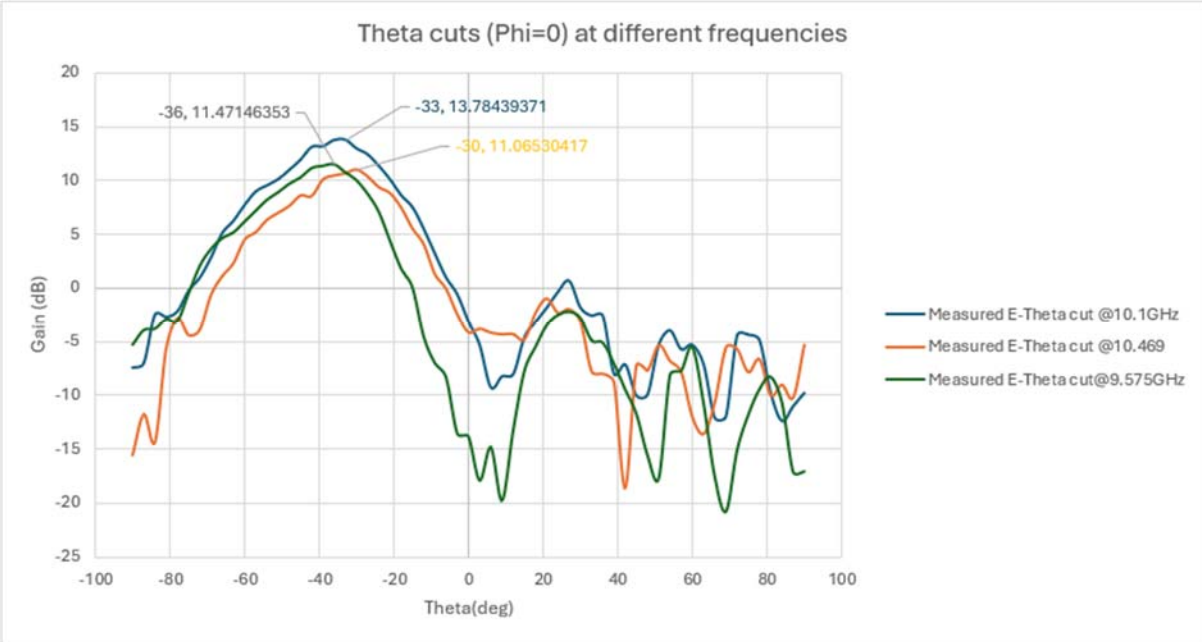

(a)

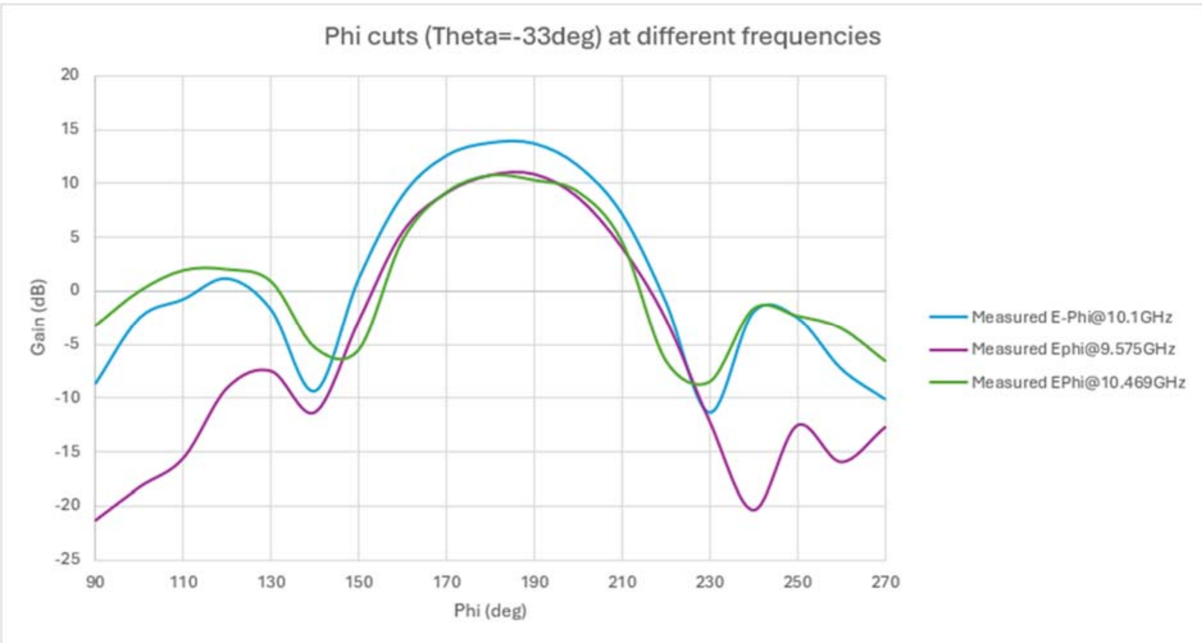

(b)

Figure 7-16: Pattern changes with frequency (a) Theta cuts (b)Phi cuts

7.4 Four patch antennas array attached to a reflecting substrate

The scaled four patch antenna array attached to a reflecting substrate and the measurement set-up are shown in Figure 7-17.

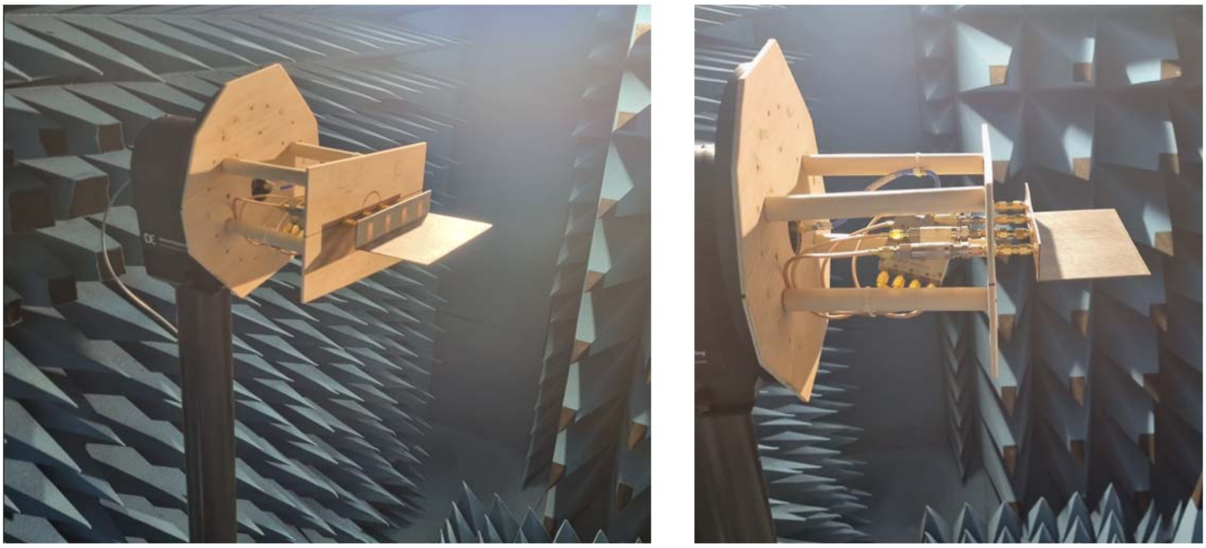

Figure 7-17: Four patch antennas with reflecting substrate test setup

Port 2 from the Vector Network Analyser has been split through a 4-way splitter to provide the input for each patch. At the input of each patch, a phase shifter (PTS-A3A8-18-15*f) ensured that the relative phase between the four patches was zero.

The measured vs simulated return losses of each port is shown in Figure 7-18. As it can be observed, the resonance was shifted to the right by approximately 76 MHz on the first patch, 68 MHz on the second patch, 29 MHz on the third patch and 17 MHz on the fourth patch. The 10 dB fractional bandwidth was approximately 3.2% on the first patch, 3.4% on the second patch, 3.4% on the third patch and 3.3% on the fourth patch.

The corresponding measured phases of the S11, S22, S33 and S44 are illustrated in Figure 7-19, resulting an input impedance of (45.81-0.7101j)Ω for Patch#1, (43.21+1.798j)Ω for Patch#2, (43.69+0.2582j)Ω for Patch#3 and (44.16-1.034j)Ω for Patch#4.

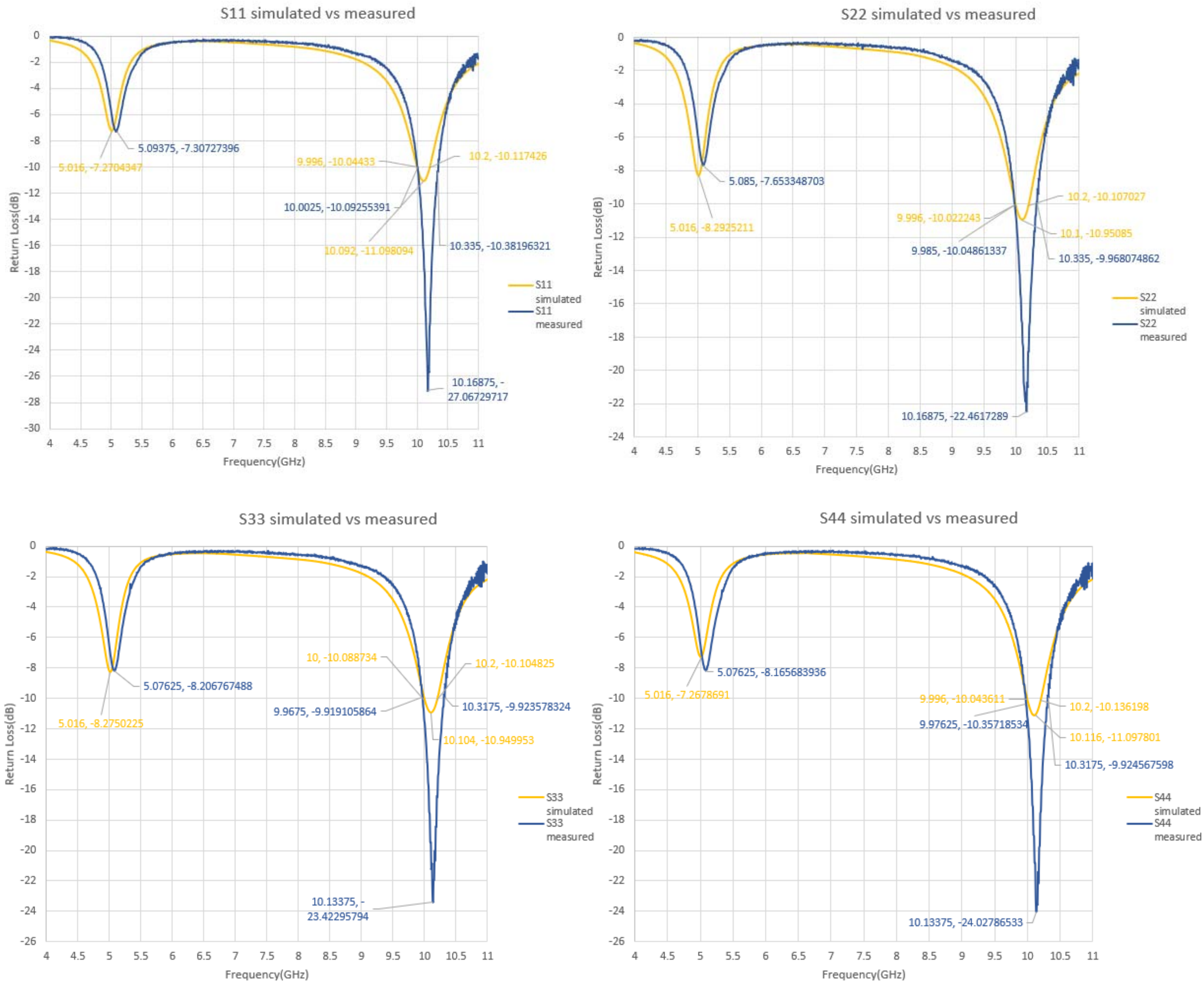

Figure 7-18: The measured vs simulated return loss of Patch#1 (S11), Patch#2(S22), Patch#3 (S33) and Patch#4 (S44)

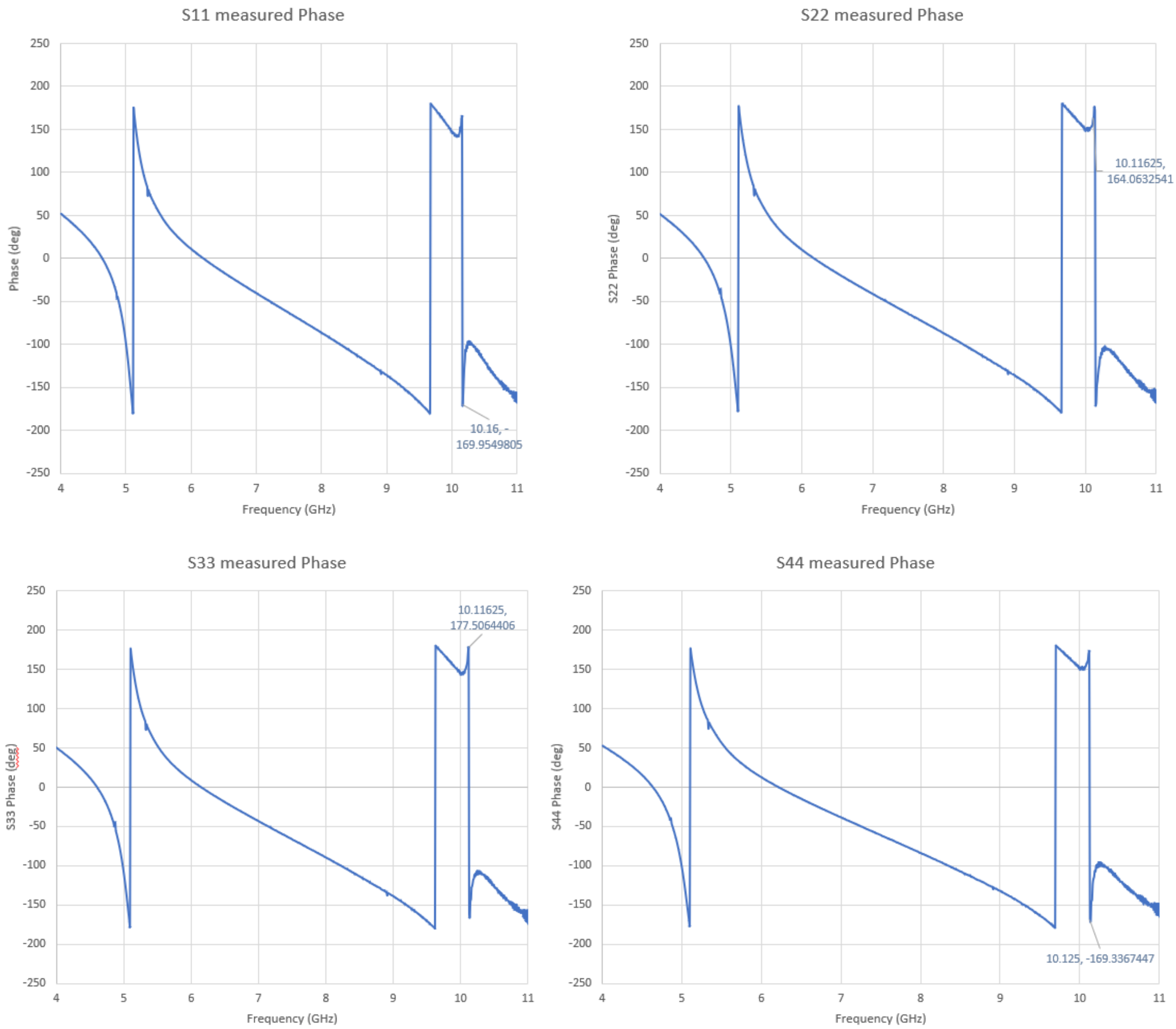

Figure 7-19: The phase of the measured S11, S22, S33 and S44 relating to Figure 7-18

Figure 7-20 presents the S11 of the installed (overall) antenna array, i.e. the S11 into the 4-way splitter. The subsequent measurements (pattern cuts) for this antenna have been taken at 10.1 GHz.

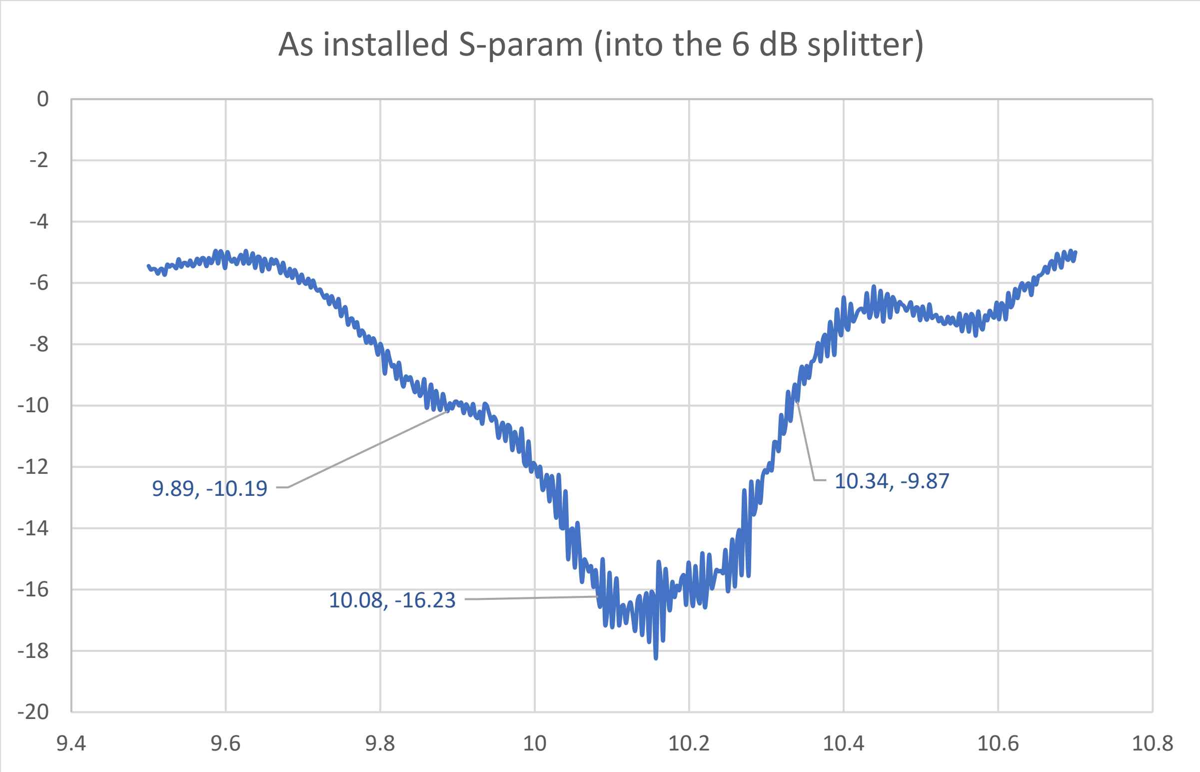

Figure 7-20: |S11| of the four-element patch antenna array at proximity of the ground plane. Patches operating in the 2nd mode.

The radiation pattern, Theta and Phi cuts of the co- and cross-polarisation are presented in Figure 7-21. Although he measured and simulated patterns look very similar, the E-Theta cuts show that the measured pattern has a narrower beamwidth compared to the simulated pattern. The reason for seeing a noisy S11 measurement is the same as the one explained for Figure 7-14, i.e. the reflections occurring from the reference antenna and from the feeding network.

The measured gain is slightly higher by approximately 1 dB compared to the gain from the simulation. The E-Phi cuts shows that the simulated beamwidth in Phi direction is slightly wider compared to the measured beamwidth (16˚ vs 18˚). The two Phi cuts are well aligned at 180˚, which means that the reference antenna and the antenna under test were well aligned in Azimuth.

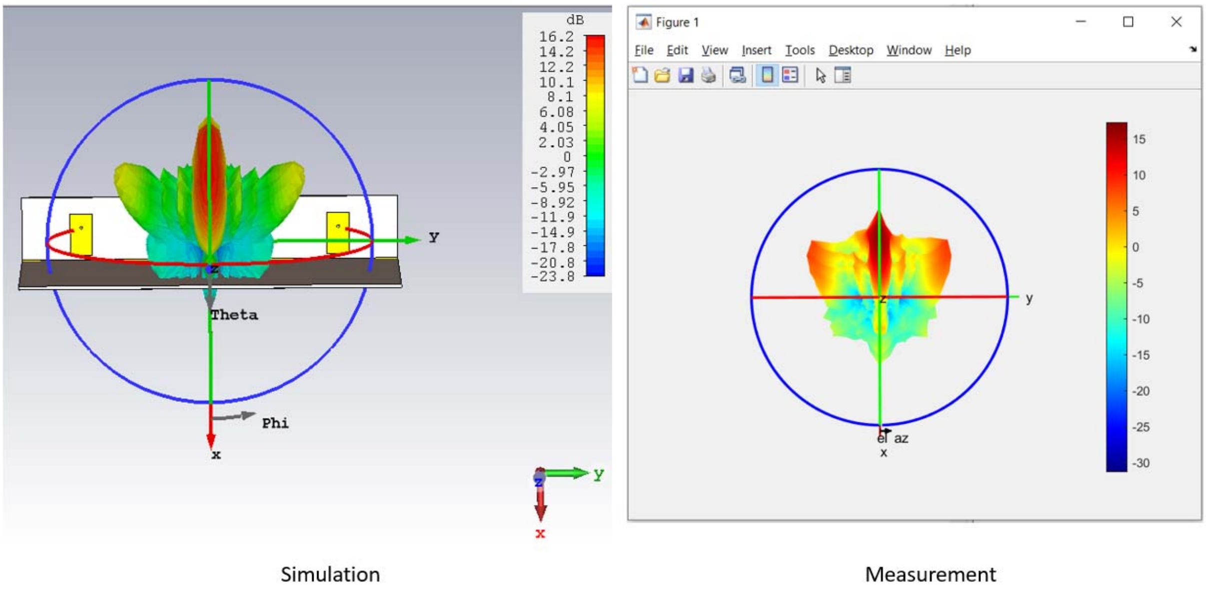
dB
16.2
14.2
12.2
10.1
8.1
6.08
4.05
2.03
0
-2.97
-5.95
-8.92
-11.9
-14.9
-17.8
-20.8
-23.8
Theta
Phi
y
x
z
Figure 1
File Edit View Insert Tools Desktop Window Help
15
10
5
0
-5
-10
-15
-20
-25
-30
el az
Simulation
Measurement

(a)

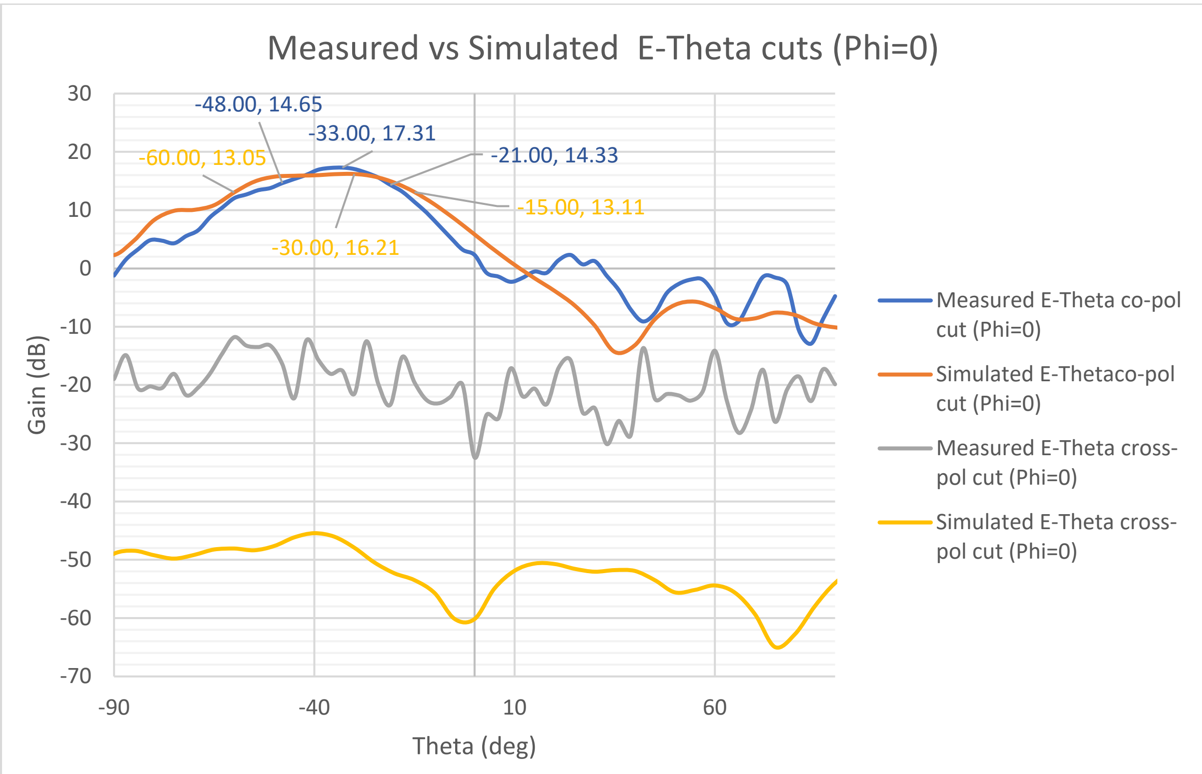
Measured vs Simulated E-Theta cuts (Phi=0)
-48.00, 14.65
-33.00, 17.31
-60.00, 13.05
-21.00, 14.33
-15.00, 13.11
-30.00, 16.21
30
20
10
0
-10
-20
-30
-40
-50
-60
-70
Gain (dB)
-90
-40
10
60
Theta (deg)
Measured E-Theta co-pol cut (Phi=0)
Simulated E-Thetaco-pol cut (Phi=0)
Measured E-Theta cross-pol cut (Phi=0)
Simulated E-Theta cross-pol cut (Phi=0)

(b)

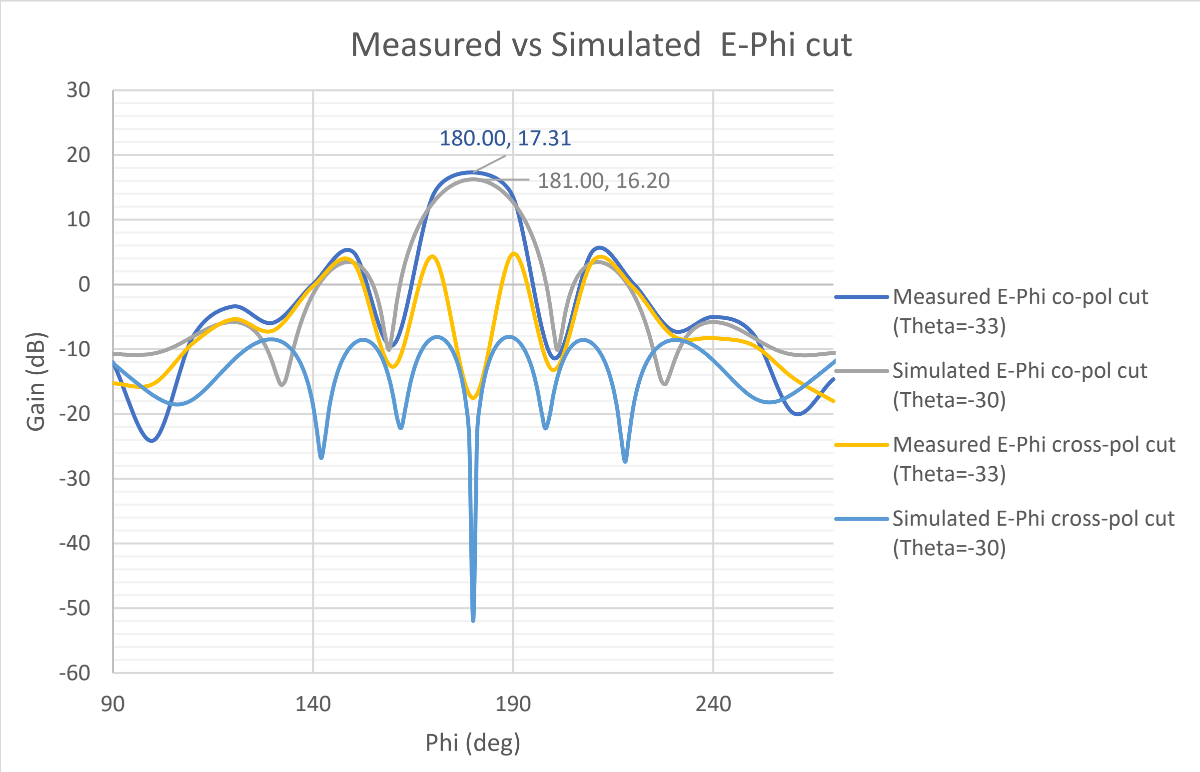

(c)

Figure 7-21: Simulated versus measured co-pol patterns (a) and Co-pol and Cross-pol Theta cuts (b) and Phi cuts (c) of four-element patch antennas in the presence of the reflecting substrate

Again, the measured cross-pol levels are higher than those from simulations, and this could be explained by the feed asymmetry of each patch and the reflections that occur from behind of the antenna under test, where the feeding network was kept.

The gain drop (~3 dB) over frequency is shown in Figure 7-22.

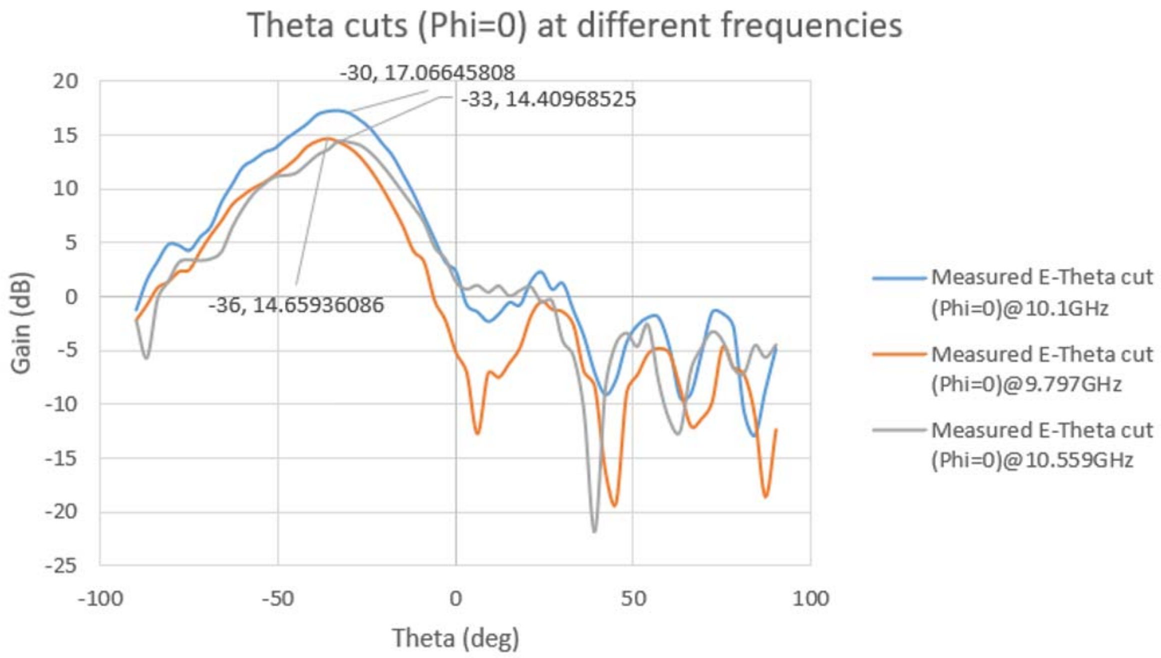

(a)

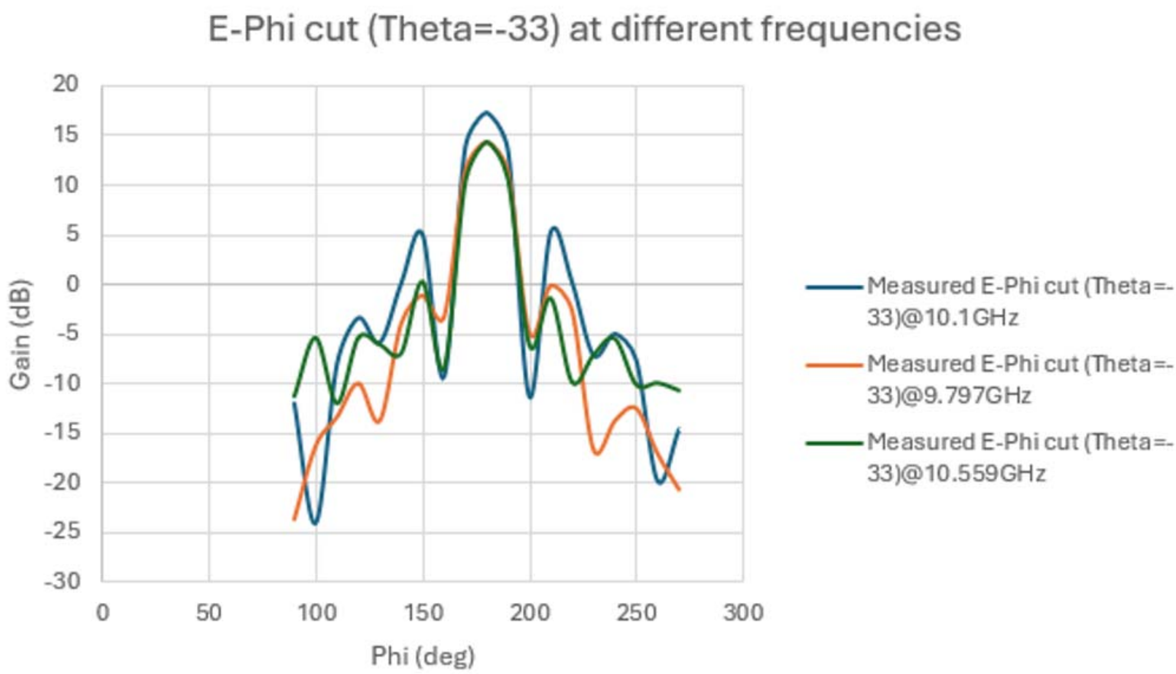

(b)

Figure 7-22: Pattern changes with frequency (a) Theta cut (b) Phi cut relating to the array in Figure 7-17

7.5 Four patch antennas array attached to a reflecting substrate with reflecting patches

The reflecting substrate of the antenna presented in the previous section is added/covered by reflecting patches, scaled to operate at 10 GHz. Given that the reflecting substrate has a slightly different dielectric constant compared to what it has been presented in Chapter 5 (2.2 instead of 2.0), and that the length of the feeding patches has changed slightly to account for the extra inductance introduced with the real model of the Huber and Suhner SMA connector, the dimensions of the scaled reflecting patches have been modified by approximately two points of a millimetre to bring the resonance of the whole structure back close to 10 GHz.

The measurement set-up of four patches attached to a reflecting substrate with reflecting patches is shown in Figure 7-23.

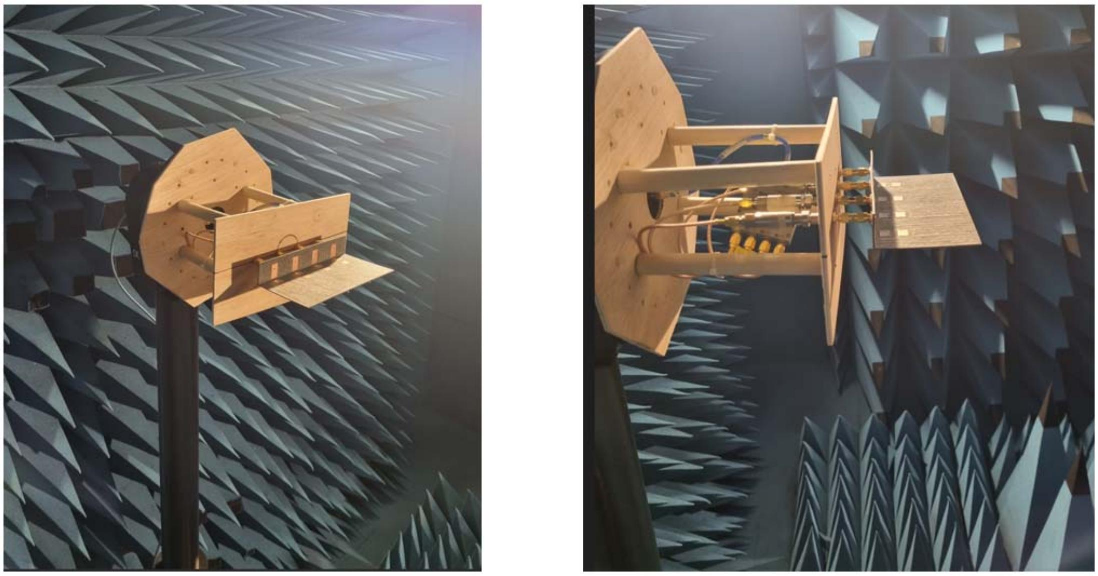

Figure 7-23: Four-element patch antenna array in presence of reflecting substrate covered by reflecting patches. Test setup.

As in the previous antenna, Port 2 from the Vector Network Analyser has been split through a 4-way splitter to provide the input for each patch. At the input of each patch, a phase shifter (PTS-A3A8-18-15*f) ensured that the relative phase between the four patches was zero.

The measured vs simulated return losses of each port is shown in Figure 7-24.

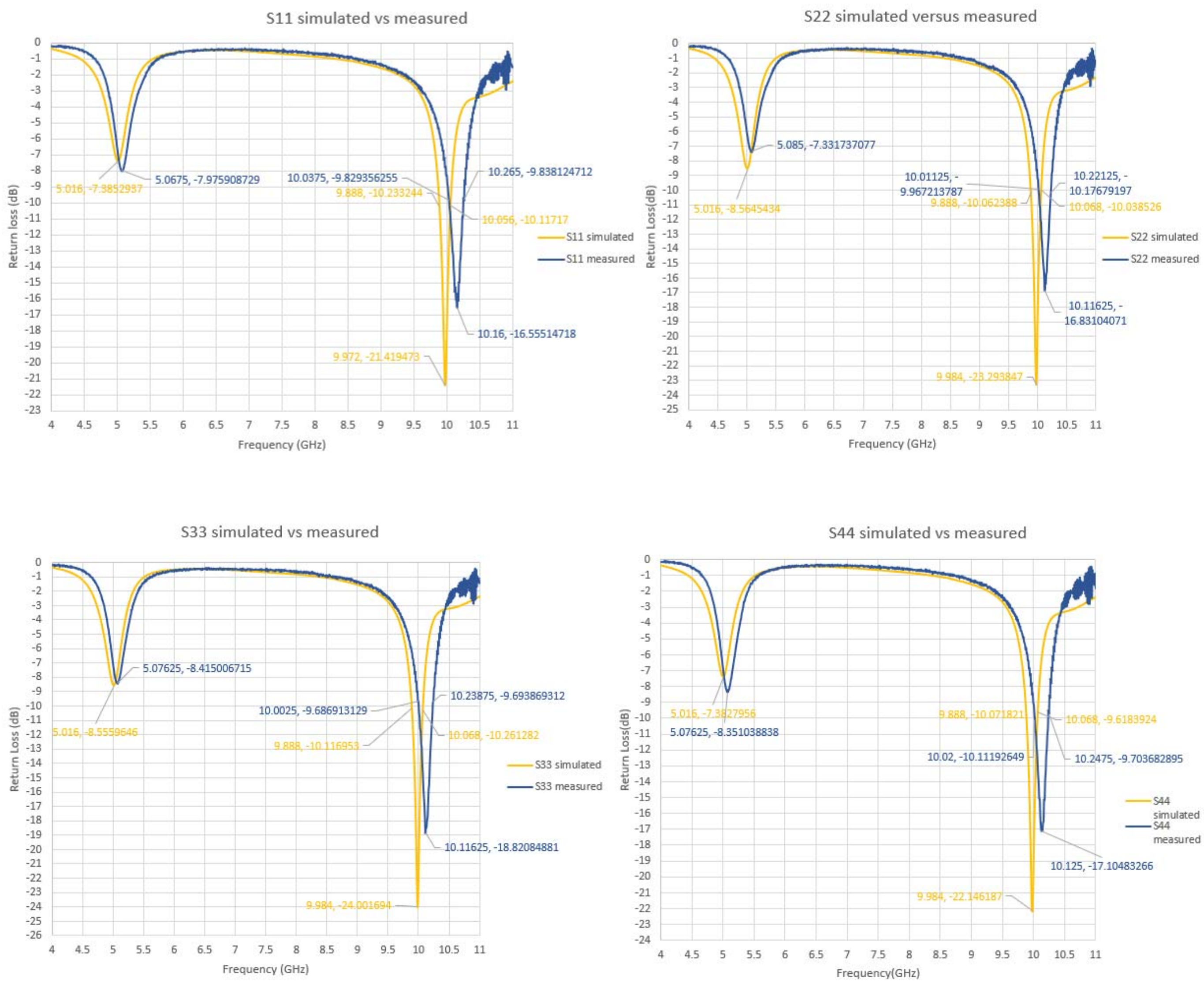

Figure 7-24: The measured vs simulated return loss of Patch#1 (S11), Patch#2(S22), Patch#3 (S33) and Patch#4 (S44)

It can be observed that the resonance is shifted to the right by approximately 188 MHz for the first patch, 132 MHz for the second patch, 132 MHz for the third patch and 141 MHz for the fourth patch. The 10 dB fractional bandwidth is approximately 2.2% for the first patch, 2.0% for the second patch, 2.3% for the third patch and 2.2% for the fourth patch.

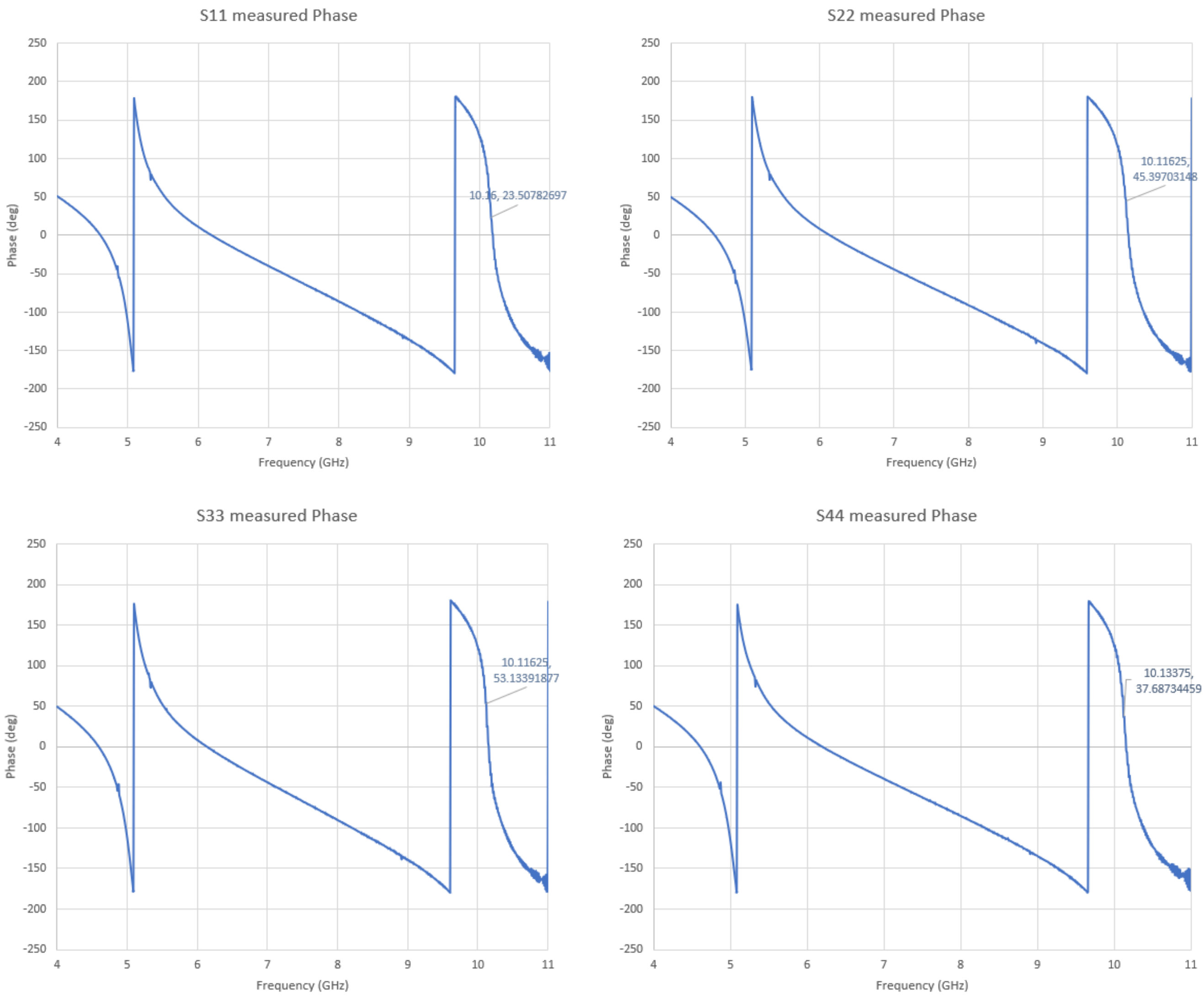

Figure 7-25: The phase of the measured S11, S22, S33 and S44 relating to Figure 7-24

The corresponding measured phases of the S11, S22, S33 and S44 are illustrated in Figure 7-25, resulting an input impedance of (62.25+7.919j)Ω for Patch#1, (59.82+12.53j)Ω for Patch#2, (56.35+10.47j)Ω for Patch#3 and (61.40+10.69j)Ω for Patch#4.

Figure 7-26 presents the S11 of the overall antenna array in Figure 7-23; ie: the S11 into the 4-way splitter. For consistency, the subsequent measurements (pattern cuts) on this antenna have been taken at 10.1 GHz.

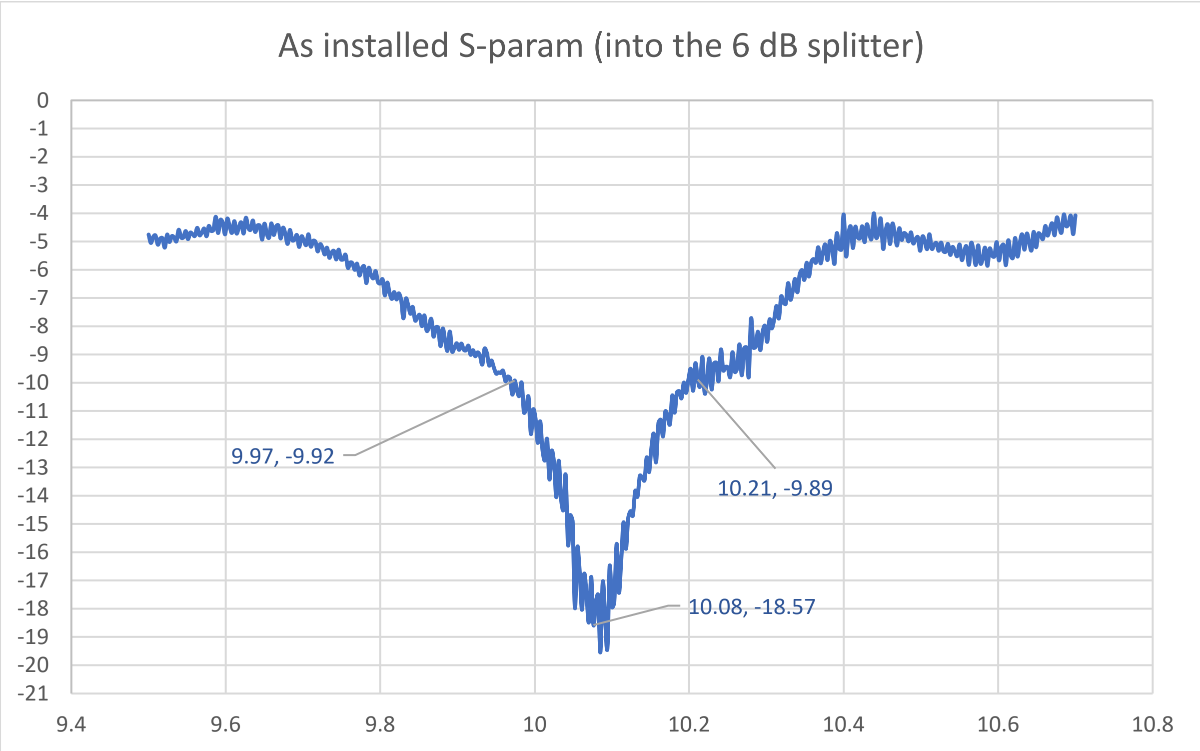

Figure 7-26: S11 of the array in Figure 7-23

The radiation pattern, Theta and Phi cuts of the co- and cross-polarisation are presented in Figure 7-27. The measured and simulated patterns look very similar, and the E-Theta cuts show that the measured pattern beamwidth is similar to the simulated beamwidth (27˚ vs 29˚). The measured gain is within 0.5 dB of the simulated gain (18.8

dB vs 18.96 dB). The two E-Theta pattern cuts appear to be off-set by approximately 4˚. This offset could be due to a misalignment in elevation between the antenna under test and the reference antenna, but it could also be due to the reflecting patches on the reflecting substrate radiate. The radiated power by these patches combine in a slightly higher elevation angle compared to the simulations, which would suggest that the feeding patches plane is not perfectly perpendicular to the reflecting substrate, and that the reflecting patches are illuminated at a different (higher) angle compared to the simulations. The E-Phi cuts shows that the simulated beamwidth in Phi direction is wider compared to the measured beamwidth (27˚ vs 21˚), however, if the simulation cut is taken at the same angle as for the measurement cut (-27˚), the beamwidths become more similar.

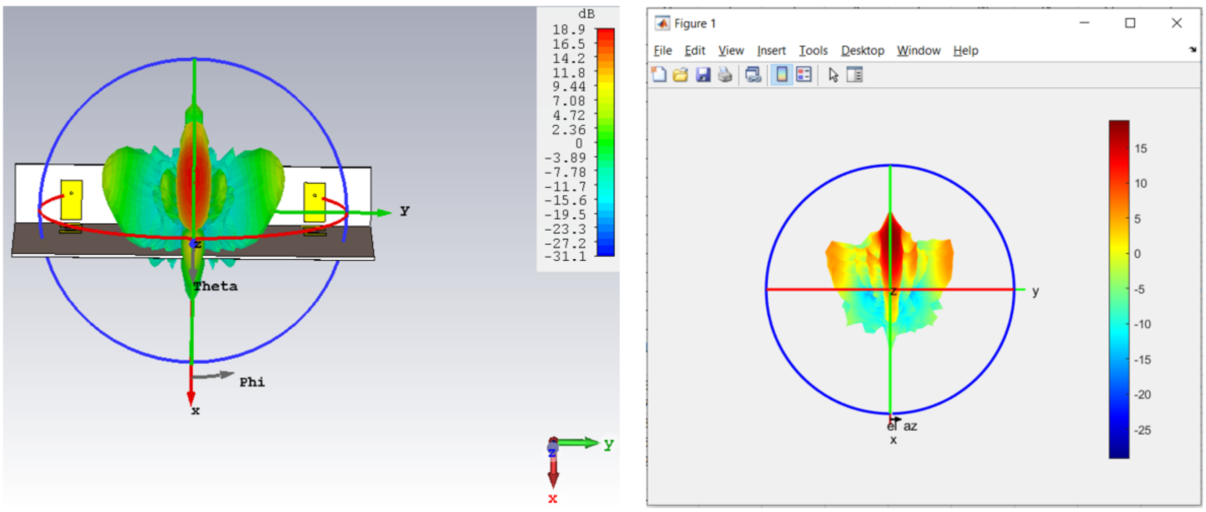

Simulation

Measurement

(a)

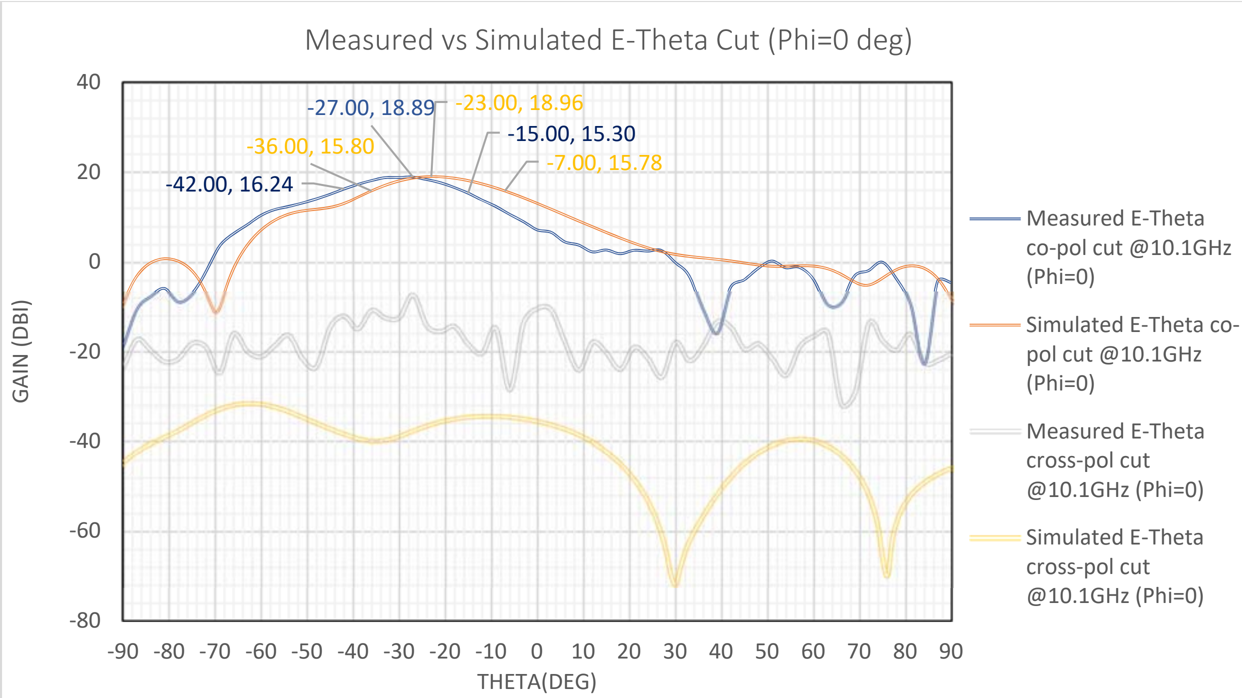

(b)

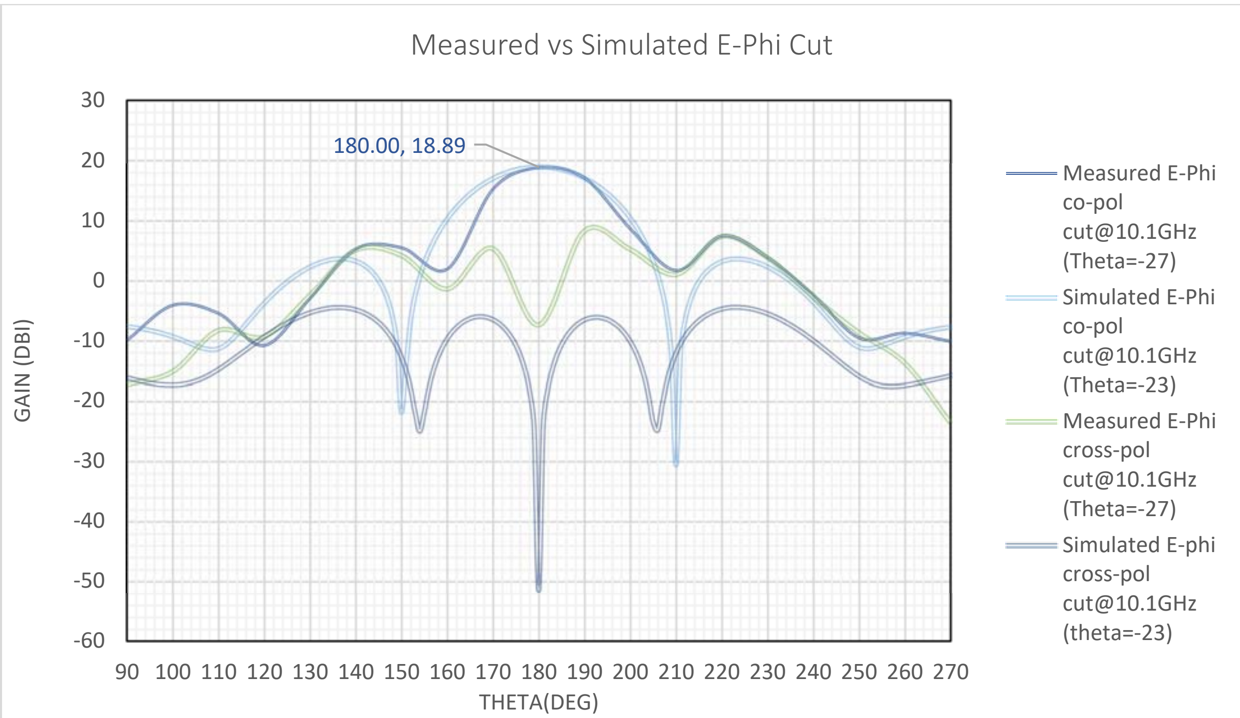

(c)

Figure 7-27: Simulated versus measured co-pol patterns (a) and Co-pol and Cross-pol Theta cuts (b) and Phi cuts (c) of four-element patch antenna array with reflecting patches on reflecting substrate. Each patch in the array operates in 2nd mode.

The presence of the reflecting patches on the reflecting substrate has improved the gain by approximately 1.5 dB compared to 2.5 dB improvement seen in simulations. This could be because of the angle under which the reflecting patches are illuminated by the fed patches.

Again, the measured cross-pol levels are higher than the simulations, and that could be explained by the feed asymmetry of each patch and the reflections that occur from behind of the antenna under test, where the feeding network was kept.

The gain drop (~3 dB) over frequency is shown in Figure 7-28.

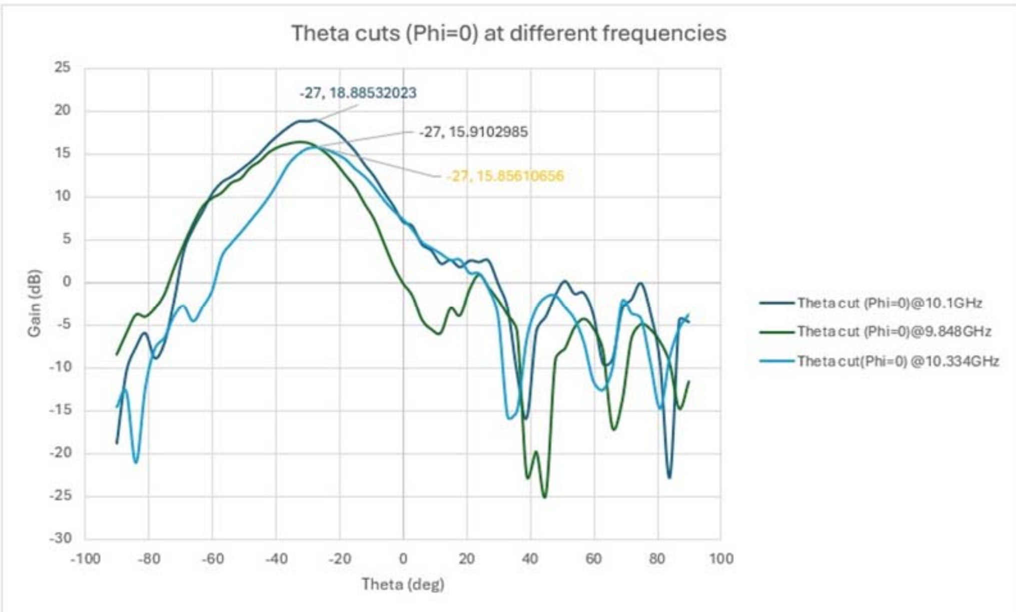

(a)

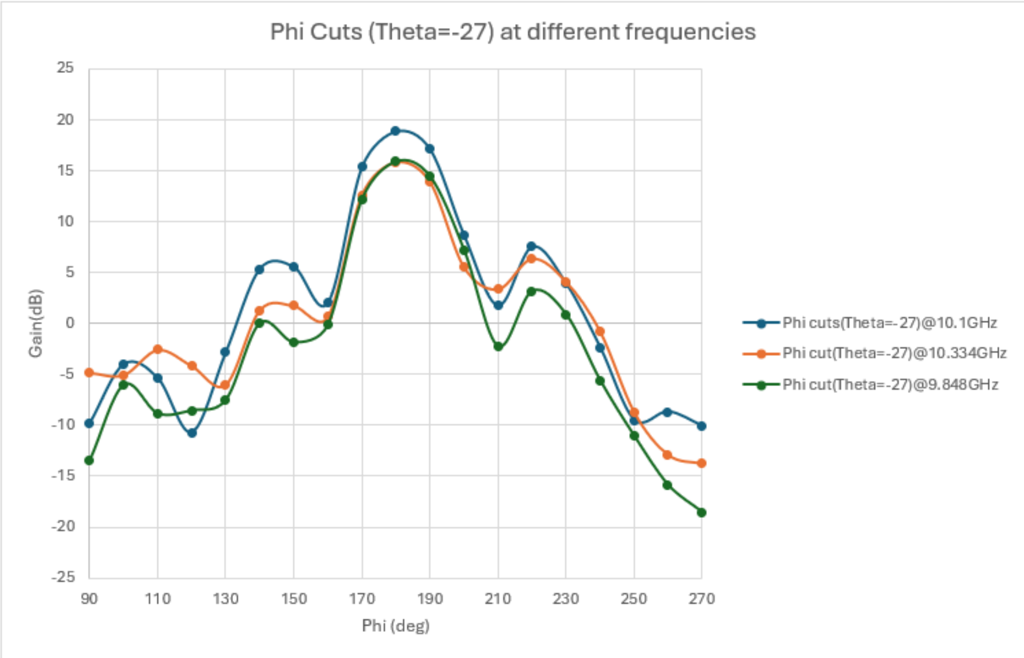

(b)

Figure 7-28: Pattern changes with frequency (a) Theta cut (b) Phi cut relating to array in Figure 7-23

7.6 Four patch antenna array in presence of reflecting substrate covered with reflecting patches with phase shifters

The four-element antenna array presented in the previous section is equipped with phase shifters on each SMA connector to evaluate the scan the beam in Azimuth (ZY plane). Table 7-1 presents the simulation results when progressive phase is introduced at the input of the scaled antennas. As it can be observed, on the scaled antennas, similar angular beam travelling is obtained in Phi Direction (approx. 62˚), as it has been obtained in Chapter 6, for a 3 dB decrease of the main lobe magnitude.

Table 7-1: Beam scanning of the 10 GHz scaled antenna with Huber and Suhner SMA connector

Structure scaled for 10GHz, with H&S SMA connector								
Progressive Phase (deg)	0	30	60	90	120	140	150	180
Phi Lobe Magnitude (dB)	19	18.9	18.5	17.9	17	16.2	15.7	14
Phi Lobe Direction (deg)	180	-172	-164	-158	-153	-149	-147	144
Phi 3dB BW (deg)	23.1	23.2	22.9	21.4	20.9	20.8	-20.5	19.2
Phi Sidelobes (dB)	-14.8	-13	-11.8	-11.1	-10.2	-7.3	-4.9	-9.1
Theta Lobe Magnitude (dB)	19	18.9	18.5	17.9	17	16.2	15.7	13.9
Theta Lobe Direction (deg)	-25	-25	-26	-28	-29	-32	-32	-35
Theta 3dB BW (deg)	29.7	27.5	23.2	20.7	18.4	18.2	17.7	16.4
Theta Sidelobes (dB)	-15.3	-17	-18	-18.4	-17.7	-14.7	-13.8	-11.1

On the measured antenna array, a -30˚ progressive phase shift has been imposed at the input of each feeding patch through the installed phase shifters to steer the beam in Azimuth.

Each phase shifter was capable of producing only 150˚ of phase shift at 10 GHz. Figure 7-29 represents a part of the phase shifter's datasheet, which describes its performance.

PTS-A3A8-18-15*f	18GHz Phase adjustable SMA plug to SMA jack 15°×f(GHz); 18Ghz VSWR 1.4
Interface	
Standard	MIL-STD-348B
Mechanically compatible with	2.92 & 3.5
Electrical Data	
Impedance	50Ω
Frequency Range	DC To 18GHz
VSWR	≦1.15(DC to 6GHz);≦1.25 (6 to 12GHz); ≦1 .4 (12 to 18GHz)
Insertion Loss	≦0.5 dB
Insulation Resistance	≧5000MΩ
Dielectric Withstanding Voltage (at sea	1500 V rms
level) Working Voltage (at sea level)	500 V rms

*Figure 7-29: PTS-A3A8-18-15*f phase shifter's performance*

Initially, the phase at the input of each feed of a patch was measured and the relative phase between patches was calculated. The required phase at the input of each patch was determined by adding a progressive phase of -30˚ to the relative phase value. The obtained values are shown in Figure 7-30. As it can be observed, the highest phase value was required on phase shifter #4 (-152.2˚).

	Initial Phase	Relative Phase	Relative Phase+30deg progressive phase	Required Phase	Realised Phase	Loss
Shifter 4	-39.5	-22.7	-112.7	-152.2	-153.5	-8.2
Shifter 3	-49	-13.2	-73.2	-122.2	-122.4	-8.6
Shifter 2	-62.2	0	-30	-92.2	-92.5	-8.26
Shifter 1	-27.9	-34.3	-34.3	-62.2	-62.6	-8.17

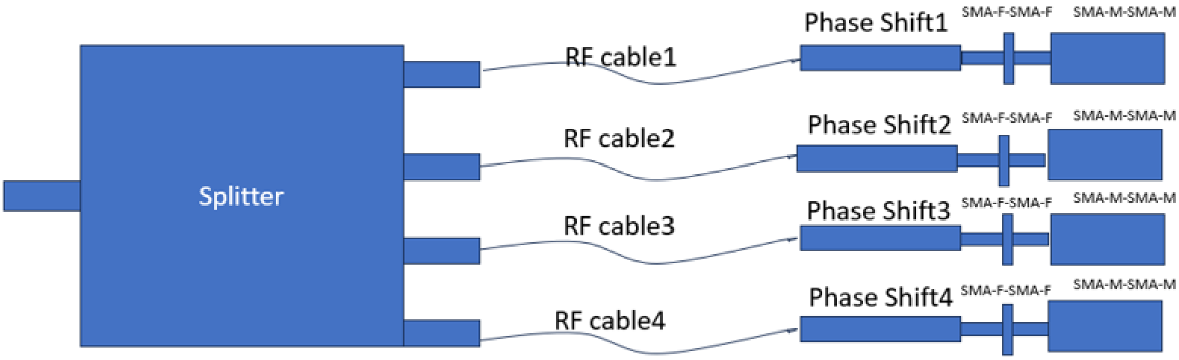

Figure 7-30: The required phase shift and realised phase at the input of each patch antenna

The radiation pattern, with Theta and Phi pattern cuts are presented in Figure 7-31. The measured and simulated patterns are similar and the measured gain is within 0.5 dB of the simulated gain (18.4 dB vs 18.7 dB). As in the previous section, the two E-Theta pattern cuts appear to be off-set by approximately 4˚.

This offset could be the result of a misalignment in elevation between the antenna under test and the reference antenna, but it could also be due to error in radiation of the reflecting patches on the reflecting substrate. The radiated power by these patches combine in a slightly higher elevation angle compared to the simulations, which would suggest that the plane of the feeding patches is not perfectly perpendicular to the reflecting substrate, and that the reflecting patches are illuminated at a different (higher) angle compared to the simulations.

The E-Phi cuts show that the simulated beamwidth in Phi direction is slightly wider compared to the measured beamwidth, and is in off-set by 3˚ compared to the measurements.

It must be mentioned that the Phi measurement step size was 10˚, and therefore on each frequency, only 19 points were interpolated to give the Phi pattern cuts. This means that in reality, the beam widths could be wider than the plots where the measured points have been interpolated.

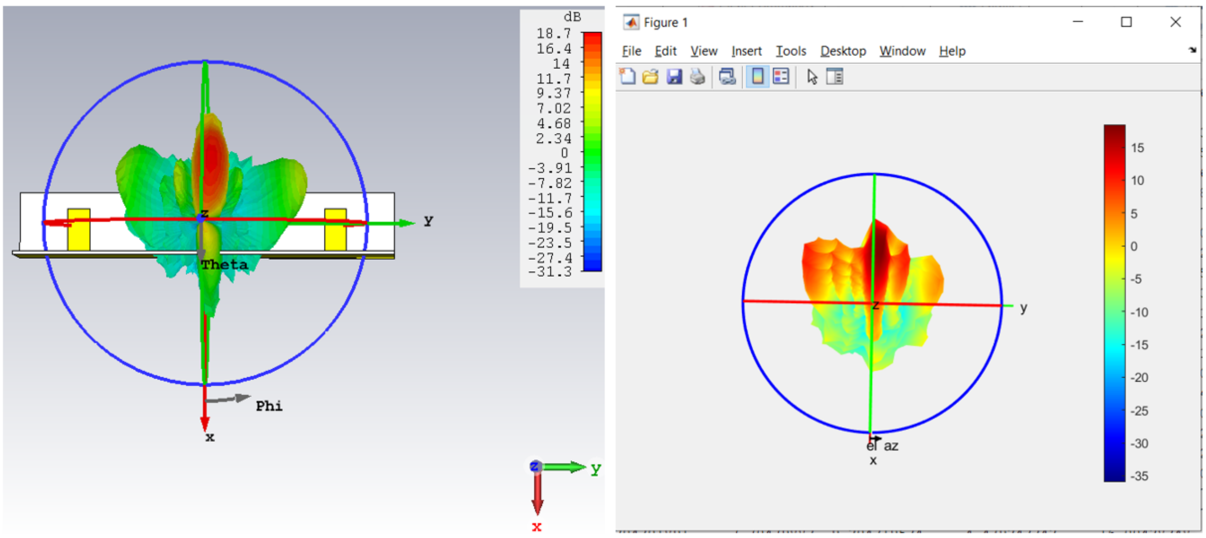

(a)

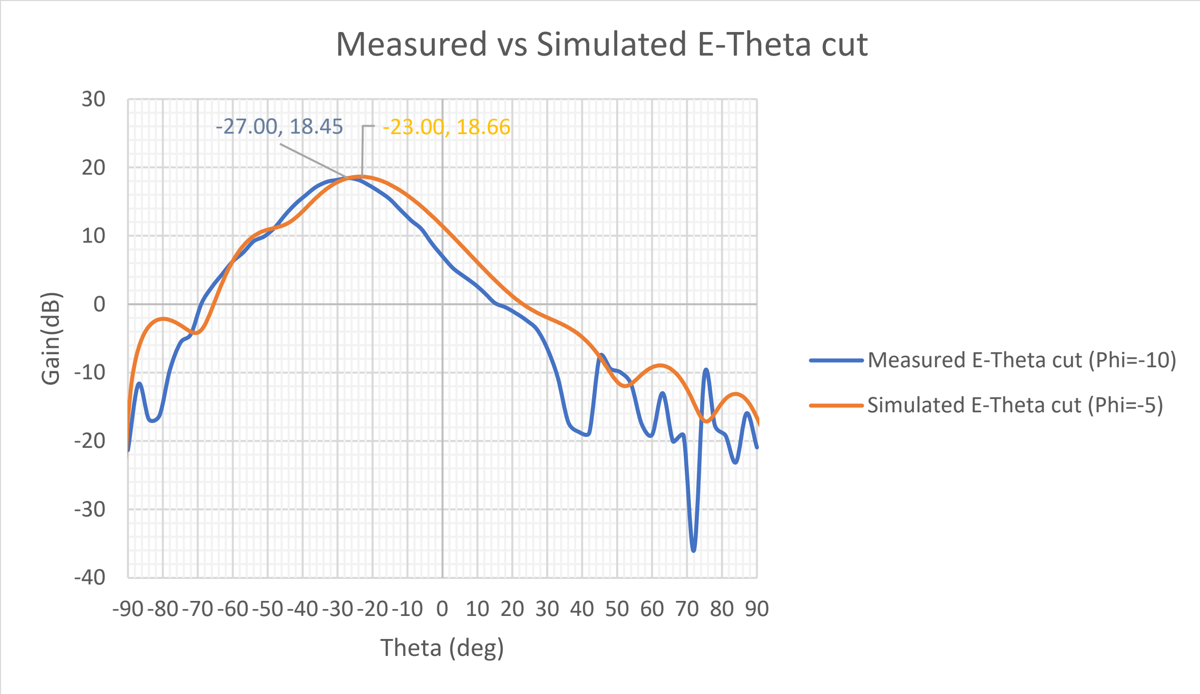

(b)

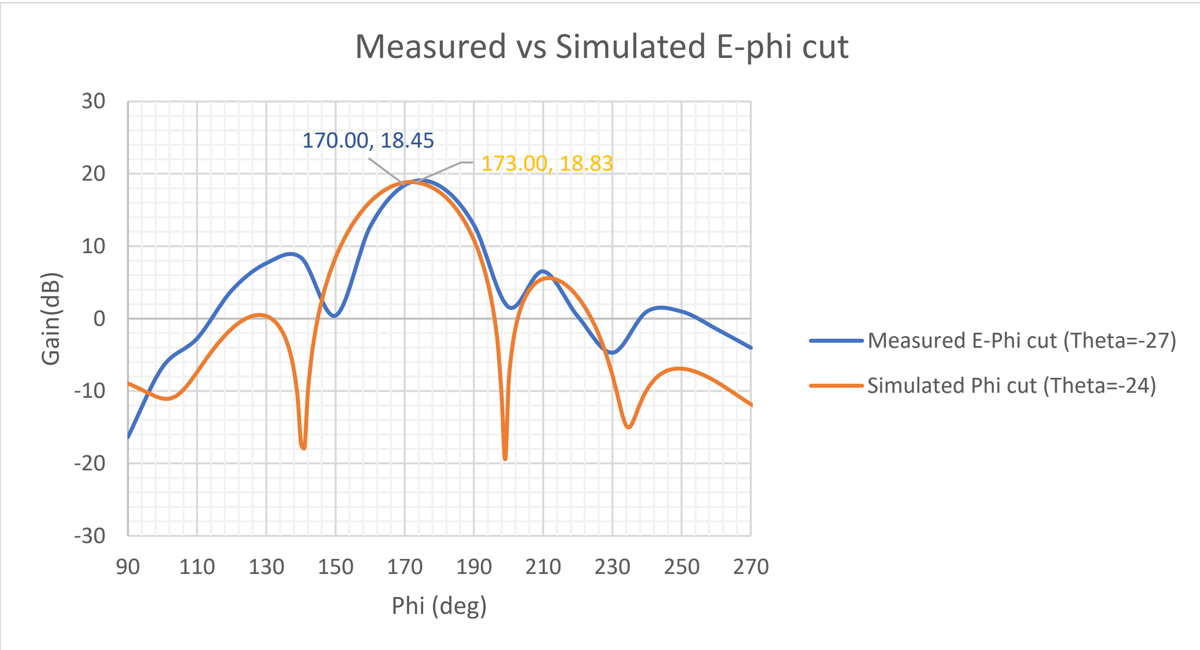

(c)

Figure 7-31: Simulated versus measured co-pol patterns (a) Theta cuts (b) and Phi cuts (c) of four element patch antenna array with reflecting patches on reflecting substrate utilizing phase shifters to steer the radiation beam

The measurement results showed that with 30˚ progressive phase at the input of the patches, the beam steered by approximately 10˚, which is very close to the simulation results, where the beam steered by approximately 7˚-8˚.

7.7 Conclusions

A set of 5 antennas scaled to operate close to 10 GHz was built and tested to prove that the concept and the simulations presented in the previous chapters at 30 GHz (mm-wave) are correct. The antennas have been tested in the anechoic chamber using 19 measurement points (per frequency) for Phi cuts (10˚ Phi steps) and 61 points (per frequency) for Theta cuts (3˚ Theta steps). These points have been interpolated to give the plots presented in this chapter.

The measurement results presented good correlation with the simulations, proving that the antennas have been designed, built and tested correctly, and that the efficiencies of the tested antennas are in the range of the efficiencies obtained by simulation.

The pattern cuts revealed slightly higher gain on measured patterns and narrower beamwidths, but this could be caused by the relatively small number of points taken for Phi cuts and the interpolation between the measured points. The measured cross-polarisation levels where higher than in simulations. That could be explained by a higher patch feed asymmetry due to manufacturing errors, and also the reflections caused by the feeding network placed at the back of the antennas.

The presence of the reflecting patches improved the gain of the antenna only by 1.5 dB (compared to 2.5 dB shown by simulation), which could indicate that the feeding patches did not illuminate/excite the reflecting patches under the same angle as in simulations. If the feeding patches plane is not perpendicular to the reflecting substrate, then the reflecting patches would be excited under a different angle and that would affect the results.

Overall, the measurement results proved that the second mode concept of the patch antenna as exploited in this work for the first time is useful and that the patch antenna gain can be improved by exciting the second mode of operation while adding an adjacent reflecting substrate. Further improvement was achieved when reflecting patches are arranged appropriately over the reflecting substrate.

8. Conclusions and future work

8.1 Conclusions

A novel microstrip patch antenna array (57 mm x 28.5 mm x 9.5 mm) has been designed to operate at 30 GHz, which provided 19 dBi of gain. The microstrip patches operate in the second mode, TM020, where the main beam is split symmetrically about the boresight axis. By adding an adjacent reflecting substrate vertically to the patch substrate, the gain of the patch has been enhanced. Further improvement in the gain has been shown possible by employing reflector patches on the reflecting substrate. Therefore, the so designed antenna structures in single or array form can be considered to benefit from a reflect array architecture where the fed patches/patch illuminate/s the reflecting elements. The reflecting patches have been designed based on the reflect-array element theory.

This antenna design meets the antenna requirements introduced through a scenario with 58 satellites orbiting 550 km above the Earth.

The antenna beam is shown to steer in Azimuth by imposing progressive phase shift at the input of the feeding patches. The beam was shifted approximately 62˚ for a 3 dB drop in gain. An attempt to shift the beam in elevation was made, by adding a second row of feeding patches above the existing ones (i.e.: then the array is 2D). This attempt proved unsuccessful, as the array element radiation pattern and the array factor pattern produced sidelobes, which reduced the gain of the antenna.

To test that the theory and simulations presented were correct, a set of five antennas have been scaled to operate at 10 GHz (171 mm x 85.5 mm x 28.5 mm). The reason for the scaled version is the availability of an industrial measurement system in x-band (which by the way is within the microwave satellite band). The scaled versions of the antennas have been built in the Essex lab and tested in the anechoic chamber at Surrey Satellite site. Largely, the measurement results showed good agreement with the simulations, and the gains of the antennas obtained were as expected theoretically (via simulation). Some high cross-polarisation levels have been detected in some cases, but that could be due to the inevitable feeding asymmetry of the array elements and also because of the reflections caused by the feeding network placed behind the antenna under test.

The measured beamwidths appeared to be slightly narrower than those from simulations, and that could be because the coarse Phi measurement step (10˚) for each frequency and the interpolation of the measured points in a graph.

Contrary to the theoretical expectation, however, the reflecting patches improved the gain only by approximately 1.5 dB compared to the simulation prediction of 2.5 dBi, and one reason for this could be that the feeding patches were not illuminating the reflecting patches at the same angle as in the simulations. This could happen if the feeding patches plane is not perpendicular enough to the reflecting substrate.

Given the observed limitations of the tested antennas, a way forward to improve their performance is to have them remeasured into the anechoic chamber, where the feeding network placed at the back of the antenna is covered with absorbing material. This will stop any radiation caused at the back of the antenna under test. Also, the Phi step size should be decreased to provide more measurement points. If the cross-polarisation level is still high it means that the feeding asymmetry of the feeding patches is the main cause of this issue. Following the solutions given in [164], one way to improve the cross-polarisation level is to employ differential feeding on one patch and rotational feeding on antenna array.

8.2 Future Work

A closer look into the reflecting elements on the reflecting substrate can be beneficial, as different shape elements may result in improving the antenna gain further. The potential beam scanning in the elevation should also be re-explored, especially if new reflecting elements are used.

The gain of the feeding patch can perhaps be improved further, and also, other dielectric materials, which are cheaper and easier to procure, could be used.

Further future research works (which can be suggested) encompass experimental works at 30 GHz including fabrication, measurement and may be redesign of various antennas considered in this work while employing appropriate integrated phase shifters within the arrays for beam steering. For example, liquid crystal phase shifters [146] are very small and can be fairly easily integrated within a layer of planar arrays. Of course, this activity is by itself a major research task.

REFERENCES

[1]: M. Rabani, H. Shiraz, "Improvement of microstrip patch antenna gain and bandwidth at 60 GHz and X bands for wireless applications", *IET Microwave Antennas & Propagation, pp. 1167-1173, April 2016.*

[2]: A. Kumar, R. Khandelwal, A. Makhdumi, S. Singh, "A review on gain enhancement techniques of microstrip antenna", *Intelligent Engineering and Management (ICIEM), pp. 476-479, 2021.*

[3]: S. Akinola, I. Hashimu, G. Singh, "Gain and Bandwidth Enhancement Techniques of Microstrip Antenna: A Technical Review", *International Conference on Computational Intelligence and Knowledge Economy, pp.175-180, December 2019.*

[4] G. Kristensson, P. Waller, A. Derneryd, "Radiation efficiency and surface waves for patch antennas on inhomogeneous substrate", *IEE Microwaves, Antennas and Propagation, pp. 477-483, 2003.*

[5] B. Nel, A. Skrivervik, M. Gustafsson, "Radiation Efficiency and Gain Bounds for Microstrip Patch Antennas", *IEEE Transactions on Antennas and Propagation, pp. 873-883, 2025.*

[6]: Application of Kuiper Systems LLC for Authority to Launch and Operate a Non-Geostationary Satellite Orbit System in Ka-band Frequencies, Technical Appendix, Available at: https://cdn.arstechnica.net/wp-content/uploads/2019/07/amazon-Technical-Appendix.pdf, Accessed: 11/12/2021.

[7]: ITU Radio Regulations, Available at: https://life.itu.int/radioclub/rr/art22.pdf, Accessed: 11/12/2021.

[8]: W. He, B. Xu, Y. Yao, D. Colombi, Z. Ying and S. He, "Implications of Incident Power Density Limits on Power and EIRP Levels of 5G Millimeter-Wave User Equipment", *IEEE Access, pp.148214-148225, 2020*.

[9]: P. Arapoglou, S. Cioni, E. Re, A. Ginesi, "Direct Access to 5G New Radio User Equipment from NGSO Satellites in Millimeter Waves", *2020 10th Advanced Satellite Multimedia Systems Conference and the 16th Signal Processing for Space Communications Workshop (ASMS/SPSC), pp.1-8, 2020.*

[10]: D. A. Ogundele, Y. A. Adediran, "History of Satellite Broadcasting: Development and Advancement of Radio and Television Technology", *National Space Research and Development Agency (NASRDA)*, *2015.*

[11]: V. Mignone, M-A. Vázquez-Castro, "The Future of Satellite TV: The Wide Range of Applications of the DVB-S2 Standard and Perspectives", *Proc. IEEE 99(11), pp. 1905-192, 2011.*

[12]: The Satellite Industry Association, Available at: https://sia.org/satellites-services/mobile-communications/, Accessed: 21/04/2021.

[13]: System Assessment and Validation for Emergency Responders: SAVER Tech Note, Available at: https://www.dhs.gov/sites/default/files/publications/Satellite-Phones-TN_0615-508_0.pdf, Accessed: 21/04/2021.

[14]: I. L. Mayorga, B. Soret, M. Röper, D. Wübben, B. Matthiesen, A. Dekorsy, P. Popovski, "LEO Small-Satellite Constellations for 5G and Beyond-5G Communications", *IEEE Access, pp. 184955-184964, 2020.*

[15]: Iridium Blog, Available at: https://www.iridium.com/blog/2018/09/11/satellites-101-leo-vs-geo/, Accessed: 21/04/2021.

[16]: K. Dredge, M. Arx, I. Timmins, "LEO constellations and tracking challenges", Available at: *www.satelliteevolutiongroup.com/articles/LEO-Constellations&Tracking.pdf* , Accessed: 20/01/2018.

[17]: S. Cakaj, B. Kamo, V. Kolici, O. Shurdi, "The Range and Horizon Plane Simulation for Ground Stations of LEO Satellites", *IJCNS, pp. 585-589, 2011.*

[18]: S. Cakaj, M. Fischer, A. Scholtz, "Practical Horizon Plane for Low Earth Orbit (LEO) Satellite Ground Stations", *WSEAS International Conference on Telecommunications and Informatics, pp. 62-67, 2009.*

[19]: S. Cakaj, B. Kamo, A. Lala, A. Rakipi, "The Coverage Analysis for Low Earth Orbiting Satellites at Low Elevation", *IJACSA, pp. 6-10, 2014.*

[20]: Y. Su, Y. Liu, Y. Zhou, J. Yuan, H. Cao, and J. Shi "Broadband LEO Satellite Communications: Architectures and Key Technologies", *Space Information Networks, pp. 55-61, 2019.*

[21]: SpaceX Non-Geostationary Satellite System, Attachment A, Technical Information to Supplement Schedule S, 2015, Available at: https://fcc.report/IBFS/SAT-MOD-20181108-00083/1569860.pdf, Accessed: 20/01/2018.

[22]: Request for Modification of the Authorization for the SpaceX NGSO Satellite System, Available at: https://docs.fcc.gov/public/attachments/FCC-21-48A1.pdf , Accessed: 20/01/2018.

[23]: Application for Modification of Authorization for the SpaceX NGSO Satellite System, Available at: https://fcc.report/IBFS/SAT-MOD-20200417-00037/2274315.pdf, Accessed: 20/01/2018.

[24]: I. Portillo, B. Cameron, E. Crawley, “A Technical Comparison of Three Low Earth Orbit Satellite Constellation Systems to Provide Global Broadband”, *Acta Astronautica, pp. 1-16, 2019.*

[25]: SpaceX Non-Geostationary Satellite System Attachment on A Technical Information to Supplement Schedule S, Available at: https://fcc.report/IBFS/SAT-MOD-20181108-00083/1569860.pdf, Accessed: 20/01/2018.

[26]: FCC - SpaceX V-Band Non-Geostationary Satellite System, Attachment A, Technical Information to Supplement Schedule S, Available at: https://fcc.report/IBFS/SAT-LOA-20170301-00027/1190019.pdf, Accessed: 20/01/2018.

[27]: What is Stralink?, Available at: https://uk.pcmag.com/networking/132246/what-is-starlink-spacexs-much-hyped-satellite-internet-service-explained, Accessed: 04/05/2020.

[28]: FCC – OneWeb Non-Geostationary Satellite System, Attachment A, Technical Information to Supplement Schedule S, Available at:

https://licensing.fcc.gov/myibfs/download.do?attachment_key=1134939#, Accessed: 04/05/2020.

[29]: Ofcom – Strategic Review of Satellite and Space Science use of spectrum – Call for input, Available at: https://www.ofcom.org.uk/__data/assets/pdf_file/0014/51260/oneweb.pdf, Accessed 04/05/2020.

[30]: Oneweb launches, Available at: https://www.oneweb.world/launches, Accessed: 07/05/2021.

[31]: Petition for Declaratory Ruling to Grant Access to the U.S. Market for Telesat's NGSO Constellation, Available at: FCC INTERNATIONAL BUREAU, Accessed: 07/05/2021.

[32]: Application for Modification of Market Access Authorization, Available at: https://fcc.report/IBFS/SAT-MPL-20200526-00053/2378318.pdf, Accessed: 07/05/2021.

[33]:https://www.circleid.com/posts/20201229-telesat-proposal-for-larger-constellation-canadian-darpa-contracts/, accessed on 07/05/2021.

[34]:Telesat Update-Proposal for a Larger Constellation, Available at: https://www.telesat.com/wp-content/uploads/2021/04/Telesat-Lightspeed-Specifications-Sheet.pdf , Accessed: 07/05/2021.

[35]: M. Mitry, "Routers in space: Kepler communications' CubeSats will create an Internet for other satellites", *IEEE Spectrum, pp. 38-43, 2020.*

[36]: SpaceX Falcon9, Available at: https://www.spacex.com/vehicles/falcon-9/, Accessed: 08/05/2021.

[37]: One Web's Approach to to Space Debris Mitigation, Available at: https://www.unoosa.org/documents/pdf/hlf/HLF2017/presentations/Day3/Special_Session/Presentation2.pdf, Accessed: 08/05/2021.

[38]: Telesat Reply on FCC Orbital Debris Mitigation, Available at: https://ecfsapi.fcc.gov/file/1109723118843/Telesat%20Reply-FCC%20Orbital%20Debris-9Nov2020.pdf, Accessed: 08/05/2021.

[39]: B. Lee, J. Lee, K. Choi "Analysis of a Station-Keeping Manoeuvre Strategy for Three Geostationary Satellites Collocation", *IFAC Proceedings Volumes, pp. 295-300, 1998.*

[40]: A. Rolinski, D. Carlson, R. Coates, "The X-Y Antenna Mount for Data Acquisition from Satellites", *IRE Transactions On Space Electronics and Telemetry, pp.159-163, 1962.*

[41]: C. Balanis, *Antenna Theory Analysis and Design*, Fourth Edition, Wiley, 2016.

[42]: D. Pozar, *Microwave Engineering*, Fourth Edition, John Wiley and Sons, 2011.

[43]: D. Roddy, *Microwave Technology*, Prentice Hall,1986.

[44]: R. Mailloux, *Phased Array Antenna Handbook*, Second Edition, Artech House, 2005.

[45]: R. James, F. Fernandez, S. Day, S. Bulja, D. Mirshekar-Syahkal and M. Yazdanpanahi, "Finite element analysis of a balanced microstrip line filled with nematic liquid crystal", *IEEE MTT-S Int. Microwave Symp. Dig., Boston, pp. 133-136, 2009*.

[46]: M. Abbasi, M. Dahri, M. Jamaluddin, N. Seman, M. Kamarudin, N. Sulaiman, "Millimeter Wave Beam Steering Reflectarray Antenna Based on Mechanical Rotation of Array", *Special Section on Antenna and Propagation for 5G and Beyond, pp. 145685-145691, 2019.*

[47]: P. Delos, B. Broughton, J. Kraft, "Phased Array Antenna Patterns—Part 1: Linear Array Beam Characteristics and Array Factor", *Analog Devices, pp. 1-7, 2020.*

[48]: N. Host, H. Vo, C. Chen, "Causes of Low Scanning Angle Issues in Phased Array Antennas", *IEEE Antennas and Propagation, pp. 101-102, 2013.*

[49]: D. Pozar, D. Schaubert, "Scan Blindness in Infinite Phased Arrays of Printed Dipoles", *IEEE Transactions on Antennas and Propagation, pp. 602-610, 1984.*

[50]: F. Capolino, S. Boscolo, "Elimination of Scan Blindness in Phased Array Antennas Using a Grounded-Dielectric EBG Material*", IEEE Antennas and Wireless Propagation Letters, pp.106-109, 2016.*

[51]: P. Delos, B. Broughton, and J. Kraft, "Phased Array Antenna Patterns - Part 2: Grating Lobes and Beam Squint", *Analog Devices, pp. 1-5, 2020.*

[52]: Metamaterial Surface Antenna Technology, Available at: https://www.kymetacorp.com/wp-content/uploads/2019/06/Metamaterial-Surface-Antenna-Technology.pdf, Accessed: 24/05/2021.

[53]: Kymeta Interoperability, Available at: https://www.kymetacorp.com/news/kymeta-interoperability-kepler-leo-satellites-promises-powerful-connectivity-future-kymeta-u8-terminal/, Accessed: 24/05/2021.

[54]: Kymeta U8 Antenna datasheet, Available at: https://www.kymetacorp.com/wp-content/uploads/2021/02/700-00071-000-revF-Kymeta-u8-antenna-product-sheet.pdf, Accessed: 24/05/2021.

[55]: Phasor Corporation, Available at: https://www.hanwha-phasor.com/, Accessed: 27/05/2021.

[56]: Square Space, Available at: https://static1.squarespace.com/static/5a94914f5ffd20adbfc1b2f4/t/5eb45a9108f6802da116e371/1588877971963/smw0520.pdf, Accessed: 31/05/2021.

[57]: Isotropic Corporation, Available at: https://www.isotropicsystems.com/, Accessed: 31/05/2021.

[58]: Satixfy Multi-Beam Phased Array, Available at: http://www.satixfy.com/wp-content/uploads/2019/04/SatixFy-TF-Reprint-2019-04.pdf, Accessed: 01/06/2021.

[59]: Satixfy Corporation, Available at: https://www.satixfy.com/, Accessed: 01/06/2021.

[60]: Thinkom Corporation, Available at: https://www.thinkom.com/, Accessed: 20/06/2021.

[61]: J. Gao, X. Lei, J. Wu, T. Li, "Theoretical Model for Patterns of VICTS Antenna", *17th IEEE International Conference on Communication Technology, pp. 728-731, 2017*.

[62]: First look at Starlink Phased Array antenna PCB, Available at: https://www.reddit.com/r/rfelectronics/comments/k14vl0/first_look_at_starlink_phased_array_antenna_pcb/, Accessed: 22/06/2021.

[63]: Z. Ying, "Antennas in Cellular Phones for Mobile Communications", *Proceedings of the IEEE, pp 2286-2296, 2012.*

[64]: Ofcom and 5G, Available at: https://www.ofcom.org.uk/about-ofcom/latest/features-and-news/clearing-up-myths-5g-and-coronavirus, Accessed: 30/06/2021.

[65]: C. Balanis, *Modern Antenna Handbook*, First Edition, John Wiley and Sons, 2008.

[66]: T. Handdrell, M. Phocas, N. Ricquier, "Mobile Phone GPS Antenna", *Antenna Technology, pp. 29-35, 2010.*

[67]: C. Chiu, Y. Chi, "Multi band folded loop antenna for smart phones*", Progress in Electromagnetic Research, pp. 213-226, 2010.*

[68]: P. Wang, Y. Shao, D. Huang and M. Basit, “A Compact Coupled-Fed Loop Antenna for Mobile LTE Smartphones”, *International Journal of Antennas and Propagation, pp. 1-8, 2018.*

[69]: M. Khalifa, L. Khashan, H. Badawy, Fawzy Ibrahim, “Broadband Printed-Dipole Antenna for 4G/5G Smartphones”, *Journal of Physics: Conference Series, pp. 1-9, 2019.*

[70]: H. Ullah, F. Tahir, “Broadband planar antenna array for future 5G communication standards”, *IET Microwaves, Antennas & Propagation, pp. 2661-2668, 2019.*

[71]: A. Munir, Hermanto, ”Normal Mode 3.3 GHz Bifilar Helical Antenna for Wireless Communication”, *Proc. of the 2017 IEEE Region 10 Conference (TENCON), Malaysia, pp. 2923-2926, 2017.*

[72]: A. Pandey, S. Pathak, “Design of Normal Mode Circularly Polarised Helical Antenna at 5.3 GHz”, *7th Uttar Pradesh Section International Conference on Electrical, Electronics and Computer Engineering, pp. 1-3, 2020.*

[73]: Update on 5G spectrum in the UK, Available at: https://www.ofcom.org.uk/__data/assets/pdf_file/0021/97023/5G-update-08022017.pdf, Accessed: 28/08/2021.

[74]: S. Kumar, A. Dixit, R. Malekar, H. Raut, L. Shevada, “Fifth Generation Antennas: A Comprehensive Review of Design and Performance Enhancement Techniques”, *IEEE Access, pp. 163568- 163593, 2020.*

[75]: P. Arapoglou, S. Cioni, E. Re, A. Ginesi, “Direct Access to 5G New Radio User Equipment from NGSO Satellites in Millimeter Waves”, *10th Advanced Satellite*

Multimedia Systems Conference and the 16th Signal Processing for Space Communications Workshop (ASMS/SPSC), pp.1-8, 2020.

[76]: M. Marcus, “ITU WRC-19 Spectrum Policy Results”, *IEEE Wireless Communications, pp. 4-5, 2019.*

[77]: Telesat to Redefine Global Broadband Connectivity with Telesat Lightspeed, the World’s Most Advanced Low Earth Orbit (LEO) Satellite Network, Available at: https://www.telesat.com/press/press-releases/manufacturer-announcement/, Accessed: 07/05/2021.

[78]: 5G mobile technology: a guide, Available at: https://www.ofcom.org.uk/__data/assets/pdf_file/0015/202065/5g-guide.pdf, Accessed: 28/07/2021.

[79]: Satellite Solutions for 5G - ECC Report, Available at: https://www.ecodocdb.dk/document/category/ECC_Reports?status=ACTIVE, Accessed: 16/02/2019.

[80]: P. Zhong, T. Wang, S. Wang, “A UWB antenna for 5G millimeter wave frequency band”, *2020 International Conference on Microwave and Millimetre Wave Technology, pp. 1-3, 2020.*

[81]: J. Kulkarni, C. Sim, “Low-Profile, Multiband & Wideband ‘C-Shaped’ Monopole Antenna for 5G and WLAN Applications”, *2020 International Conference on Radar, Antenna, Microwave, Electronics and Telecommunications, pp. 366-371, 2020.*

[82]: M. Ullah, M. Khan, R. Kabir, M. Alim, “High Performance 5G Microstrip Dipole Antennas for 39 GHz Band”, *2019 IEEE International Conference on Signal Processing, Information, Communication & Systems (SPICSCON), pp. 74-77, 2019.*

[83]: S. Wu, A. Zhao and Y. Zhao, “Wideband Dipole Antenna and Array Based on Liquid Crystal Polymer for 5G Applications”, *2019 IEEE Asia-Pacific Microwave Conference (APMC), pp. 438-440, 2019.*

[84]: A. Kaddour, J. Milbrandt, C. Menudier, T. Marc, P. Pouliguen, P. Potier, M. Romier, “Performances of Magneto-Electric Dipoles in an Antennas Array with a Reduced Beam Forming Network”, *Proceedings of the 16th European Radar Conference, pp. 385-388, 2019.*

[85]: M. LI , K. LUK, “A Low-profile Magneto-electric Dipole Antenna”, *2012 IEEE International Workshop on Electromagnetics: Applications and Student Innovation Competition, pp. 1-2, 2012.*

[86]: B. Feng, J. LAI, Q. Zeng, K. Chung, “A Dual-Wideband and High Gain Magneto-Electric Dipole Antenna and Its 3D MIMO System With Metasurface for 5G/WiMAX/WLAN/X-Band Applications”, *IEEE access, pp. 33387-33398, 2018.*

[87]: G. Scalise, L. Boccia, G. Amendola, “An Ultralow Profile Magneto Electric Dipole for 5G Applications”, *TELSIKS, pp. 141-143, 2019.*

[88]: J. Zeng, K. Luk, “Millimeter-wave Magneto-electric Dipole Antenna”, *2013 Asia-Pacific Microwave Conference Proceedings, pp. 304-306, 2019.*

[89]: G. Scalise, L. Boccia, G. Amendola, M. Rousstia, A. Shamsafar, “Magneto-Electric Dipole antenna for 5-G applications”, *2020 14th European Conference on Antennas and Propagation (EuCAP), pp. 1-3, 2020.*

[90]: M. Nakajima, M. Ishikawa, and G. Sato, “28 GHz Side-Edge Loop Antenna with End-Fire Radiation Polarized Vertically to Substrate”, *2019 IEEE International*

Symposium on Antennas and Propagation and USNC-URSI Radio Science Meeting, pp. 877-878, 2019.

[91]: H. Zou, Y. Li, M. Peng, M. Wang, and G. Yang, “Triple-Band Loop Antenna for 5G/WLAN UnbrokenMetal-Rimmed Smartwatch”, *2018 IEEE International Symposium on Antennas and Propagation & USNC/URSI National Radio Science Meeting, pp. 463-464, 2018.*

[92]: W. Li, W. Chung, F. Hsiao, P. Chen, “Coupled-Fed Loop MIMO Antennas with Diverse Radiation Patterns for 5G Notebook Applications”, *2020 IEEE International Symposium on Antennas and Propagation and North American Radio Science Meeting, pp. 1323-1324, 2020.*

[93]: Y. Cheng, Y. Dong, “Compact Wideband Yagi Loop Antenna Array for 5G Millimeter-Wave Applications”, *2020 IEEE Asia-Pacific Microwave Conference (APMC), pp. 1081-1083, 2020.*

[94]: A. Hood, T. Karacolak, E. Topsakal, “A Small Antipodal Vivaldi Antenna for Ultrawide-Band Applications*”, IEEE Antennas and Wireless Propagation Letters (Volume 7), pp. 656-660, 2008.*

[95]: J. Qiu, Z. Yao, S. Qiu, N. Wang, “Research on an Antipodal Vivaldi Antenna Array for 5G Mobile Communication”, *2019 International Symposium on Antennas and Propagation (ISAP), pp. 1-2, 2019.*

[96]: A. Dixit, S. Kumar, “A Miniaturized Antipodal Vivaldi Antenna for 5G Communication Applications”, *2020 7th International Conference on Signal Processing and Integrated Networks (SPIN), pp. 800-803, 2020.*

[97]: S. Zhu, H. Liu, Z. Chen, P. Wen, “A Compact Gain-Enhanced Vivaldi Antenna Array with Suppressed Mutual Coupling for 5G mmWave Application”, *IEEE Antennas and Wireless Propagation Letters, pp. 776-779, 2018.*

[98]: Y. He, J. Papapolymerou, “Conformal Antipodal Vivaldi Antenna With Parasitic Elements For 5G Millimeter Wave Applications”, *2019 IEEE International Symposium on Antennas and Propagation and USNC-URSI Radio Science Meeting, pp. 271-272, 2019.*

[99]: A. Nakra, A. Vats, A. De, “Design Of High Bandwidth Circularly Polarised Antipodal Vivaldi Array for 5G Applications”, *2021 2nd International Conference for Emerging Technology (INCET), pp. 1-4, 2021.*

[100]: Y. Fu, D. Zhou, Y. Zhang, D. Lv, D. Zhang, “A Miniaturized Gain-Enhanced Antipodal Vivaldi Antenna for 5G Application”, *2020 International Conference on Microwave and Millimeter Wave Technology (ICMMT), pp.1-3, 2020.*

[101]: A. Praveena, V. Ponnapalli, “A Review on Design Aspects of Fractal Antenna Arrays”, *2019 International Conference on Computer Communication and Informatics (ICCCI), pp. 1-3, 2019.*

[102]: S. Haider, M. Wali, F. Tahir, M. Khan, “A Fractal Dual-Band Polarization Diversity Antenna for 5G Applications”, *2017 IEEE International Symposium on Antennas and Propagation & USNC/URSI National Radio Science Meeting, pp. 763-764, 2017.*

[103]: S. Raj, N. Kishore, G. Upadhyay, S. Tripathi, V. Tripathi, “A Compact Design of Circularly Polarized Fractal Patch Antenna for 5G Application”, *2018 IEEE MTT-S International Microwave and RF Conference (IMaRC), pp. 1-3, 2018.*

[104]: R. Malik, P. Singh, H. Ali and T. Goel, “A Star Shaped Superwide band Fractal Antenna for 5G Applications”, *2018 3rd International Conference for Convergence in Technology (I2CT), pp. 1-6, 2018.*

[105]: S. Patil, V. Rohokale, “Multiband Smart Fractal Antenna Design for Converged 5G Wireless Networks”, *2015 International Conference on Pervasive Computing (ICPC), pp. 1-5, 2015.*

[106]: S. Gundala, V. SrinivasaBaba, A. Vijaya, “Compact High Gain Hexagonal Fractal Antenna for 5G applications”, *2019 IEEE International Conference on Advanced Networks and Telecommunications Systems (ANTS), pp. 1-7, 2019.*

[107]: Dewiani, E. Palantei, R. Madika, M. Baharuddin, S. Syarif, “Design of Reconfigurable Planar Inverted F Antenna for 5G Implementation”, *2019 IEEE International Conference on Communication, Networks and Satellite (Comnetsat), pp. 41-46, 2019.*

[108]: A. Ghasemi and K. Wu, “A Wideband Planar Inverted-F Antenna for Ka-Band 5G System Applications”, *2020 IEEE International Symposium on Antennas and Propagation and North American Radio Science Meeting, pp. 1515-1516, 2020.*

[109]: K. Morshed, K. Esselle, M. Heimlich, D. Habibi, I. Ahmad, “Wideband Slotted Planar Inverted-F Antenna for Millimeter-Wave 5G Mobile Devices”, *2016 IEEE Region 10 Symposium (TENSYMP), pp.194-197, 2016.*

[110]: X. Yuan, Z. Chen, T. Gu, T. Yuan, “A Wideband PIFA-Pair-Based MIMO Antenna for 5G Smartphones”, *IEEE Antennas and Wireless Propagation Letters, pp. 371-375, 2021.*

[111]: Y. Chen, Q. Chu, “An UWB Inverted F Antenna with Coupled Feeding for 5G smartphone”, *2019 Cross Strait Quad-Regional Radio Science and Wireless Technology Conference (CSQRWC), pp. 1-2, 2019.*

[112]: P. Lu, R. Song, R. Fang, D. He, “Graphene film based Inverted-F Antenna for 5G Mobile Communications”, *2019 IEEE International Conference on Computational Electromagnetics (ICCEM), pp. 1-3, 2019.*

[113]: X. Hui, F. Shang, “An Inverted-F Antenna for 5G Communication Based on All-Metal Architecture”, *2020 International Conference on Microwave and Millimeter Wave Technology (ICMMT), pp. 1-3, 2020.*

[114]: M. Ye, Y. Zhang, C. Wu, J. Cheng, Z. Liu, “Dual-band Inverted-F Antenna with Tunable Inductor and Capacitor for 5G Mobile Communication”, *2018 IEEE International Conference on Integrated Circuits, Technologies and Applications (ICTA), pp. 149-150, 2018.*

[115]: Global Position System Low Noise Amplifier, Available at: https://www.nxp.com/docs/en/brochure/75016740.pdf, Accessed: 21/11/2021.

[116]: D. Pozar, “Microstrip Antennas”, *Proceedings of the IEEE, pp. 79-91, 1992.*

[117]: N. Kaur, N. Sharma, N. Singh, “A Study Of Different Feeding Mechanisms In Microstrip Patch Antenna”, *International Journal of Microwaves Applications, pp. 5-9, 2017.*

[118]: P. Soh, M. Rahim, A. Asrokin, and M. Aziz, “Comparative Radiation Performance of Different Feeding Techniques for a Microstrip Patch Antenna”, *2005 Asia-Pacific Conference on Applied Electromagnetics, pp. 35-40, 2005.*

[119]: K. Carver, J. Mink, “Microstrip Antenna Technology”, *IEEE Transactions on Antennas and Propagation, pp. 2-24, 1981.*

[120]: S. Chakravarthy, N. Sarveshwaran, S. Sriharini, M. Shanmugapriya, “Comparative Study on Different Feeding Techniques of Rectangular Patch Antenna”, *2016 Thirteenth International Conference on Wireless and Optical Communications Networks (WOCN), pp. 1-6, 2016.*

[121]: N. Kumar, N. Sharma, “The Various Feeding Techniques of microstrip Patch Antenna Using HFSS”, *International Journal of Electronics and Communication Engineering, pp. 23-29, 2019.*

[122]: H. Lu, W. Wang, Z. Wang, Z. Duan, Y. Liu, “Probe Compensation-Fed Wideband Microstrip Antenna with U-Shaped Parasitic Elements for 5G/WLAN/WiMAX Applications”, *2019 International Workshop on Antenna Technology (iWAT), pp. 25-28, 2019.*

[123]: J. James, P. Hall, *Handbook of Microstrip Antennas*, IEE Electromagnetic Waves Series 28, Peter Peregrinus, 1989.

[124]: R. Harrington, *Time Harmonic Electromagnetic Fields*, McGraw-Hill, 1961.

[125]: P. Dottorato, “Analysis and Design of the Rectangular Microstrip Patch Antennas for TM0n0 operating mode”, *Microwave Journal, pp. 1-10, 2024.*

[126]: I. Khuda, K. Raza, S. Akhtar, H. Naqvi, “On the Design of Electromagnetically Coupled Microstrip Antenna”, *Asian Journal of Engineering, Sciences and Technology, pp. 1-8, 2014.*

[127]: L. Ma, C. Hu, J. Pei, “Polarization Tracking Study of Earth Station in Satellite Communications”, *Earth Science Research, pp.10-18, 2016.*

[128]: B. Evans, *Satellite Communication Systems*, 3rd Edition, IET 2008.

[129]: D. Roddy, *Satellite Communications*, 3rd Edition, McGraw-Hill 2001.

[130]: Nasimuddin, X. Qing, Z. Chen, "Compact Asymmetric-Slit Microstrip Antennas for Circular Polarization", *IEEE Transactions on Antennas and Propagation, pp. 285-288, 2011.*

[131]: M. Sahal, V. Tiwari, "Review of Circular Polarization techniques for design of Microstrip Patch Antenna", *International Conference on Recent Cognizance in Wireless Communication & Image Processing, pp. 663-669, 2015.*

[132]: Nasimuddin, X. Qing, and Z. Chen, "Compact Asymmetric-Slit Microstrip Antennas for Circular Polarization", *IEEE Transactions on Antennas and Propagation, pp. 285-288, 2011.*

[133]: K. Lam, K. Luk, K. Lee, H. Wong, K. Ng, "Small Circularly Polarized U-Slot Wideband Patch Antenna", *IEEE Antennas and Wireless Propagation Letters, pp. 87-90, 2011.*

[134]: H. Wong, K. So, K. Ng, K. Luk, C. Chan, Q. Xue, "Virtually Shorted Patch Antenna for Circular Polarization", *IEEE Antennas and Wireless Propagation, pp. 1213-1216, 2010.*

[135]: Nasimuddin, Z. Chen, X. Qing, "Asymmetric-Circular Shaped Slotted Microstrip Antennas for Circular Polarization and RFID Applications", *IEEE Transactions on Antennas and Propagation, pp. 3821-3828, 2010.*

[136]: E. Carrasco, J. Encinar, "Reflectarray antennas: A review", *Forum for Electromagnetic Research Methods and Application Technologies (FERMAT), pp. 1-16, 2016.*

[137]: P. Nayeri, F. Yang, A. Elsherbeni, *Reflectarray antennas; Theory, Designs and Application*, John Wiley and Sons, 2018.

[138]: E. Carrasco, J. Encinar, “Reflectarray Antennas: A review”, *Foundation for Research on Information Technologies in Society (IT’IS), pp. 1-16, 2016.*

[139]: J. Shaker, M. Chaharmir, J. Ethier, *Reflectarray Antennas: Analysis, Design Fabrication and measurement*, Artech House 2014.

[140]: C. Balanis, *Antenna Theory: Analysis and Design*, Harper & Row,1982.

[141]: D. Guta, Y. Antar, *Microstrip and Printed Antennas: New Trends, Techniques and Applications*, John Wiley & Sons, 2011.

[142]: R. Javor, X. Wu, K. Chang, “Design and Performance of a Microstrip Reflectarray Antenna”, *IEEE Transactions on Antennas and Propagation, pp. 932-939, 1995.*

[143]: M. Chaharmir, “Reflectarray with Variable Slots on Ground Plane”, *IEEE Proceeding of Microwaves, Antennas and Propagation, pp. 436-439, 2003.*

[144]: E. Carassco, J. Encinar, M. Barba, “Wideband Reflectarray Antenna Using True-Time Delay Lines”, *Proceedings of 2nd European Conference on Antennas and Propagation (EUCAP), pp. 1-6, 2007.*

[145]: D. Pozar, T. Metzler, “Analysis of a Reflectarray Antenna using Microstrip Patches of Variable Size”, *Electronics Letters, pp. 1820-1823, 1993.*

[146]: R. Marin, A. Mössinger, J. Freese, A. Manabe, R. Jakoby, “Realization of 35 GHz Steerable Reflectarray Using Highly Anisotropic Liquid Crystal”, *2006 IEEE Antennas and Propagation Society International Symposium, pp. 4307-4310, 2006.*

[147]: R. Marin, A. Mössinger, J. Freese, S. Müller, R. Jakoby, "Basic Investigations of 35 GHz Reflectarrays and Tunable Unit-Cells for Beamsteering Applications", *2005 European Microwave Conference, pp. 1-4, 2005.*

[148]: R. Marin, A. Mössinger, J. Freese, R. Jakoby, "Characterization of 35 GHz Tunable Reflectarray Unit-Cells Using Highly Anisotropic Liquid Crystal", *Engineering, Physics, Materials Science, pp.1-4, 2006.*

[149]: G. Palomino, M. Barba, J. Encinar, R. Cahill, R. Dickie, P. Baine, M. Bain, "Design and Demonstration of an Electronically Scanned Reflectarray Antenna at 100 GHz Using Multiresonant Cells Based on Liquid Crystals", *IEEE Transactions on Antennas and Propagation, pp. 3722-3727, 2015.*

[150]: G. Palomino, R. Florencio, J. Encinar, M. Barba, R. Dickie, R. Cahill, P. Baine, M. Bain, R. Boix, "Accurate and Efficient Modeling to Calculate the Voltage Dependence of Liquid Crystal-Based Reflectarray Cells", *IEEE Transactions on Antennas and Propagation, pp. 2659-2668, 2014.*

[151]: G. Palomino, J. Encinar, M. Barba, "Accurate Electromagnetic Modeling of Liquid Crystal Cells for Reconfigurable Reflectarrays", *Proceedings of the 5th European Conference on Antennas and Propagation (EUCAP), pp. 997-1001, 2011.*

[152]: G. Palomino, J. Encinar, M. Barba, "Design and evaluation of multi-resonant unit cells based on liquid crystals for reconfigurable reflectarrays", *IET Microwave, Antennas and Propagation, pp. 348–354, 2012.*

[153]: G. Palomino, P. Baine, R. Dickie, M. Bain, J. Encinar, R. Cahill, M. Barba, G. Toso, "Design and Experimental Validation of Liquid Crystal Based Reconfigurable Reflectarray Elements With Improved Bandwidth in F-Band", *IEEE Transactions on Antennas and Propagation, pp. 1704-1713, 2013.*

[154]: W. Hu, M. Ismail, R. Cahill, J. Encinar, V. Fusco, H. Gamble, D. Linton, R. Dickie, N. Grant, S. Rea, “Liquid-crystal-based reflectarray antenna with electronically switchable monopulse patterns”, *Electronics Letters, pp. 744-745, 2007.*

[155]: M. Ismail, M. Dahri, “Microwave Absorption Analysis of Reflectarray Resonant Elements based on Non-Homogeneous Substrate”, *15th International Symposium on Antenna Technology and Applied Electromagnetics, pp. 1-3, 2012.*

[156]: S. Bildik, O. Karabey, C. Fritzsch, R. Jakoby, “Temperature Investigations of Liquid Crystal Based Reconfigurable Refiectarrays”, *2012 15 International Symposium on Antenna Technology and Applied Electromagnetics, pp.1-4, 2012.*

[157]: Javor, R. D., X. Wu, K. Chang, “Design and Performance of a Microstrip Reflectarray Antenna*”, IEEE Transactions on Antennas and Propagation, pp. 932-939, 1995.*

[158]: T. Chermaine, C. Tong, “Reflectarray Design for Satellite Applications”, *DSO National Laboratories, Singapore.*

[159]: B. Du, “Analysis and design of simple, low loss and low cost reconfigurable reflectarrays”, *Master Thesis, University of Toronto, 2017*.

[160]: J. Huang, J. Encinar, *Reflectarray Antennas*, IEEE, John Wiley&Sons, 2008;

[161]: J. Torres, N. Ortiz, R. González, N. López, P. Ibernón, “Accurate Optical Observations of Space Objects in GEO and applicability to closer LEO regimes”, *7th European Conference on Space Debris, ESA/ESOC, pp. 1-9, 2017.*

[162]: A. Derneryd, “A Theoretical Investigation of the Rectangular Microstrip Antenna Element”, *IEEE Transactions on Antennas and Propagation, pp. 532-535, 1978.*

[163]: P. Deo, “Beam Steerable Square Loop Antenna over Hybrid High Impedance Surface”, *PhD Thesis, Swansea University, 2011.*

[164]: S. Bhardwaj, Y. Samii, “Revisiting the Generation of Cross-Polarization in Rectangular Patch Antennas: A Near-Field Approach”, *IEEE Antennas and Propagation Magazine, pp. 14-38, 2014.*

[165]: J. Osborn, L. Blacketer, M. Townson, O. Farley, “Astrosat: forecasting satellite transits for optical astronomical observations”, *Monthly notices of the Royal Astronomical Society, pp.1848-1853, 2021.*

[166]: M. Nishamol, V. Sarin, D. Tony, P. Mohanan, K. Vasudevan, “Single Feed Circularly Polarized Cross patch Antenna”, *2009 Applied Electromagnetics Conference (AEMC), pp. 1-3, 2009.*